



Al Sariri, Tahani Mohammed Sulaiman (2023) *Multiscale and numerical simulation of cancer hyperthermia based on magnetic nanoparticles delivery*. PhD thesis.

<https://theses.gla.ac.uk/83398/>

Copyright and moral rights for this work are retained by the author

A copy can be downloaded for personal non-commercial research or study, without prior permission or charge

This work cannot be reproduced or quoted extensively from without first obtaining permission in writing from the author

The content must not be changed in any way or sold commercially in any format or medium without the formal permission of the author

When referring to this work, full bibliographic details including the author, title, awarding institution and date of the thesis must be given

Enlighten: Theses

<https://theses.gla.ac.uk/>
research-enlighten@glasgow.ac.uk

Multiscale and Numerical Simulation of Cancer Hyperthermia Based on Magnetic Nanoparticles Delivery

Tahani Mohammed Sulaiman Al Sariri

Submitted in fulfilment of the requirements for the
Degree of Doctor of Philosophy

School of Mathematics and Statistics
College of Science and Engineering
University of Glasgow



University
of Glasgow

October 2022

Abstract

Cancer is one of the primary causes of death worldwide. The hyperthermia cancer treatment which is used nowadays is very harmful, because it destroys both tumorous and healthy cells at the same time. Magnetic nanoparticles with different sizes and materials are used to improve cancer hyperthermia and minimize its side effects by localizing the heat within the tumour only. These particles destroy both the cancer and tumour cells by transforming the energy of the magnetic field to heat. The purpose of this thesis is to study the heat distribution in the tumour, which in turn helps to find the optimal hyperthermia treatment. Also, we aim to study the interaction between the tumour and surrounding tissues.

In this thesis we derive new systems of homogenised partial differential equations (PDEs) describing blood transport, delivery of nanoparticles, and heat transport to investigate cancer hyperthermia driven by the application of the magnetic field applied to nanoparticles. We assume that the particles are injected into the tumour vessels and then they extravasate to the tumour interstitial space if they are sufficiently small to be transported through the pores of the vascular walls. Otherwise, the adhesion between the particles and vessels' wall is to be considered as a primary transport mechanism, and the particles cannot be transported from the vessels to the tumour interstitium. We study the influence of vessels' geometry as the tumour vessels are not regular and their tortuosity varies within the tumour. In addition, we investigate the effect of various injection conditions on the temperature maps. The temperature should be above 42°C to destroy cancer cells but for at most two hours to avoid heating the surrounding healthy tissue. We determine the best magnetic intensity, injection time, wall shear rate, and concentration of nanoparticles to achieve the above-mentioned condition. To investigate the relation between the tumour and the surrounding healthy tissue and the impact of the magnetic field on the fluid flow, we derive a new system of homogenised differential equations which expresses the fluid flow of the tumour that interacts with surrounding healthy tissue and influenced by a non-homogeneous magnetic force. The latter is obtained starting from the previously derived differential equations which in this context represents the mesoscale differential equations. We exemplify the results for the case of a homogenous magnetic force that is applied in the direction of the mesoscale cylindrical tumour region.

Contents

Abstract	i
Acknowledgements	viii
Declaration	ix
Publications and Presentations	x
List of notations	xii
1 Introduction	1
1.1 Motivation	1
1.2 Thesis' structure	2
1.3 Background	4
1.3.1 Cancer	4
1.3.2 Nanoparticles	7
1.3.3 The asymptotic homogenization method	13
1.3.4 Previous works	16
2 Multiscale model of IONP delivery and heat transport	22
2.1 Introduction	22
2.2 Mathematical modeling	23
2.2.1 Interstitial fluid transport	25
2.2.2 Microvascular flow	25
2.2.3 Transport of particles	25
2.2.4 Heat convection in the tumour	26
2.2.5 Interface conditions	27
2.3 Non-dimensional form of the model	28
2.4 The asymptotic homogenisation method	29
2.4.1 The upscaled governing equations for the vessels	30
2.4.2 The upscaled governing equations in the tumour interstitium	35
2.4.3 The macroscale model obtained via asymptotic homogenisation	39

2.4.4	The effective coefficients and microscale cell problems	40
2.5	The mathematical model for a spherical tumour	43
2.5.1	Initial and boundary conditions	44
2.6	Results and discussion	45
2.6.1	Particle transport	46
2.6.2	Heat Transport	49
2.6.3	The influence of absorption rate and vessels' tortuosity on the heat distribution	52
2.7	The difference between our approach and the one by Nabil and Zunino [94]	55
2.8	Concluding remarks	56
3	Optimal hyperthermic condition in vascular tumours	58
3.1	Introduction	58
3.2	Mathematical modelling	60
3.2.1	Fluid flow	61
3.2.2	Advection, diffusion, and adhesion of nanoparticles	62
3.2.3	Heat convection and diffusion	63
3.2.4	Non-dimensionalisation of the model	66
3.2.5	The homogenised model	67
3.2.6	The homogenised model in radial symmetry	69
3.3	Results and Discussion	71
3.3.1	The role of vessels' tortuosity	73
3.3.2	A parametric study of hyperthermic temperature and duration	78
3.4	Concluding remarks	81
4	The tumour fluid flow and surrounding healthy tissue	84
4.1	Introduction	84
4.2	Mathematical modelling	85
4.3	The derivation of fluid flow in mesoscale	87
4.3.1	The influence of the magnetic force on the fluid flow	88
4.3.2	The dimensional form of the model	89
4.3.3	The fluid flow for the tumour and healthy cells with magnetic force	90
4.4	Non-dimensional form of the model	91
4.5	Model derivation via the asymptotic homogenisation technique	93
4.5.1	The asymptotic homogenisation steps	93
4.6	The solution of the mesoscale cell problems	102
4.7	The homogenised solution at the macroscale	105
4.8	Concluding remarks	109

5 Conclusion	113
5.1 Conclusion summary	113
5.2 Future work	115

List of Tables

2.1	List of parameters and their values.	46
2.2	The computational result for the non-dimensional vessels' thermal conductivity with different vessels tortuosity from the analysis by Penta and Ambrosi [103] and Mascheroni and Penta [85]. The parameters r_c is the radius of the vessels, ω is the frequency of the vessels, and A is the vessels' amplitude.	49
3.1	The values of model's parameters.	72
3.2	Particle diffusivity and thermal conductivity values for various vessel geometry. The parameter λ is a label for tortuosity, ω is the vessels' frequency, A is the amplitude of the vessels, and r_c is the radius of the vessels.	74
3.3	Properties of magnetic nanoparticles.	77
3.4	Estimates for the hyperthermic temperature and duration available from the published literature.	79
4.1	The value of the parameters.	103
4.2	The components of the vessels and interstitial hydraulic conductivities \bar{D} , and \bar{G} for the whole tissue which combines the tumour and healthy tissues along x, y, and z.	107

List of Figures

1.1	Image of vessels' structure.	5
1.2	A schematic of delivering the drugs by the nanoparticles into the tumour as discussed by Cho et al. [27].	9
1.3	Example of multiscale method (Homogenization technique).	14
2.1	The description of the tumour compartments and the exchange of fluid, mass, and heat between them.	24
2.2	A schematic of the macroscale and the microscale difference.	24
2.3	The ratio between the homogenised and base vessels' diffusive conductivities values.	42
2.4	The distribution of nanoparticles in the tumour regions at time (6h-24h).	47
2.5	The distribution of nanoparticles in the tumour regions at time (24h-96h).	48
2.6	The nanoparticles delivery in the tumour with high uptake rate.	49
2.7	Temperature maps for the first 24h in both the vessels (a) and the interstitium (b) vs radius-low uptake rate.	50
2.8	Temperature maps in both the vessels (a) and the interstitium (b) vs radius-(low uptake rate) from day 1 (24h) to day 4 (96h).	51
2.9	The structural difference between the healthy and tumour vessels.	51
2.10	The vessels' temperature vs the radius r with different vessels' structures at time 24h.	52
2.11	The vessels' concentration or temperature vs the tumour radius r for a healthy non-tortuous microstructure.	53
2.12	Temperature maps vs normalised radius at increasing absorption rate for different microvascular geometries after 24h.	54
3.1	A schematic diagram of hyperthermia cancer treatment using large size of magnetic nanoparticles (MNP). The region Ω_v is for the tumor vessels, Ω_t is the tumour interstitium, and Γ (the vessels' wall) is the interface between the two regions.	61
3.2	A schematic description of the boundary condition related to the concentration of nanoparticles.	70

3.3 The concentration of nanoparticles c_v as a function of tumour radius r for various values of vessels' tortuosity as specified in the legends and for time moment (a) $t = 20$ minutes (b) $t = 50$ minutes (c) $t = 2$ hours and (d) $t = 5$ hours. 75

3.4 The concentration of nanoparticles vs time, and the density of nanoparticles that adhering the vessels' wall vs radius of tumour. 76

3.5 The temperature maps with different particles material that adhere to the vessels' wall and vessels' tortuosity. 78

3.6 A figure describing the computation of hyperthermic temperature and time in the present work. 80

3.7 Computation of the hyperthermic time and temperature, and optimal values of magnetic field intensity and injection time. 81

3.8 Regions of safe and effective hyperthermia treatment in the parameter space of the model. 82

4.1 The three levels of homogenization that describe the interaction between the healthy and tumour cells. The volume portion Ω_{Hv} denotes the healthy vessels, Ω_{Ht} is the healthy interstitium, Ω_{Tv} is the tumour vessels, and Ω_{Tt} is the tumour interstitium. 86

4.2 The solution of the auxiliary vectors at the mesoscale. 105

4.3 The pressures maps of the vessels' and interstitial compartments and the direction of the fluid flow with different size of the tumour. 110

4.4 The pressure difference of the vessels and interstitial compartments with different tumour radius (a) 0.1 (b) 0.3 (c) 0.5. The values of the parameters are specified in Table 4.1 and Table 4.2. 111

4.5 The pressures maps with magnetic force applying on the z-direction. 112

Acknowledgements

Foremost, all praise and thanks to Allah.

Then, I would like to express my profound gratitude to my first supervisor Raimondo Penta who assisted me with big patience to complete my work. He was a very supportive and positive person. Also, special thanks to my second supervisor Radostin Simitev who assisted me to improve my research skills and taught me many new things. Words are not enough to thank these two persons for all their efforts to complete my PhD research.

I also would like to express my deepest appreciation to my son (Al Khalil) who was with me in the whole PhD journey. He was my best friend, and he was the only one who made me happy under all the stresses that I have faced. Also, my PhD would not be completed without the support and motivation that I got from my lovely husband (Ahmed). He always believes in me and in my abilities. Although he was in my country, he did his best to help me in different ways.

Special and big thanks to my parents, mother- and father-in-law, brothers, sisters, nephews (including the sole of my nephew 'Ayman'), and close friends for their prayer and support during my PhD. Also, big thanks to my neighbours and friends in Glasgow who were my second family abroad.

Finally, I would like to acknowledge my sponsors Ministry of Higher Education, and Sultan Qaboos University for providing me the scholarship and necessary funding to complete my PhD program.

Declaration

This thesis is represented a work that is done in the period (2018-2022) at the School of Mathematics and Statistics to achieve the degree of Doctor of Philosophy at university of Glasgow. With the exception of Chapter 1, which contain introductory material, I declare that all work in this thesis was carried out by myself with supervision from Dr. Raimondo Penta and Prof. Radostin Simitev, unless otherwise explicitly stated.

Publications and Presentations

The main results of this work are published in different journals or in progress for publication.

- Chapter 2 is published as
Tahani Al Sariri and Raimondo Penta. "Multi-scale modelling of nanoparticle delivery and heat transport in vascularised tumours." *Mathematical Medicine and Biology: A Journal of the IMA*, Volume 39, Issue 4, December 2022, Pages 332–367.

<https://doi.org/10.1093/imammb/dqac009>

- Chapter 3 is published as
Al Sariri, Tahani, Radostin D. Simitev, and Raimondo Penta. "Optimal heat transport induced by magnetic nanoparticle delivery in vascularised tumours." *Journal of Theoretical Biology* (2022): 111372.

<https://doi.org/10.1016/j.jtbi.2022.111372>

- Chapter 4 is in preperation for publication
Al Sariri, Tahani and Raimondo Penta. "Multiscale homogenisation of the role of an applied magnetic field on the fluid flowing in heterogeneous cancerous tissues."

The findings contained in this thesis have been disseminated in different conferences.

- The results related to 'Multi-scale modelling of nanoparticle delivery and heat transport in vascularised tumours' were presented in:
 - Poster competition organized by Oman embassy on 8th of November 2020.
 - Poster presentation in BYMAT conference on 3^d of December 2022.
 - Presentation in BMC BAMC 2021 conference
 - Poster presentation in 5th Soft tissue modelling on 3^d June 2021.
- The results related to 'Optimal heat transport induced by magnetic nanoparticle delivery in vascularised tumours' were presented as
 - Presentation in BAMC 2022.

- Poster in poster competition organized by Soft-Mech group on 31 of May 2022.
- Poster online presentation in ECMTB (12th European Conference on Mathematical and Theoretical Biology) on 19-23 September 2022.
- The results related to 'The multiscale model of the tumour fluid flow and surrounding healthy tissue subjected to magnetic force' were presented as
 - Presentation in IMG conference on 22-26 August 2022.
- The following presentations were aimed at a general audience
 - Three minute thesis presentation in 2020 (in person), and in 2021 (online).
 - Visualize your thesis in one minute video on 23^d of August 2021. It is available online, see, <https://www.youtube.com/watch?v=xvT7FY-4GWI>.

List of notations

These are the list of the symbols and the others needed are in the text.

Ω_t	Tumour interstitial domain [Chapter 2, 3]
Ω_v	Vessels' domain [Chapter 2, 3]
Ω_T	Tumour tissue region [Chapter 4]
Ω_H	Healthy tissue region [Chapter 4]
Γ	Interface condition between the tumour vessels and interstitial compartments [Chapter 2, 3]
Γ_m	Interface condition between the tumour and healthy regions [Chapter 4]
ϵ	Ratio between the vessels and tumour scales [Chapter 2, 3]
ε	Ratio between the tumour and the whole tissue that consists of tumour and healthy tissues [Chapter 4]
c_v	Concentration of nanoparticles in the vessels [Chapter 2, 3]
c_t	Concentration of nanoparticles in the tumour interstitium [Chapter 2, 3]
\mathbf{u}_t	Tumour interstitial fluid velocity [Chapter 2, 3]
\mathbf{u}_v	The vessels' fluid velocity [Chapter 2, 3]
p_t	Tumour interstitial fluid pressure [Chapter 2, 3]
p_v	The vessels' fluid pressure [Chapter 2, 3]
T_t	The temperature of the tumour interstitium [Chapter 2, 3]
T_v	The temperature of the vessels [Chapter 2, 3]
p_H	The pressure of the vessels in the healthy region [Chapter 4]
p_T	The pressure of the vessels in the tumour region [Chapter 4]
g_H	The pressure of the interstitium in the healthy region [Chapter 4]
g_T	The pressure of the interstitium in the tumour region [Chapter 4]
\mathbf{u}_T	The fluid velocity of the vessels in the tumour region [Chapter 4]
\mathbf{u}_H	The fluid velocity of the vessels in the healthy region [Chapter 4]
\mathbf{v}_T	The fluid velocity of the interstitium in the tumour region [Chapter 4]
\mathbf{v}_H	The fluid velocity of the interstitium in the healthy region [Chapter 4]

D_v	Diffusivity of the nanoparticles in the capillaries [Chapter 2, 3]
D_t	Diffusivity of the nanoparticles in the interstitium [Chapter 2, 3]
K_t	Thermal conductivity of the tumour [Chapter 2, 3]
K_v	Thermal conductivity of the vessels [Chapter 2, 3]
d	Reference micro-scale [Chapter 2, 3]
L	Reference macro-scale [Chapter 2, 3]
L_p	Vessels' permeability [Chapter 2, 3]
t	The time [Chapter 2, 3, 4]
L_H	The permeability of healthy vessels [Chapter 4]
L_T	The permeability of the tumour vessels [Chapter 4]
K_H	The hydraulic conductivity of the healthy vessels [Chapter 4]
K_T	The hydraulic conductivity of the tumour vessels [Chapter 4]
E_H	The hydraulic conductivity of the healthy interstitium [Chapter 4]
E_T	The hydraulic conductivity of the tumour interstitium [Chapter 4]
Ω_{Hv}	The domain of the vessels' healthy region [Chapter 4]
Ω_{Tv}	The domain of the vessels' tumour region [Chapter 4]
Ω_{Ht}	The domain of interstitial compartments for the healthy region [Chapter 4]
Ω_{Tt}	The domain of interstitial compartments for the tumour region [Chapter 4]
L_m	The average size of the whole tissue [Chapter 4]
\mathbf{x}	The macroscale variable [Chapter 2, 3, 4]
\mathbf{y}	The microscale variable [Chapter 2, 3, 4]

Chapter 1

Introduction

1.1 Motivation

Cancer is one of the most relevant diseases that causes death. It is considered as a genetic disease that develops due to unrestricted, fast, and random division of the cells. According to UK cancer research, the number of cancer cases was around 375,400 in 2016-2018 and the number of deaths caused by cancer was around 167,200 in 2017-2019 [19]. These numbers are growing every year due to the human life habit [18], and around 40% of people diagnosis with cancer in their life [137]. Cancer hyperthermia treatment is an example of the strategies that are used to treat cancer. We concentrate on this type of treatment because of different factors and benefits of using it as discussed by Espinosa et al. [42]. First, the heat has an impact on the cell nucleus and proteins as it can inhibit the DNA, RNA, protein synthesis, and chromosomal damage. Secondly, the response of healthy and tumour tissues to heat is different, because they have different vascular structure. For example, the thermal dose of 45°C at 30-60 min improves the blood perfusion in the healthy cells which causes dissipation of heat and prevents extreme increasing of temperature. On the other hand, the tumour is less responsive to the heat dissipation due to its vasculature structure which is hyper-permeable, tortuous, and disorganized. Therefore, it is possible to increase the temperature of the tumour without influencing the surrounding healthy tissue. Thirdly, the hyperthermia can also break the collagen fibers which helps to improve the distribution of chemotherapeutics. Finally, the recent researches show that the hyperthermia treatment using nanoparticles can lead to cell death without macroscopic rise in temperature. This can be explained as the high temperature increases within the lysosomes, leading to cell death. This is very useful to be applied in apoptosis-resistant cancer cells. The most common nanoparticles that are used in hyperthermia treatment are gold nanoparticles mediated by photothermal therapy, and magnetic nanoparticles mediated by magnetic field. In the case of gold nanoparticles, the photothermal NIR (near-infra red) has limitation on the tumour depth that can be reached [66]. Therefore, this strategy might not be efficient to kill malignant cells uniformly. As a result, magnetic nanoparticles will be more appropriate to be used in the hyperthermia

treatment which is the one that we are studying in this research.

The biological system of the tumour consists of different components at different length scales. The distance between the tumour vessels is very small in comparison with the size of the tumour. The latter length is also small when we compare it with the whole tissue that consists the tumour and healthy cells. A complete analysis and solution of such heterogeneous media is very complicated and not easy to be solved in three dimensions. Therefore, the asymptotic homogenization technique can be used for porous media and it is applied here to combine different scales together. This leads to the derivation of a new system of equations at a coarser scale based on information at a finer scale. In this way the problem is simplified and can be solved in three dimensions at a reduced computational cost.

In this thesis we discuss different models of cancer hyperthermia treatment using magnetic nanoparticles which are obtained by means of multiscale homogenisation. To address the models, we need to study the fluid flow, as well as particles and heat transport. The aim of this work can be stated in different points as follows.

- Illustrating the distribution of the heat generated by magnetic nanoparticles in the tumour tissue. Here, we assume that the nanoparticles can be transported between the tumour vessels and interstitial compartments.
- Identifying the optimal values of different parameters that are related to vessels' structure, and particles and magnetic field properties to achieve the required hyperthermia treatment by considering the adhesion between the particles and vessels wall.
- Determining the interaction between the tumour and surrounding healthy tissue. Here, we primarily focus on the fluid flow, and provide a basis for future extensions for both drug and heat transport.

The thesis is structured in chapters as described in the next section.

1.2 Thesis' structure

In Chapter 1 we introduce the topic and we illustrate the motivation and background for conducting the present analysis.

In Chapter 2 we focus on modelling of cancer hyperthermia driven by the application of the magnetic field to magnetic nanoparticles. We assume that the particles are interacting with the tumour environment by extravasating from the vessels into the interstitial space. We start from Darcy's and Stokes' problems in the interstitial and fluid vessels compartments. Advection–diffusion of nanoparticles takes place in both compartments (as well as uptake in the tumour

interstitium), and a heat source proportional to the concentration of nanoparticles drives heat diffusion and convection in the system. The system under consideration is intrinsically multiscale. The distance between adjacent vessels (the microscale) is much smaller than the average tumour size (the macroscale). We then apply the asymptotic homogenisation technique to retain the influence of the micro-structure on the tissue scale distribution of heat and particles. We derive a new system of homogenised partial differential equations (PDEs) describing blood transport, delivery of nanoparticles and heat transport. The new model comprises a double Darcy's law, coupled with two double advection–diffusion–reaction systems of PDEs describing fluid, particles and heat transport and mass, drug and heat exchange. The role of the micro-structure is encoded in the coefficients of the model, which are to be computed solving appropriate periodic problems. The structure of the microvessels coincides with the one implemented and discussed in [103]. We show that the heat distribution is impaired by increasing vessels' tortuosity and that regularization of the micro-vessels can produce a significant increase (1–2 degrees) in the maximum temperature. We quantify the impact of modifying the properties of the magnetic field depending on the vessels' tortuosity.

After we find how the heat is transported in the tumour, we aim to control the heat production by finding the optimal hyperthermia treatment using magnetic nanoparticles. Therefore, in Chapter 3, we describe a novel mathematical model for blood flow, delivery of large size of nanoparticles, and heat transport in vascularised tumour tissue. The model, which is derived via the asymptotic homogenization technique, provides a link between the macroscale behaviour of the system and its underlying, tortuous micro-structure, as parameterised in Penta and Ambrosi [103]. It consists of a double Darcy's law, coupled with a double advection-diffusion-reaction system describing heat transport, and an advection-diffusion-reaction equation for transport and adhesion of particles. Particles are assumed sufficiently large and do not extravasate to the tumour interstitial space but blood and heat can be exchanged between the two compartments. Numerical simulations of the model are performed using a finite element method to investigate cancer hyperthermia induced by the application of magnetic field applied to injected iron oxide nanoparticles. Since tumour microvasculature is more tortuous than that of healthy tissue and thus suboptimal in terms of fluid and drug transport, we study the influence of the vessels' geometry on tumour temperature. Effective and safe hyperthermia treatment requires tumour temperature within certain target range, generally estimated between 42°C and 46°C , for a certain target duration, typically 0.5 h to 2 h. As temperature is difficult to measure in situ, we use our model to determine the ranges of tortuosity of the microvessels, magnetic intensity, injection time, wall shear stress rate, and concentration of nanoparticles required to achieve given target conditions.

In the previous two models, we just focus on the tumour tissue only, but the tumour in

reality interacts with surrounding tissues. Also, that will allow us to test the impact of the optimal values that are founded in the previous chapter on the healthy cells. As a result, in Chapter 4, new theoretical and numerical investigations are addressed to illustrate the fluid flow interaction between the tumour and surrounding healthy tissue that are influenced by inhomogeneous magnetic force. We start from the final macroscale fluid flow system of Al Sariri and Penta [3] which is considered here as the mesoscale. Moreover, we combine the latter with the fluid flow in porous media influenced by a body force as discussed by Penta et al. [106] to find the final macroscale system. We have started with four equations that describe the fluid pressures in the vessels and interstitial compartments of the tumour and healthy regions in the mesoscale. However, we end up with two partial differential equations only in the macroscale in which one equation combines the vessel's fluid flow of both regions and the other on for interstitial compartments. The influence of each region is encoded in the value of vessels' permeability, hydraulic conductivity tensors, and the magnetic forces which can be obtained by solving the mesoscale systems. We start solving the system by assuming that the magnetic force is homogeneous and it is applied in the z -direction. The uniform magnetic force does not affect the fluid pressures at the macroscale. However, the homogeneous magnetic force has an impact on the fluid flow.

1.3 Background

1.3.1 Cancer

Tumours are cancerous tissues consisting of different cells which interact with each other by heterotypic interaction i.e. involving both cancerous and non-cancerous cells and constituents. Cancer arises from damages in DNA which causes mutations. These mutations later transform the normal cells to the malignant ones. Also, the mutations increase the proliferation rate and decrease the death rate of the malignant cell which help the tumour to grow faster than any other cells. The initial size of the tumour is a few millimeters in diameter and it takes months or years to exceed this size. The tumour cells receive nutrients from the surrounding. Therefore, the cells which are close to the surrounding can get the nutrients, but the cells at the center are far and cannot get adequate nutrients. As a result, tumour angiogenic factor (TAF) will be sent to the surrounding to produce vessels capable of providing nutrients more uniformly in the inner regions. When the TAF reaches the endothelial cells, the endothelial cell (EC) produces the sprouts towards the tumour. These vascular connections help the tumour to get nutrients which speed up its growing. Subsequently, the malignant cells spread in different parts of the body.

As a result, the cancer cells are characterised by different hallmarks which enable them to develop and growth in the body. The cancer cells preserve the chronic proliferative signals and

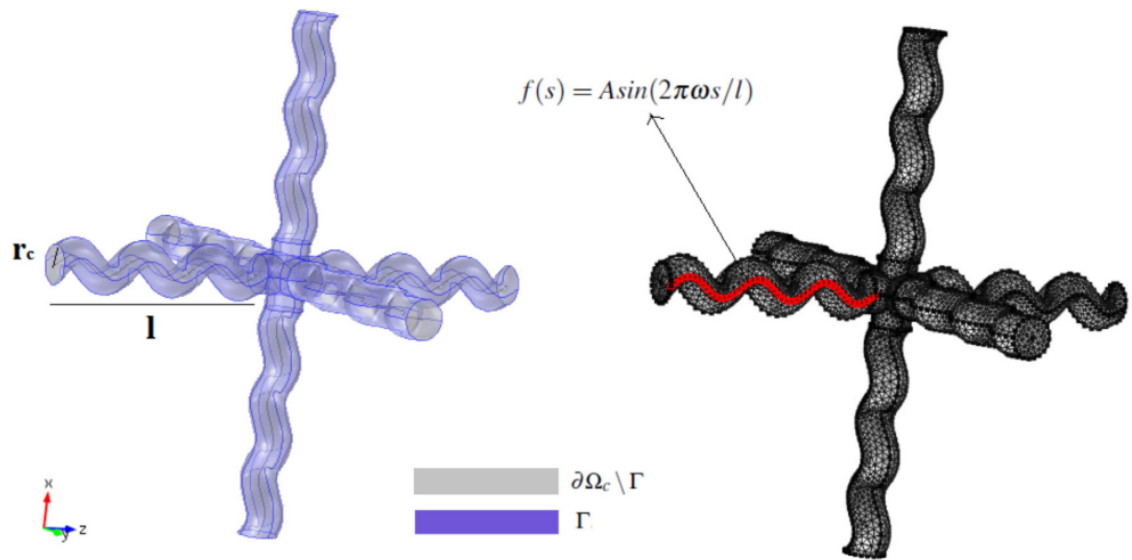


Figure 1.1: Image of vessels' structure. The microscale representative capillary Ω_c with Γ is the curved surface of the capillary branches, while the periodic boundaries are $\partial\Omega_c/\Gamma$. The parameter r_c is the capillary radius, l is the one-sided branch length, ω is the vessels' frequency, A is the vessels' amplitude, and s is the local parametrisation of the spatial coordinate, such that $0 < s < l$. This figure is reproduced from Penta and Ambrosi [103] with permission from Elsevier.

avoid the suppressors genes which regulate cell duplication. While normal cells replication is limited, cancer cells can grow in an uncontrolled way thus producing the tumour mass. In addition, tumours are capable of obtaining nutrients and oxygen from the angiogenic microvasculature. Subsequently, the malignant cells spread in different parts of the body, as reported by Hanahan and Weinberg [57].

The structure of the vascular networks in tumours

The geometry and functionalities of tumour vessels are different from healthy ones as they are characterised by irregular diameter, leakiness, heterogeneous, abnormal branching pattern [86], and tortuosity [59]. All of these factors play a role on the angiogenesis, tumor growth, metastasis, and drug delivery. For the vessels' leakiness, the size of vessels' pores has been reported as approximately 40 – 200 nm [121] by means of electron microscopy measurements for both brain and peripheral tumors, while using intra-vital fluorescence microscopy, the pores' size for malignant brain was observed to range between 7 – 100 nm, and for peripheral tumors approximately between 200 – 1200 nm [62]. Penta and Ambrosi [103], and Mascheroni and Penta [85] discussed the relation between vessels' geometry (tortuosity) and fluid and drug transport. They showed that the capillary hydraulic conductivity and diffusion of macromolecules are highly impaired by tortuosity. They designed the structure of the microvessels as three interconnected three-dimensional domains (see Figure 1.1), where the center line of each branch is defined by

the function

$$f(s) = A \sin(2\pi\omega s/l),$$

where A is the amplitude, ω is the spatial frequency, s is the local parametrisation along the branch, and l is branch length and we have $0 \leq s \leq l$, [103]. The tumour interstitium is the domain which is complementary to vessels' compartment in the cubic cell.

The geometry of the vessels changes by varying the spatial frequency ω and the amplitude A (this latter is varied in fractions of the vessels radius r_c which corresponds to the radius of the interconnected cylinder at $\omega = 0$, or, equivalently, the radius of each of the circular periodic faces $\partial\Omega \setminus \Gamma$).

Penta and Ambrosi [103] performed finite elements three-dimensional simulations of periodic Stokes' problems by varying the value of the amplitude and spatial frequency of this microstructure. In that work, they identify the tortuosity of the vessels with this couple of parameters A and ω , and the associated value of the parameters which are affected by these changes. The parameters affected by changes in the tortuosity are the vessels volume portion, the interstitium volume portion, the microvessels interface area, and the capillary hydraulic conductivity. Mascheroni and Penta [85] used the microstructure conceived in [103] to obtain the value of particles diffusivity at varying tortuosity, i.e. by varying the amplitude A and spatial frequency ω along the center line.

In other contexts, the tortuosity of the vessels can be measured using metric distance which is calculated by dividing the actual vessel path length by the linear distance between the endpoints [125]. However, this method is less accurate with very high vessels frequency and the sum of angles metrics (SOAM) can be used in this case. The latter measured by dividing the total angles in the vessels' curves by the sum of the path lengths as discussed by Bullitt et al. [17].

Therefore, to enhance the drugs or particles delivery in the tumours, we need to normalize the vessels which can be achieved by varying vessels size, shape, and branching. Izumi et al. [67], Jain [68] clarified that VEGF inhibitors, angiogenesis inhibitors, and even herceptin can be used to normalize the tumour vessels. The vessels normalization decreases the leakiness of the vessels and the resistance of blood flow which are caused by the vessels' tortuosity and diameter. As a result, normalizing the vessels structure improves the blood flow, and drug delivery in the tumour [86].

Strategies for treating cancer

There are different types of cancer treatment and each of these strategies has advantages and disadvantages side effects. For example, surgical treatment is used usually to remove large tumour and cryosurgery (i.e. the technique of destroying a tumour by delivering an extremely cold liquid) is used to treat precancerous or tumour which is not spread to different parts [136]. In chemotherapy, the anti-cancer drug is administered the tumour as pills, injection, or applied on

the skin. These chemotherapeutic methods unfortunately destroy both the healthy and the tumour cells and cause many side effects like hair loss, vomiting, anemia, and many others. Also, many researches suggest the use of gene therapy to treat cancer cells. This strategy is aimed at inhibiting the angiogenesis process (i.e. the sprouting of new blood vessels) to stop the spreading of the tumour [46].

Hyperthermia cancer treatment is an anti-cancer therapy in which the tumour is exposed to high temperature causing cell death. The word hyperthermia comes from Greek, '*hyper*' which means above or over, and '*thermo*', which means hot [130]. Hyperthermia is a type of cancer treatment which damages the proteins and the structure of the tumour [148]. This strategy is usually used together with radiation therapy or chemotherapy, because it can reach some cancer cells which cannot be destroyed directly by the radiations alone. Hyperthermia treatment can be applied locally or all over the body depending on the type of tumour, size, and location [25, 26]. There exist three main types of hyperthermia treatments depending on the extent of the application, that is, whole-body, regional and local [120]. The whole-body hyperthermia involves heating the whole body using different heat sources such as radio-frequency waves, microwaves, or ultrasound waves, but there are negative implications for the healthy cells. This method is reported to be effective for melanoma [26]. Regional hyperthermia commonly used to heat big selective area like an organ and it requires thermal perfusion during the therapy [43]. Local hyperthermia is the newest method and it is used to destroy the tumour in small selective area, but it requires a heat source produced from nanoparticles like magnetic nanoparticles [45]. Hyperthermia efficiency for destroying cancer cells is related to the temperature that can be reached in appropriate period of time during the treatment without affecting the healthy tissues. At temperature more than 42.5°C, the cancer cells have higher possibility to die and their rate of death rises as the temperature increases [6, 92].

1.3.2 Nanoparticles

Nanoparticles are ultra-fine particles that were discovered in 20th century, and the scientific description of the metal and optical properties of the nanoparticles was defined by Michael Faraday in 1857 [133]. However, the accurate measurement and visualization of nanoparticles was developed by Richard Adolf Zsigmondy in 1914 using dark field ultra-microscopy. These particles can be categorized depending on their size, origin (i.e. can be nature or anthropogenic), and their chemical composition (i.e. can be organic or inorganic). Nanoparticles are used to improve different sensing devices due to their chemical and physical properties [82].

In 1950 and 1960 the first preliminary attempts to use nanoparticles in the context of drug delivery were made depending on their chemical and physical properties [129]. The latter are related to the materials used to make the particles, and the relevant examples include copper, zinc, titanium,

magnesium, gold, alginate, and silver [58]. Nanoparticles have better penetration and low risk comparing with any other drugs [87]. The nanocarriers (i.e. the drug delivery vectors) control the releasing of medicine inside the tumour to avoid the toxicity in the surrounding. Nanoparticles are able to remain in the blood without causing any toxicity. Their sizes should be big enough to avoid the leakage in the blood and small enough to get away from the macrophages which exist in the reticuloendothelial system (i.e. part of immune system). These particles also should have a hydrophilic surface which prevents capturing them by the macrophages. Further, the nanoparticles have the ability of doing the multifunctional job, so they can carry multiple drugs at the same time [27]. Moreover, the shape of nanoparticles plays important role on their different biological properties like drug delivery, deformability, biodistribution, uptake, and toxicity. For example, the spherical nanoparticles is less toxic, faster, and more easily delivered to the tumour in comparison with rod or fiber nanoparticles [24, 80]. Also, spherical nanoparticles can flow through the vessels better than the non-spherical ones [75]. This is due to increased adhesion between non-spherical nanoparticles and vessel walls.

There are two methods that are used to build the structure of nanoparticles which are bottom-up approach, and top-down approach. The former is also called *construction method* which means that the nanoparticles are made from simple substances like atoms which are converted to clusters, and finally to nanoparticles [149]. The latter approach is the opposite, as a bulk material like a complex molecule is destructed to smaller units which are used to make the nanoparticles using different technique including laser ablation, and mechanical milling [41]. Different shapes and sizes of nanoparticles can then be obtained by changing different parameters during the nanoparticles synthesis process.

Delivery of nanoparticles

The nanoparticles are delivered to the tumour by two ways which are passive and targeting deliver. In the passive case, the nanoparticles are injected into the vessels. Then, due to high permeability of the tumour vessels (the pores of the vessels measuring approximately 600 nm), the nanoparticles are transported from the vessels into the tumour interstitial compartment. After that, the particles interact with the tissue and release the drugs. This approach minimizes the toxicity and drug transport to the healthy vessels which possess very low permeability.

It was during the 19th century that Paul Ehrlich described the active process, which means that the nanoparticles will be delivered to a specific area in the body [56]. In this approach, the nanoparticles should be carried in nanocarriers that have effective ligand and antigens that can be targeted to the tumour only [139]. Once the particles ligand binds to the receptor on the cell surface, the particles move inside the cell via the endosome (a membrane with a diameter of approximately 500 nm, through which particles enter the cell). When the pH value of the endosome is changed to acidic and lysosome (A membrane contains digestive enzyme) is active,

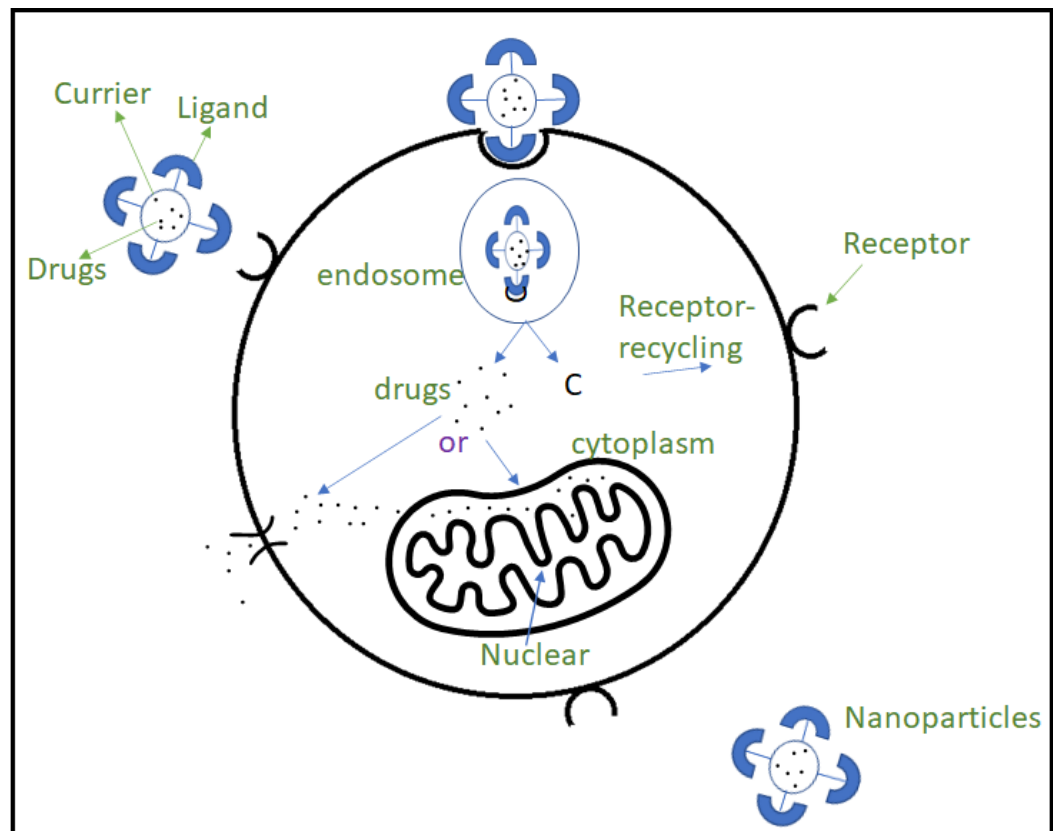


Figure 1.2: A schematic of delivering the drugs by the nanoparticles into the tumour as discussed by Cho et al. [27].

the lysosome destroys the nanocarriers. Subsequently, the drugs are released and proceeded to cytoplasm (a substance located around nucleus of the cell). After that, the drugs targeted to certain organ and the receptors returns to the surface of the cell to be bound with other ligands [27], see Figure 1.2.

The production and types of nanoparticles

Nanoparticles are produced using different materials like proteins, polysaccharides (type of carbohydrates) and synthetic polymers (can be made in the industry using petroleum oil). The type of the material that is used in nanoparticles production depends on the size of nanoparticles, surface characteristic, degree of biodegradability (i.e. degradation of such material to small substances), biocompatibility (i.e. beneficial response at certain situation), toxicity, and drug release profile [90].

There are different types of nanoparticles, such as:

Silver nanoparticle which is used as antimicrobial agent because of its ability against bacteria, viruses, and other micro-organisms. Also, this type of nanoparticles is used in textile industries,

water treatment, and sun cream lotion [58].

Gold nanoparticle which is used to identify protein interaction, and different classes of bacteria. Also, it is used to detect presence of DNA in a sample, and cancer cells specially in cancer diagnosis [58]. Gold nanoparticle is characterised by biocompatibility and it is used to improve radiation therapy using different photon beams [153].

Alloy nanoparticle which is Ag-Au nanoparticle has very high electrical conductivity in comparison with other nanoparticles [58].

Magnetic nanoparticle is widely used in cancer treatment, drug delivery, DNA analysis, magnetic resonance imaging (MRI), and cell sorting manipulation [58]. Magnetic nanoparticle is characterised by biocompatibility and biodegradability and it converts the electromagnetic energy to heat. However these particles can also be cleared very fast by immune system [66].

Carbon nanoparticle is used specifically for drug delivery, as they have the ability to recognize the receptor on the surface of cancer cells. However, this nanoparticle can exhibit high levels of toxicity [84].

Polymeric nanoparticle is nontoxic material and they are excellent in biodegradability and biocompatibility, but it needs multisteps to maintain the drug benefits which require high cost [84].

In this thesis we focus more on improving cancer hyperthermia treatment using magnetic nanoparticles.

Magnetic nanoparticles

Magnetic nanoparticles are divided into metallic nanoparticles like Fe-Co, Fe-Ni, Fe-Pt, and Co-Pt, and metal oxidation or Iron Oxides (Ferrites) like FeO, Fe₂O₃, and Fe₃O₄. Metal nanoparticles are higher in magnetization but they are not stable and they are easy to be oxidized and that affects their magnetization [55]. The materials like Fe, Ni, Co are used to produce most of magnetic nanoparticles. The material Fe is ferromagnetic material and Fe-nanoparticles with size <20 nm are called superparamagnetic. The Co-nanoparticles can be stored for one week without having any oxidation. Few reports or researches dealt with the nickel nanoparticles and some studies showed that their surface is easy to be oxidized to NiO.

The first time that the magnetic material is applied to organism is by Greek scientist and astronomer, Thales of Miletus in 624–547 BC. In 1962, the first discussion of using magnetism in biomedical and medical diagnosis was published. In 1970, the magnetism and magnetic

resonance imaging (MRI) were used in reality in medicine for cancer treatment [134].

Magnetic nanoparticles are biocompatible and nontoxic material [84] and they are used in medical application as they can induce particles rotation and motion which increase the temperature of the tumour by using magnetic field. Magnetite (Fe_2O_4) and maghemite (Fe_2O_3) are the most commonly used magnetic nanoparticles in various studies because of their low toxicity and well-known metabolism pathways (i.e. how the nanoparticles interact with other components) [143]. Magnetic nanoparticles is used to improve hyperthermia cancer treatment as it localizes the heat into the tumour and minimize the side effects on the surrounding healthy cells. Also, these particles are suitable for multi-functional treatment like theranostics which means both the diagnosis and therapy treatments are combined together. This type of treatment is more precise, fast on delivering drugs, and improves patients' outcomes [84].

Despite the fact that magnetic nanoparticles can improve hyperthermia treatment in various ways, the difficulties on controlling the distribution of its generated heat complicates achieving the required temperature to destroy the tumour [119].

In this thesis we discuss about two different types of magnetic nanoparticles. In Chapter 2 we focus on individual nanoparticles characterised by a very small size, so that they can be exchanged across the vessels' walls. In chapter 3 we consider bigger nanoparticles which are carried via the vascular magnetic nanocarrier that cannot normally extravasate from the vessels to the interstitial space. The Iron Oxide nanoparticles (IONPs) and Vascular magnetic nanoconstructs (VMNs) discussed by the Authors in [94] represent relevant examples of the nanoparticle types we discuss in Chapters 2 and 3, respectively.

Producing heat by magnetic nanoparticles

The fluid with magnetic nanoparticles can be injected into the tumour directly. A magnetic field is applied, causing heat to be produced by four mechanisms, which are, hysteresis, eddy current, Neel or Brownian relaxation, and frictional losses [45]. However, superparamagnetic nanoparticles are dominated more by Neel (τ_N) and Brownian relaxation (τ_B) times which will be used in this work. In this strategy, when the magnetic field is applied, the particles rotate and vibrate around them selves (Neels relaxation) and around the fluid (Brownian relaxation) [100]. Therefore, the temperature of cancer cell is increased more than the healthy cells by approximately 2 – 3°C [45]. Furthermore, the heat generated by Brownian relaxation influences more the growth of the tumour when comparing with Neels as the heat generated by τ_B is more than τ_N ($\tau_B \gg \tau_N$) [124]. The performance of this strategy is affected by the properties of nanoparticles, including their size, shape, and magnetic field properties, as well as the perfusion of blood in the tissue [51, 127].

The hyperthermia treatment using magnetic nanoparticles depends on different features like heating efficiency, targeting, and clearance of nanoparticles. Heating efficiency can be defined

by specific absorption rate (SAR) which is in general can be expressed as done by Perigo et al. [109]

$$\text{SAR} = \frac{\text{absorbed power}}{\text{mass of nanoparticles}}. \quad (1.1)$$

There exist more sophisticated models to express the absorption rate as a function of the magnetic field intensity, frequency, magnetisation, such as the one proposed in [8], namely:

$$\text{SAR} = \frac{\pi\mu_0 H_0^2 f}{\rho_n} \chi, \quad (1.2)$$

where $\mu_0 = 4\pi \cdot 10^{-7} \text{ N A}^{-2}$ is the magnetic permeability, H_0 is the magnetic field intensity, f is the magnetic field frequency, χ is the magnetic field susceptibility, and ρ_n is the density of magnetic nanoparticles. The magnetic susceptibility χ depends on the magnetic field frequency, volume of nanoparticles, and total relaxation time. Therefore, equation (1.2) can be written as (3.12) in Chapter 3.

The formula (1.2) shows that SAR depends on the magnetic field features, such as the frequency f and the intensity H_0 . The nanoparticles' structure (in terms of size and shape), as well as the material, which affects magnetization and density also plays a role (see the more detailed analysis of this formula in Chapter 3).

The product of field strength and frequency should not exceed a proper threshold $2 - 5 \cdot 10^9 \text{ A m}^{-1} \text{ s}^{-1}$ [37], [54] and in some sources $5 \cdot 10^8 \text{ A m}^{-1} \text{ s}^{-1}$ [97] to avoid harming the body [127].

There is direct relationship between the size and magnetization of nanoparticles. Small magnetic nanoparticles have small surface and lower internal spin which decrease the magnetization of nanoparticles and consequently the value of SAR declines. Furthermore, the shape of nanoparticles plays an important role on the magnetization and absorption power of nanoparticles. Noh et al. [98] concluded that the cubic nanoparticles theoretically and experimentally have more magnetization when comparing with the spherical ones. This is due to their different geometry which affects their response to the applied magnetic field. Nanorods particles is better than cubic and spherical nanoparticles with similar volume in hyperthermia efficiency due to their high saturation magnetization and unidirectional shape anisotropy [35]. Furthermore, the heating efficiency of nano-octopods is higher than the sphere, because of their shape anisotropy [96].

The thesis focuses on spherical nanoparticles, as this is the shape which is most commonly used in experiments.

Challenges of using nanoparticles

Several studies have been conducted on nanoparticles both in *vivo* and in *vitro*, but few of them are used in clinical experiments. This is due to the biological challenges which are related to nanoparticles toxicity and degradation, distribution of heat, and few administration or penetration routes [83]. For example, usually the nanoparticles are injected through the vessels which cause elimination of the particles due to the plasma clearance and can not interact with the target site [116]. However, there are different researches in *vivo* and in *vitro* showed that proper application of magnetic field and magnetic nanoparticles can help in tackling this issue. In this case the concentration of nanoparticles and the strength of magnetic field in human safe limit should be taken into account [50]. Moreover, properties of the nanoparticles are focused on cells and animals models, such that findings can not always be applied to humans in straight forward way [122]. Furthermore, it is very difficult to control the nanoparticles predestination and their free radicals (i.e. atoms with free electrons that are generated by nanoparticle surfaces can damage DNA and proteins of any cell) in the body and that can affects negatively on the healthy cells, lung, liver, and kidney. Also, 80% of nanoparticles can remain in blood for 84 days which causes toxicity as shown in *vivo* and in *vitro* experiments [7]. In addition, safe dose of IONP in oral administration causes vomiting, nausea, or flatulence [7]. Furthermore, the clinical trials never use the nanoparticles as the first therapies, and they are used mostly for patients who have drugs resistance [50]. By doing so, nanoparticles are less likely to affect the patients who will receive treatment from nanoparticles. Finally, although several studies and models have shown the impact of nanoparticles on immunotherapy in *vitro* and in *vivo*, that was never shown in clinical trials [50].

1.3.3 The asymptotic homogenization method

In general, real-world physical systems are organised across multiple scales, as they consist of different hierarchical levels of organization characterised by different properties, see Figure 1.3. As such, since it is very challenging, if not impossible in some cases, to resolve all the microscale details (especially in three dimensions), homogenisation techniques prove to be very useful to model multiphase, and multiphysics systems. Furthermore, experiment measurements are typically performed at the coarser scales, and the difference between the various scales cannot always be captured. Therefore, homogenisation techniques can be used to inform macroscale models with relevant microscale information at a reduced computational cost.

The idea or the concept of homogenization was used long time ago. For example, Navier (1821), and Poisson (1829) found a macroscopic elastic coefficients from the molecular model [16]. Cauchy (1828) derived two coefficients of elastic model from more complex molecular model. Then, to the best of our knowledge, the first idea of possibility changing the scales was born in 1970s by Keller. However, the method is extremely improved in 1990s to treat different

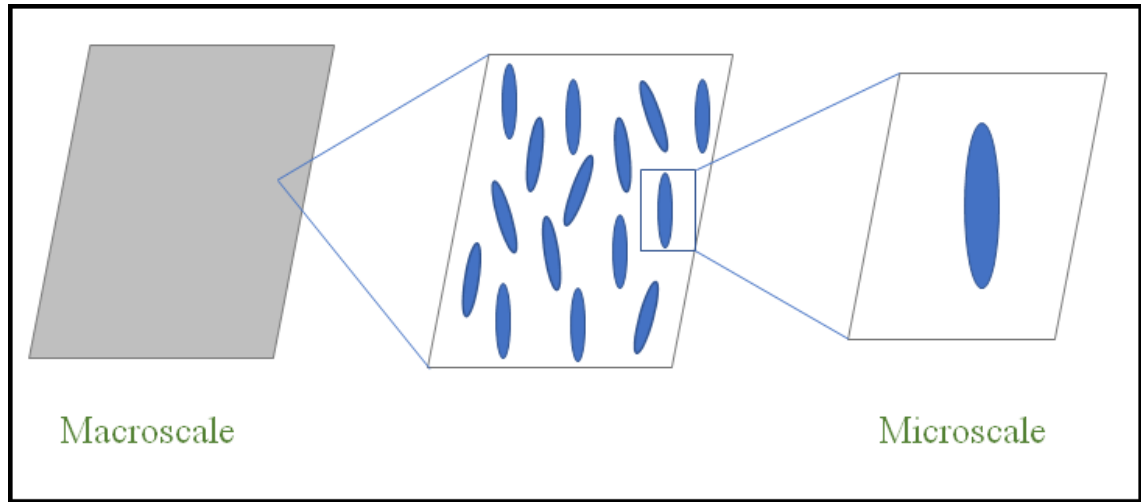


Figure 1.3: Example of multiscale method (Homogenization technique).

complex heterogeneity problems in various fields like engineering, life science, and biomechanics [16]. The main aim of the homogenization is to model the tiny scales or the heterogeneous medium in large, continuous, and simpler medium.

In this thesis, the asymptotic homogenization technique is being used as it has been successfully applied to a large variety of real world scenarios including previous investigations related to fluid and drug transport in biological tissues and vascularised tumours, see, e.g. [32, 85, 101, 102, 103, 105, 126]. Also, the domain of such physical problem can be split it to small regions that have different modelling equations, and this is what we have it in all our work. Now, in order to obtain the macroscopic equations in terms of microscopic description of the problem, we need to follow different steps.

First, we can distinguish between the two scales in any model by assuming that these two scales are well separated, and then the small parameter ϵ can be defined as

$$\epsilon = \frac{d}{L} \ll 1, \quad (1.3)$$

where d represents the size of tiny scale, and L is the size of the large scale.

Therefore, we can define two formally independent variables \mathbf{y} (the local) and \mathbf{x} (the global) related by

$$\mathbf{y} = \frac{\mathbf{x}}{\epsilon}. \quad (1.4)$$

Secondly, we enforce periodicity with respect to the small scale variable \mathbf{y} , and we assume

that every unknown field can be represented in power series of ϵ_0 as

$$v(\mathbf{x}, t) \equiv v^{(\epsilon)}(\mathbf{x}, \mathbf{y}, t) = \sum_{l=0}^{\infty} v^{(l)}(\mathbf{x}, \mathbf{y}, t) \epsilon^l = v^{(0)}(\mathbf{x}, \mathbf{y}, t) + \epsilon v^{(1)}(\mathbf{x}, \mathbf{y}, t) + \epsilon^2 v^{(2)}(\mathbf{x}, \mathbf{y}, t) + \dots \quad (1.5)$$

Also, the differential operators transform according to the chain rule as

$$\nabla \rightarrow \nabla_x + \frac{1}{\epsilon} \nabla_y; \quad \nabla^2 \rightarrow \frac{1}{\epsilon^2} \nabla_y^2 + \frac{2}{\epsilon} \nabla_y \cdot \nabla_x + \nabla_x^2. \quad (1.6)$$

Thirdly, we equate the same power of ϵ^l , ($l = 0, 1, 2, \dots$) to find suitable differential equations in order to close the problem for the leading order variables $v^{(0)}$. As we would like to obtain a system defined at the large scale only, for fields which retain a dependence at the tiny scale variable \mathbf{y} , we can integrate them over the periodic cell

$$\langle v \rangle = \frac{1}{|\Omega_Q|} \int_{\Omega_Q} v(\mathbf{x}, \mathbf{y}, t) dy, \quad \text{or} \quad (1.7)$$

$$\langle v \rangle = \frac{1}{|\Omega|} \int_{\Omega_Q} v(\mathbf{x}, \mathbf{y}, t) dy, \quad (1.8)$$

where $|\Omega|$ is the volume of the periodic cell, and Ω_Q is cell portion on which the integration is performed, with corresponding volume $|\Omega_Q|$. All the fields $v^{(l)}$, $l = 0, 1, \dots$ are supposed to be \mathbf{y} -periodic. The integration in equation (1.7) is used in Chapter 2 and 3, where the integration in (1.8) is applied in Chapter 4 as it is more suitable in order to illustrate the results which are shown in that context.

In particular, the cell volume portion $|\Omega_Q|$, and the surface area S are defined by

$$S = \int_{\Gamma} dS_y, \quad (1.9)$$

$$|\Omega_Q| = \int_{\Omega_Q} dV_y. \quad (1.10)$$

In our case we enforce macroscopic uniformity (the medium structure of the macroscale is entirely periodic, i.e. the periodic cell is always the same for each point \mathbf{x} of the macroscale domain) such that S , $|\Omega|$ are constants. Analyses of non-macroscopically uniform structures is beyond the scope of this work, however, they could be relevant in several contexts and alternative approaches to deal with such heterogeneities can be found in Dalwadi and King [32], Penta et al. [101, 102] and references therein.

The weakness of applying the homogenization technique is that there are many theoretical results of homogenization without any supporting numerical simulation in the context of practical applications. It is also essential to have a clear understanding of the interplay between the different scales.

1.3.4 Previous works

This section discusses different concepts that have been used and mentioned in this thesis such as tumour fluid flow, particles transport, heat distribution, adhesion between the particles and the vessels wall, and interplay between the tumour and surrounding tissues, as well as previous papers that we have consulted.

Fluid flow

Studying the fluid flow plays an important role in tumour and metastasis growth, oxygen and nutrient delivery, and drug delivery. Most of the drugs and nanoparticles are injected through the vessels, then due to the vessels permeability, the nanoparticles cross the tumour interstitial space to reach the cancer cells. However, due to the abnormal structure of the vessels discussed in Section 1.3.1 and high interstitial fluid pressure, the extravasation of the drugs between the vessels and tumour interstitium decreases. Analyses of the fluid dynamics via experiments are limited by the equipment available in terms of scales and details that can be spatially resolved [89]. Mathematical modelling can therefore be very helpful in obtaining an improved understanding of the fluid flow that takes place across multiple scales. The fluid flow in the tumour covers the blood, lymph, and interstitial fluid. The interstitial flow can be considered laminar, and can usually be determined by means of the Darcy's law (i.e. the flow is proportional to the pressure gradient). Lymphatic flow is also laminar and it also involves immune and cancer cells. The Navier-Stokes' equation is used to describe the lymphatic flow [48]. In general, the blood consists of different elements like red blood cells, white blood cells, water, plasma, proteins, organic molecules, and electrolytes. The blood is considered as Newtonian if the shear stress is proportional to the shear rate, with the viscosity playing the role of a proportionality constant [12]. The plasma represents 93% of the blood, and it is very often considered as a Newton fluid. In general, the blood can be modeled as a purely Newtonian fluid if the radius of the vessels is much bigger than the red cells, otherwise more refined models could be considered. For example, Penta et al. [102] considered the blood as viscous fluid characterise by a spatially varying viscosity.

Navier-Stokes' equation in absence of body forces can be summarized as,

$$\rho \left(\frac{\partial \mathbf{u}_v}{\partial t} + (\mathbf{u}_v \cdot \nabla) \mathbf{u}_v \right) = \nabla \cdot T_n, \quad (1.11)$$

where \mathbf{u}_v is the blood velocity, and ρ is the fluid density. The left hand side of equation (1.11) refers to the inertial force. The Cauchy stress tensor T_n in the right hand side is defined as

$$T_n = -pI + 2\mu \frac{\nabla \mathbf{u}_v + (\nabla \mathbf{u}_v)^T}{2}, \quad (1.12)$$

for the Newtonian fluid. The Navier-Stokes' equation for an incompressible Newtonian fluid

reduces to

$$\rho \left(\frac{\partial \mathbf{u}_v}{\partial t} + (\mathbf{u}_v \cdot \nabla) \mathbf{u}_v \right) = -\nabla p_v + \mu \nabla^2 \mathbf{u}_v, \quad (1.13)$$

where we have substituted the expression (1.12) in the balance (1.11) and accounted for the incompressibility constraint

$$\nabla \cdot \mathbf{u}_v = 0. \quad (1.14)$$

Here, μ is the blood viscosity, p_v is the pressure of the blood, and $\mu \nabla^2 \mathbf{u}_v$ takes into account the viscous character of the fluid.

The Reynolds number (Re) is the ratio between the inertial force and the viscous force which is used to describe the turbulent of the fluid flow. If the Re is very small, we call it laminar flow and if it is very high, then we call it turbulent flow. In the porous medium the inertial force is very small and can be neglected as the fluid velocity is less than 10^{-4} m/s².

There are many previous works that studied the fluid flow in the tumour. Penta et al. [102] discussed the theoretical homogenized results of the fluid flow in microvascularized tumour. They represented the tumour in three dimensions and divided it into two compartments, the tumour vessels and the interstitium. They used Darcy's law for the tumour interstitium and Stokes' equation ignoring the inertial and body forces for the blood flow. They also took into account the interface between the two compartments. The final macroscale system described double Darcy's law for the fluid flow with fluid mass as source term. After that, Penta and Ambrosi [103] computed the hydraulic conductivities by solving the cell problems at the microscale which was used to find the pressures and velocities of the fluid in macroscale. They varied the vessels geometry and investigated its impact on the fluid flow.

Zhan et al. [151] studied the influence of the tumour size and IFP on particles transport. The IFP rises with increasing in tumour size. Also, the fluid flux from the vessels to the tumour interstitium and per tumour volume (V) is defined by the product of the permeability of the vessels wall, density of the vessels, and the difference of vessels pressure and IFP. It has been observed that the flux is lower when the tumor size is large, as the IFP and (S/V) are greater in this case.

Jain et al. [70] found that the IFP can be declined by decreasing the surface area of the tumour to the volume (S/V), vessels' permeability (L_p), tumour size (L), and increasing tumour hydraulic conductivity (κ) which is analyzed using

$$\alpha = L \sqrt{\frac{L_p S}{\kappa V}}. \quad (1.15)$$

Also, they have deduced that the interstitial fluid velocity is higher on the boundary of the tumour, where the IFP is maximum at the center of the tumour.

Particle transport

The mathematical modelling of particles delivery in the tumour is very complex due to the tumour and vascular structures, and the interplay between the cellular factors and drug or particles transport. The diffusion model is used to design the particles transport from more than 60 years ago. Fick's law of diffusion in one dimension can be used to determine the concentration of nanoparticles, see Peppas and Narasimhan [107]. The diffusion coefficient in this equation in case of porous media depends on the porosity that reflects the volume of the pores and tortuosity which design the structure of the pores.

Goodman et al. [52] discussed the penetration of nanoparticles in multicellular spheroids in *vivo* and in *vitro*. Their model accounted for particle concentrations binding with receptors, binding sites in tumours, and internalized particles. Also, they studied the influence of particles size on particles delivery in the tumour. They concluded that the particles binding and size, and tissue porosity are important features for designing the nanoparticles. For example, particles with size 200 nm can not penetrate with spherical tumour, but particles with size 20-40 nm can do that. Also, the penetration of nanoparticles can be improved by increasing the porosity of the tissue. Steuperaert et al. [132] illustrated a 3D model for drug transport using advection-diffusion-reaction equation. A reaction term reflects the sum of drug uptake by vessels and tissues.

Penta et al. [102] modeled the drug concentration in the tumour vessels using advection-diffusion equation and advection-diffusion-reaction equation for the interstitial compartment. As the vessels wall is semi-permeable, they studied the mass flux between the two compartments which depends on the difference of the concentrations, blood flux, permeability of the vessels membrane, and the osmotic coefficient. They applied the homogenization technique and they end up with double advection-diffusion-reaction equations, and with mass exchange between them formally appearing as reaction and source terms in the model. Mascheroni and Penta [85] used the results obtained by Penta et al. [102], and Penta and Ambrosi [103] to derive the effective diffusivity tensors and they computed the concentration of the drugs with different vessels tortuosity. Penta and Ambrosi [103], and Mascheroni and Penta [85] concluded that increased vessel tortuosity reduced fluid transport, as well as convective and diffusive transport in tumours.

Heat convection

Nabil and Zunino [94], and Nabil et al. [95] discussed the hyperthermia cancer treatment using magnetic nanoparticles of different sizes. Nabil et al. [95] modelled fluid, and nanoparticles transport in the tumour vessels and interstitial compartments, where they studied the heat convection in the tumour only as they assumed a constant temperature for the blood. They represented the vessels in one dimension and tumour in three dimensions using embedded multiscale technique. They used Darcy's law in three dimensions to express the fluid flow in the

tissue and Stokes' equation in one dimension for the blood flow. Also, the lymphatic drainage was taken into account. For the particles transport, they studied the concentration of iron oxide nanoparticles in the vasculature and tissue regions. They used advection-diffusion equation to compute the concentration of nanoparticles in the vessels. The vessels wall was considered as semi-permeable membrane and due to small size of the nanoparticles, the particles can diffuse into the tumour tissue. They also studied the heat distribution in the tumour and they assumed that the temperature of the blood is constant. They used convection-diffusion equation with heat source that depends on the absorption rate and the average concentration of nanoparticles. The Robin condition is used to express the heat flux on the boundary of the tissue. In order to solve their problem, they assumed that the particles are injected for 40 min, and the tissue is exposed to a magnetic field for 20 to 40 min, as they followed Johannsen et al. [71], Mornet et al. [91]. According to their results, the concentration of nanoparticles dropped sharply after stopping the injection of nanoparticles, and 50% of them are absorbed by the tumour. The temperature of the tumour is increased by 2K and strictly decreases after 40 min.

Nabil and Zunino [94] assumed that iron oxide nanoparticles (ION) are carried inside the vascular magnetic nanoconstructs (VMN). In this case, the particles are large and cannot be transported through the vessels membrane. Therefore, advection-diffusion-reaction equation in one dimension is used to describe the concentration of ION and the adhesion between the particles and vessels wall was taken into account. Also, they computed the density of nanoparticles on the boundary of the vessels that depends on the adhesion rate. As for the temperature, they followed their previous model except that the heat source depends on particle concentration and density in the vessels since particles were not present in the tissues. The results were analyzed at four different circulation times. They found that the concentration decreases and the density increases at increasing the circulation time. After 40 minutes following the injection of the nanoparticles, the magnetic field was applied, and at that time the temperature increased by 10-12 °C.

Cervadoro et al. [23] studied the hyperthermia cancer treatment using super iron oxide nanoparticles. They were interested in finding the minimum hyperthermia temperature of $>42^{\circ}\text{C}$, and the minimum thermal ablation of $>50^{\circ}\text{C}$ for tumour tissue. They considered tumour as inner region surrounded by healthy tissue as outer region and they determined the temperatures using Pennes' bioheat equation. Also, they assumed that the temperature maps depend on absorption rate of the fluid and nanoparticles SAR . They deduced that the characteristics of nanoparticles like size and shape, magnetic field properties like magnetic intensity and frequency, and blood perfusion have an impact on SAR which is the main factor to achieve the required temperature. Moreover, they concluded that the concentration of nanoparticles does not affect SAR , but it increases the temperature.

Saeedi et al. [117] investigated how the heat generated in the tumour and the cell death depend on the position of magnetic nanoparticles inside the tissue using the experiment and computer simulation. Also, they found that heating the tumour to 55°C with an exposition to magnetic

field for 30 min is the best set of conditions to destroy the tumour and with negligible influence on the healthy tissues.

Salloum et al. [119] examined *in vivo* the impact of the blood flow and the amount of nanofluid to approach the required temperature which is 43°C. The experiment was applied on the rat limb (tissue) by injecting the nanofluid for two times and applying the magnetic field 20 minutes after injecting the nanoparticles. The blood perfusion is proportional to the density of the tissue and blood flow rate, and inversely proportional to the mass of the tissue. Also, the value of *SAR* in their case depends on the distance of nanoparticles from the injection site. They found that under their experiment protocols, they can achieve the required temperature by increasing the concentration of injected nanoparticles.

Adhesion phenomenon

Decuzzi and Ferrari [38] illustrated the adhesion between the nanoparticles and vessels wall with different sizes and shapes. They found that oblate nanoparticles adhered to the vessels wall more than spherical particles. Also, nanoparticle size and shape are affected by the density of receptors and vessels shear stress ratio. Furthermore, the adhesion probability P_a can be computed as discussed by Piper et al. [110] using

$$P_a = m_r m_l K_A^0 A_c \exp \left[-\frac{\lambda_a f_a}{K_B T} \right], \quad (1.16)$$

where m_r is the density of the receptors, m_l is the density of the ligand, K_A^0 is constant, A_c is the interaction area between the particles and the substrate, f_a is the force per ligand-receptors, λ_a is the length of legend-receptors, T is the temperature, and K_B is Boltzman energy.

The adhesion phenomena affects the particles transport in the tumour specially in the case of passive transport, as the particles are injected in the vessels. Nabil and Zunino [94] accounted for the adhesion of large nanoparticles to vessels walls and calculated the adhesion rate using the formula $\Pi = P_a |WSR| p_d / 2$. Here, *WSR* is the wall shear rate, p_d is the particles diameter, and they assumed that the adhesion propability P_a is a constant. Also, they computed the density of nanoparticles that adhered to the vessels wall by integrating Π and the particles' concentration over the time.

Interplay between the tumour and healthy tissues

Sefidgar et al. [123] studied the fluid flow and particle transport in vascularized tumours within the healthy tissues using three approaches which are, neglecting the vessel network, a static network with a constant radius for tumour vessels, and varying the vessel radius as a function of metabolic stimuli. They found that the IFP is uniform in the first case, where it is heterogeneous in the second and third cases. Also, they deduced that unorganised vessels network caused

heterogeneous drug transport. Therefore, the drugs took long time to reach the entire region of the tumour (around 27h). This is due to the low diffusion and negligible convection which impaired the transport of the drugs. Therefore, continuous injection should be applied to improve the distribution. Also, tumor boundaries showed the highest concentration.

Chapter 2

Multiscale modelling of nanoparticle delivery and heat transport in vascularised tumours

[This chapter is published as : Al Sariri, T., Penta, R., 2022. Multi-scale modelling of nanoparticle delivery and heat transport in vascularised tumours. *Mathematical Medicine and Biology*. <https://doi.org/10.1093/imammb/dqac009>].

2.1 Introduction

In this chapter we aim to describe the temperature maps related to hyperthermia cancer treatment performed via magnetic nanoparticles transported by means of the passive mechanisms (i.e. the formulation is applicable to particles which are sufficiently small to extravasate from the vessels to the tumour). We account for the three-dimensional character of both the tumour and the vessels, which are considered as two interacting domains as done by Mascheroni and Penta [85], Penta and Ambrosi [103]. In the latter papers, the authors found that the vessels' tortuosity impaired the fluid and macromolecules drug flow in vascularised tumours. Herein, we extend their results to cover the influence of geometrical tortuosity on heat transport in the context of cancer hyperthermia. The vessels' fluid flow is governed by the Stokes' problem, while we assume that the interstitial transport is described by the Darcy's law. The governing equations describing drug transport are of advection-diffusion type in the vessels and of advection-diffusion-reaction type in the tumour interstitium. Diffusive and advective heat transport in both compartments is likewise formally represented by a double advection-diffusion-reaction model. The vessel's wall is modeled as a porous semi-permeable membrane, so as to allow the interplay of fluid, mass, and heat between compartments.

We address the sharp length scale that exists between the typical intercapillary distance and the average tumour size by means of the asymptotic homogenisation technique, as summarised

for example in the works by Bakhvalov and Panasenko [10], Cioranescu and Donato [29], Davit et al. [36], Penta and Gerisch [104], Taffetani et al. [138]. Our macroscale results comprise a double Darcy's system of PDEs describing fluid transport within and between compartments, and double advection-diffusion-reaction equations for both drug and heat transport. The influence of the micro-structure appears in the hydraulic conductivities, particle diffusion coefficients, and thermal conductivities which can be determined by solving appropriate periodic cell problems. The macroscale system of partial differential equations is solved by finite elements in a spherical coordinate setting. The results elucidate the role of tortuosity and absorption rate, as well as their mutual interplay, on heat transport generated by nanoparticles in vascularised tumours.

This chapter is structured into different sections which are organised as follows. In Section 2.2 we describe the mathematical model by emphasising the main assumptions and underlying physical phenomena. These include the differential equations for fluid flow, particle transport, and heat convection in both the tumour vessels and the interstitial compartment. Also, we address the fluid, drug, and heat exchange which takes place across the interface via setting up appropriate interface conditions. In Section 2.3 the differential equations are formulated in non-dimensional form. In Section 2.4 we apply the asymptotic homogenisation technique and derive the macroscale results. Then, we briefly discuss how the homogenised coefficients are determined on the basis of a microstructure. In Section 2.5 the differential equations describing particle and heat transport are written in spherical coordinates and supplemented by corresponding macroscale initial and boundary conditions. In Section 2.6 the results obtained via numerical simulations are illustrated and discussed. In Section 2.7 our methodology, model assumption, and results are qualitatively compared with Nabil and Zunino [94]. In Section 2.8 concluding remarks are presented.

2.2 Mathematical modeling

In this work, we address mathematical modelling of cancer hyperthermia therapy carried out via nanoparticles delivery. We represent the vascularised tumor as a three-dimensional domain $\Omega \subseteq \mathbb{R}^3$. The tumour tissue comprises two regions. The interstitium is denoted here by Ω_t and the blood vessels' network by Ω_v , such that $\bar{\Omega}_t \cup \bar{\Omega}_v = \bar{\Omega}$.

The tumour system under consideration is multiscale in nature and the typical distance between adjacent blood vessels $d \approx (50 - 100) \mu\text{m}$ is much smaller than the average size $L \approx 0.5 \text{ cm}$ of the cancerous region, as reported by Penta et al. [102]. Therefore, we define the small parameter

$$\epsilon = \frac{d}{L} \ll 1. \quad (2.1)$$

We are interested in describing heat transport and the subsequent temperature distribution which is driven by nanoparticles which are considered as being transported as passive scalars (changing

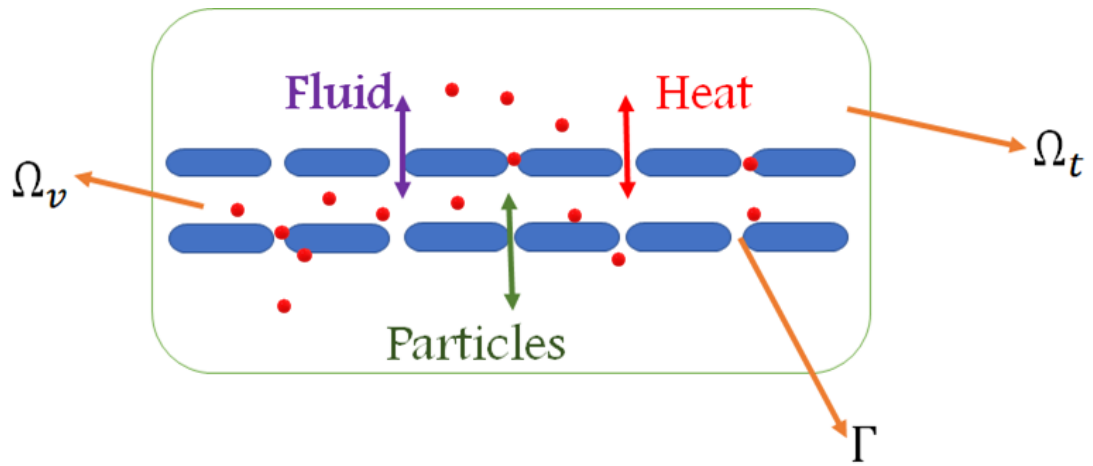


Figure 2.1: The description of the tumour compartments and the exchange of fluid, mass, and heat between them. The symbols Ω_v is the domain of the blood vessels, Ω_t is the domain of the tumour interstitium, and Γ is the interface between the two domains.

of particles concentration does not affect the fluid flow properties). Therefore, we can assume that the delivery of nanoparticles is occurring via diffusion through both the vessels and the interstitium, advection due to the fluid flow in both compartments, and extravasation across the vessels' walls. In the next section we illustrate the governing equations for fluid, drug, and heat transport in both the vessels and the interstitial space.

All the variables in this model such as the pressure p , the concentration c , the velocity \mathbf{u} , and the temperature T are functions of both \mathbf{x} and t .

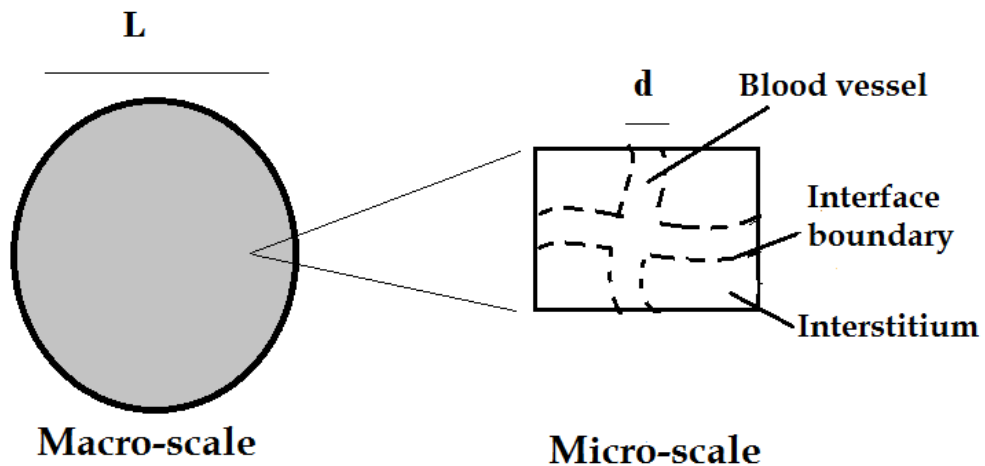


Figure 2.2: A schematic of the macroscale and the microscale difference. The microscale (comprising the interstitial space and the vessels) on the right, and the macroscale domain, where the difference between the tumour constituents are homogenised, on the left. This figure is taken from Al Sariri and Penta [3].

2.2.1 Interstitial fluid transport

The tumour interstitial region is represented as a non deformable and isotropic porous medium governed by Darcy's law:

$$\mathbf{u}_t = -\kappa \nabla p_t \quad \text{in } \Omega_t, \quad (2.2)$$

together with the incompressibility constraint

$$\nabla \cdot \mathbf{u}_t = 0 \quad \text{in } \Omega_t, \quad (2.3)$$

where \mathbf{u}_t , κ , and p_t are the interstitial fluid velocity, conductivity, and pressure, respectively.

We refer to [105] for an analysis of asymptotic homogenisation for deformable porous media, where the interstitial fluid velocity is replaced by the interstitial fluid velocity relative to the velocity of the solid porous matrix (which is here set to zero as the porous matrix is assumed to be rigid).

2.2.2 Microvascular flow

The blood flowing in small capillaries is considered as an incompressible viscous fluid and it is transported in the body through the vessels. Although non-Newtonian effects may become relevant in small capillaries, we assume that the blood is a Newtonian fluid as a first approximation, as done for example by Shipley and Chapman [126].

Therefore, as we are considering low Reynolds' number flow, we assume that the blood dynamics in the vessels can be described by Stokes' problem (i.e. inertia is neglected), which, in absence of body forces, reads

$$\mu \nabla^2 \mathbf{u}_v = \nabla p_v \quad \text{in } \Omega_v, \quad (2.4a)$$

$$\nabla \cdot \mathbf{u}_v = 0 \quad \text{in } \Omega_v, \quad (2.4b)$$

where \mathbf{u}_v , μ , and p_v are the fluid velocity, viscosity, and pressure in the blood vessels, respectively.

2.2.3 Transport of particles

We assume that the particles are injected through the vessels and due to their small sizes and the permeability of the vessels membrane, the particles can be exchanged between the two compartments. Then, the particles can be absorbed by the tumour interstitial compartment, where metabolic reactions are assumed to take place. The concentration dynamics of the particles in the vessels c_v can be described by the advection-diffusion equation in Ω_v . Absorption of particles in the interstitial compartment is represented by a linear uptake term. Therefore, the governing

equations for the interstitial and vessels concentrations c_t and c_v , respectively, read

$$\frac{\partial c_v}{\partial t} + \nabla \cdot (c_v \mathbf{u}_v - D_v \nabla c_v) = 0 \quad \text{in } \Omega_v, \quad (2.5a)$$

$$\frac{\partial c_t}{\partial t} + \nabla \cdot (c_t \mathbf{u}_t - D_t \nabla c_t) = -\Lambda c_t \quad \text{in } \Omega_t, \quad (2.5b)$$

where D_v , D_t , and Λ are the particles' diffusivities in the vessels and in the interstitium and the uptake rate, respectively.

2.2.4 Heat convection in the tumour

The heat generated in the tumour is driven by application of a magnetic field which affects the nanoparticles injected into the bloodstream. The magnetic field causes the rotation and vibration of nanoparticles. These rotations generate the heat which produce an increase in the tumour temperature [100].

The temperatures in the vessel T_v and in the interstitium T_t are determined by a system of advection-diffusion equations. The heat generated by the magnetic field is represented by the heat source $\alpha f(c_{t,v})$ and, for the sake of simplicity, here we assume

$$f(c_v) = c_v, \quad \text{and} \quad f(c_t) = c_t, \quad (2.6)$$

where $c_{t,v}$ is the nanoparticles concentration in the vessels or interstitial compartment. The efficacy of the heat produced by the magnetic nanoparticles depends on the absorption rate α [94]. The latter parameter is in turn related to magnetic field properties (such as intensity and frequency) and particles' shape, although such features are not explicitly taken into account in the present work. The coupled system of partial differential equations then reads

$$\frac{\partial T_t}{\partial t} + \nabla \cdot (T_t \mathbf{u}_t - \frac{K_t}{\gamma_t \rho_t} \nabla T_t) = \frac{\alpha}{\gamma_t \rho_t} c_t \quad \text{in } \Omega_t, \quad (2.7a)$$

$$\frac{\partial T_v}{\partial t} + \nabla \cdot (T_v \mathbf{u}_v - \frac{K_v}{\gamma_v \rho_v} \nabla T_v) = \frac{\alpha}{\gamma_v \rho_v} c_v \quad \text{in } \Omega_v. \quad (2.7b)$$

Here, K_t and K_v are the thermal conductivities in the interstitium and in the vessels, respectively. The parameters ρ_t and γ_t are the tissue density and specific heat capacity, while ρ_v , γ_v are the blood density and the blood specific heat capacity.

We believe here that the impact of the particles uptake rate via the tumour interstitium plays the role via the advection-diffusion-reaction equation (2.5b).

2.2.5 Interface conditions

The interface between the two domains is denoted by $\Gamma = \partial\Omega_v \cap \partial\Omega_t$. The fluid flow across the vessel is assumed to be continuous and depending on the pressures' difference between the two domains. We assume that the blood flux across the vessel wall is determined by Starling's law, i.e.

$$\mathbf{u}_t \cdot \mathbf{n} = \mathbf{u}_v \cdot \mathbf{n} = L_p(p_v - p_t) \quad \text{on } \Gamma. \quad (2.8)$$

The vector \mathbf{n} represents the unit outward vector normal to the vessels' wall. The parameter L_p represents the permeability of the blood vessels which reflects the leakage of the vessels' wall. In order to close the problem we need to specify a condition for the tangent component of the blood velocity to account for slip over the porous interface. We assume a Beavers and Joseph condition as done by Penta et al. [102], Shipley and Chapman [126], i.e.

$$\mathbf{u}_v \cdot \boldsymbol{\tau}_v = -\frac{\sqrt{k}}{\varphi} [(\mathbf{n} \cdot \nabla) \mathbf{u}_v] \cdot \boldsymbol{\tau}_v \quad \text{on } \Gamma, \quad (2.9)$$

where φ is a non-dimensional parameter which is related to the porous surface properties, and $\boldsymbol{\tau}_v$ denotes both of the unit vectors tangent to the vessels' walls. The parameter k is the tissue permeability, which is related to the hydraulic conductivity κ by the following relationship

$$\kappa = \frac{k}{\mu}. \quad (2.10)$$

The mass flux is assumed to be continuous and proportional to the particles' concentration difference between the vessels and tumour

$$(c_v \mathbf{u}_v - D_v \nabla c_v) \cdot \mathbf{n} = (c_t \mathbf{u}_t - D_t \nabla c_t) \cdot \mathbf{n} = P(c_v - c_t) \quad \text{on } \Gamma, \quad (2.11)$$

where P is the diffusive membrane permeability. In this work, transvascular advection across the vessels' membrane, as investigated for instance by Mascheroni and Penta [85], is neglected for the sake of simplicity, although the theoretical derivation that follows could be readily extended to such contributions.

The heat flux is likewise expressed in terms of the temperature difference between the two domains Ω_t and Ω_v as follows

$$\left(T_v \mathbf{u}_v - \frac{K_v}{\gamma_v \rho_v} \nabla T_v \right) \cdot \mathbf{n} = \frac{\beta}{\gamma_v \rho_v} (T_v - T_t) \quad \text{on } \Gamma, \quad (2.12a)$$

$$\left(T_t \mathbf{u}_t - \frac{K_t}{\gamma_t \rho_t} \nabla T_t \right) \cdot \mathbf{n} = \frac{\beta}{\gamma_t \rho_t} (T_v - T_t) \quad \text{on } \Gamma, \quad (2.12b)$$

where β is the heat transfer coefficient, and (2.12a) and (2.12b) represent interface conditions for

T_v and T_t , respectively.

2.3 Non-dimensional form of the model

In this section we perform a non-dimensional analysis of the system of partial differential equations (2.2)-(2.7b) supplemented with interface conditions (2.8)-(2.9) and (2.11-2.12b) as follows:

$$\mathbf{u}_z = \frac{Cd^2}{\mu} \mathbf{u}'_z, \quad p_z = CLp'_z, \quad \nabla = \frac{1}{L} \nabla', \quad t = \frac{L\mu}{Cd^2} t', \quad c_z = C_r c'_z, \quad T_z = TT'_z. \quad (2.13)$$

The index $z = v, t$ denotes either the vessels or the tumour, while C_r , T , C , d , and L are the reference concentration, temperature, pressure gradient, inter-capillary distance, and average tumour size, respectively.

By dropping the primes for the sake of simplicity of notation, the dimensionless partial differential equations can be written as

$$\epsilon^2 \nabla^2 \mathbf{u}_v = \nabla p_v \quad \text{in } \Omega_v, \quad (2.14a)$$

$$\nabla \cdot \mathbf{u}_v = 0 \quad \text{in } \Omega_v, \quad (2.14b)$$

$$\mathbf{u}_t = -\bar{\kappa} \nabla p_t \quad \text{in } \Omega_t, \quad (2.14c)$$

$$\nabla \cdot \mathbf{u}_t = 0 \quad \text{in } \Omega_t, \quad (2.14d)$$

$$\frac{\partial c_v}{\partial t} + \nabla \cdot (c_v \mathbf{u}_v - \bar{D}_v \nabla c_v) = 0 \quad \text{in } \Omega_v, \quad (2.14e)$$

$$\frac{\partial c_t}{\partial t} + \nabla \cdot (c_t \mathbf{u}_t - \bar{D}_t \nabla c_t) = -\Upsilon c_t \quad \text{in } \Omega_t, \quad (2.14f)$$

$$\frac{\partial T_v}{\partial t} + \nabla \cdot (T_v \mathbf{u}_v - \bar{K}_v \nabla T_v) = \bar{\alpha}_v c_v \quad \text{in } \Omega_v, \quad (2.14g)$$

$$\frac{\partial T_t}{\partial t} + \nabla \cdot (T_t \mathbf{u}_t - \bar{K}_t \nabla T_t) = \bar{\alpha}_t c_t \quad \text{in } \Omega_t, \quad (2.14h)$$

with boundary conditions:

$$\mathbf{u}_v \cdot \boldsymbol{\tau} = -\epsilon \bar{\varphi} [(\mathbf{n} \cdot \nabla) \mathbf{u}_v] \cdot \boldsymbol{\tau} \quad \text{on } \Gamma, \quad (2.15a)$$

$$\mathbf{u}_v \cdot \mathbf{n} = \epsilon \bar{L} (p_v - p_t) \quad \text{on } \Gamma, \quad (2.15b)$$

$$\mathbf{u}_t \cdot \mathbf{n} = \epsilon \bar{L} (P_v - P_t) \quad \text{on } \Gamma, \quad (2.15c)$$

$$(c_v \mathbf{u}_v - \bar{D}_v \nabla c_v) \cdot \mathbf{n} = \epsilon \bar{P} (c_v - c_t) \quad \text{on } \Gamma, \quad (2.15d)$$

$$(c_t \mathbf{u}_t - \bar{D}_t \nabla c_t) \cdot \mathbf{n} = \epsilon \bar{P} (c_v - c_t) \quad \text{on } \Gamma, \quad (2.15e)$$

$$(T_v \mathbf{u}_v - \bar{K}_v \nabla T_v) \cdot \mathbf{n} = \epsilon \bar{\beta}_v (T_v - T_t) \quad \text{on } \Gamma, \quad (2.15f)$$

$$(T_t \mathbf{u}_t - \bar{K}_t \nabla T_t) \cdot \mathbf{n} = \epsilon \bar{\beta}_t (T_v - T_t) \quad \text{on } \Gamma, \quad (2.15g)$$

where the primes have been dropped for the sake of simplicity.

The non-dimensional numbers are defined as

$$\bar{L} = \frac{L_p L^2 \mu}{d^3}, \quad \bar{\kappa} = \frac{\kappa \mu}{d^2}, \quad \bar{\varphi} = \frac{\sqrt{\bar{\kappa}}}{\varphi}, \quad \bar{P} = \frac{PL\mu}{Cd^3}, \quad \Upsilon = \frac{\Lambda\mu}{LCd^2}, \quad (2.16)$$

$$\bar{\alpha}_v = \frac{\alpha C_r L \mu}{\rho_v \gamma_v T C d^2}, \quad \bar{\alpha}_t = \frac{\alpha C_r L \mu}{\rho_t \gamma_t T C d^2}, \quad \bar{\beta}_v = \frac{\beta L \mu}{\rho_v \gamma_v C d^3}, \quad \bar{\beta}_t = \frac{\beta L \mu}{\rho_t \gamma_t C d^3}. \quad (2.17)$$

Here, $\bar{\kappa}$ is the non-dimensional hydraulic conductivity. The coefficients Υ and $\bar{\alpha}$ are non-dimensional uptake rate and absorption rate. The numbers \bar{L} , \bar{p} , $\bar{\beta}$, and $\bar{\varphi}$ are the non-dimensional vessels' hydraulic and diffusive permeabilities, heat transfer coefficient, and Beavers and Joseph coefficients, respectively. The non-dimensional diffusivities of the particles in the vessels and the tumour are the reciprocal of their corresponding Peclet's numbers, i.e.

$$\bar{D}_v = \frac{1}{Pe_v}, \quad \bar{D}_t = \frac{1}{Pe_t}, \quad (2.18)$$

where

$$Pe_v = \frac{LCd^2}{D_v \mu}, \quad Pe_t = \frac{LCd^2}{D_t \mu}. \quad (2.19)$$

The non-dimensional thermal conductivities are given by

$$\bar{K}_v = \frac{K_v \mu}{\rho_v \gamma_v LC d^2}, \quad \bar{K}_t = \frac{K_t \mu}{\rho_t \gamma_t LC d^2}. \quad (2.20)$$

The ϵ scaling appearing on the right hand side of interface conditions equations (2.15b-2.15g) is the appropriate one to ensure that blood, drug, and heat fluxes inside the tumour stays finite in the limit $\epsilon \rightarrow 0$, as observed by Penta et al. [102]. Furthermore, we assume that the parameters appearing in equations (2.16-2.20) are finite in the limit as ϵ approaches zero. This is done consistently with the approach carried out by Penta et al. [102] and ensures that both drug and thermal diffusivities, which are well-known to play a crucial role in the nanoparticles' dynamics, are captured at leading order. There exist different scaling choices in the literature, see, e.g., the work by Shipley and Chapman [126], where the authors perform the upscaling of the equations describing fluid and drug transport in vascularised tumours and their choice concerning distinguished limits of the Peclet's numbers results in a suite of reaction-advection models.

2.4 The asymptotic homogenisation method

The application of the multiscale method in our model is motivated by a large difference in sizes between the inter-vessel distance and the tumour radius, as assumed by Penta et al. [102], Shipley and Chapman [126]. In particular, we assume that these two scales are well separated, so that

the small parameter ϵ defined in equation (2.1) is much smaller than 1. Therefore, we can define two formally independent variables \mathbf{y} (the microscale) and \mathbf{x} (the macroscale) related by

$$\mathbf{y} = \frac{\mathbf{x}}{\epsilon}. \quad (2.21)$$

We assume that any variable in the model is \mathbf{y} -periodic and can be written in terms of ϵ as

$$v(\mathbf{x}, t) \equiv v^{(\epsilon)}(\mathbf{x}, \mathbf{y}, t) = \sum_{l=0}^{\infty} v^{(l)}(\mathbf{x}, \mathbf{y}, t) \epsilon^l = v^{(0)}(\mathbf{x}, \mathbf{y}, t) + \epsilon v^{(1)}(\mathbf{x}, \mathbf{y}, t) + \epsilon^2 v^{(2)}(\mathbf{x}, \mathbf{y}, t) + \dots, \quad (2.22)$$

where v collectively represents any variable described in our model namely p_z , c_z , \mathbf{u}_z , or T_z , (with $z = v, t$).

Also, the differential operators can be written using the chain rule as follows

$$\nabla \rightarrow \nabla_x + \frac{1}{\epsilon} \nabla_y; \quad \nabla^2 \rightarrow \frac{1}{\epsilon^2} \nabla_y + \frac{2}{\epsilon} \nabla_y \cdot \nabla_x + \nabla_x^2. \quad (2.23)$$

We apply the asymptotic homogenization technique to the model using equations (2.22)-(2.23) to obtain new differential equations in power of ϵ . Then, we equate the same power of ϵ to find the differential equations in the leading order terms $v^{(0)}$. In order to create a complete macroscale system, we have to integrate all variables that are microscale dependent over the periodic cell

$$\langle v \rangle_z = \frac{1}{|\Omega_z|} \int_{\Omega_z} v(\mathbf{x}, \mathbf{y}, t) dy, \quad z = t, v, \quad (2.24)$$

where $|\Omega_v|$ and $|\Omega_t|$ are the vessels and interstitial cell volume portions.

2.4.1 The upscaled governing equations for the vessels

The multiscale differential equations governing the fluid flow, particle, and heat transport in the vessels can be obtained from equations (2.14a)-(2.14b), (2.14e), and (2.14g) with interface conditions (2.15a), (2.15b), (2.15d), and (2.15f). We have, by enforcing equation (2.22)-(2.23)

and multiplying each equation by a suitable power of ϵ :

$$\epsilon \nabla_y^2 \mathbf{u}_v^{(\epsilon)} + 2\epsilon^2 \nabla_y \cdot \nabla_x \mathbf{u}_v^{(\epsilon)} + \epsilon^3 \nabla_x^2 \mathbf{u}_v^{(\epsilon)} = \epsilon \nabla_x p_v^{(\epsilon)} + \nabla_y p_v^{(\epsilon)} \quad \text{in } \Omega_v, \quad (2.25a)$$

$$\epsilon \nabla_x \cdot \mathbf{u}_v^{(\epsilon)} + \nabla_y \cdot \mathbf{u}_v^{(\epsilon)} = 0 \quad \text{in } \Omega_v, \quad (2.25b)$$

$$\begin{aligned} & \epsilon^2 \frac{\partial c_v^{(\epsilon)}}{\partial t} + \nabla_x \cdot \left(\epsilon^2 c_v^{(\epsilon)} \mathbf{u}_v^{(\epsilon)} - \epsilon^2 \bar{D}_v \nabla_x c_v^{(\epsilon)} - \epsilon \bar{D}_v \nabla_y c_v^{(\epsilon)} \right) + \\ & \nabla_y \cdot \left(\epsilon c_v^{(\epsilon)} \mathbf{u}_v^{(\epsilon)} - \epsilon \bar{D}_v \nabla_x c_v^{(\epsilon)} - \bar{D}_v \nabla_y c_v^{(\epsilon)} \right) = 0, \quad \text{in } \Omega_v, \end{aligned} \quad (2.25c)$$

$$\begin{aligned} & \epsilon^2 \frac{\partial T_v^{(\epsilon)}}{\partial t} + \nabla_x \cdot \left(\epsilon^2 T_v^{(\epsilon)} \mathbf{u}_v^{(\epsilon)} - \epsilon^2 \bar{K}_v \nabla_x T_v^{(\epsilon)} - \epsilon \bar{K}_v \nabla_y T_v^{(\epsilon)} \right) + \\ & \nabla_y \cdot \left(\epsilon T_v^{(\epsilon)} \mathbf{u}_v^{(\epsilon)} - \epsilon \bar{K}_v \nabla_x T_v^{(\epsilon)} - \bar{K}_v \nabla_y T_v^{(\epsilon)} \right) = \bar{\alpha}_v c_v^{(\epsilon)} \quad \text{in } \Omega_v. \end{aligned} \quad (2.25d)$$

The interface conditions are:

$$\mathbf{u}_v^{(\epsilon)} \cdot \mathbf{n} = \epsilon \bar{L} \left(p_v^{(\epsilon)} - p_t^{(\epsilon)} \right) \quad \text{on } \Gamma, \quad (2.26a)$$

$$\mathbf{u}_v^{(\epsilon)} \cdot \boldsymbol{\tau} = -\bar{\varphi} \left[\left(\mathbf{n} \cdot (\epsilon \nabla_x + \nabla_y) \mathbf{u}_v^{(\epsilon)} \right) \cdot \boldsymbol{\tau} \right] \quad \text{on } \Gamma, \quad (2.26b)$$

$$\left(\epsilon c_v^{(\epsilon)} \mathbf{u}_v^{(\epsilon)} - \epsilon \bar{D}_v \nabla_x c_v^{(\epsilon)} - \bar{D}_v \nabla_y c_v^{(\epsilon)} \right) \cdot \mathbf{n} = \epsilon^2 \bar{P} (c_v^{(\epsilon)} - c_t^{(\epsilon)}) \quad \text{on } \Gamma, \quad (2.26c)$$

$$\left(\epsilon T_v^{(\epsilon)} \mathbf{u}_v^{(\epsilon)} - \epsilon \bar{K}_v \nabla_x T_v^{(\epsilon)} - \bar{K}_v \nabla_y T_v^{(\epsilon)} \right) \cdot \mathbf{n} = \epsilon^2 \bar{\beta}_v \left(T_v^{(\epsilon)} - T_t^{(\epsilon)} \right) \quad \text{on } \Gamma. \quad (2.26d)$$

We now equate the same coefficients for ascending powers of ϵ .

For ϵ^0 we obtain

$$\nabla_y p_v^{(0)} = 0 \quad \text{in } \Omega_v, \quad (2.27a)$$

$$\nabla_y \cdot \mathbf{u}_v^{(0)} = 0 \quad \text{in } \Omega_v, \quad (2.27b)$$

$$\mathbf{u}_v^{(0)} \cdot \mathbf{n} = 0 \quad \text{on } \Gamma, \quad (2.27c)$$

$$\mathbf{u}_v^{(0)} \cdot \boldsymbol{\tau} = -\bar{\varphi} \left[\mathbf{n} \cdot (\nabla_y \mathbf{u}_v^{(0)}) \right] \cdot \boldsymbol{\tau} \quad \text{on } \Gamma, \quad (2.27d)$$

$$\nabla_y^2 c_v^{(0)} = 0 \quad \text{in } \Omega_v, \quad (2.27e)$$

$$\left(\nabla_y c_v^{(0)} \right) \cdot \mathbf{n} = 0 \quad \text{on } \Gamma, \quad (2.27f)$$

$$\nabla_y^2 T_v^{(0)} = 0 \quad \text{in } \Omega_v, \quad (2.27g)$$

$$\left(\nabla_y T_v^{(0)} \right) \cdot \mathbf{n} = 0 \quad \text{on } \Gamma. \quad (2.27h)$$

For ϵ^1 :

$$\nabla_y^2 \mathbf{u}_v^{(0)} = \nabla_x p_v^{(0)} + \nabla_y p_v^{(1)} \quad \text{in } \Omega_v, \quad (2.28a)$$

$$\nabla_x \cdot \mathbf{u}_v^{(0)} + \nabla_y \cdot \mathbf{u}_v^{(1)} = 0 \quad \text{in } \Omega_v, \quad (2.28b)$$

$$\mathbf{u}_v^{(1)} \cdot \mathbf{n} = \bar{L} \left(p_v^{(0)} - p_t^{(0)} \right) \quad \text{on } \Gamma, \quad (2.28c)$$

$$\mathbf{u}_v^{(1)} \cdot \boldsymbol{\tau} = -\bar{\varphi} \left[\mathbf{n} \cdot \left(\nabla_x \mathbf{u}_v^{(0)} + \nabla_y \mathbf{u}_v^{(1)} \right) \right] \cdot \boldsymbol{\tau} \quad \text{on } \Gamma, \quad (2.28d)$$

$$\nabla_y^2 c_v^{(1)} = 0 \quad \text{in } \Omega_v, \quad (2.28e)$$

$$\left(\nabla_y c_v^{(1)} \right) \cdot \mathbf{n} = - \left(\nabla_x c_v^{(0)} \right) \cdot \mathbf{n} \quad \text{on } \Gamma, \quad (2.28f)$$

$$\nabla_y^2 T_v^{(1)} = 0 \quad \text{in } \Omega_v, \quad (2.28g)$$

$$\left(\nabla_y T_v^{(1)} \right) \cdot \mathbf{n} = - \left(\nabla_x T_v^{(0)} \right) \cdot \mathbf{n} \quad \text{on } \Gamma. \quad (2.28h)$$

For ϵ^2

$$\begin{aligned} & \frac{\partial c_v^{(0)}}{\partial t} + \nabla_x \cdot \left(c_v^{(0)} \mathbf{u}_v^{(0)} - \bar{D}_v \nabla_x c_v^{(0)} - \bar{D}_v \nabla_y c_v^{(1)} \right) + \\ & \nabla_y \cdot \left(c_v^{(1)} \mathbf{u}_v^{(0)} + c_v^{(0)} \mathbf{u}_v^{(1)} - \bar{D}_v \nabla_x c_v^{(1)} - \bar{D}_v \nabla_y c_v^{(2)} \right) = 0 \quad \text{in } \Omega_v, \end{aligned} \quad (2.29a)$$

$$\left(c_v^{(1)} \mathbf{u}_v^{(0)} + c_v^{(0)} \mathbf{u}_v^{(1)} - \bar{D}_v \nabla_x c_v^{(1)} - \bar{D}_v \nabla_y c_v^{(2)} \right) \cdot \mathbf{n} = \bar{P} (c_v^{(0)} - c_t^{(0)}) \quad \text{on } \Gamma, \quad (2.29b)$$

$$\begin{aligned} & \frac{\partial T_v^{(0)}}{\partial t} + \nabla_x \cdot \left(T_v^{(0)} \mathbf{u}_v^{(0)} - \bar{K}_v \nabla_x T_v^{(0)} - \bar{K}_v \nabla_y T_v^{(1)} \right) + \\ & \nabla_y \cdot \left(T_v^{(0)} \mathbf{u}_v^{(1)} + T_v^{(1)} \mathbf{u}_v^{(0)} - \bar{K}_v \nabla_x T_v^{(1)} - \bar{K}_v \nabla_y T_v^{(2)} \right) = \bar{\alpha}_v c_v^{(0)} \quad \text{in } \Omega_v, \end{aligned} \quad (2.29c)$$

$$\left(T_v^{(0)} \mathbf{u}_v^{(1)} + T_v^{(1)} \mathbf{u}_v^{(0)} - \bar{K}_v \nabla_x T_v^{(1)} - \bar{K}_v \nabla_y T_v^{(2)} \right) \cdot \mathbf{n} = \bar{\beta}_v \left(T_v^{(0)} - T_t^{(0)} \right) \quad \text{on } \Gamma. \quad (2.29d)$$

Now, we determine the macroscale relationships for the leading order velocity and pressure $\langle \mathbf{u}_v^{(0)} \rangle_v$ and $p_v^{(0)}$.

Equation (2.27a) implies:

$$p_v^{(0)} = p_v^{(0)}(\mathbf{x}, t). \quad (2.30)$$

This means that the leading order pressure in the vessels is \mathbf{y} -constant.

Using equation (2.28a) from the ϵ^1 condition, together with (2.27b), (2.27c), and (2.27d) from the ϵ^0 conditions, we obtain a Stokes' type problem for $\mathbf{u}_v^{(0)}$ and $p_v^{(1)}$, that is

$$\left\{ \begin{array}{l} \nabla_y^2 \mathbf{u}_v^{(0)} = \nabla_x p_v^{(0)} + \nabla_y p_v^{(1)} \quad \text{in } \Omega_v, \\ \nabla_y \cdot \mathbf{u}_v^{(0)} = 0 \quad \text{in } \Omega_v, \\ \mathbf{u}_v^{(0)} \cdot \mathbf{n} = 0 \quad \text{on } \Gamma, \\ \mathbf{u}_v^{(0)} \cdot \boldsymbol{\tau} = -\bar{\varphi} \left[(\mathbf{n} \cdot \nabla_y) \mathbf{u}_v^{(0)} \right] \cdot \boldsymbol{\tau} \quad \text{on } \Gamma. \end{array} \right. \quad (2.31)$$

Exploiting linearity, the solutions for $\mathbf{u}_v^{(0)}$ and $p_v^{(1)}$ can be formulated in terms of the following ansatz

$$\mathbf{u}_v^{(0)} = -\mathbf{W}(\mathbf{x}, \mathbf{y}) \nabla_x p_v^{(0)}, \quad (2.32a)$$

$$p_v^{(1)} = -\mathbf{m}(\mathbf{x}, \mathbf{y}) \nabla_x p_v^{(0)} + \bar{p}(\mathbf{x}, t). \quad (2.32b)$$

The auxiliary tensor \mathbf{W} and the auxiliary vector \mathbf{m} are the solution of the Stokes' cell problem:

$$\nabla_y^2 \mathbf{W}^T = \nabla_y \mathbf{m} - I \quad \text{in } \Omega_v, \quad (2.33a)$$

$$\nabla_y \cdot \mathbf{W}^T = 0 \quad \text{in } \Omega_v, \quad (2.33b)$$

$$\mathbf{W}^T \mathbf{n} = 0 \quad \text{on } \Gamma, \quad (2.33c)$$

$$\mathbf{W}^T \boldsymbol{\tau} = -\bar{\varphi} [(\nabla_y \mathbf{W}^T) \mathbf{n}] \boldsymbol{\tau} \quad \text{on } \Gamma. \quad (2.33d)$$

Integrating (2.32a) over Ω_v leads to the average leading order velocity in the vessels,

$$\langle \mathbf{u}_v^{(0)} \rangle_v = -\mathbf{Y}_v \nabla_x p_v^{(0)}. \quad (2.34)$$

Here,

$$\mathbf{Y}_v = \langle \mathbf{W} \rangle_v = \frac{1}{|\Omega_v|} \int_{\Omega_v} \mathbf{W} dy. \quad (2.35)$$

Equation (2.34) shows that the vessels' fluid flow obeys Darcy's law with hydraulic conductivity tensor \mathbf{Y}_v given by relationship (2.35).

In order to find the equation for the leading order pressure leading term $p_v^{(0)}$, we take the average of (2.28b) and make use of interface condition (2.28c), as well as the divergence theorem with respect to \mathbf{y} , as follows:

$$\langle \nabla_x \cdot \mathbf{u}_v^{(0)} \rangle_v + \langle \nabla_y \cdot \mathbf{u}_v^{(1)} \rangle_v = 0, \quad (2.36)$$

$$\langle \nabla_x \cdot \mathbf{u}_v^{(0)} \rangle_v = -\frac{1}{|\Omega_v|} \int_{\Gamma} \mathbf{u}_v^{(1)} \cdot \mathbf{n} dS_y, \quad (2.37)$$

$$= -\frac{1}{|\Omega_v|} \int_{\Gamma} \bar{L}(p_v^{(0)} - p_t^{(0)}) dS_y. \quad (2.38)$$

Therefore,

$$\nabla_x \cdot \langle \mathbf{u}_v^{(0)} \rangle_v = -\frac{1}{|\Omega_v|} \int_{\Gamma} \bar{L}(p_v^{(0)} - p_t^{(0)}) dS_y. \quad (2.39)$$

Thus, by means of (2.34),

$$\nabla_x \cdot (\mathbf{Y}_v \nabla_x p_v^{(0)}) = \frac{1}{|\Omega_v|} \int_{\Gamma} \bar{L}(p_v^{(0)} - p_t^{(0)}) dS_y. \quad (2.40)$$

Equation (2.40) is the macroscale governing equation for the leading order pressure $p_v^{(0)}$.

The leading order concentration $c_v^{(0)}$ can be found by using first equations (2.27e) and (2.27f), from which we deduce that the zero-th order concentration in the vessels depends on the macroscale only, i.e.

$$c_v^{(0)} = c_v^{(0)}(\mathbf{x}, t). \quad (2.41)$$

We can formulate an ansatz for the solution $c_v^{(1)}$ of problem (2.28e)-(2.28f) by exploiting linearity as follows

$$c_v^{(1)} = -\mathbf{a} \cdot \nabla_x c_v^{(0)} + \bar{c}(\mathbf{x}, t), \quad (2.42)$$

where $\mathbf{a}(\mathbf{x}, \mathbf{y})$ is an auxiliary vector and \bar{c} is an arbitrary \mathbf{y} -constant function. The solution (2.42) holds true provided that

$$\nabla_y^2 \mathbf{a} = \mathbf{0} \quad \text{in } \Omega_v, \quad (2.43a)$$

$$(\nabla_y \mathbf{a}) \mathbf{n} = \mathbf{n} \quad \text{on } \Gamma. \quad (2.43b)$$

Integrating (2.29a) and using the divergence theorem with respect to \mathbf{y} , and subsequently making use of interface condition (2.29b) from equating the same power of ϵ^2 yields

$$\frac{\partial c_v^{(0)}}{\partial t} + \nabla_x \cdot \left(c_v^{(0)} \langle \mathbf{u}_v^{(0)} \rangle_v - \bar{D}_v \nabla_x c_v^{(0)} - \bar{D}_v \langle \nabla_y c_v^{(1)} \rangle_v \right) + \frac{1}{|\Omega_v|} \int_{\Gamma} \bar{P} (c_v^{(0)} - c_t^{(0)}) dS_y = 0, \quad (2.44)$$

where the additional contribution over the boundary $\partial\Omega_v \setminus \Gamma$ vanishes due to \mathbf{y} -periodicity.

Using the ansatz (2.42), we obtain:

$$\frac{\partial c_v^{(0)}}{\partial t} + \nabla_x \cdot \left(c_v^{(0)} \langle \mathbf{u}_v^0 \rangle - F_v \nabla_x c_v^{(0)} \right) + \frac{1}{|\Omega_v|} \int_{\Gamma} \bar{P} (c_v^{(0)} - c_t^{(0)}) dS = 0, \quad (2.45)$$

where

$$F_v = \bar{D}_v (I - \langle (\nabla_y \mathbf{a})^T \rangle_v) \quad (2.46)$$

is the effective diffusivity tensor in the vessels, and \bar{D}_v is defined according to (2.18) and (2.19). Equation (2.45) is an advection-diffusion-reaction equation for $c_v^{(0)}$ and it describes the macroscale drug dynamics in the vessels.

A macroscale equation for the heat transport in the vessels can be obtained by following the same steps described above for particle transport. The solution of (2.27g) and (2.27h) is

$$T_v^{(0)} = T_v^{(0)}(\mathbf{x}, t). \quad (2.47)$$

Therefore, $T_v^{(0)}$ is \mathbf{y} -constant.

The solution of the problem obtained by collecting (2.28g) and (2.28h) from the ϵ^1 condition

can be formulated in terms of the following ansatz for $T_v^{(1)}$:

$$T_v^{(1)} = -\mathbf{g} \cdot \nabla_x T_v^{(0)}(\mathbf{x}, t) + \bar{T}(\mathbf{x}, t), \quad (2.48)$$

where the auxiliary vector \mathbf{g} is the solution of the following cell problem

$$\nabla_y^2 \mathbf{g} = 0 \quad \text{in } \Omega_v, \quad (2.49a)$$

$$(\nabla_y \mathbf{g}) \mathbf{n} = \mathbf{n} \quad \text{on } \Gamma. \quad (2.49b)$$

Integrating (2.29c) and exploiting (2.29d), and performing the same steps as equations (2.29a) and (2.29b) we reach the following macroscale result

$$\frac{\partial T_v^{(0)}}{\partial t} + \nabla_x \cdot \left(T_v^{(0)} \langle \mathbf{u}_v^{(0)} \rangle - N_v \nabla_x T_v^{(0)} \right) + \frac{1}{|\Omega_v|} \bar{\beta}_v \int_{\Gamma} \left(T_v^{(0)} - T_t^{(0)} \right) dS = \bar{\alpha}_v c_v^0, \quad (2.50)$$

with

$$N_v = \bar{K}_v (I - \langle (\nabla_y \mathbf{g})^T \rangle_v), \quad (2.51)$$

where N_v is the heat conductivity tensor for the vessels' compartment with \bar{K}_v is defined in (2.20). The differential equation (2.50) is an advection-diffusion-reaction type equation describing the behavior of the leading order temperature $T_v^{(0)}$ at the macroscale.

2.4.2 The upscaled governing equations in the tumour interstitium

In order to provide the macroscale differential equations for fluid flow, particle transport, and heat distribution related to the tumour interstitial compartment, we follow the same steps as in the vessels' case. The multi-scale equations (2.14c), (2.14d), (2.14f), (2.14h), with interface conditions (2.15c), (2.15e), and (2.15g) can be expressed as:

$$\epsilon \mathbf{u}_t^{(\epsilon)} = -\epsilon \bar{\kappa} \nabla_x p_t^{(\epsilon)} - \kappa \nabla_y p_t^{(\epsilon)} \quad \text{in } \Omega_t, \quad (2.52a)$$

$$\epsilon \nabla_x \cdot \mathbf{u}_t^{(\epsilon)} + \nabla_y \cdot \mathbf{u}_t^{(\epsilon)} = 0 \quad \text{in } \Omega_t, \quad (2.52b)$$

$$\mathbf{u}_t^{(\epsilon)} \cdot \mathbf{n}_t = \epsilon \bar{L} \left(p_t^{(\epsilon)} - p_v^{(\epsilon)} \right) \quad \text{on } \Gamma. \quad (2.52c)$$

$$\begin{aligned} & \epsilon^2 \frac{\partial c_t^{(\epsilon)}}{\partial t} + \nabla_x \cdot \left(\epsilon^2 c_t^{(\epsilon)} \mathbf{u}_t^{(\epsilon)} - \epsilon^2 \bar{D}_t \nabla_x c_t^{(\epsilon)} - \epsilon \bar{D}_t \nabla_y c_t^{(\epsilon)} \right) + \\ & \nabla_y \cdot \left(\epsilon c_t^{(\epsilon)} \mathbf{u}_t^{(\epsilon)} - \epsilon \bar{D}_t \nabla_x c_t^{(\epsilon)} - \bar{D}_t \nabla_y c_t^{(\epsilon)} \right) = -\epsilon^2 \Upsilon c_t^{(\epsilon)} \quad \text{in } \Omega_t, \end{aligned} \quad (2.53a)$$

$$\left(\epsilon c_t^{(\epsilon)} \mathbf{u}_t^{(\epsilon)} - \epsilon \bar{D}_t \nabla_x c_t^{(\epsilon)} - \bar{D}_t \nabla_y c_t^{(\epsilon)} \right) \cdot \mathbf{n}_t = \epsilon^2 \bar{P} \left(c_t^{(\epsilon)} - c_v^{(\epsilon)} \right) \quad \text{on } \Gamma. \quad (2.53b)$$

$$\begin{aligned} \epsilon^2 \frac{\partial T_t^{(\epsilon)}}{\partial t} + \nabla_x \cdot \left(\epsilon^2 T_t^{(\epsilon)} \mathbf{u}_t^{(\epsilon)} - \epsilon^2 \bar{K}_t \nabla_x T_t^{(\epsilon)} - \epsilon \bar{K}_t \nabla_y T_t^{(\epsilon)} \right) + \\ \nabla_y \cdot \left(\epsilon T_t^{(\epsilon)} \mathbf{u}_t^{(\epsilon)} - \epsilon \bar{K}_t \nabla_x T_t^{(\epsilon)} - \bar{K}_t \nabla_y T_t^{(\epsilon)} \right) = \epsilon^2 \bar{\alpha}_t c_t^{(\epsilon)} \quad \text{in } \Omega_t, \end{aligned} \quad (2.54a)$$

$$\left(\epsilon T_t^{(\epsilon)} \mathbf{u}_t^{(\epsilon)} - \epsilon \bar{K}_t \nabla_x T_t^{(\epsilon)} - \bar{K}_t \nabla_y T_t^{(\epsilon)} \right) \cdot \mathbf{n}_t = \epsilon^2 \bar{\beta}_t \left(T_t^{(\epsilon)} - T_v^{(\epsilon)} \right) \quad \text{on } \Gamma. \quad (2.54b)$$

Here, $\mathbf{n}_t = -\mathbf{n}$ is the unit vector normal to the interface pointing from the interstitial compartment into the vessels' one. Equating the same coefficient of ϵ^0 we obtain

$$\nabla_y p_t^{(0)} = 0 \quad \text{in } \Omega_t, \quad (2.55a)$$

$$\nabla_y \cdot \mathbf{u}_t^{(0)} = 0 \quad \text{in } \Omega_t, \quad (2.55b)$$

$$\mathbf{u}_t^{(0)} \cdot \mathbf{n}_t = 0 \quad \text{on } \Gamma, \quad (2.55c)$$

$$\nabla^2 c_t^{(0)} = 0 \quad \text{in } \Omega_t, \quad (2.55d)$$

$$\left(\nabla_y c_t^{(0)} \right) \cdot \mathbf{n}_t = 0 \quad \text{on } \Gamma, \quad (2.55e)$$

$$\nabla^2 T_t^{(0)} = 0 \quad \text{in } \Omega_t, \quad (2.55f)$$

$$\left(\nabla_y T_t^{(0)} \right) \cdot \mathbf{n}_t = 0 \quad \text{on } \Gamma, \quad (2.55g)$$

while for ϵ^1

$$\mathbf{u}_t^{(0)} = -\bar{\kappa} \nabla_x p_t^{(0)} - \bar{\kappa} \nabla_y p_t^{(1)} \quad \text{in } \Omega_t, \quad (2.56a)$$

$$\nabla_x \cdot \mathbf{u}_t^{(0)} + \nabla_y \cdot \mathbf{u}_t^{(1)} = 0 \quad \text{in } \Omega_t, \quad (2.56b)$$

$$\mathbf{u}_t^{(1)} \cdot \mathbf{n}_t = \bar{L} \left(p_t^{(0)} - p_v^{(0)} \right) \quad \text{on } \Gamma, \quad (2.56c)$$

$$\nabla^2 c_t^{(0)} = 0 \quad \text{in } \Omega_t, \quad (2.56d)$$

$$\left(\nabla_x c_t^{(0)} \right) \cdot \mathbf{n}_t = \left(\nabla_y c_t^{(1)} \right) \cdot \mathbf{n}_t \quad \text{on } \Gamma, \quad (2.56e)$$

$$\nabla^2 T_t^{(0)} = 0 \quad \text{in } \Omega_t, \quad (2.56f)$$

$$\left(\nabla_x T_t^{(0)} \right) \cdot \mathbf{n}_t = \left(\nabla_y T_t^{(1)} \right) \cdot \mathbf{n}_t \quad \text{on } \Gamma, \quad (2.56g)$$

Finally, for ϵ^2 we have

$$\begin{aligned} & \frac{\partial c_t^{(0)}}{\partial t} + \nabla_x \cdot \left(c_t^{(0)} \mathbf{u}_t^{(0)} - \bar{D}_t \nabla_x c_t^{(0)} - \bar{D}_t \nabla_y c_t^{(1)} \right) + \\ & \nabla_y \cdot \left(c_t^{(1)} \mathbf{u}_t^{(0)} + c_t^{(0)} \mathbf{u}_t^{(1)} - \bar{D}_t \nabla_x c_t^{(1)} - \bar{D}_t \nabla_y c_t^{(2)} \right) = -\Upsilon c_t^{(0)} \quad \text{in } \Omega_t, \end{aligned} \quad (2.57a)$$

$$\left(c_t^{(1)} \mathbf{u}_t^{(0)} + c_t^{(0)} \mathbf{u}_t^{(1)} - \bar{D}_t \nabla_x c_t^{(1)} - \bar{D}_t \nabla_y c_t^{(2)} \right) \cdot \mathbf{n}_t = \bar{P}(c_t^{(0)} - c_v^{(0)}) \quad \text{on } \Gamma, \quad (2.57b)$$

$$\begin{aligned} & \frac{\partial T_t^{(0)}}{\partial t} + \nabla_x \cdot \left(T_t^{(0)} \mathbf{u}_t^{(0)} - \bar{K}_t \nabla_x T_t^{(0)} - \bar{K}_t \nabla_y T_t^{(1)} \right) + \\ & \nabla_y \cdot \left(T_t^{(0)} \mathbf{u}_t^{(1)} + T_t^{(1)} \mathbf{u}_t^{(0)} - \bar{K}_t \nabla_x T_t^{(1)} - \bar{K}_t \nabla_y T_t^{(2)} \right) = \bar{\alpha}_t c_t^{(0)} \quad \text{in } \Omega_t, \end{aligned} \quad (2.57c)$$

$$\left(T_t^{(0)} \mathbf{u}_t^{(1)} + T_t^{(1)} \mathbf{u}_t^{(0)} - \bar{K}_t \nabla_x T_t^{(1)} - \bar{K}_t \nabla_y T_t^{(2)} \right) \cdot \mathbf{n}_t = \bar{\beta}_t (T_t^{(0)} - T_v^{(0)}) \quad \text{on } \Gamma. \quad (2.57d)$$

Firstly, we find the macroscale equation of $\langle \mathbf{u}_t^{(0)} \rangle_t$ in terms of $p_t^{(0)}$. Equation (2.55a) leads to:

$$p_t^{(0)} = p_t^{(0)}(\mathbf{x}, t).$$

Therefore $p_t^{(0)}$ is \mathbf{y} -constant. Substituting (2.56a) from the ϵ^1 conditions into (2.55b) and (2.55c) obtained from the ϵ^0 conditions yields:

$$\nabla_y^2 p_t^{(1)} = 0 \quad \text{in } \Omega_t, \quad (2.58a)$$

$$\nabla_y p_t^{(1)} \cdot \mathbf{n}_t = -\nabla_x p_t^{(0)} \cdot \mathbf{n}_t \quad \text{on } \Gamma. \quad (2.58b)$$

The solution $p_t^{(1)}$ is given by:

$$p_t^{(1)} = -\mathbf{r}(\mathbf{x}, \mathbf{y}) \cdot \nabla_x p_t^{(0)} + \bar{p}_t(\mathbf{x}, t), \quad (2.59)$$

where the auxiliary vector \mathbf{r} solves the cell problem

$$\nabla_y^2 \mathbf{r} = \mathbf{0} \quad \text{in } \Omega_t, \quad (2.60a)$$

$$(\nabla_y \mathbf{r}) \mathbf{n}_t = \mathbf{n}_t \quad \text{on } \Gamma. \quad (2.60b)$$

Applying the average integral over Ω_t to (2.56a) and substituting (2.59), leads to

$$\begin{aligned} \langle \mathbf{u}_t^{(0)} \rangle_t &= -\frac{\bar{K}}{|\Omega_t|} \int_{\Omega_t} \left(\nabla_x p_t^{(0)} - \nabla_y \left(\mathbf{r} \cdot \nabla_x p_t^{(0)} \right) \right) dy = -\frac{\bar{K}}{|\Omega_t|} \int_{\Omega_t} \left(I - (\nabla_y \mathbf{r})^T \right) \nabla_x p_t^{(0)} dy \\ &= -\bar{K} \Upsilon_t \nabla_x p_t^{(0)}, \end{aligned} \quad (2.61)$$

where

$$\Upsilon_t = I - \frac{1}{|\Omega_t|} \int_{\Omega_t} (\nabla_y \mathbf{r})^T dy. \quad (2.62)$$

Here, \mathbf{Y}_t is the fluid hydraulic conductivity tensor for interstitial compartment. Equation (2.61) shows that the macroscale fluid flow in the tumor interstitium is also governed by Darcy's law.

The macroscale equation governing the tumour interstitial pressure leading term $p_t^{(0)}$ can be found by taking the average over Ω_t and applying the divergence theorem to (2.56b). Then using (2.56c), we obtain:

$$\nabla_x \cdot \left(\bar{\kappa} \mathbf{Y}_t \nabla_x p_t^{(0)} \right) = \frac{\bar{L} \left(p_t^{(0)} - p_v^{(0)} \right)}{|\Omega_t|} S, \quad (2.63)$$

where we exploited the fact that both $p_t^{(0)}$ and $p_v^{(0)}$ depend on the macroscale only and S is the microscale surface of the capillaries defined by

$$S = \int_{\Gamma} dS_y. \quad (2.64)$$

Secondly, we find the multiscale differential equation for particle concentration in the interstitium. Equations (2.53a), and (2.53b) are formally identical to (2.25c) and (2.26c), when the following analogies are made:

$$\mathbf{u}_v \rightarrow \mathbf{u}_t, \quad c_v \rightarrow c_t, \quad \bar{D}_v \rightarrow \bar{D}_t, \quad \frac{\partial c_v}{\partial t} \rightarrow \frac{\partial c_t}{\partial t} + \Upsilon c_t, \quad |\Omega_v| \rightarrow |\Omega_t|, \quad \text{and} \quad \mathbf{n} \rightarrow \mathbf{n}_t = -\mathbf{n}. \quad (2.65)$$

The asymptotic homogenization procedure provides tumour interstitial macroscale differential equation which is similar to (2.45);

$$\frac{\partial c_t^{(0)}}{\partial t} + \nabla_x \cdot \left(c_t^{(0)} \langle \mathbf{u}_t^{(0)} \rangle_t - \mathbf{F}_t \nabla_x c_t^{(0)} \right) + \frac{S}{|\Omega_t|} \bar{P} \left(c_t^{(0)} - c_v^{(0)} \right) = -\Upsilon c_t^{(0)}, \quad (2.66)$$

where we have observed that both $c_v^{(0)}$ and $c_t^{(0)}$ depend only on the macroscale \mathbf{x} . Equation (2.66) represents the macroscale advection-diffusion-reaction describing interstitial particles' transport with effective diffusivity tensor

$$\mathbf{F}_t = \bar{D}_t (I - \langle (\nabla_y \mathbf{b})^T \rangle_t), \quad (2.67)$$

where \bar{D}_t is defined according to (2.18) and (2.19). The vector \mathbf{b} solves the cell problem (2.43a) and (2.43b) in tumour interstitial domain, which is

$$\nabla_y^2 \mathbf{b} = \mathbf{0} \quad \text{in} \quad \Omega_t, \quad (2.68a)$$

$$(\nabla_y \mathbf{b}) \mathbf{n}_t = \mathbf{n}_t \quad \text{on} \quad \Gamma. \quad (2.68b)$$

Finally, the differential equation for the leading order temperature in the interstitial compartment

can be computed by following the above steps together with the following identifications:

$$\mathbf{u}_v \rightarrow \mathbf{u}_t, \quad T_v \rightarrow T_t, \quad \bar{K}_v \rightarrow \bar{K}_t, \quad \frac{\partial T_v}{\partial t} \rightarrow \frac{\partial T_t}{\partial t} - \bar{\alpha} f(c_t), \quad |\Omega_v| \rightarrow |\Omega_t|, \quad \text{and} \quad \mathbf{n} \rightarrow \mathbf{n}_t = -\mathbf{n}. \quad (2.69)$$

Therefore, the multiscale advection-diffusion-reaction for the leading order temperature in the interstitial compartment $T_t^{(0)}$ reads

$$\frac{\partial T_t^{(0)}}{\partial t} + \nabla_x \cdot \left(T_t^{(0)} \langle \mathbf{u}_t^{(0)} \rangle_t - \mathbf{N}_t \nabla_x T_t^{(0)} \right) + \frac{S}{|\Omega_t|} \bar{\beta}_t \left(T_t^{(0)} - T_v^{(0)} \right) = \bar{\alpha}_t c_t^{(0)}, \quad (2.70)$$

with

$$\mathbf{N}_t = \bar{K}_t (I - \langle (\nabla_y \mathbf{e})^T \rangle_t) \quad (2.71)$$

is the thermal conductivity tensor for interstitial compartment, and \bar{K}_t is defined in (2.20).

The vector \mathbf{e} solves the cell problem given by (2.49a) and (2.49b), but in the interstitial cell portion, that is:

$$\nabla_y^2 \mathbf{e} = \mathbf{0} \quad \text{in} \quad \Omega_t, \quad (2.72a)$$

$$(\nabla_y \mathbf{e}) \mathbf{n}_t = \mathbf{n}_t \quad \text{on} \quad \Gamma. \quad (2.72b)$$

2.4.3 The macroscale model obtained via asymptotic homogenisation

From the previous section, we obtain the macroscale differential equations for the zero-th order pressures, velocities, concentrations, and temperatures $p_t^{(0)}$, $p_v^{(0)}$, $\langle \mathbf{u}_t^{(0)} \rangle_t$, $\langle \mathbf{u}_v^{(0)} \rangle_v$, $c_t^{(0)}$, $c_v^{(0)}$, $T_t^{(0)}$ and $T_v^{(0)}$. These can be summarized as follows

$$\begin{cases} \langle \mathbf{u}_v^{(0)} \rangle_v = -\Upsilon_v \nabla_x p_v^{(0)}, \\ \langle \mathbf{u}_t^{(0)} \rangle_t = -\bar{\kappa} \Upsilon_t \nabla_x p_t^{(0)}, \end{cases} \quad (2.73)$$

$$\begin{cases} \nabla_x \cdot \left(\Upsilon_v \nabla_x p_v^{(0)} \right) = \frac{\bar{L}(p_v^{(0)} - p_t^{(0)})}{|\Omega_v|} S, \\ \nabla_x \cdot \left(\bar{\kappa} \Upsilon_t \nabla_x p_t^{(0)} \right) = \frac{\bar{L}(p_t^{(0)} - p_v^{(0)})}{|\Omega_t|} S, \end{cases} \quad (2.74)$$

$$\begin{cases} \frac{\partial c_v^{(0)}}{\partial t} + \nabla_x \cdot \left(c_v^{(0)} \langle \mathbf{u}_v^{(0)} \rangle_v - \mathbf{F}_v \nabla_x c_v^{(0)} \right) + \frac{S}{|\Omega_v|} \bar{P} \left(c_v^{(0)} - c_t^{(0)} \right) = 0, \\ \frac{\partial c_t^{(0)}}{\partial t} + \nabla_x \cdot \left(c_t^{(0)} \langle \mathbf{u}_t^{(0)} \rangle_t - \mathbf{F}_t \nabla_x c_t^{(0)} \right) + \frac{S}{|\Omega_t|} \bar{P} \left(c_t^{(0)} - c_v^{(0)} \right) = -\Upsilon c_t^{(0)}, \end{cases} \quad (2.75)$$

$$\left\{ \begin{array}{l} \frac{\partial T_v^{(0)}}{\partial t} + \nabla_x \cdot \left(T_v^{(0)} \langle \mathbf{u}_v^{(0)} \rangle_v - N_v \nabla_x T_v^{(0)} \right) + \frac{S}{|\Omega_v|} \bar{\beta}_v \left(T_v^{(0)} - T_t^{(0)} \right) = \bar{\alpha}_v c_v^{(0)}, \\ \frac{\partial T_t^{(0)}}{\partial t} + \nabla_x \cdot \left(T_t^{(0)} \langle \mathbf{u}_t^{(0)} \rangle_t - N_t \nabla_x T_t^{(0)} \right) + \frac{S}{|\Omega_t|} \bar{\beta}_t \left(T_t^{(0)} - T_v^{(0)} \right) = \bar{\alpha}_t c_t^{(0)}, \end{array} \right. \quad (2.76)$$

where $Y_v(\mathbf{x})$, $\bar{\kappa}Y_t(\mathbf{x})$, $F_v(\mathbf{x})$, $F_t(\mathbf{x})$, $N_v(\mathbf{x})$, $N_t(\mathbf{x})$ are effective hydraulic, diffusion, and thermal conductivity tensors in the vessels' and interstitial compartments, respectively. Here, $|\Omega_v|$ denotes the vessel volume, $|\Omega_t|$ is the interstitial volume, and S is the vessels' wall surface.

The system of equations (2.74) describes transport in a porous medium with mass transfer between compartments. The leakage of the blood across the vessels is reflected in the mass exchange between the two compartments which is proportional to the difference between the leading order pressures.

The particles' transport in the vessels' and interstitial compartments depends on the fluid flow and it is represented by the system of coupled advection-diffusion-reaction equations (2.75).

Similarly, the system of coupled advection-diffusion-reaction equations in (2.76) describes the heat transport at the macroscale and the temperatures' profiles depend on both fluid and particles' transport.

Moreover, the macroscale coefficients, namely hydraulic conductivity tensors, diffusion tensors, and thermal conductivity tensors, can be determined by solving the cell problems (2.33a-2.33d), (2.60a, 2.60b), (2.43a, 2.43b), (2.68a, 2.68b), (2.49a, 2.49b), and (2.72a, 2.72b), respectively.

For instance, the cell problems related to interstitial fluid flow, drug transport, and heat transport, are to be closed by a further condition for uniqueness to be achieved (for example by assuming the null cell average of the auxiliary variables in the cell), as illustrated by Cioranescu and Donato [29], Penta et al. [102].

2.4.4 The effective coefficients and microscale cell problems

In order to close the system of PDEs at the macroscale, we need to compute the effective coefficients by solving appropriate cell problems at the microscale. The differential problems which are related to the hydraulic conductivity tensors are discussed by Penta and Ambrosi [103]. The authors solved the differential problems numerically and investigated the influence of the vessels' tortuosity on the hydraulic conductivity tensors. Mascheroni and Penta [85] extended the analysis carried out by Penta and Ambrosi [103] to compute the effective diffusion coefficients by solving the cell problems related to drug transport, i.e. finding the solution for the auxiliary variables which are called \mathbf{a} , and \mathbf{b} in the present manuscript, c.f. (2.43a)- (2.43a), and (2.68a)- (2.68a). They also varied the geometrical tortuosity and found its impact on the tensors F_v and F_t . Changing the vessels' shape or tortuosity implies changes in the interstitial and vessels'

volumes. Both the vessels' hydraulic conductivity and particles' diffusivity are affected by the vessels' tortuosity. In particular, Penta and Ambrosi [103] show that the hydraulic conductivity exhibits a nonlinear decreasing profile at increasing tortuosity, while Mascheroni and Penta [85] show that also diffusion decreases as tortuosity increases, although to a lesser extent. In contrast, the interstitial coefficients are not significantly affected by microscale changes in the geometry under consideration. Penta and Ambrosi [103] solved the problem which corresponds to those related to the interstitial fluid, drug, and thermal auxiliary variables \mathbf{r} , \mathbf{b} , and \mathbf{e} in our work, i.e. (2.60a)-(2.60b), (2.68a)-(2.68b), and (2.72a)-(2.72b), respectively. In particular, these latter problems (2.60a)-(2.60b), (2.68a)-(2.68b), and (2.72a)-(2.72b) are equivalent, so the auxiliary variables \mathbf{r} , \mathbf{b} , and \mathbf{e} solve the same problem and

$$\nabla_{\mathbf{y}}\mathbf{r} = \nabla_{\mathbf{y}}\mathbf{b} = \nabla_{\mathbf{y}}\mathbf{e}. \quad (2.77)$$

Penta and Ambrosi [103] concluded that as long as the vessels' volume fraction is much smaller than the interstitial one, the influence of the microscale on the interstitial coefficients is negligible, i.e. they observed that

$$\langle \nabla_{\mathbf{y}}\mathbf{r} \rangle_t = \langle \nabla_{\mathbf{y}}\mathbf{b} \rangle_t = \langle \nabla_{\mathbf{y}}\mathbf{e} \rangle_t \approx 0. \quad (2.78)$$

As such, from now on we focus on the microscale cell problems in the vessels' compartments and account for (2.78), so that, by recalling the definitions (2.62), (2.67), and (2.71), we can assume

$$\mathbf{Y}_t = \mathbf{I}; \quad \mathbf{F}_t = \bar{D}_t \mathbf{I}; \quad \mathbf{N}_t = \bar{K}_t \mathbf{I}. \quad (2.79)$$

By following Mascheroni and Penta [85], Penta and Ambrosi [103], we enforce invariance with respect to the three orthogonal axes so that the auxiliary tensors in the vessels \mathbf{W} , \mathbf{F}_v , \mathbf{N}_v are proportional to the identity tensor.

In particular, for the diffusivity \mathbf{F}_v and thermal conductivity \mathbf{N}_v , we have:

$$\mathbf{F}_v = \tilde{D}_v \mathbf{I}, \quad \mathbf{N}_v = \tilde{N}_v \mathbf{I}.$$

such that:

$$\begin{aligned} \tilde{D}_v &= \bar{D}_v \left(1 - \left\langle \frac{\partial a_1}{\partial y_1} \right\rangle_v \right) = \bar{D}_v \left(1 - \left\langle \frac{\partial a_2}{\partial y_2} \right\rangle_v \right) = \bar{D}_v \left(1 - \left\langle \frac{\partial a_3}{\partial y_3} \right\rangle_v \right), \\ \tilde{N}_v &= \bar{K}_v \left(1 - \left\langle \frac{\partial g_1}{\partial y_1} \right\rangle_v \right) = \bar{K}_v \left(1 - \left\langle \frac{\partial g_2}{\partial y_2} \right\rangle_v \right) = \bar{K}_v \left(1 - \left\langle \frac{\partial g_3}{\partial y_3} \right\rangle_v \right), \end{aligned}$$

where we can further notice that \mathbf{a} and \mathbf{g} are actually the solution to the exact same cell problem (2.43a-2.43b) or equivalently (2.49a-2.49b). This leads to the solution of a standard Laplace

problem, which reads, for example for the component g_1

$$\nabla^2 g_1 = 0 \quad \text{in } \Omega_v, \quad (2.80a)$$

$$\nabla g_1 \cdot \mathbf{n} = n_1 \quad \text{on } \Gamma, \quad (2.80b)$$

supplemented by a further condition to ensure uniqueness, e.g.

$$\langle g_1 \rangle_v = 0 \quad \text{in } \Omega_v. \quad (2.81)$$

The analysis that follows is carried out by varying the tortuosity of the microvessels according to Penta and Ambrosi [103].

We exploit the solutions of the cell problem (2.80a-2.80b), which is solved by Mascheroni and Penta [85], to investigate the role of tortuosity on the homogenised thermal conductivity \tilde{N}_v by varying the Amplitude and spatial frequency ω . The profile of the relative thermal conductivity (and diffusivity)

$$\tilde{D}_v / \bar{D}_v = \tilde{N}_v / \bar{K}_v = 1 - \left\langle \frac{\partial a_1}{\partial y_1} \right\rangle_v = 1 - \left\langle \frac{\partial g_1}{\partial y_1} \right\rangle_v, \quad (2.82)$$

which is based on the results reported by [85], is shown in Figure 2.3.

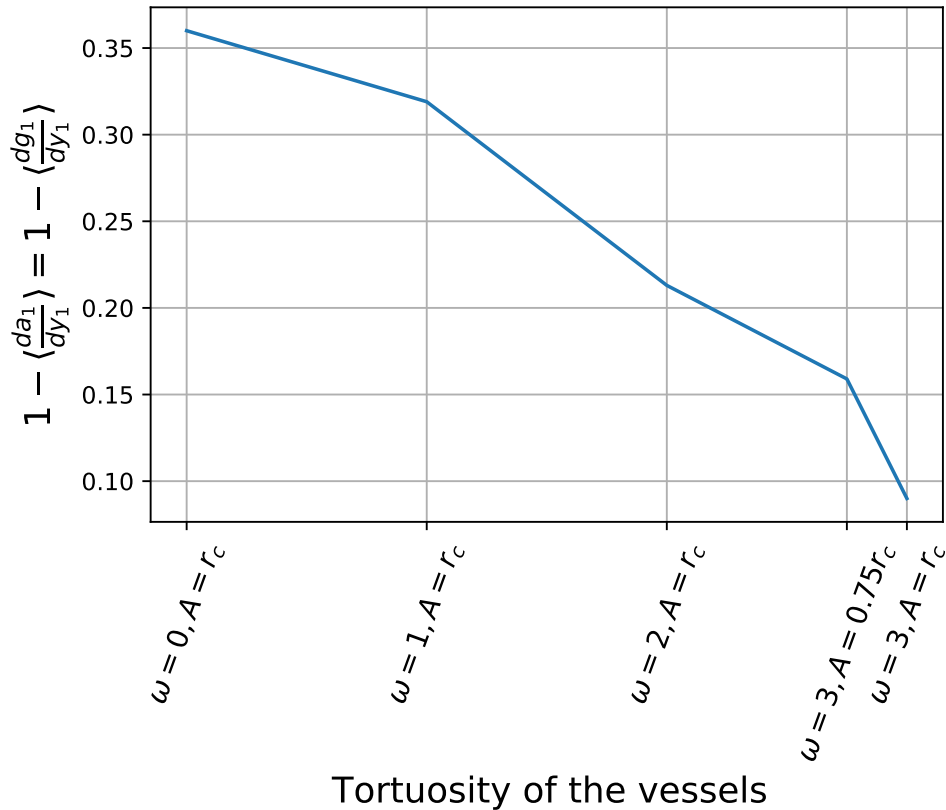


Figure 2.3: The ratio between the homogenised and base vessels' diffusive conductivities values. The values of the parameters are taken from Table 2.2. This figure is plotted by Al Sariri and Penta [3].

2.5 The mathematical model for a spherical tumour

We assume that the vascularised tumour can be represented in spherical coordinates with radius R . Also, we presume that the symmetric tumour is isolated and it interacts with surrounding environment through the vessels. Assuming radial symmetry, the model reads as follows:

$$\begin{cases} \frac{\partial c_v^{(0)}}{\partial t} + \frac{1}{r^2} \frac{\partial}{\partial r} \left(r^2 \left(c_v^{(0)} \langle u_v^{(0)} \rangle_v - \tilde{D}_v \frac{\partial c_v^{(0)}}{\partial r} \right) \right) + \frac{S}{|\Omega_v|} \bar{P} \left(c_v^{(0)} - c_t^{(0)} \right) = 0 & \text{in } \Omega, \\ \frac{\partial T_v^{(0)}}{\partial t} + \frac{1}{r^2} \frac{\partial}{\partial r} \left(r^2 \left(T_v^{(0)} \langle u_v^{(0)} \rangle_v - \tilde{N}_v \frac{\partial T_v^{(0)}}{\partial r} \right) \right) + \frac{S}{|\Omega_v|} \bar{\beta}_v \left(T_v^{(0)} - T_t^{(0)} \right) = \bar{\alpha}_v c_v^{(0)} & \text{in } \Omega, \end{cases} \quad (2.83)$$

$$\begin{cases} \frac{\partial c_t^{(0)}}{\partial t} + \frac{1}{r^2} \frac{\partial}{\partial r} \left(r^2 \left(c_t^{(0)} \langle u_t^{(0)} \rangle_t - \bar{D}_t \frac{\partial c_t^{(0)}}{\partial r} \right) \right) + \frac{S}{|\Omega_t|} \bar{P} \left(c_t^{(0)} - c_v^{(0)} \right) = -\Upsilon c_t^{(0)} & \text{in } \Omega, \\ \frac{\partial T_t^{(0)}}{\partial t} + \frac{1}{r^2} \frac{\partial}{\partial r} \left(r^2 \left(T_t^{(0)} \langle u_t^{(0)} \rangle_t - \bar{K}_t \frac{\partial T_t^{(0)}}{\partial r} \right) \right) + \frac{S}{|\Omega_t|} \bar{\beta}_t \left(T_t^{(0)} - T_v^{(0)} \right) = \bar{\alpha}_t c_t^{(0)} & \text{in } \Omega, \end{cases} \quad (2.84)$$

where $0 \leq r \leq R$ and $0 \leq t \leq \mathcal{T}$, where \mathcal{T} is the time interval under investigation.

The macroscale system describing the fluid transport (2.73-2.74) was solved analytically when accounting for spherical symmetry by Penta and Ambrosi [103]. In this case, the system to be solved reads (neglecting from now on the labelling indicating the leading order character of every field $^{(0)}$ for the sake of simplicity of notation):

$$\frac{1}{r} \frac{d^2}{dr^2} (r p_v) = M_v (p_v - p_t) \quad \text{in } \Omega, \quad (2.85a)$$

$$\frac{1}{r} \frac{d^2}{dr^2} (r p_t) = -M_t (p_v - p_t) \quad \text{in } \Omega, \quad (2.85b)$$

$$u_v(r) = -H_v \frac{dp_v}{dr} \quad \text{in } \Omega, \quad (2.85c)$$

$$u_t(r) = -\tilde{H}_t \frac{dp_t}{dr} \quad \text{in } \Omega, \quad (2.85d)$$

$$\frac{dp_v}{dr} \Big|_{r=0} = \frac{dp_t}{dr} \Big|_{r=0} = 0, \quad (2.85e)$$

$$p_v|_{r=R} = \bar{p}_v > 0, \quad p_t|_{r=R} = 0. \quad (2.85f)$$

The above system of equation was solved by Penta and Ambrosi [103] by accounting for boundary conditions which are consistent with Jain et al. [70] and references therein, i.e. those for an isolated tumour with fluid flow driven by the difference between the vascular and the interstitial pressures (the vascular pressure is actually considered constant in Jain et al. [70] and references therein). In the above, H_v is the vessels' hydraulic conductivity parameter which, according to Penta and Ambrosi [103], ranges from $2.20 \cdot 10^{-4}$ for a regular microvasculature to $4.89 \cdot 10^{-6}$

for the most tortuous scenario, and satisfies:

$$Y_v = H_v I, \quad H_v = \langle W_{11} \rangle_v = \langle W_{22} \rangle_v = \langle W_{33} \rangle_v, \quad (2.86)$$

The parameter $\tilde{H}_t = \bar{\kappa} H_t$, where

$$Y_t = H_t I, \quad H_t = \langle Y_{t11} \rangle_t = \langle Y_{t22} \rangle_t = \langle Y_{t33} \rangle_t, \quad (2.87)$$

and $H_t = 1$ in our case by means of (2.78).

The solutions of the system (2.85a)-(2.85f) derived by Penta and Ambrosi [103] are summarized below.

$$p_v = \frac{1}{M_v + M_t} \left(M_t + \frac{M_v \sinh(\tilde{\alpha} \hat{r})}{\hat{r} \sinh(\tilde{\alpha})} \right), \quad (2.88a)$$

$$p_t = \frac{M_t}{M_v + M_t} \left(1 - \frac{\sinh(\tilde{\alpha} \hat{r})}{\hat{r} \sinh(\tilde{\alpha})} \right), \quad (2.88b)$$

where $\hat{r} = r/R$ (relative radius position), and

$$\tilde{\alpha} = R \sqrt{(M_v + M_t)}, \quad (2.89)$$

with

$$M_v = \frac{\bar{L} S}{H_v |\Omega_v|}, \quad M_t = \frac{\bar{L} S}{\tilde{H}_t |\Omega_t|}. \quad (2.90)$$

2.5.1 Initial and boundary conditions

We assume that no particle is present in the whole system at $t = 0$. Also, both the nanoparticles and the heat fluxes must vanish in the tumour centre as a consequence of the radial symmetry assumption. We assume a vessels' bolus injection with clearance time ς at the boundary of the macroscale domain, which means that the concentration of the particles declines exponentially due to body elimination effects in the plasma, as shown by Chou et al. [28]. We also assume the continuity of particles' concentration at the boundary of the interstitial region. The initial temperatures are set to be the standard vessels' temperature 310.15K. Following the approach by Nabil and Zunino [94], we impose Robin condition on the boundary of the tumour interstitium to account for the heat transfer between the tumour and the vessels' mediated by intermediate layers of tissue [23, 72, 94, 117]. The initial and boundary conditions can be summarised as follows.

$$\left\{ \begin{array}{l} c_t|_{t=0} = c_v|_{t=0} = 0, \\ (u_v c_v - \tilde{D}_v \frac{\partial c_v}{\partial r})|_{r=0} = (u_t c_t - \bar{D}_t \frac{\partial c_t}{\partial r})|_{r=0} = 0, \\ c_v|_{r=R} = e^{-t/\varsigma}, \quad c_t|_{r=R} = c_v. \end{array} \right. \quad (2.91)$$

$$\begin{cases} T_v|_{t=0} = T_t|_{t=0} = 1, \\ (u_v T_v - \tilde{N}_v \frac{\partial T_v}{\partial r}) \Big|_{r=0} = (u_t T_t - \bar{K}_t \frac{\partial T_t}{\partial r}) \Big|_{r=0} = 0, \\ T_v|_{r=R} = 1, \quad (u_t T_t - \bar{K}_t \frac{\partial T_t}{\partial r}) \Big|_{r=R} = \bar{\beta}_t (T_v - T_t). \end{cases} \quad (2.92)$$

The finite element software Comsol Multiphysics is used to solve the model and the values of the parameters are provided in Table 2.1.

In particular, both the drug and the heat transport systems (2.83)-(2.84) have been implemented by means of the convection-diffusion module in coefficient form equipped with boundary and initial conditions (2.91)-(2.92) and parameters taken from Table 2.1. The spatial discretization is carried out by means of P2 elements, while for the discretization in time an implicit Backward Differentiation Formula (BDF) method is embraced, similarly to Mascheroni and Penta [85]. Although the system is solved in non-dimensional form, the temperatures and the absorption rate are shown in dimensional form in the plots to foster the Reader's clarity in terms of comparison against previous literature.

2.6 Results and discussion

Mascheroni and Penta [85] studied the macromolecules distribution in both the vessels and the interstitial compartment using the advection-diffusion-reaction equations derived by Penta et al. [102]. The reaction terms are related to the uptake of anti-cancer agents, as well as additional contributions due to the upscaling of transvascular diffusion of particles. The authors presented the result for a spherical tumour, and they discussed the impact of tortuosity on drug transport.

In the present work, we extend the works by Mascheroni and Penta [85], Penta et al. [102] to heat transport and solve the resulting systems of PDEs to obtain the temperature maps which are driven by nanoparticles' transport in the context of cancer hyperthermia. Although the drug transport analysis carried out here differs from the one by Mascheroni and Penta [85] in terms of the choice of parameters (which are related to nanoparticles and macromolecules, respectively), as well as macroscale boundary conditions (we assume continuity of concentrations at the tumour boundary as done by Penta and Ambrosi [103] here, while zero diffusive interstitial drug flux is assumed by Mascheroni and Penta [85]), a qualitative comparison concerning the drug transport problem is still possible, and provides a benchmark supporting the reliability of the results presented here.

We commence by first presenting our results concerning the solution of the drug transport problem and then show the results concerning temperatures maps against the relative radial position at varying microvessels' tortuosity and absorption rate.

The main results show that geometrical tortuosity can significantly impair heat transport

Table 2.1: List of parameters and their values.

Symbols	Parameter	Value	Unite	Reference
μ	Blood viscosity	4×10^{-3}	kg/(m s)	[94]
L_p	Vessels' permeability	1.78×10^{-11}	m/(Pa s)	[85]
κ	Tumour hydraulic conductivity	2.1×10^{-13}	m ² /(Pa s)	[85]
D_v	Diffusivity of the nanoparticles in the capillaries	3.3×10^{-10}	m ² /s	[85]
D_t	Diffusivity of the nanoparticles in the interstitium	1.0×10^{-11}	m ² /s	[85]
K_t	Thermal conductivity of the tumour	0.52	W/(m K)	[141]
K_v	Thermal conductivity of the vessels	0.51	W/(m K)	[141]
β	Heat transfer coefficient	20	W/m ² K	[94]
Λ	Uptake Rate in the tumour	1.07×10^{-11}	s ⁻¹	[85]
p	Diffusive permeability of the membrane	1.7×10^{-7}	m/s	[85]
d	Reference microscale	4.0×10^{-5}	m	[85]
L	Reference macroscale	1.0×10^{-2}	m	[85]
C	Reference pressure gradient	5×10^2	Pa/m	[85], [126], [103]
\mathcal{S}	Reference plasma clearance time	432	s	[85]
α	Absorption rate	6×10^6	W/Kg	[23]
γ_t	Tissue's specific heat	3470	J/Kg K	[94]
ρ_t	Tissue's density	1060	Kg/m ³	[94]
γ_v	Vessels' specific heat	3617	J/Kg K	[88]
ρ_v	Vessels' density	1050	Kg/m ³	[88]
C_r	Reference concentration	100	mg/ml	[37]
T	Reference blood temperature	310.15	K	

within the tumour and that a higher magnetic field can be required to reach a temperature which is sufficiently high to kill tumour cells by cancer hyperthermia. We provide a detailed and more quantitative description of the results below.

2.6.1 Particle transport

The results displayed in Figure 2.4 and Figure 2.5 are presented in terms of the leading order concentrations in the tumour and the vessels against the non-dimensional radius within a chosen period of time of 24 hours and 96 hours, respectively.

Figures 2.4 and 2.5 clearly show that the nanoparticles diffuse to the tumour center and the

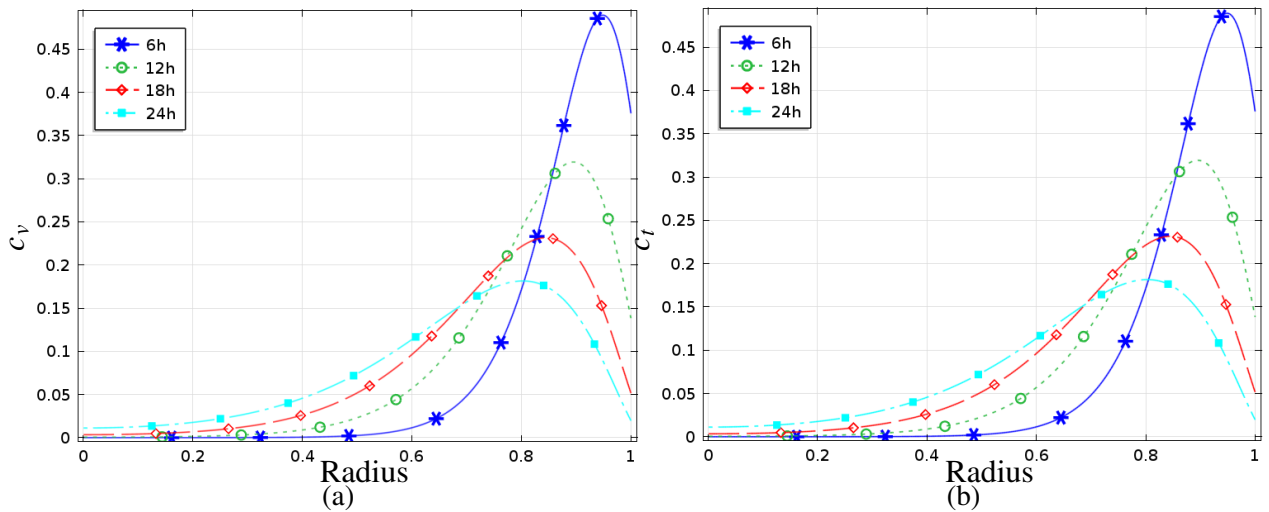


Figure 2.4: The distribution of nanoparticles in the tumour regions at time (6h-24h). The vessels (a) and interstitial (b) particles distribution vs tumour radius - low uptake rate case ($1.07 \times 10^{-11} \text{ s}^{-1}$). All other parameter values are as specified in Table 2.1. These figures are derived by Al Sariri and Penta [3].

concentration profiles of both compartments are similar. This is due to vessels' permeability and the role played by the exchange of particles between the two compartments, which is proportional to $\frac{S}{|\Omega_v|} \bar{P} (c_v^{(0)} - c_t^{(0)})$ or $\frac{S}{|\Omega_t|} \bar{P} (c_t^{(0)} - c_v^{(0)})$. Given the physiological values of \bar{P} , no significant differences between c_v and c_t can be appreciated, in analogy with [85]. Also, the influence of uptake rate does not play a prominent role here as its value is very small, see Table 2.1. Both figures display that the concentration peak is reached close to the boundary. This is because the dynamics is dictated by the bolus injection boundary conditions. As such, as there is a continuous (but exponentially decreasing in time) drug supply, at earlier times there can be regions where the concentration is higher than that at the boundary before diffusion and uptake take over.

Due to the assumption of drug delivered intravascularly via a bolus injection on the boundary, the particles' concentration decreases steadily after 6h (432) at $r=R$ and reaches zero after two days which cause the over all decline on the concentration. However, a fraction of the initial concentration is still able to reach the tumour centre by the end of the time interval under investigation. In the period of time (24h-72h), the particles' concentration in the center increases from 1% to approximately 7% of the initial concentration. After that, the concentration in the center starts to decrease slightly, i.e. in the period (72h-96h). In addition, the concentration in the last two days reaches a plateau when moving towards the center.

Nabil and Zunino [94] presented their result in a cubic symmetric setting and they found that the particles concentration decreases with time. Moreover, the concentration of nanoparticles in the vessels becomes almost uniform at the end of the circulation time they investigate, which is 48 hours.

Nanoparticles and in general drugs are eventually metabolised by tissue. This is done at a specific rate, also referred to as the *uptake* rate, which depends on the properties of the tissue

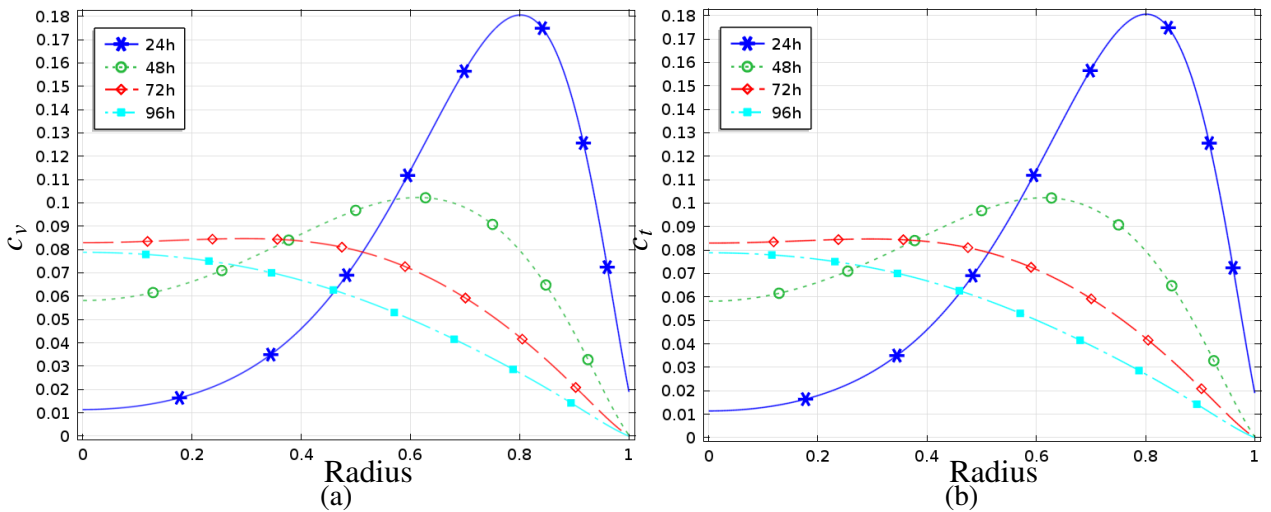


Figure 2.5: The distribution of nanoparticles in the tumour regions at time (24h-96h). The vessels (a) and interstitial (b) particles distribution vs tumour radius - low uptake rate case ($1.07 \times 10^{-11} \text{ s}^{-1}$). All other parameter values are as specified in Table 2.1. These figures are deduced by Al Sariri and Penta [3].

and drugs at hand, as discussed by Tchoryk et al. [142]. Mascheroni and Penta [85] compared two specific macromolecules characterised by different uptake rates, with order of magnitudes varying from 10^{-11} s^{-1} to 10^{-5} s^{-1} , as also mentioned by Weinberg et al. [146]. In Figure 2.6 we show the influence of high tissue uptake rate on the particle distribution in vascularised tumours, and we then increase the value of the uptake rate from $1.07 \cdot 10^{-11} \text{ s}^{-1}$ (see Table 2.1) to 10^{-5} s^{-1} .

The concentrations in both compartments are decreasing and are approximately approaching zero in the center for all periods of time. High uptake rate leads to fast washing out of the particles, such that only few of them can reach the center of the tumour. The particles in this case are metabolised very fast by the tumour before they are transported into the tumor center. Also, we have similar profiles for both compartments here, even in the case of higher uptake rates, because the influence of the vessels' permeability is more significant than the uptake rate given the high physiological values at hand. We would obtain different profiles if we significantly decreased the permeability of the vessels. In this case, the impact of the uptake rate would play a more prominent role in determining a difference between the homogenised concentration profiles. However, the difference cannot be appreciated by making use of appropriate physiological values of the relevant parameters at hand.

The concentrations profiles are qualitatively in agreement with Mascheroni and Penta [85] and this is shown for the case of the most tortuous vessels' network considered by Penta and Ambrosi [103] and Mascheroni and Penta [85], that is $\omega = 3$ and $A = r_c$, see also Table 2.2 and Figure 2.9.

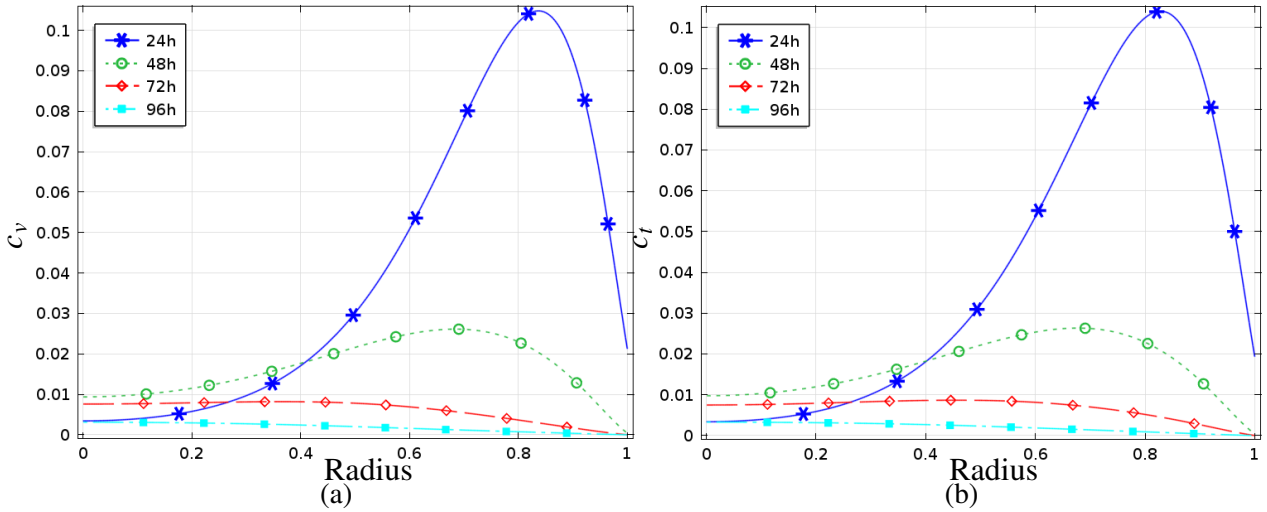


Figure 2.6: The nanoparticles delivery in the tumour with high uptake rate ($1.07 \times 10^{-5} \text{ s}^{-1}$). All other parameter values are as specified in Tables 2.1, and 2.2. The vessels (a) and interstitial (b) particles distribution vs tumour radius. These figures are derived by Al Sariri and Penta [3].

2.6.2 Heat Transport

Table 2.2: The computational result for the non-dimensional vessels' thermal conductivity with different vessels tortuosity from the analysis by Penta and Ambrosi [103] and Mascheroni and Penta [85]. The parameters r_c is the radius of the vessels, ω is the frequency of the vessels, and A is the vessels' amplitude.

ω	A	$ \Omega_v $	$ \Omega_t $	S	H_v	$I - \left\langle \frac{\partial g_1}{\partial y_1} \right\rangle_v = I - \left\langle \frac{\partial a_1}{\partial y_1} \right\rangle_v$
0	0	$8.1 \cdot 10^{-2}$	6.149	2.30	$2.20 \cdot 10^{-4}$	$3.6 \cdot 10^{-1}$
1	r_c	$7.6 \cdot 10^{-2}$	6.154	2.32	$1.69 \cdot 10^{-4}$	$3.19 \cdot 10^{-1}$
2	r_c	$6.9 \cdot 10^{-2}$	6.162	2.57	$6.24 \cdot 10^{-5}$	$2.13 \cdot 10^{-1}$
3	$0.75r_c$	$6.8 \cdot 10^{-2}$	6.162	2.82	$2.02 \cdot 10^{-5}$	$1.59 \cdot 10^{-1}$
3	r_c	$6.5 \cdot 10^{-2}$	6.165	3.25	$4.89 \cdot 10^{-6}$	$0.9 \cdot 10^{-1}$

We now present the major results obtained by solving the full system of macroscale coupled PDEs (2.83)-(2.84) by finite elements. The tortuosity of the microstructure is varied according to the values reported by Penta and Ambrosi [103] and Mascheroni and Penta [85] corresponding to five representative geometries, and the two extreme cases are shown in Figure 2.7. We have observed that the temperature increases and reaches its maximum after one day, then starts to decline and the maximum temperature varies with vessels tortuosity. As we have also remarked in the introduction, increasing the tortuosity reduces fluid and particles convection within the tumour, as show by Penta and Ambrosi [103] and Mascheroni and Penta [85]. As such, this leads in turn to impaired heat convection driving a decline in temperatures. Therefore, the more regular the vessels, the lower magnetic field intensity (which is here encoded in the absorption

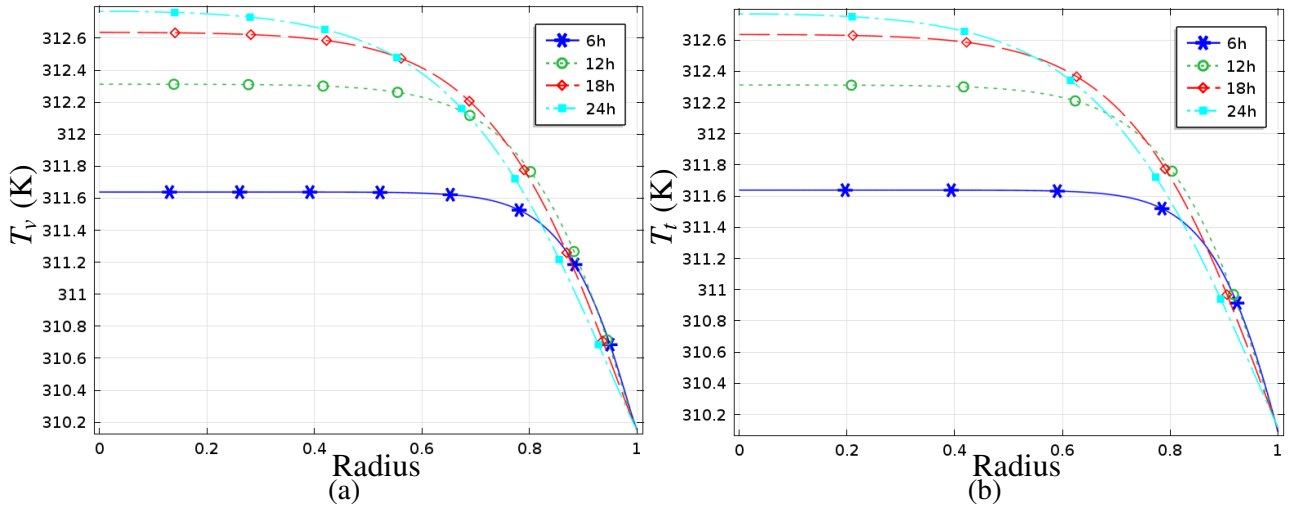


Figure 2.7: Temperature maps for the first 24h in both the vessels (a) and the interstitium (b) vs radius-low uptake rate. All the parameters values are taken from Tables 2.1, and 2.2. These figures are plotted by Al Sariri and Penta [3].

rate coefficient) is needed to reach the desired target temperature.

The plots showing the vessels' and interstitial temperature maps are shown in Figures 2.7 and 2.8 at different times, for the first 24h and from day 1 (24h) to day 4 (96h), respectively. These results are related to the most tortuous (i.e. corresponding to the case $\omega = 3$, $A = r_c$ reported in Table 2) vessels' microvasculature considered by Penta and Ambrosi [103], see Figure 2.9. Figure 2.7 clearly shows that the temperature increases with time as it reaches its maximum after 24h. It then starts to decline steadily with time, because the concentration in the blood decreases exponentially according to the bolus injection, cf. initial condition (2.91).

Also, for all period of times under investigation, the temperature in the center is higher than the boundary, as the particles are transported towards the center. This can be explained by the fact that heat transport is driven by a significant diffusive component as opposed to drug transport, which is mostly driven by convection instead (cf. thermal conductivities K_t or K_v vs the particles diffusion coefficients D_v or D_t in Table 2.1. In fact, the non-dimensional diffusion coefficients as defined in (2.18) are of order $\approx 10^{-4}$ to 10^{-5} as opposed to the non-dimensional thermal conductivities which are of the order of $\approx 10^{-1}$ to unity). This explains the difference between the drug concentration and temperature profiles, despite both phenomena being governed by formally a similar set of advection-diffusion-reaction equations. In fact, the role of advection is more prominent in driving drug transport rather than heat transport, as it can also be observed by the more localised concentration peaks (cf. Figure 2.5), as opposed to the smoother and more uniform heat transport process, which is reflected in the temperature profiles as per Figures 2.7 and 2.8. At 24h the temperature in the center is approximately 313K (39.8 °C) where in the boundary it reaches the blood temperature (310.15K) which is prescribed via the boundary condition. This is also in agreement with temperature profile previously reported in other works

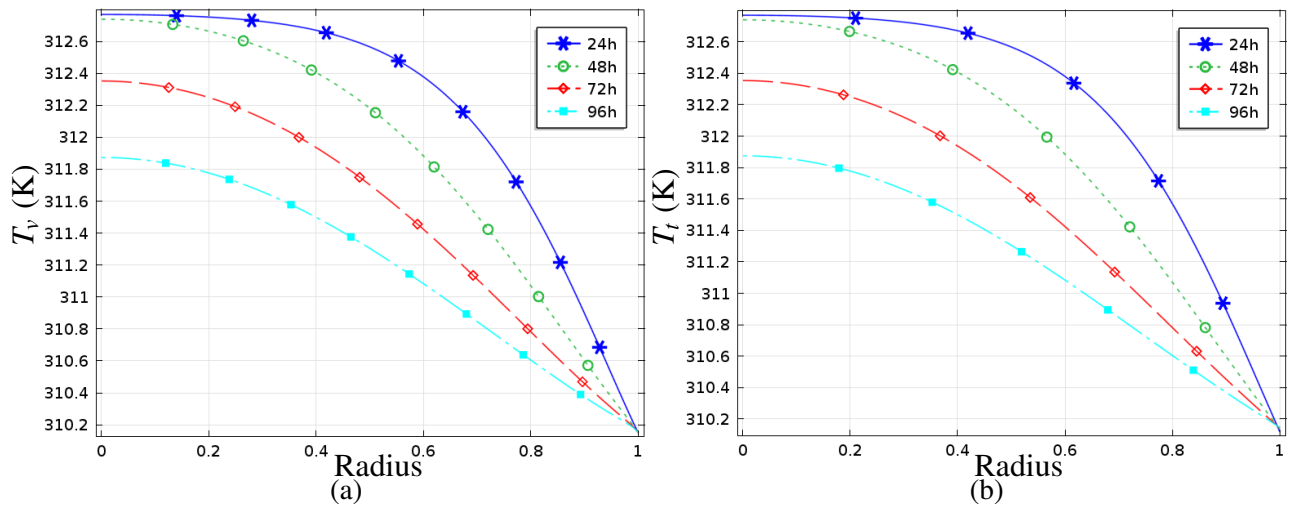


Figure 2.8: Temperature maps in both the vessels (a) and the interstitium (b) vs radius-(low uptake rate) from day 1 (24h) to day 4 (96h). All the parameters values are taken from Tables 2.1, and 2.2. These figures are established by Al Sariri and Penta [3].

which address this problem using different modelling frameworks such as those by Bagaria and Johnson [9], Dutz and Hergt [40], Golneshan and Lahonian [51].

Furthermore, the temperature maps for the tumor vessels and interstitial compartments are similar because the heat convection strongly depends on the concentration, as well as the heat transfer coefficients $\bar{\beta}_t$ and $\bar{\beta}_v$, whose physiological values are high enough to make the difference between the two profiles negligible, as in the case of the drug concentration profiles.

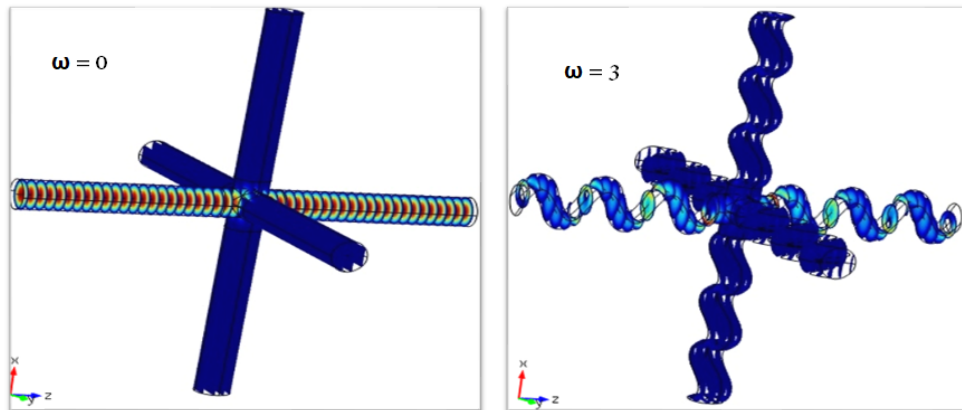


Figure 2.9: The structural difference between the healthy and tumour vessels. The most tortuous micro-vasculature (on the right) vs the regular one (on the left) as setup by [103]. This figure is taken from [3].

The distribution of heat in the tumour is in agreement with Nabil and Zunino [94] as they reported that the temperature in the center of the cube is higher than in the edges. However Nabil and Zunino [94] found that the temperature increases with time (48h). This discrepancy is related to our different set of boundary conditions. In our case we have an exponential decrease in the particles' concentration, which is directly proportional to the heat source related to the

magnetic absorption rate, thus eventually causing a temperature decline over time.

2.6.3 The influence of absorption rate and vessels' tortuosity on the heat distribution

The previous analyses in Section 2.6.2 are related to tumour microvessels, which are most tortuous and leaking vessels with ($\omega = 3, A = r_c$) as opposed to the healthy ones ($\omega = 0$), see e.g., the works by Penta and Ambrosi [103], Shipley and Chapman [126], and Carmeliet and Jain [20].

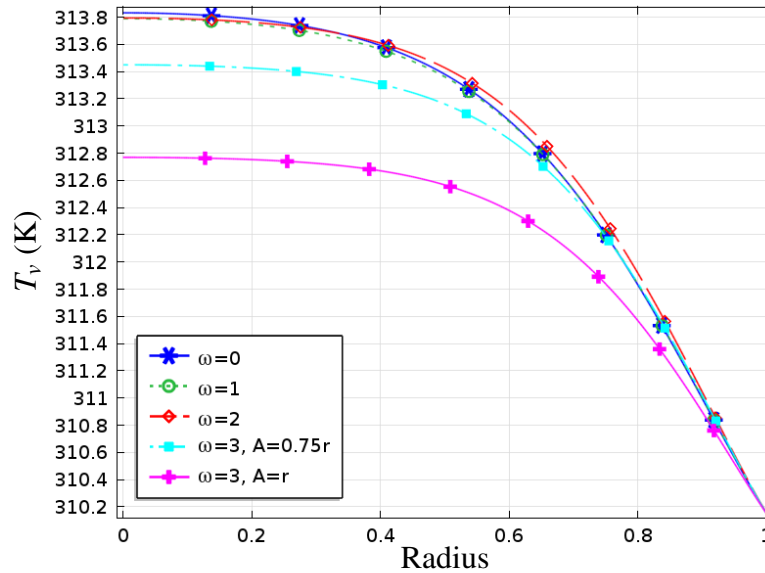


Figure 2.10: The vessels' temperature vs the radius r with different vessels' structures at time 24h. All the parameters values are taken from Tables 2.1, and 2.2. This figure is plotted by Al Sariri and Penta [3].

The structure of the vessels and their tortuosities are not uniform and they vary from one point to another in the tumour mass, as described by Penta et al. [102]. Mascheroni and Penta [85], Penta and Ambrosi [103] discussed the impact of the vessels' geometry on fluid and drug transport, respectively. They deduced that the vessels' tortuosity leads to a relevant decrease in both hydraulic and diffusivity properties of the vessels thus impairing fluid and drug convection within the tumour. Here, we perform a parametric analysis by varying the tortuosity of the vessels' micro-structure and capture its effect on the temperature maps. We make use of the setting which has been exploited by Penta et al. [102]. The data associated with the various parameters involved are reported by Mascheroni and Penta [85], Penta and Ambrosi [103]. The results show that heat transport is impaired at increasing vessels' tortuosity from the most regular vessels characterised by $\omega = 0$ (representing healthy vessels) to the most tortuous vessels (representing tumour vessels at an advanced stage) with $\omega = 3, A = r$. The temperatures varies between approximately $39.8^{\circ}\text{C} - 40.9^{\circ}\text{C}$ as we improve the regularity of the vessels. Also, we have observed (see Figure 2.10) that the temperature decreases more remarkably from the

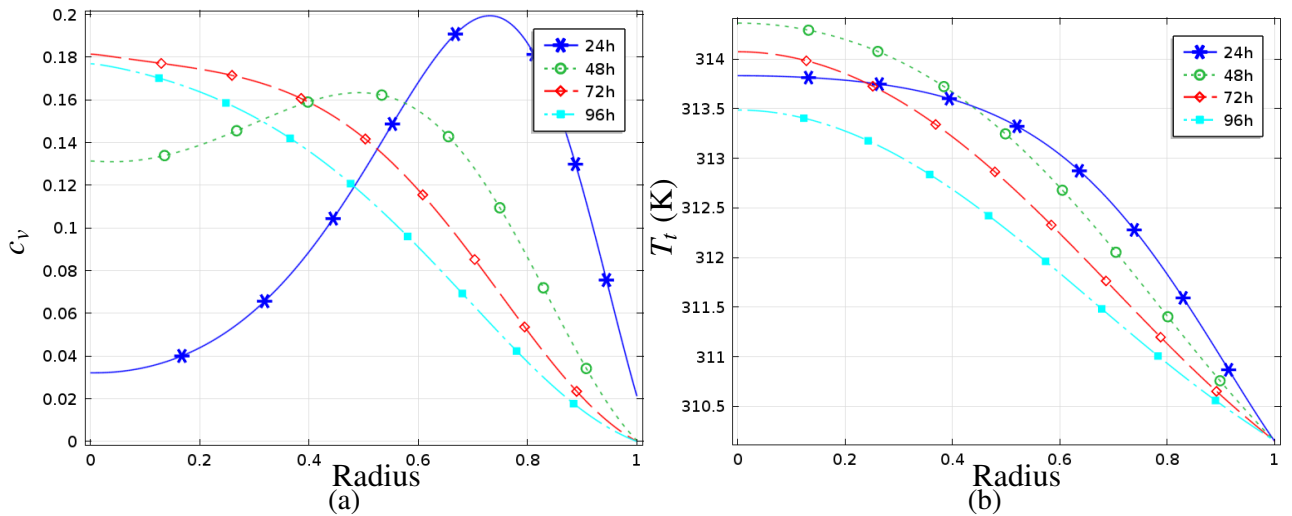


Figure 2.11: (a) The vessels' concentration or (b) temperature vs the radius r for a healthy non-tortuous microstructure ($\omega = 0$) with low uptake rate. All the parameters values are taken from Tables 2.1, and 2.2. These results are found by Al Sariri and Penta [3].

vasculature corresponding to $\omega = 3$, $A = 0.75r$ and the most tortuous one ($\omega = 3$, $A = r$). This is ultimately related to impaired drug and fluid transport, and the latter (especially fluid convection) decreases sharply when the microscale fluid profile is no longer parabolic, as show in Figure 2.9 and discussed by Penta and Ambrosi [103].

As the particles are transported smoothly in the healthy vessels and the concentration is high even in the second day, the temperature reaches its maximum 41.5°C after two days, see Figure 2.11. The difference in maximum temperatures between the regular vessels and most tortuous ones is approximately 1.5 degrees.

The temperatures achieved with different tortuosities are very close to the medical and experimental results which show that 42°C is the appropriate temperature for hyperthermia treatment and 43°C - 44°C for magnetic hyperthermia treatment, see also the works by Laurent et al. [78], Ling-Yun et al. [81], Silva et al. [128].

Furthermore, the absorption rate (which is proportional to the magnetic field intensity) plays important role on the heat distribution as it mediates the temperature increase which is cause by the nanoparticles' concentration. Therefore, we have varied the value of absorption rate α at increasing tortuosity to detect the impact of these variations on temperature maps. The absorption rate of magnetic nanoparticles is proportional to the square of the magnetic field intensity, as well as its frequency. It also varies with respect to the nanoparticles size and material, and a range of variation of four orders of magnitude, i.e. from 10^3 W/Kg to 10^7 W/Kg, as reported by Cervadoro et al. [23].

We have observed a linear relationship between the absorption rate and the heat distribution for each geometry under investigation, see Figure 2.12.

Compared to the values of hydraulic conductivity, diffusivity, and thermal conductivities

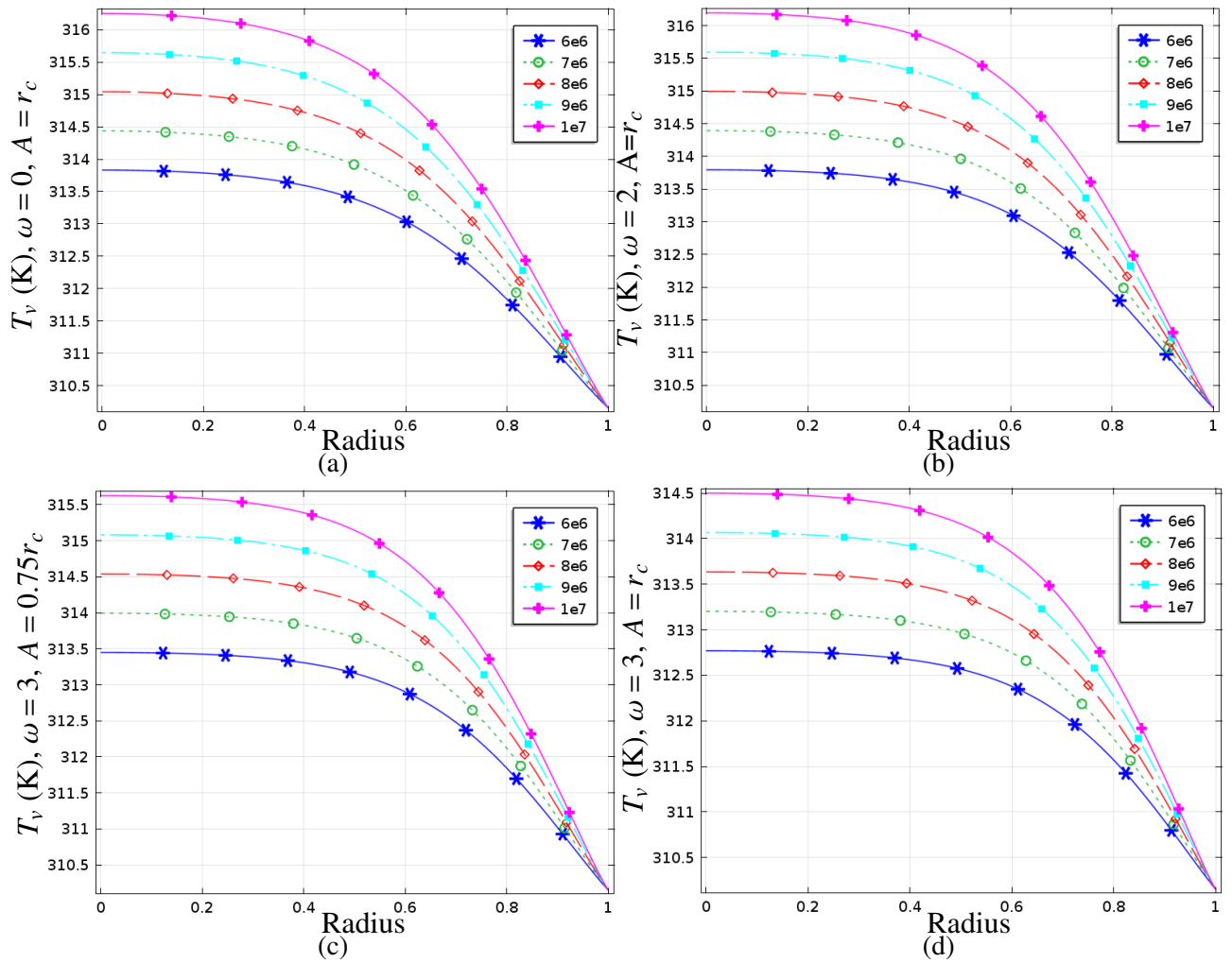


Figure 2.12: Temperature maps vs normalised radius at increasing absorption rate for different microvascular geometries after 24h. The various colors of the curves is related to different values of magnetic absorption rate α . The parameters ω is the vessels' frequency, A is the amplitude of the vessels, and r_c is the radius of the vessels. All the parameters values are taken from Tables 2.1, and 2.2. These figures are established by Al Sariri and Penta [3].

for different vessels tortuosity, we observed that the temperature increases by 6% in the most regular vessels when the absorption rate increases by one order of magnitude. However, the temperature increases by 4.6% for the most tortuous vessels when the same change of absorption rate is applied. Moreover, when the value of the absorption rate is $6 \cdot 10^6$ W/Kg, the temperature difference between the tortuous and regular vessels is almost one degree, while the difference is approximately two degrees when the value of absorption rate is 10^7 W/kg.

The absorption rate of nanoparticles can be varied in practice during experiments in order to have the suitable temperature which is required to kill the cancer cells.

2.7 The difference between our approach and the one by Nabil and Zunino [94]

Nabil and Zunino [94] discussed the hyperthermia cancer treatment using iron oxide nanoparticles (IONP) by primarily focussing on the adhesion mechanisms (so that excited particles do not extravasate from the vessels to the tumour). However, this work is different from the one by Nabil and Zunino [94] as here the tumour is modeled as a three-dimensional domain which comprises the interstitial spaces and the vessels. The two domains are separated by an interface which represents the vessels' walls. Moreover, there are some differences between the two works related to the macroscale geometry, computational technique and other concepts such as external boundary conditions. For instance, Nabil and Zunino [94] represent the tumour at the macroscale as a cube for the sake of simplifying the numerical computations. In contrast, we modelled the vascularised tumour as a sphere as an analogy with the works by Penta et al. [102], Penta and Ambrosi [103], Shipley and Chapman [126]. This geometry has significant implications on the fluid and drug transport profile and also this particular shape is very convenient when comparing results against experiments, as shown by Jain and Baxter [69]. In addition, the homogenization technique adopted by Nabil and Zunino [94] relies on the *immersed boundary method*, as illustrated by Cattaneo and Zunino [21, 22]. The vessels are dealt with as though they were one-dimensional lines, nevertheless carrying relevant three-dimensional information via appropriate singularities on the boundaries. Our new model retained the three-dimensional character of both the vessels and the interstitial spaces, and asymptotic homogenisation is being used to perform the upscaling and achieve computational feasibility. In this way, the geometrical differences between the vessels and tumour are smoothed out on the macroscale. Moreover, in the present work we encode information related to the fine scale structure of the individual compartments, as well as the transport which is occurring across the vessels' walls. The latter is reflected into appropriate sources at the macroscopic scale. In the work by Nabil and Zunino [94], the interface is not resolved as the vessels are immersed in the three dimensional tumour. However, in their case information concerning fluid, drug, and heat transport across the interface is retained and it appears likewise as a source in the resulting macroscale model. Furthermore, the vessels temperature is constant in their work, but it varies in our work, as the vessels are represented by a separate compartment in three dimensions which is described by its own governing equations. In addition, Nabil and Zunino [94] consider different time steps which depend on the size of nanoparticles. A 40 minutes time interval appropriate for very small nanoparticles and 12h, 24h, and 48h for large ones which are called vascular magnetic nanoparticles (VMN). In our case, we do not focus here on the size of nanoparticles and we focus on a 4 days time interval (and highlight the dynamics which takes place during day 1 by means of 4 different time points at 6, 12, 18, and 24h). Finally, we have assumed microscale periodicity which is a limitation of the present model. It allows us to deal with complicated and potentially tortuous microvessels which

are often encountered when dealing with vascularised cancer, as shown by Jain et al. [70], Penta et al. [102].

2.8 Concluding remarks

We have derived in this chapter a new mathematical model which describes the heat transport occurring in vascularised tumours due to magnetic nanoparticles delivered intravascularly, as per current cancer hyperthermia protocols.

We have derived the results by means of the asymptotic homogenisation technique to obtain a tissue-scale macroscopic description of the coupling between fluid, particles, and heat transport, as well as their exchange across the vessels' membranes.

The new coupled system comprises six partial differential equations describing both interstitial and vascular pressures, concentrations of nanoparticles, and temperatures.

A double Darcy's system describes fluid flow, while the concentration of nanoparticles and heat transport are both governed by double advection-diffusion-reaction system of PDEs.

The impact of the micro-structure is reflected in the effective tensors of coefficients representing the hydraulic and thermal conductivities, as well as particles' diffusion. These latter can be computed by solving periodic cell problems where the geometry of the micro-vessels is clearly resolved. The role of transvascular mass, heat, and particles transport and uptake appears in suitable macroscale exchange terms which provide the coupling between the governing equations in the vessels and the tumour.

We have solved the full model by means of finite elements, and we have observed that vessels' tortuosity can impair heat transport within the tumour mass, so that regularization of the micro-vessels can produce a significant (1-2 degrees) increase in the maximum temperature which is reached in the tumour center under the same therapeutic conditions (which are here reflected in the tumour absorption rate, which is in turn related to the magnetic field and nanoparticles' properties). Furthermore, we have investigated the impact of a change in the absorption rate for different micro-vessels' geometries, and this analysis can pave the way for informed cancer hyperthermia parameters depending on the geometry of the microvessels, which is ultimately related to the tumour stage. For example, the heat distribution with absorption rate 10^7 fluctuates between approximately 43.5 °C - 41.5 °C, which is aligned with the required temperature to destroy cancer cells, as mentioned in Section 2.6.3.

In Chapter 2 we have studied the distribution of the heat for different tumour microstructures and particles absorption rate property. However, the rationale behind employing magnetic nanoparticles is to improve hyperthermia treatment by destroying the tumour without affecting the surrounding healthy tissues. Therefore, the magnetic nanoparticles should kill the cancer cells within safe conditions. As such, in the next Chapter, we investigate the optimal parameters

related to the nanoparticles, vessels' structure, and magnetic field to achieve safe hyperthermic conditions (in terms of temperature and time) by using large size of nanoparticles that adhere to the vessels' wall.

Chapter 3

Optimal heat transport induced by magnetic nanoparticle delivery in vascularised tumours

[This chapter is published as : Al Sariri, T., Simitev, R.D. and Penta, R., 2022. Optimal heat transport induced by magnetic nanoparticle delivery in vascularised tumours. *Journal of Theoretical Biology*, p.111372.].

3.1 Introduction

Magnetic nanoparticles are increasingly being used for cancer hyperthermia treatment as they can produce a heat source localised in the tumour region without significantly affecting the surrounding healthy tissue, e.g. Colombo et al. [31], Das et al. [34]. The main clinical determinants of the efficacy of hyperthermia in destroying cancer cells are (a) the temperature achieved within the tissue above normal body temperature and (b) the duration of time for which this abnormal temperature is maintained. In the article we refer to these as “hyperthermic temperature” and “hyperthermic duration” and they are also commonly known as hyperthermia “thermometric parameters”. For the treatment to be effective but safe both the hyperthermic temperature and the hyperthermic duration must be kept within certain target ranges [2, 76]. The hyperthermic temperature and duration depend on the properties of the nanoparticles employed, (e.g. shape, density, magnetisation), the properties of the externally applied magnetic field (frequency and intensity) and the properties of the tumour tissue as these affect blood perfusion (vascularisation, tortuosity) as discussed by Shubitidze et al. [127] and Golneshan and Lahonian [51]. Direct in situ measurements of hyperthermic temperature and duration are usually impossible and it is the main goal of this work to estimate the values of these important clinical measures using a newly-developed mathematical model of a vascularised tumour.

There is large uncertainty and variability in the estimates of safe and effective thermometric

parameter values and ranges reported in the literature. One clinical study reports that hyperthermic temperature must be greater than 41°C and must be maintained for a hyperthermic duration of over 60 minutes [2]. Another study finds that approximately 90% of the cells can be eradicated with hyperthermic temperature greater than 43°C [13]. However, hyperthermic temperature that is too large, e.g. larger than 43.5°C or 44°C , is found to increase the general levels of cytotoxicity in the body [99]. Similarly, general levels of thermotolerance in the body are found to limit hyperthermic duration to about 60 minutes [79]. In general, the thermometric parameters cannot be expected to have single fixed values, rather the effects of a hyperthermia treatment likely vary on a spectrum [14].

Even when target values of the hyperthermic temperature and duration are known with sufficient accuracy, it remains a non-trivial task to fine-tune the parameters of a hyperthermia treatment procedure so that these thermometric targets are achieved. It is usually very difficult to measure temperature in situ within a tumour tissue non-invasively and even more so while treatment is underway and as a consequence a variety of experimental and theoretical investigations have been reported in the literature. Muela et al. [93] suggest optimal parameters for hyperthermia treatment by estimating the specific absorption rate (SAR) of biomineralized magnetite nanoparticles by simulation of the dynamic hysteresis loops from the Landau–Lifshitz–Gilbert equation which are then compared to experimental measurements in water and agarose gel. Roohi et al. [114, 115] estimate the optimal location, dosage, duration time of injecting magnetic nanoparticles employing a dual phase lag bioheat equation in conjunction with a mass transfer model for magnetic particles and proceed by optimising the protocol using a simulated annealing algorithm. Tang [140] use machine learning procedures and heuristic algorithms to predict magnetic nanoparticle infusion in tumour tissue and then estimate the temperature field. Further attempts in this direction are reported by Lang et al. [77], Saeedi et al. [117] and Cervadoro et al. [23] to mention few recent ones.

The main advantage of this chapter lies in the development and use of a cutting-edge multiscale mathematical model of a vascularised tumour. Both the hyperthermic temperature and duration are influenced by the properties of the injected nano-particles (e.g. the diameter of the particles and their shape), injection conditions, and, especially for vascularised tumours, by the structural and functional characteristics of the microvessels, such as their geometrical arrangement and wall shear rate. In particular, the geometrical properties of the tumour vascularisation are well-known to significantly affect blood and drug transport in cancer [69, 70]. The role of the microvessels' geometry has been further elucidated and quantified by means of suitable homogenisation approaches, which are capable of providing a link between the microscale, where the distance between individual vessels can be clearly identified, and the macroscale of the tissues, where experimental measurements are usually ultimately performed.

In this chapter, we extend the analysis carried out by Al Sariri and Penta [3] (previous Chapter) to large nanoparticles, thus by starting from a new homogenised model which is derived by taking

into account that nanoparticles cannot extravasate from the vessels into the tumour interstitium. As such, the drug dynamics is present in the vessels' only and we explicitly take into account the role of particles adhesion. The specific absorption rate that determines heat generation under applied magnetic field is computed using a Brownian and Neels relaxation formula. The model allows to estimate the spatiotemporal distribution of temperature within the tumor tissue and we use this to make accurate estimates of the hyperthermic temperature and duration as functions of the parameters that describe nanoparticle properties (magnetic material, size), microvasculature properties (tortuosity, hydraulic conductivity, thermal conductivity, adhesion rate) and the properties of applied magnetic field (intensity and frequency). The chapter is organized as follows. In Section 3.2, we describe the new homogenised model which describes the interplay between fluid, nanoparticles, and heat transport in a vascularised tumour subjected to the action of an applied magnetic field. The role of nanoparticles adhesion and a comparison between this work and Al Sariri and Penta [3] is highlighted. In Section 3.3, we discuss the results. In Section 3.3.1 we focus on both temporal and spatial temperature and nanoparticles' concentration maps at varying tortuosity and for different nanoparticles' material. In Section 3.3.2 we discuss the optimal heat transport parameters to achieve physiologically safe hyperthermic temperature and duration. Finally, we discuss limitations of the model and further perspectives in Section 3.4.

3.2 Mathematical modelling

The velocity of nanoparticles in the vessels is in general heterogeneous. The particles which are closer to the walls of the vessels are slower than the others. This is due to the friction force between the particles and the vessel membrane in a process which is known as *adhesion*. The typical *extravasation* transport mechanism consists of nanoparticles being transported into the tumour interstitium through the pores of the vessels (these are for example of the order of 40-200 nm diameter for brain and peripheral tumour according to the analysis performed by Sarin et al. [121] by means of electronic microscopy techniques). However, transport of nanoparticles depends on the ratio between particle size and vessel wall pore size [135]. Nanoparticles with diameter less than 10 nm can be easily filtered by the renal system and they can be captured by spleen and liver if their size is greater than 200 nm. The optimal nanoparticle diameter is therefore usually estimated to range from 20 to 200 nm, as discussed by Thomas et al. [144]. Here we study transport of large (80 nm diameter) spherical magnetic nanoparticles in three-dimensional vascularised tumours. As such, we assume that nanoparticles adhere to vessel walls and extravasation is ruled out. The tumour, which is identified with a three-dimensional domain Ω , is assumed to comprise of two regions, namely, tumour vessels Ω_v and tumour interstitium Ω_t . Therefore, vessel walls play the role of the interface between these two compartments, which is here denoted by $\Gamma = \partial\Omega_v \cap \partial\Omega_t$. The system is intrinsically multiscale due to the sharp difference

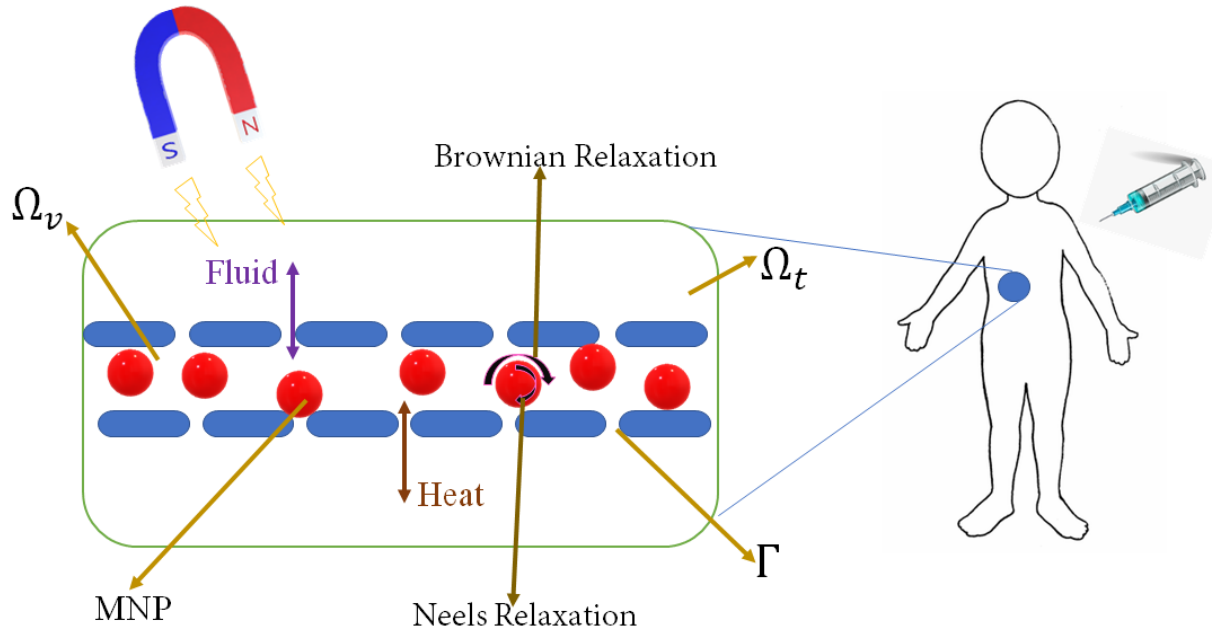


Figure 3.1: A schematic diagram of hyperthermia cancer treatment using large size of magnetic nanoparticles (MNP). The region Ω_v is for the tumor vessels, Ω_t is the tumour interstitium, and Γ (the vessels' wall) is the interface between the two regions.

between the average intercapillary distance d and the size of the whole tumour tissue L , therefore motivating the development of a multiscale modelling approach. In particular, we define a small parameter ϵ which expresses these two characteristics lengths as

$$\epsilon = \frac{d}{L}. \quad (3.1)$$

Next we illustrate the mathematical modelling assumptions which we embrace as a starting point to describe transport of fluid, nanoparticles' delivery and convection-diffusion of heat in the context of cancer hyperthermia.

3.2.1 Fluid flow

We consider the blood as an incompressible viscous fluid modelled by the following Stokes' problem

$$\mu \nabla^2 \mathbf{u}_v = \nabla p_v \quad \text{in } \Omega_v, \quad (3.2a)$$

$$\nabla \cdot \mathbf{u}_v = 0 \quad \text{in } \Omega_v, \quad (3.2b)$$

where \mathbf{u}_v and p_v are the blood velocity and pressure in the capillaries, while μ is the blood viscosity.

We assume that the tumour interstitium is an isotropic porous medium, so that interstitial fluid

flow can be described by Darcy's law

$$\mathbf{u}_t = -\kappa \nabla p_t \quad \text{in } \Omega_t, \quad (3.3a)$$

$$\nabla \cdot \mathbf{u}_t = 0 \quad \text{in } \Omega_t. \quad (3.3b)$$

Here, \mathbf{u}_t and p_t are the fluid velocity and pressure in the tumour interstitium, and κ is the tissue conductivity.

The fluid is supplied continuously through the vessels' membrane and the flow relies on the pressure differences between the two regions, so that the flux continuity condition across the interface Γ reads

$$\mathbf{u}_t \cdot \mathbf{n} = \mathbf{u}_v \cdot \mathbf{n} = L_p(p_v - p_t) \quad \text{on } \Gamma. \quad (3.4)$$

The above relationship is also known as *Starling's law* in the biophysical literature, and in general states that the fluid flux is proportional to the difference between the interstitial and vascular pressure, as well as the difference between the oncotic pressures in those compartments. However, following [102], we are here neglecting the oncotic pressure contribution by considering that this pressure jump is often negligible for most tumour types, as reported for example in [70].

We specify the tangential components of the fluid flowing in the vessels by means of a Beavers and Joseph condition which accounts for the slip over a porous surface as discussed for example by Penta et al. [102], Shipley and Chapman [126]

$$\mathbf{u}_v \cdot \boldsymbol{\tau}_v = -\frac{\sqrt{\kappa}}{\varphi} [(\mathbf{n} \cdot \nabla) \mathbf{u}_v] \cdot \boldsymbol{\tau}_v \quad \text{on } \Gamma. \quad (3.5)$$

Here, \mathbf{u}_t , \mathbf{u}_v , and p_v , p_t are the interstitial and capillary velocities and pressures, respectively, L_p is the permeability of membrane, $\boldsymbol{\tau}_v$ collectively denotes both of the unit vector tangent to the vessels' wall, κ is tissue conductivity, φ is a non-dimensional parameter encoding structural properties of the membrane, and \mathbf{n} is the unit outward vector normal to the vessels' wall.

3.2.2 Advection, diffusion, and adhesion of nanoparticles

The concentration of magnetic nanoparticles c_v which is delivered intravascularly is governed by the following advection-diffusion equation

$$\frac{\partial c_v}{\partial t} + \nabla \cdot (c_v \mathbf{u}_v - D_v \nabla c_v) = 0 \quad \text{in } \Omega_v, \quad (3.6)$$

where the parameter D_v is the diffusivity of the particles. Mass transport in the vessels is affected by particles' size and shape [65].

The adhesion between nanoparticles with different sizes and shapes and the vessels wall

was discussed by [38]. The adhesion probability depends directly on the receptors and ligands densities, and the interaction area between the particle and the substrate. The Authors of the latter work found that oblate nanoparticles adhere to the vessels wall more than the spherical particles. Furthermore, the optimal size and shape for nanoparticles are influenced by the ratio between the density of the receptors and vessels' shear stress.

Here, we focus on spherical nanoparticles with size greater than the vessels' pore size, so that we explicitly take into account the adhesion between the particles and vessels' wall. We model the latter by means of the following interface condition

$$(c_v \mathbf{u}_v - D_v \nabla c_v) \cdot \mathbf{n} = \Pi c_v \quad \text{on } \Gamma. \quad (3.7)$$

Following the analysis carried out by [94], we assume that

$$\Pi = z |\xi| \frac{p_d}{2}, \quad (3.8)$$

where z is the adhesion probability, $|\xi|$ is the wall shear rate, and p_d is the diameter of the particle. The density of nanoparticles Ψ adhering to the vessels' wall is computed by

$$\frac{d\Psi}{dt} = \Pi c_v \quad \text{in } \Omega_v. \quad (3.9)$$

Here, the density Ψ physically represents the density of nanoparticle on the vascular wall. However, we here follow the approach embraced by [94], in that the role of adhesion is encoded in the parameter Π but Ψ is directly related to the integral in time of the actual concentration c_v , and as such is defined in Ω rather than solely on Γ . This assumption can be considered admissible as long as the radius of the capillary is very small in comparison with the other characteristic lengths of the system.

3.2.3 Heat convection and diffusion

The heat generated within the tumour vessels and in the tumour interstitium is due to the magnetic field which is applied after injecting the nanoparticles. The field causes rotation and vibrations of the particles around themselves and around the field.

We use the Brownian and Neels relaxation formula to identify the absorption rate which is directly related to the heat distribution in the tumour tissue.

Heat transport in both the vessels (T_v) and the tumour interstitial (T_t) space are then described by a coupled system of heat convection-diffusion equations. We assume that there exists a volume heat source in the vessels which is proportional to both the concentration of nanoparticles c_v and the density of those adhering to the walls ψ , with proportionality constant given by the absorption rate α . In addition, we account for the heat exchanged between the vessels and the

interstitial compartment. Finally, we also consider the influence of a given volume source in the interstitial space in order to fully capture the influence of the heat generated by the magnetic nanoparticles under the influence of an applied magnetic field. In this case, as the heat and (vascular) drug transport problems are decoupled, we assume that such a source is proportional to the absorption rate α and to a given function \mathcal{R} which is in turn intended to be related to the average concentration of nanoparticles that are generating the heat which then plays a role in the whole tissue. The resulting governing equations can be written as

$$\gamma_t \rho_t \left[\frac{\partial T_t}{\partial t} + \nabla \cdot \left(T_t \mathbf{u}_t - \frac{K_t}{\gamma_t \rho_t} \nabla T_t \right) \right] = \alpha \mathcal{R} \quad \text{in } \Omega_t, \quad (3.10a)$$

$$\gamma_v \rho_v \left[\frac{\partial T_v}{\partial t} + \nabla \cdot \left(T_v \mathbf{u}_v - \frac{K_v}{\gamma_v \rho_v} \nabla T_v \right) \right] = \alpha (\psi + c_v) \quad \text{in } \Omega_v, \quad (3.10b)$$

where K_v , K_t , γ_v , γ_t , and ρ_v , ρ_t are the vessels and interstitial heat conductivities, specific heat capacities, and compartment densities, respectively. The parameter $\psi = \frac{\Psi}{L}$ has the dimensions of a concentration and represents an effective concentration of particles due to adhesion. The model can be derived for a generic given volume source \mathcal{R} , so that we shall specify its functional form when introducing the solution of the macroscale model at a later stage.

We assume that heat can be exchanged between the tumour and the vessels, such that the heat flux across the membrane is proportional to the difference between the temperatures in the two compartments, as follows

$$\left(T_v \mathbf{u}_v - \frac{K_v}{\gamma_v \rho_v} \nabla T_v \right) \cdot \mathbf{n} = \frac{\beta}{\gamma_v \rho_v} (T_v - T_t) \quad \text{on } \Gamma, \quad (3.11a)$$

$$\left(T_t \mathbf{u}_t - \frac{K_t}{\gamma_t \rho_t} \nabla T_t \right) \cdot \mathbf{n} = \frac{\beta}{\gamma_t \rho_t} (T_t - T_v) \quad \text{on } \Gamma, \quad (3.11b)$$

where β is the heat transfer coefficient.

The heat generated by magnetic nanoparticles strongly depend on the absorption rate α , which depends on particles' size, shape, material, as well as magnetic field properties, i.e. intensity and frequency. According to Avolio et al. [8], the parameter α is defined as

$$\alpha = \frac{\mu_0^2 \pi f H_0^2 M_d^2 V}{3 \rho_n K_B T} \frac{2 \pi f \tau_{\text{eff}}}{1 + (2 \pi f \tau_{\text{eff}})^2}, \quad (3.12)$$

where μ_0 is the magnetic permeability, M_d is the magnetization of nanoparticles, K_B is Boltzmann's constant, T is the temperature, f is the field frequency, H_0 is the field intensity, and τ_{eff} is the overall relaxation time which can be defined as

$$\frac{1}{\tau_{\text{eff}}} = \frac{1}{\tau_N} + \frac{1}{\tau_B}, \quad (3.13)$$

with

$$\tau_N = \tau_0 e^{\frac{k_i V}{K_B T}}, \quad \tau_B = \frac{3\eta V_H}{K_B T}. \quad (3.14)$$

Here, τ_0 is Larmor's time constant, k_i is the magnetic anisotropy constant, η is nanoparticles' carrier liquid viscosity, and V_H is the hydrodynamic volume which is computed by Torres et al. [145] using

$$V_H = \pi \frac{(p_d + \delta)^3}{6}, \quad (3.15)$$

where $\delta = 2$ nm.

Also, the parameter ρ_n in equation (3.12) is the density of injected nanoparticles and it is different from Ψ which represents the density of particles adhering to the vessels wall.

Remark (Current model vs [3]). *Al Sariri and Penta [3] discussed the hyperthermia cancer treatment using magnetic nanoparticles which can extravasate across the vessels' walls. Therein, the concentration of nanoparticles was then studied in both regions of the tumour tissue by means of advection-diffusion equations. The authors assumed that the particles could be uptaken by tumour interstitium after having been delivered intravascularly, such that*

$$\frac{\partial c_v}{\partial t} + \nabla \cdot (c_v \mathbf{u}_v - D_v \nabla c_v) = 0 \quad \text{in } \Omega_v, \quad (3.16a)$$

$$\frac{\partial c_t}{\partial t} + \nabla \cdot (c_t \mathbf{u}_t - D_t \nabla c_t) = -\Lambda c_t \quad \text{in } \Omega_t, \quad (3.16b)$$

where the parameter Λ denoted the uptake rate in the tumour interstitium. In addition, they accounted for transvascular transport of nanoparticles via the following interface conditions

$$(c_v \mathbf{u}_v - D_v \nabla c_v) \cdot \mathbf{n} = (c_t \mathbf{u}_t - D_t \nabla c_t) \cdot \mathbf{n} \quad (3.17)$$

$$= P(c_v - c_t) \quad \text{on } \Gamma, \quad (3.18)$$

where P represents the diffusive permeability of the vessels' membranes. The differential equations governing heat transport by Al Sariri and Penta [3] is analogous to that describe by the system (3.10a)-(3.10b) with interface conditions (3.11a)-(3.11b), however the absorption rate α was considered as a single, constant parameter, and its value was taken from Cervadoro et al. [23]. Also, the heat source of the system (3.10a)-(3.10b) did not depend on the density of adhering particles Ψ , as Al Sariri and Penta [3] considered transport of small nanoparticles and therefore ignored nanoparticles' adhesion.

Next we perform a non-dimensional analysis of the model, which will then be upscaled by means of the asymptotic homogenisation technique.

3.2.4 Non-dimensionalisation of the model

We rewrite the system of equations (3.2a)-(3.7), (3.9), and (3.10a)-(3.11b) in non-dimensional form by using the change of variables

$$c_v = C_r c'_v, \quad \mathcal{R} = C_r \mathcal{R}', \quad \mathbf{u}_v = \frac{Cd^2}{\mu} \mathbf{u}'_v, \quad t = \frac{L\mu}{Cd^2} t', \quad (3.19)$$

$$\nabla = \frac{1}{L} \nabla', \quad p = CLp', \quad T = XT', \quad \Psi = LC_r \Psi', \quad (3.20)$$

where C_r is the reference of concentration, C is pressure gradient, X is the reference temperature, d is the distance between capillaries, and L is the average size of the tumour. The corresponding non-dimensional system of PDEs, after having neglected the primes for the sake of simplicity of notation, can be written as

$$\mathbf{u}_t = -\bar{\kappa} \nabla p_t \quad \text{in } \Omega_t, \quad (3.21a)$$

$$\nabla \cdot \mathbf{u}_t = 0 \quad \text{in } \Omega_t, \quad (3.21b)$$

$$\epsilon^2 \nabla^2 \mathbf{u}_v = \nabla p_v \quad \text{in } \Omega_v, \quad (3.21c)$$

$$\nabla \cdot \mathbf{u}_v = 0 \quad \text{in } \Omega_v, \quad (3.21d)$$

$$\frac{\partial c_v}{\partial t} + \nabla \cdot (c_v \mathbf{u}_v - \bar{D}_v \nabla c_v) = 0 \quad \text{in } \Omega_v, \quad (3.21e)$$

$$\frac{d\Psi}{dt} = \bar{\Pi}_1 c_v \quad \text{in } \Omega_v, \quad (3.21f)$$

$$\left[\frac{\partial T_t}{\partial t} + \nabla \cdot (T_t \mathbf{u}_t - \bar{K}_t \nabla T_t) \right] = \bar{\alpha}_t \mathcal{R} \quad \text{in } \Omega_t, \quad (3.21g)$$

$$\left[\frac{\partial T_v}{\partial t} + \nabla \cdot (T_v \mathbf{u}_v - \bar{K}_v \nabla T_v) \right] = \bar{\alpha}_v (\psi + c_v) \quad \text{in } \Omega_v, \quad (3.21h)$$

with boundary conditions

$$\mathbf{u}_t \cdot \mathbf{n} = \mathbf{u}_v \cdot \mathbf{n} = \bar{L}_p (p_v - p_t) \quad \text{on } \Gamma, \quad (3.22a)$$

$$\mathbf{u}_t \cdot \boldsymbol{\tau} = -\epsilon \bar{\varphi} [(\mathbf{n} \cdot \nabla) \mathbf{u}_t] \cdot \boldsymbol{\tau} \quad \text{on } \Gamma, \quad (3.22b)$$

$$(c_v \mathbf{u}_v - \bar{D}_v \nabla c_v) \cdot \mathbf{n} = \epsilon \bar{\Pi} c_v \quad \text{on } \Gamma, \quad (3.22c)$$

$$(T_v \mathbf{u}_v - \bar{K}_v \nabla T_v) \cdot \mathbf{n} = \epsilon \bar{\beta}_v (T_v - T_t) \quad \text{on } \Gamma, \quad (3.22d)$$

$$(T_t \mathbf{u}_t - \bar{K}_t \nabla T_t) \cdot \mathbf{n}_t = \epsilon \bar{\beta}_t (T_t - T_v) \quad \text{on } \Gamma. \quad (3.22e)$$

The non-dimensional numbers are defined as follows

$$\bar{\kappa} = \frac{\kappa\mu}{d^2}, \quad \bar{\Pi} = \frac{\Pi L}{Ud}, \quad \bar{\Pi}_1 = \frac{\Pi\mu}{Cd^2}, \quad \bar{L}_p = \frac{L_p L\mu}{d^2}, \quad \bar{\varphi} = \frac{\sqrt{\kappa}}{\varphi d}, \quad (3.23a)$$

$$\bar{\beta}_v = \frac{\beta L\mu}{Cd^3\gamma_v\rho_v}, \quad \bar{\beta}_t = \frac{\beta L\mu}{Cd^3\gamma_t\rho_t}, \quad (3.23b)$$

$$\bar{\alpha}_t = \frac{\alpha C_r L\mu}{XCd^2\gamma_t\rho_t}, \quad \bar{\alpha}_v = \frac{\alpha C_r L\mu}{XCd^2\gamma_v\rho_v}, \quad (3.23c)$$

while the non-dimensional diffusivities and heat conductivities for the vessels and tumour interstitium are given by

$$\bar{D}_v = \frac{D_v\mu}{LCd^2}, \quad \bar{K}_v = \frac{K_v\mu}{\rho_v\gamma_v LCd^2}, \quad \bar{K}_t = \frac{K_t\mu}{\rho_t\gamma_t LCd^2}. \quad (3.24)$$

3.2.5 The homogenised model

The homogenised model can be derived by applying the asymptotic (periodic) homogenisation technique as discussed by Al Sariri and Penta [3], Penta et al. [102], Shipley and Chapman [126] to our system. We first decouple spatial variations by introducing a microscale \mathbf{y} , which is related to the macroscale \mathbf{x} by

$$\mathbf{y} = \frac{\mathbf{x}}{\epsilon}, \quad (3.25)$$

where ϵ now plays the role of an asymptotic parameter. We further assume that any variable q in the system is \mathbf{y} -periodic and can be written in power series of ϵ as follows

$$q(\mathbf{x}, t) = q(\mathbf{x}, \mathbf{y}, t) = \sum_{l=0}^{\infty} q^{(l)}(\mathbf{x}, \mathbf{y}, t)\epsilon^l = q^{(0)}(\mathbf{x}, \mathbf{y}, t) + \epsilon q^{(1)}(\mathbf{x}, \mathbf{y}, t) + \epsilon^2 q^{(2)}(\mathbf{x}, \mathbf{y}, t) + \dots \quad (3.26)$$

The differential operators transform according to the chain rule as

$$\nabla \longrightarrow \nabla_x + \frac{1}{\epsilon} \nabla_y, \quad \nabla^2 \longrightarrow \nabla_x^2 + \frac{2}{\epsilon} \nabla_x \nabla_y + \frac{1}{\epsilon^2} \nabla_y^2. \quad (3.27)$$

Using (3.26), we apply the asymptotic homogenisation technique by expressing all the fields in terms of power series of ϵ and accounting for the chain rule (3.27). This leads to a multiscale system of PDEs, where we can then equate the same powers of ϵ in order to obtain a number of differential conditions which can be used to close a system of PDEs for the leading (zero-th) order fields, or their cell average, defined by

$$\langle q \rangle_j = \frac{1}{|\Omega_j|} \int_{\Omega_j} q(\mathbf{x}, \mathbf{y}, t) dy. \quad (3.28)$$

Here, j can be either v or t and $|\Omega_j|$ denotes the vessels (interstitial) cell volume portion. The derivation of the model is carried out as in Al Sariri and Penta [3] by taking into account the differences highlighted in the Remark discussed in Section 3.2.3.

The macroscale differential equations describing velocities and pressures are analogous to those reported by Al Sariri and Penta [3] (Chapter 2) and read

$$\left\langle \mathbf{u}_v^{(0)} \right\rangle_v = -\mathbf{Y}_v \nabla_x p_v^{(0)}, \quad (3.29a)$$

$$\left\langle \mathbf{u}_t^{(0)} \right\rangle_t = -\bar{\kappa} \mathbf{Y}_t \nabla_x p_t^{(0)}, \quad (3.29b)$$

$$\nabla_x \cdot \left(\mathbf{Y}_v \nabla_x p_v^{(0)} \right) = \frac{\bar{L} \left(p_v^{(0)} - p_t^{(0)} \right)}{|\Omega_v|} S, \quad (3.29c)$$

$$\nabla_x \cdot \left(\bar{\kappa} \mathbf{Y}_t \nabla_x p_t^{(0)} \right) = \frac{\bar{L} \left(p_t^{(0)} - p_v^{(0)} \right)}{|\Omega_t|} S, \quad (3.29d)$$

where S is the surface of the microvessels. These differential equations show that the velocities in both compartments obey Darcy's law and the fluid flow depends on the pressure difference between them. The effective tensors \mathbf{Y}_t and \mathbf{Y}_v are defined as

$$\mathbf{Y}_v = \frac{1}{|\Omega_v|} \int_{\Omega_v} \mathbf{W} dy, \quad \mathbf{Y}_t = I - \left\langle (\nabla_y \mathbf{r})^T \right\rangle_v. \quad (3.30)$$

For the homogenization process related to the concentration, we have that equation (3.6) is analogous to equation (2.14e) from Chapter 2, however the interface condition on Γ (3.22c) is different from (2.15d). Therefore, by applying the same upscaling method as described in 2, the macroscale differential equation for the concentration of nanoparticles $c_v^{(0)}$ reads

$$\frac{\partial c_v^{(0)}}{\partial t} + \nabla_x \cdot \left(c_v^{(0)} \left\langle \mathbf{u}_v^{(0)} \right\rangle_v - \mathbf{F}_v \nabla_x c_v^{(0)} \right) + \frac{S}{|\Omega_v|} \bar{\Pi} c_v^{(0)} = 0, \quad (3.31)$$

with $c_v^{(0)}$ is \mathbf{y} -constant as investigated in Chapter 2, and the diffusivity tensor \mathbf{F}_v is

$$\mathbf{F}_v = \bar{D}_v \left(I - \left\langle (\nabla_y \mathbf{a})^T \right\rangle_v \right). \quad (3.32)$$

Here, \bar{D}_v is defined in (3.24).

Equation (3.21f) shows that the density $\Psi^{(0)}$ is the integral in terms of $c_v^{(0)}$ (which is \mathbf{y} -constant). Therefore, $\Psi^{(0)}$ is also \mathbf{y} -constant, and the macroscale differential equation of the nanoparticles' density $\bar{\Psi}^{(0)}$ is the governed by the same equation at leading order, i.e.

$$\frac{d\Psi^{(0)}}{dt} = \bar{\Pi}_1 c_v^{(0)}, \quad (3.33)$$

with $\bar{\Pi}_1$ is defined according to (3.23a).

Finally, the temperatures $T_t^{(0)}$ and $T_v^{(0)}$ of both compartments at the macro-scale are represented by advection-diffusion-reaction equations

$$\begin{aligned} & \frac{\partial T_v^{(0)}}{\partial t} + \nabla_x \cdot \left(T_v^{(0)} \left\langle \mathbf{u}_v^{(0)} \right\rangle_v - \mathbf{N}_v \nabla_x T_v^{(0)} \right) + \\ & \frac{S}{|\Omega_v|} \bar{\beta}_v \left(T_v^{(0)} - T_t^{(0)} \right) = \bar{\alpha}_v \left(\psi^{(0)} + c_v^{(0)} \right), \end{aligned} \quad (3.34a)$$

$$\begin{aligned} & \frac{\partial T_t^{(0)}}{\partial t} + \nabla_x \cdot \left(T_t^{(0)} \left\langle \mathbf{u}_t^{(0)} \right\rangle_t - \mathbf{N}_t \nabla_x T_t^{(0)} \right) + \\ & \frac{S}{|\Omega_t|} \bar{\beta}_t \left(T_t^{(0)} - T_v^{(0)} \right) = \bar{\alpha}_t \mathcal{R}^{(0)}. \end{aligned} \quad (3.34b)$$

The effective thermal conductivities \mathbf{N}_v and \mathbf{N}_t are expressed as:

$$\mathbf{N}_v = \bar{K}_v \left(I - \left\langle (\nabla_y \mathbf{g})^T \right\rangle_v \right), \quad \mathbf{N}_t = \bar{K}_t \left(I - \left\langle (\nabla_y \mathbf{e})^T \right\rangle_t \right), \quad (3.35)$$

where \bar{K}_v and \bar{K}_t are defined in (3.24). The auxiliary tensor \mathbf{W} , and the auxiliary variables \mathbf{r} , \mathbf{a} , \mathbf{g} , and \mathbf{e} solve the microscale cell problems which are described in details by Al Sariri and Penta [3]. The numerical solutions of these problems are illustrated in [103] and [85].

The difference between the work carried out by Al Sariri and Penta [3] and the present work resides in the different heat sources which appear in equations (3.34a) and (3.34b). These latter also depend on adhesion, which is in turn dictated by equations (3.31-3.33). Here, the drug dynamics depends on adhesion, as shown by the reaction term in equation (3.31) and by the macroscale evolution equation (3.33). This is not the case in the works by Mascheroni and Penta [85] and Al Sariri and Penta [3], where drug transport is governed by a double system of advection-diffusion-reaction equations driven by transvascular exchange of particles which arises as a direct consequence of extravasation, which is herein neglected. In the remainder of this work, we assume that the leading order heat source $\mathcal{R}^{(0)}$ is related to the heat generated by the interaction between the nanoparticles and the magnetic field in the vessels. We can capture the volumetric character of the heat generated by the vessels as a heat source in the tumour tissue by assuming a simple constitutive law for $\mathcal{R}^{(0)}$ of the form

$$\mathcal{R}^{(0)} = c_v^{(0)} + \psi^{(0)}, \quad (3.36)$$

which is analogous to that present in the vessels and represents an admissible choice as $c_v^{(0)}$ and $\psi^{(0)}$ do not depend on the microscale variable \mathbf{y} and are defined in the whole macroscale domain.

3.2.6 The homogenised model in radial symmetry

The vascularized tumour is represented by a sphere of radius R . We assume that the tumour is isolated and all external forces are neglected. The radial component of fluid velocities and

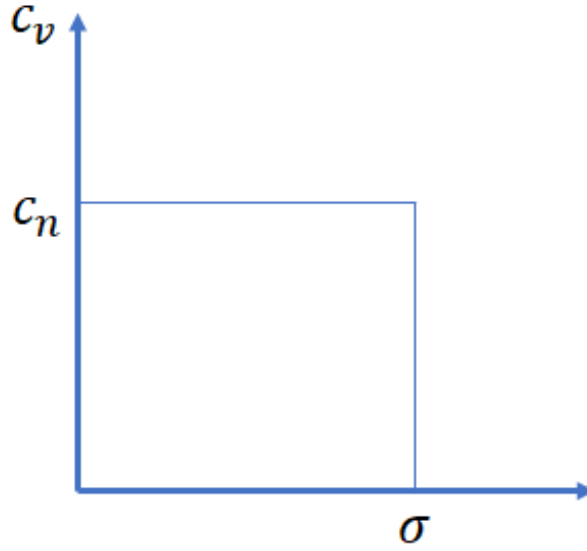


Figure 3.2: A schematic description of the boundary condition related to the concentration of nanoparticles. The parameters c_v is the nanoparticles concentration in the tumour vessels, c_n is the injected concentration of nanoparticles, and σ is the duration time of injection.

pressures are those obtained by Penta and Ambrosi [103]. The system of equations in spherical coordinates, by considering the leading order term for all variables (and neglecting the superscript ⁽⁰⁾ for the sake of simplicity of notation) reads

$$\begin{aligned} \frac{\partial c_v}{\partial t} + \frac{1}{r^2} \frac{\partial}{\partial r} \left(r^2 \left(c_v \langle \mathbf{u}_v \rangle_v - F_v \frac{\partial c_v}{\partial r} \right) \right) + \\ \frac{S}{|\Omega_v|} \bar{\Pi} c_v = 0 \quad \text{in } \Omega_v, \end{aligned} \quad (3.37a)$$

$$\frac{d\Psi}{dt} = \bar{\Pi}_1 c_v \quad \text{in } \Omega_v, \quad (3.37b)$$

$$\begin{aligned} \frac{\partial T_v}{\partial t} + \frac{1}{r^2} \frac{\partial}{\partial r} \left(r^2 \left(T_v \langle \mathbf{u}_v \rangle_v - N_v \frac{\partial T_v}{\partial r} \right) \right) + \\ \frac{S}{|\Omega_v|} \bar{\beta}_v (T_t - T_v) = \bar{\alpha}_v (c_v + \psi) \quad \text{in } \Omega_v, \end{aligned} \quad (3.37c)$$

$$\begin{aligned} \frac{\partial T_t}{\partial t} + \frac{1}{r^2} \frac{\partial}{\partial r} \left(r^2 \left(T_t \langle \mathbf{u}_t \rangle_t - N_t \frac{\partial T_t}{\partial r} \right) \right) + \\ \frac{S}{|\Omega_t|} \bar{\beta}_t (T_v - T_t) = \bar{\alpha}_t (c_v + \psi) \quad \text{in } \Omega_t. \end{aligned} \quad (3.37d)$$

All variables depend on r and t , where $0 \leq r \leq R$ and $0 \leq t \leq \mathcal{T}$.

To close the problem, we need to prescribe the initial and boundary conditions. We assumed zero concentration and due to the spherical symmetry, we consider zero flux of nanoparticles' concentration at the center of the tumour. We assume that the particles are delivered intravascularly for a time σ which means that the concentration is c_n during this time and zero after that,

see Figure 3.2.

$$c_v|_{t=0} = 0, \quad (3.38a)$$

$$(\mathbf{u}_v c_v - \bar{D}_v \partial_r c_v)|_{r=0} = 0, \quad (3.38b)$$

$$c_v|_{r=R} = \begin{cases} c_n & t < \sigma, \\ 0 & t > \sigma. \end{cases} \quad (3.38c)$$

Concerning heat transport, we set initial ($t = 0$) temperatures in both compartments to the standard blood temperature. In terms of boundary conditions, we consider zero heat flux at $r = 0$. On the tumour boundary, We prescribe the homogenised temperature in the vessels to coincide with the standard blood temperature, while we consider a Robin condition for the tumour temperature $r = R$, to account for the heat transport between the tumour interstitial and vessels compartments mediated by intermediate layer of external tissue, as in [3, 94]. Initial and boundary conditions for the heat transport system of equations are given below.

$$T_v|_{t=0} = T_t|_{t=0} = 1, \quad (3.39a)$$

$$\left(\mathbf{u}_v T_v - \bar{K}_v \frac{\partial T_v}{\partial t} \right) \Big|_{r=0} = \left(\mathbf{u}_t T_t - \bar{K}_t \frac{\partial T_t}{\partial t} \right) \Big|_{r=0} = 0, \quad (3.39b)$$

$$T_v|_{r=R} = 1, \quad \left(\mathbf{u}_t T_t - \bar{K}_t \frac{\partial T_t}{\partial t} \right) \Big|_{r=R} = \bar{\beta}_t (T_v - T_t). \quad (3.39c)$$

In this manuscript, we are consistent with the boundary conditions utilised in [3, 94]. Our set of conditions represents a situation where the nanoparticles are first injected for a period of time, cf. (3.38c), and then the magnetic field is subsequently applied, so that the temperatures distributions are then driven by heat sources which depend on the absorption rate and concentration of nanoparticles, cf. (3.34a-3.34b), and the heat transport problem is then closed by initial conditions (3.39a) and boundary conditions (3.39b-3.39c). The present problem at hand is very rich, and that future investigations on the subject could also focus on different initial and/or boundary conditions.

The hydraulic conductivity, diffusivity, and thermal conductivity coefficients are computed as discussed by Al Sariri and Penta [3], based on the microscale simulations performed by Mascheroni and Penta [85], Penta and Ambrosi [103]. The resulting values are then injected in our macroscale system of PDEs, and we use the values of the parameters in Table 3.1 to solve the model and present the results.

3.3 Results and Discussion

Penta and Ambrosi [103] discussed the solution of the fluid flow system (3.29a)-(3.29d) and

Table 3.1: The values of model's parameters.

Symbol	Parameter	Value	Unit	Reference
τ_0	Larmor time constant	10^{-9}	s	[37]
k_i	magnetic anisotropy constant	$1.1 \cdot 10^4$	J/ m ³	[47]
K_B	Boltzmann's constant	$1.38 \cdot 10^{-23}$	J/K	[47]
η	nanoparticles' carrier liquid viscosity	$2.94 \cdot 10^{-4}$	Kg/m s	[145]
z	Adhesion probability	1.5×10^{-4}	non	[94]
μ	Blood viscosity	4×10^{-3}	Pa s	[94]
L_p	vessel hydraulic Permeability	1.78×10^{-11}	m/Pa s	[85]
κ	Tumour hydraulic conductivity	2.1×10^{-13}	m ² /Pa s	[85]
D_v	The diffusivity of nano-particles in the capillaries	3.3×10^{-10}	m ² /s	[85]
D_t	The diffusivity of nano-particles in the tissue	1.0×10^{-11}	m ² /s	[85]
K_t	Thermal conductivity at tissue	0.52	W/m K	[141]
K_v	Thermal conductivity at vessel	0.51	W/m K	[141]
β	Heat transfer coefficient	20	W /m ² K	[94]
p	membrane permeability related to drug	1.7×10^{-7}	m/s	[85]
d	Reference micro-scale	4.0×10^{-5}	m	[85]
L	Reference macro-scale	1.0×10^{-2}	m	[85]
C	Reference pressure gradient	5×10^2	Pa/m	[85]
γ_t	tissue-specific heat	3470	J/Kg K	[94]
ρ_t	tissue density	1060	Kg/ m ³	[94]
γ_v	vessels-specific heat	3617	J/Kg K	[88]
ρ_v	vessels density	1050	Kg/ m ³	[88]
C_r	concentration reference	1	mg/ml	[37]

they determined the radial components of the velocities and pressures which were used to find the particles' concentration and heat convection as investigated by Mascheroni and Penta [85], and Al Sariri and Penta [3]. The authors of the mentioned works studied the influence of the geometry of the micro-vessels on the distribution of the particles and they concluded that vessels' tortuosity impairs the transport of fluid [103], particles [85], and heat [3].

Here, the differential equations (3.37a)-(3.37d), equipped with initial and boundary conditions (3.38a)-(3.38c), and (3.39a)-(3.39c), are solved via the finite element software COMSOL Multiphysics as in [3]. The plots illustrating spatio-temporal temperatures and concentration profiles in Section 3.3.1 are generated using COMSOL Multiphysics, while Python is used to generate the plots related to the parametric analysis discussed in Section 3.3.2.

Remark (Presentation of the results). *While we solve the model in non-dimensional form, results in terms of temperatures and concentrations are presented by referring to their corresponding dimensional values in the plots in order to foster the Reader's understanding. In particular, temperatures are expressed in degree Kelvin (K), and concentrations in mg/ml (or, equivalently Kg/m^3)¹. The non-dimensional time unit in this work can be computed by means of relationship (3.20) and corresponds to 50 seconds. This applies when we discuss conditions related to time intervals in dimensional form in the following sections. For example, it means that an injection time of 50 minutes corresponds to 60 non-dimensional time units. The radius and the time are expressed in non-dimensional form in the following sections. Therefore, the non-dimensional radius ranges from 0 to 1, while the chosen time interval is from 0 to 1000, which corresponds to a time interval of $5 \cdot 10^4$ seconds (≈ 13.88 hours).*

3.3.1 The role of vessels' tortuosity

We commence by investigating the role of the microvascular tortuosity on the concentration of nanoparticles in Section 3.3.1 and on the resulting temperature maps in Section 3.3.1. The results are shown in terms of vessels' concentration c_v , density Ψ , and tumour temperature T_t vs relative radius of the homogenized tumour or time. We have conducted the analysis by labelling the microstructures at varying tortuosities with the index λ . The latter actually corresponds to a specific couple of spatial frequency ω and amplitude A , as specified in Table 3.2, and are those used in [3, 85, 103] to parametrise the tumour microvessels. Each of these couple of parameters determine a different microstructure, with their associated vessels surface and corresponding cell volume portion. Given that we are focussing on the microvasculature considered by Penta and Ambrosi [103], invariance with respect to mutual orthogonal axis applies. As such, the effective hydraulic conductivities, as well as drug and thermal diffusivities, are isotropic and their values at varying tortuosities are listed in Table 3.2. These are denoted by $H_v = \langle W_{11} \rangle = \langle W_{22} \rangle = \langle W_{33} \rangle$

¹In this latter case no rescaling is needed as the reference concentration is 1 mg/ml.

Table 3.2: Particle diffusivity and thermal conductivity values for various vessel geometry. The parameter λ is a label for tortuosity, ω is the vessels' frequency, A is the amplitude of the vessels, and r_c is the radius of the vessels.

λ	ω	A	$ \Omega_v $	$ \Omega_t $	S	H_v	$1 - \left\langle \frac{\partial a, g}{\partial y_1} \right\rangle_v$
0	0	0	$8.1 \cdot 10^{-2}$	6.149	2.30	$2.20 \cdot 10^{-4}$	$3.6 \cdot 10^{-1}$
0.5	1	$0.5 r_c$	$7.9 \cdot 10^{-2}$	6.151	2.30	$2.06 \cdot 10^{-4}$	$3.53 \cdot 10^{-1}$
1	1	r_c	$7.6 \cdot 10^{-2}$	6.154	2.32	$1.69 \cdot 10^{-4}$	$3.19 \cdot 10^{-1}$
1.5	2	$0.5 r_c$	$7.6 \cdot 10^{-2}$	6.154	2.33	$1.63 \cdot 10^{-4}$	$3.18 \cdot 10^{-1}$
2	2	r_c	$6.9 \cdot 10^{-2}$	6.161	2.57	$6.24 \cdot 10^{-5}$	$2.13 \cdot 10^{-1}$
2.5	3	$0.5 r_c$	$7.2 \cdot 10^{-2}$	6.158	2.53	$7.71 \cdot 10^{-5}$	$2.47 \cdot 10^{-1}$
3	3	r_c	$6.5 \cdot 10^{-2}$	6.165	3.25	$4.89 \cdot 10^{-6}$	$0.9 \cdot 10^{-1}$

for the hydraulic conductivity, whereas the homogenised thermal and drug diffusivities are to be computed by simply multiplying their corresponding non-dimensional values by the correction factor herein denoted by $1 - \left\langle \frac{\partial a, g}{\partial y_1} \right\rangle_v$, which was computed for the considered microstructures by Mascheroni and Penta [85]. We also assume that, given the low vascular density, the interstitial hydraulic conductivity and thermal diffusivities are unaffected by the homogenisation process, as justified in [103].

Concentration of nanoparticles

The result of the differential equations (3.37a)-(3.37b) with initial and boundary conditions (3.38a)-(3.38c), is the homogenised concentration of particles in the vessels, which reflects the effective behaviour of the nanoparticles delivered intravascularly in a macroscale spherical tumour.

A concentration of 50 mg/ml of magnetic nanoparticles is injected for a time $\sigma = 50$ minutes. Figure 3.3 shows the concentration of nanoparticles at different times both during and after injection. It is clear that during the injection phase, the concentration on the boundary of the tumour is very high but cannot influence regions far from the boundary. When we stop injecting the nanoparticles at $t > 50$ minutes, the particles start to diffuse more toward the tumour centre. Also, in all cases highlighted in Figure 3.3, it is clear that tortuosity has a negative impact of nanoparticles transport, although intermediate values of the tortuosity may lead to optimal concentration peaks post injection, as in case of Figure 3.3c, where the highest concentration peak is reached at $\lambda = 2$ and after injection at $t = 2$ h. The vessels with tortuosity $\lambda = 0$ and $\lambda = 1$ correspond to approximately similar concentration of nanoparticles profiles, and the maximum is reached approximately after 6 hours, see Figure 3.4. In contrast, the concentration is very low

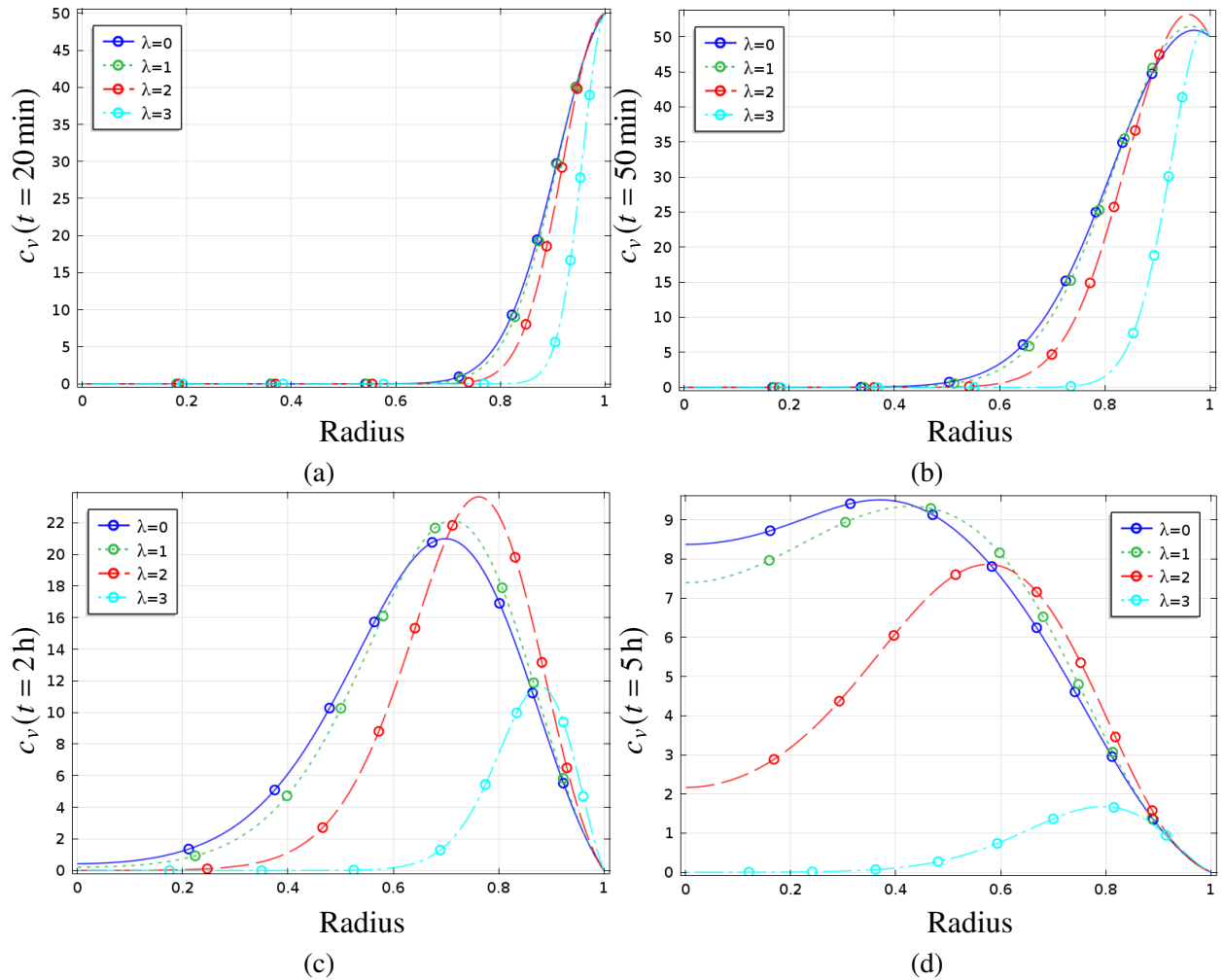


Figure 3.3: The concentration of nanoparticles c_v as a function of tumour radius r for various values of vessels' tortuosity as specified in the legends and for time moment (a) $t = 20$ minutes (b) $t = 50$ minutes (c) $t = 2$ hours and (d) $t = 5$ hours. All other parameter values are as specified in Table 3.1 and Table 3.2 except for the parameters $\sigma = 50$ minutes, and $c_n = 50$ mg/ml.

for the most tortuous vessels at $\lambda = 3$. This is because the nanoparticles are advected by the fluid and for very high tortuosity the fluid flow is dramatically impaired and no longer characterised by a parabolic profile. This ultimately causes a sharp decline in the hydraulic conductivity of the vessels, as explained by Penta and Ambrosi [103]. These obtained profiles are in qualitative agreement with those obtained by Mascheroni and Penta [85] and [3]. However, there are discrepancies between our results and previous results in terms of the amount of concentration and the time that it takes for the nanoparticles to reach the center due to the difference in boundary conditions and the presence of adhesion which is neglected in [3].

Mascheroni and Penta [85] and Al Sariri and Penta [3] dealt with drug delivered by a bolus injection accounting for an exponential decline in the concentration of nanoparticles due to plasma clearance, therefore, they observed a slower drug dynamics. In our case, the injected concentration of nanoparticles on the boundary of the tumour drops to zero directly after 50

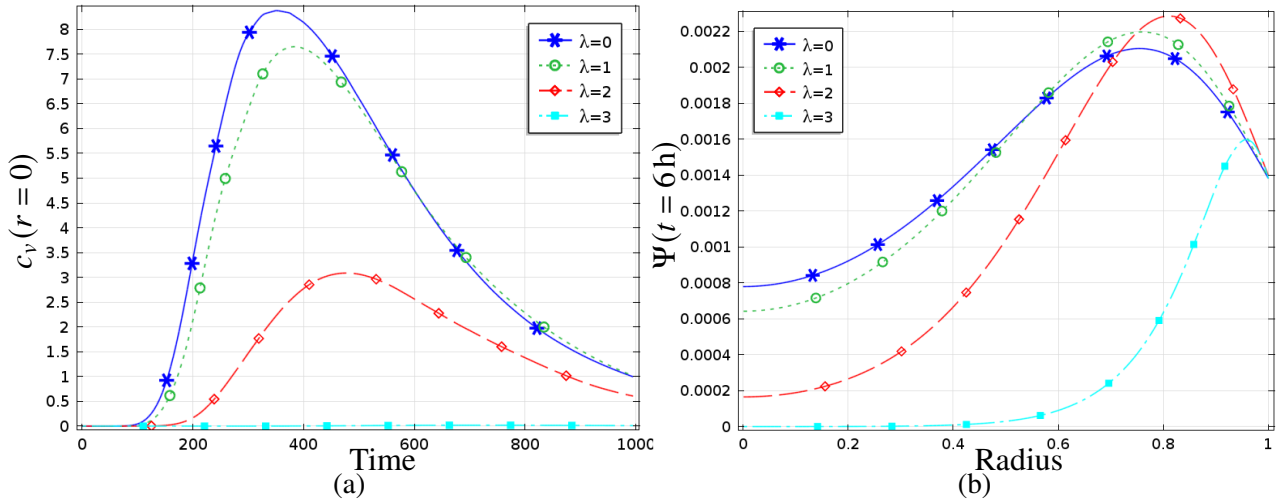


Figure 3.4: The concentration of nanoparticles vs time, and the density of nanoparticles that adhering the vessels' wall vs radius of tumour. (a) Instantaneous concentration of nanoparticles c_v at the center of tumour $r = 0$ as a function of time for various values of vessel tortuosity as specified in the figure legends. (b) Instantaneous density of nanoparticles Ψ that adhere to the wall of the vessels as a function of tumour radius for different tortuosity of the vessels. In both panels time moment is $t = 6$ hours. All other parameters are as specified in Table 3.1 and Table 3.2 except $\sigma = 50$ minutes, and $c_n = 50$ mg/ml.

minutes, and so the drug can reach the tumour centre regions by diffusive transport after a few hours post-injection.

We chose an injection time of 50 minutes to be consistent with the experiment performed by Famiani et al. [44], and we also test different injection times in the course of the parametric analysis in Section 3.3.2.

We conclude this section by discussing the role of the density of nanoparticles Ψ adhering to the vessels' walls. Its maximum is reached close to the domain boundary, and it depends on the tortuosity of the vessels, see Figure 3.4. Moreover, if we compare the profile of c_v and Ψ with different vessels' tortuosity, we can see that the peak in the case of Ψ , as well as c_v (50 minutes-2 hours) post-injection, is reached at $\lambda = 2$. This is because, while tortuosity impairs fluid convection, the adhesion of nanoparticles is supposed to increase at increasing tortuosity due to the friction between the particles and the vessels. Therefore, we suggest that, while tortuosity is in general negatively affecting nanoparticles' transport as in [85] and [3], whenever adhesion is taken into account, less regularization of the vessels' may be required to achieve optimal nanoparticles' transport. However, at $\lambda = 3$, transport still drops dramatically, as in this case the increase in nanoparticle adhesion is not sufficient to counterbalance the drop in fluid, and hence nanoparticles advection.

Finally, we also wish to remark that the concentration is prescribed as a time-dependent boundary (rather than initial) condition and injected over a period of time, such that there exists a transient period before the drug is cleared off when localised regions in space can develop where the concentration exceeds the boundary value. This can be seen by observing the concentration

Table 3.3: Properties of magnetic nanoparticles.

Material	M_d (KA/m)	ρ_n (Kg/m ³)	Reference
Fe ₃ O ₄	446	5180	[73]
fcc Fe Pt	1140	15200	[73]
Ba Fe ₂ O ₄	380	5280	[73]
Ni Fe	301	5380	[97]

profile in Figure 3.3b at $\lambda = 2$. This phenomenon typically happens when the time is still comparable to the injection time σ . For a shorter period of time the concentration delivered to the system is typically not sufficient for this to occur. For a time much longer than the injection time the concentration is already significantly lower than the boundary value being prescribed during the injection time.

Temperature maps

The differential equations (3.37c)-(3.37d) with boundary and initial conditions (3.39a)-(3.39c) are used to find the heat maps for a vascularized tumour. As mentioned in Section 3.2.3, the hyperthermia effectiveness depends on the absorption rate α , which is in turn affected by both the properties of the magnetic field, such as intensity and frequency, as well as the properties of the magnetic nanoparticles. Abenojar et al. [1] found that theoretically and experimentally the absorption rate of cubic nanoparticles is higher than the spherical nanoparticles and nano-rods are better than cubic and spherical nanoparticles [35]. However, for the sake of simplicity, in this work we focus on spherical particles and we show that cancer hyperthermia can be improved by changing nanoparticles' material, size, concentration, and also the injection duration time. Varying the material of nanoparticles requires to change their magnetization M_d and their density ρ_n , see Table 3.3. The parameter M_d is more relevant than others in the way it affects the absorption rate α as the latter is proportional to the square of M_d and inversely proportional to ρ . Figure 3.5b shows that Iron-Platinum (FePt) responds with higher temperature changes when compared with other materials typically considered in this context. Usually the magnetization of metallic nanoparticles like Iron-Platinum (FePt), Iron-Cobalt (FeCo), Cobalt-platinum (CoPt) is higher than the oxidation nanoparticles like Iron-Oxide (FeO), Maghemite (Fe₂O₃), and Magnetite (Fe₃O₄), but the former are not stable [55]. As such, in the present work we concentrate more on magnetite nanoparticles, as appropriate for application of cancer hyperthermia to human tissues [60]. Figure 3.5a shows the temperature profile arising from injection of magnetite nanoparticles with different vessels' tortuosity. The concentration of particles drives heat transport from the boundary towards the tumour center. Convection-diffusion of heat then causes the temperature to raise from the standard blood temperature, which

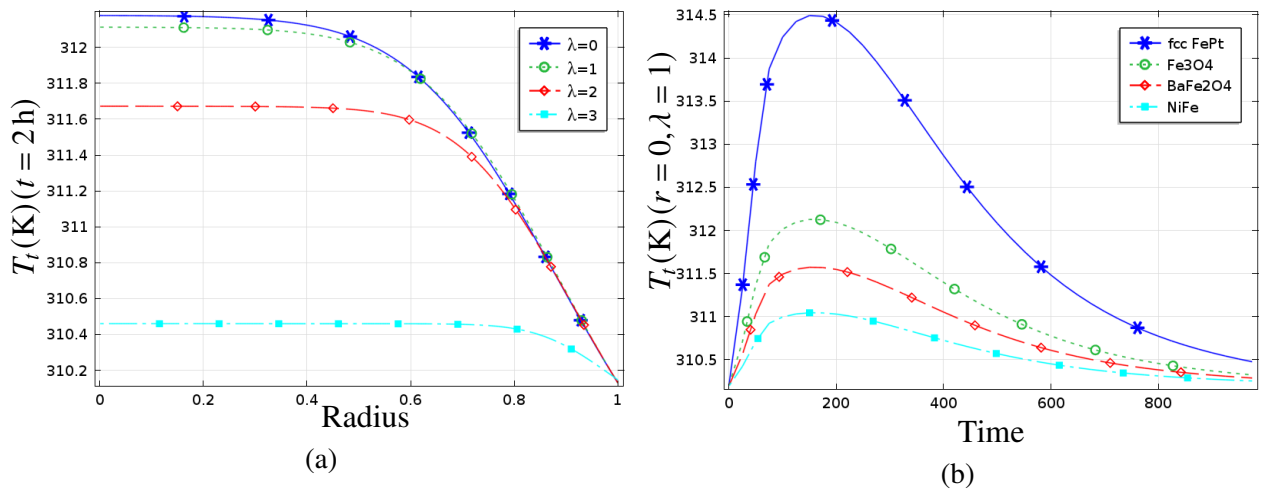


Figure 3.5: The temperature maps with different particles material that adhere to the vessels' wall and vessels' tortuosity. (a) Instantaneous tumour temperature T_t at time $t = 2$ h as a function of tumour radius r for Fe₃O₄ nanoparticles and various values of vessel tortuosity as specified in the figure legend. (b) Local tumour temperature T_t at the center of the tumour $r = 0$ as a function of time for various types of nanoparticles materials as specified in the figure legends and for vessels with tortuosity $\lambda = 1$. All other parameter values are as specified in Table 3.1 and Table 3.2 except for the parameters $H_0 = 10$ KA, $f = 300$ KHZ, $\sigma = 50$ minutes, and $c_n = 100$ mg/ml.

is prescribed at the tumour boundary, to higher values. Microvascular tortuosity is associated with a reduce increase in temperature, in agreement with previous findings reported for heat transport driven by small nanoparticles discussed by Al Sariri and Penta [3]. Moreover, the temperature increases and approaches its maximum after approximately 2.5h, then it starts to decrease as the overall concentration declines, see Figure 3.5b.

The remainder of this section is devoted to a parametric analysis which is performed to determine the optimal set of parameters (including injection conditions, magnetic field properties, nanoparticles' diameter, microvessels' tortuosity, wall shear rate) which is required to reach a physiologically safe target hyperthermic temperature and duration.

3.3.2 A parametric study of hyperthermic temperature and duration

The ranges in which the hyperthermic temperature and duration take safe and effective values depend strongly on the pathophysiology of the tumour tissue under treatment. For this reason, the published literature gives various estimates of these quantities – see the Introduction of this chapter for further discussion. Table 3.4 summarizes values of the target hyperthermic temperature and duration suggested in several clinical and experimental investigations. Based on the data in Table 3.4, we assume that the safe and effective values for the hyperthermic temperature are in the range $[42^\circ, 46^\circ]$ C and the safe and effective hyperthermic duration has values in the range $[0.5, 2]$ hours. Below these intervals hyperthermia treatment does not induce sufficiently strong sensitization to radiotherapy and chemotherapy or lead to significant direct

Table 3.4: Estimates for the hyperthermic temperature and duration available from the published literature.

Temperature (°C)	duration (minutes)	Reference
44	30	[74]
42.5	60	[108]
41.5	120	[118]
42	30	[100]
41	60	[39]
47	30	[61]

thermal ablation of cancer cells. Above these intervals undesirable damage to healthy tissue occurs.

Figure 3.6 demonstrates how the value of the hyperthermic duration is computed from the numerical results of our model. A typical example of the temperature profile as a function of time in the center of the tumour ($r = 0$) is shown in the figure for fixed values of the model parameters. Initially, the temperature increases monotonically and eventually reaches the hyperthermic temperature, $T_t = 42^\circ\text{C}$, after an initial transient time as shown by the horizontal green line in Figure 3.6. The temperature continues to increase further until it reaches a single global maximum T_{\max} and decreases monotonically after that until it eventually drops below the hyperthermic temperature. The hyperthermic duration is defined and computed as the difference between the moment in time when the temperature decreases below the hyperthermic temperature of 42°C and the moment in time when the temperature first exceeds this value. These moments are indicated in Figure 3.6 by vertical red lines. The hyperthermic duration is denoted by τ for the remainder of this section.

Figure 3.7a shows a 3D plot of the hyperthermic duration τ as a function of the intensity of the applied magnetic field H_0 and the nanoparticle injection duration σ for all other model parameters fixed at constant values. For small values of H_0 and σ the hyperthermic duration is zero as the T_{\max} has not yet exceeded the hyperthermic temperature of 42°C . As the values of H_0 and σ are increased, either separately or simultaneously, the hyperthermic temperature of 42°C is eventually exceeded and a non-vanishing value of the hyperthermic duration τ is recorded and continue to increase monotonically with increase of both H_0 and σ . The range of safe and effective hyperthermic duration values are then the values on the surface $\tau(H_0, \sigma)$ that are located between the iso-contour lines $\tau = 0.5\text{h}$ and $\tau = 2\text{h}$. These isolines are shown by a red solid curve and a red dashed curve in the plot of Figure 3.7a. Figure 3.7b shows a similar surface plot of the maximal (in time) temperature at the centre of the tumor $r = 0$ as a function of H_0 and σ for all other model parameters fixed at constant values again. The surface is monotonically

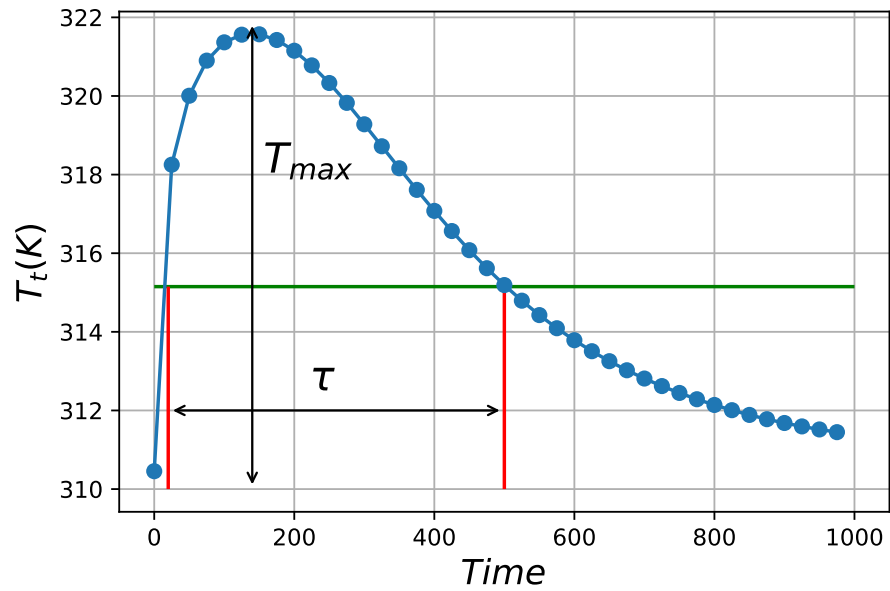


Figure 3.6: A figure describing the computation of hyperthermic temperature and time in the present work. The temperature T_t at the middle of the tumour ($r = 0$) as a function of time in the case of vessels with tortuosity $\lambda = 1$ and all other parameter values are as in Table 3.1 except $H_0 = 10$ KA, $f = 300$ KHZ, $\sigma = 50$ minutes, $c_n = 100$ mg/ml, $\xi = 15$, and $pd = 80$ nm. The two vertical red lines indicate the hyperthermic duration τ - the time interval for which the tumour temperature profile exceeds the hyperthermic temperature $T_t = 42^\circ$ C shown with a horizontal green line.

increasing, and the safe and effective range of temperature values is the one located between the iso-contours $T_{\max} = 42^\circ\text{C}$ and $T_{\max} = 46^\circ\text{C}$. These iso-contours are shown by green dash-dotted and green dotted lines in the Figure. Figure 3.7c shows the projections of the safe and effective iso-contour lines $\tau = 0.5\text{h}$ and $\tau = 2\text{h}$ determined from Figure 3.7a and the safe and effective iso-contour lines $T_{\max} = 42^\circ\text{C}$ and $T_{\max} = 46^\circ\text{C}$ determined from Figure 3.7b onto the coordinate plane (H_0, σ) that they all have in common. For successful hyperthermia treatment both the hyperthermic temperature and the hyperthermic duration must be within their safe and effective ranges. Hence, we conclude that for fixed other parameter values, the values of the intensity of the applied magnetic field H_0 and the nanoparticle injection duration σ must be chosen within the intersection of the two regions thus determined. The resulting estimate of safe and effective values (H_0, σ) are shown as a shaded region in Figure 3.7c.

The procedure described in relation to Figure 3.7 can be applied similarly to other pairs of model parameters. Figure 3.8 shows the regions of safe and effective hyperthermia treatment in the parameter planes (H_0, c_n) , (H_0, pd) , (ξ, H_0) , and (λ, H_0) , where λ is tortuosity of the vessels, pd is the diameter of nanoparticles, ξ is the wall shear rate, c_n is the injected concentration of particles at the boundary and H_0 is the magnetic field intensity. The latter is used as a common axis in order to make easier to cross-reference further parameter pairs. Figures 3.7c and 3.8 constitute a major result of our analysis. They may be used to design and optimise hyperthermia

procedures. Figure 3.8d shows that the vessels with tortuosity index between 0 and 1 reach the required temperature with much lower magnetic intensity in comparison with those structures characterise by higher tortuosity. However, this is not the case for tortuosity index $\lambda 2.5$. This is because this particular index is associated with hydraulic conductivity H_v , which is higher than that at tortuosity index 2, see Table 3.2. In all other cases, the higher the tortuosity index, the lower the vessels hydraulic conductivity.

Further discussion of these results is included in the next section.

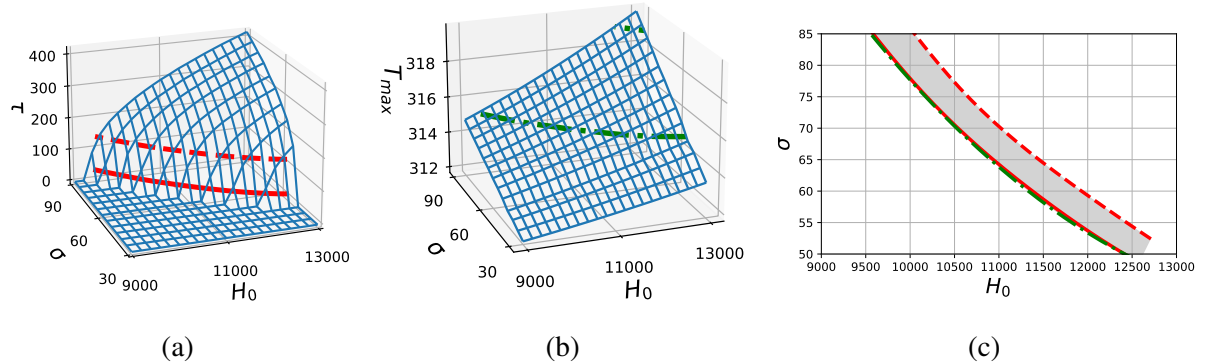


Figure 3.7: Computation of the hyperthermic time and temperature, and optimal values of magnetic field intensity and injection time. Surfaces of the hyperthermic duration $\tau(H_0, \sigma)$ in (a) and the maximal temperature at the centre of the tumour $T_{max}(H_0, \sigma)$ in (b) both shown as functions of magnetic field intensity and nanoparticle injection duration. The two red lines in (a) show the range of durations for safe and effective treatment between $\tau = 0.5$ h and $\tau = 2$ h. Similarly the two green lines indicate the range of safe and effective hyperthermic temperature range 42 – 46°C. Panel (c) shows the projections of these safe and effective isocontours onto the (H_0, σ) plane and the shaded region being the intesection where both the hyperthermic temperature and duration are within the target ranges. All other parameter values are kept fixed at values specified in Table 3.1 except $f = 300$ KHZ, $\sigma = 50$ minutes, $c_n = 100$ mg/ml, $\xi = 15$, $pd = 80$ nm.

3.4 Concluding remarks

In the third chapter, we have solved a new system of homogenised PDEs which models cancer hyperthermia in solid tumours driven by magnetic heating of large nanoparticles. The model is obtained by applying the asymptotic homogenisation technique, as done in the recent work proposed by Al Sariri and Penta [3] (previous chapter), where the role of microvascular tortuosity on heat transport driven by small nanoparticles is investigated.

The resulting governing equations in this work describe fluid transport and its exchange between the interstitial tumour space and the micro-vessels, as well as nanoparticles transport. The latter is assumed to occur solely in the vessels to which particles can adhere, as opposed to the work by Al Sariri and Penta [3], where extravasation of small nanoparticles was taken into

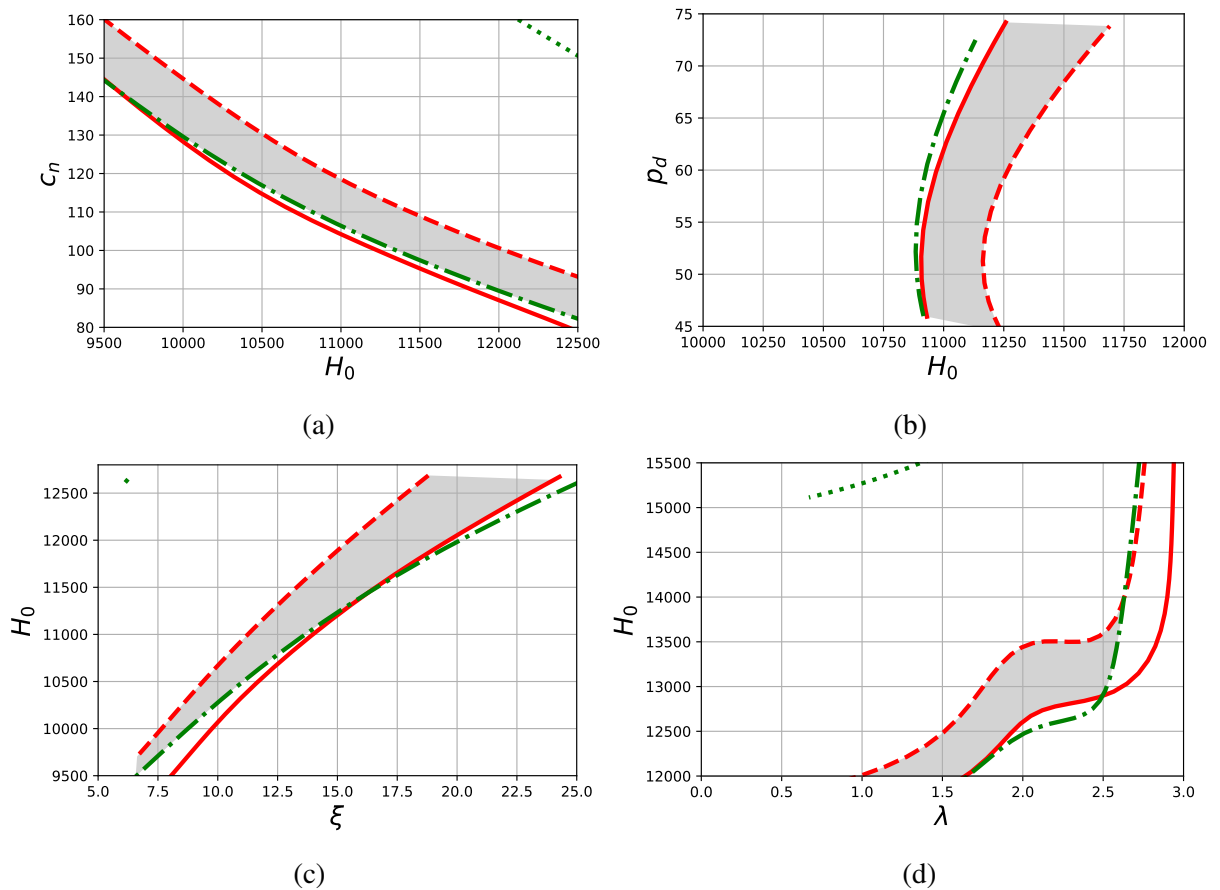


Figure 3.8: Regions of safe and effective hyperthermia treatment in the parameter space of the model. The regions are constructed as described in the caption of Figure 3.7 and are as follows (a) (H_0, c_n) , (b) (H_0, p_d) , (c) (ξ, H_0) , and (d) (λ, H_0) . In each panel, all parameters except the ones on the axes are kept fixed at values specified in Table 3.1 and $f = 300$ KHZ, $\sigma = 50$ minutes, $c_n = 100$ mg/ml, $\xi = 15$, $p_d = 80$ nm. The particles' diameter on the ordinate in figure (b) is in nm.

account, and adhesion ignored. We have performed a parametric analysis to study the role of nanoparticles and applied magnetic field properties, as well as micro-vessels tortuosity, on the temperature reached as a consequence of cancer hyperthermia (*hyperthermic temperature*), as well as the duration for which this latter is maintained (*hyperthermic duration*).

This way, we have identified the optimal cancer hyperthermia parameters for safe and effective hyperthermic temperature and duration conditions (herein identified in $42 - 46^\circ\text{C}$ for 30 minutes to 2 hours). The main results of our analysis are shown in Figures 3.7 and 3.8 in terms of particles' diameter, magnetic field intensity, vessels' shear rate, injection conditions (injected concentration and duration), as well as microvascular tortuosity.

According to our results, both the injected concentration of nanoparticles, and the time during which they are administrated, play a prominent role in reaching the desired hyperthermic conditions. The safe magnetic field intensity to be applied increases monotonically with decreasing injection time and duration, as expected.

The role of particles' diameter in the investigated range only weakly affects the safe range of magnetic intensity. On the other hand, we find that the properties of the microvessels play a crucial role in determining the hyperthermic conditions of the system.

Increasing the wall shear rate requires a corresponding increase in magnetic field intensity, although such an increase exhibits a sublinear profile. This may be due to the fact that, on the one hand, the wall shear rate determines an increase in the particles' density adhering to the vessels' walls and hence an increase in the heat source directly related to adhesion. On the other hand, an increase of the adhesion also translates in particle absorption at the macroscopic scale, so that, in turn, part of the nanoparticles flowing in the vessels are uptaken thus causing a net decrease in the heat source, as the latter also depend on the actual concentration of nanoparticles. In the scenario at hand, the latter phenomenon overtakes the former, as the concentration affects the heat source more than the density of nanoparticles adhering to the vessels, thus justifying the obtained profile.

The role of microvessels tortuosity is in agreement with the findings reported by Al Sariri and Penta [3], in that in general, regularisation of the tumour microstructure leads to an overall improvement in fluid, drug, and ultimately heat transport. However, high concentration peaks can be reached for intermediate values of the tortuosity, due to the fact that increasing the geometrical complexity of the vessels' leads to consequences which can potentially lead to opposite effects on the drug and heat dynamics.

In fact, an increased tortuosity leads to larger vessel surface, which leads to an increase in adhesion, and, at the same time, to impaired (reduce) fluid, drug, and heat convection. However, the importance of geometric regularisation in enhancing anti-cancer therapies based on drug transport for vascularised tumours is evident also in this current work and in agreement with the works developed by Mascheroni and Penta [85], Al Sariri and Penta [3], and Al Sariri et al. [4].

In the previous two chapters, we study the impact of the magnetic field on the heat distribution only. However, the magnetic field influences the fluid and particles' transport as well. We investigated the role that an applied magnetic field has on a ferrofluid [106]. A relevant example is indeed a fluid that contains a suspension of magnetic nanoparticles. Moreover, in those chapters, we studied the models related to vascularized tumour only, without taking into account the surrounding healthy tissues. Therefore, in the next chapter we discuss about the magnetic force influence on the fluid flow, and we consider that the tumour is surrounded by non-cancerous tissue, see also [112].

Chapter 4

Multiscale homogenisation of the role of an applied magnetic field on the fluid flowing in heterogeneous cancerous tissues

4.1 Introduction

In the previous two chapters, we investigated the influence of an applied magnetic field on temperature maps in tumours. As the nanoparticles are suspended in the fluid, the latter can be considered as a ferrofluid which percolates through the cancerous tissue. Therefore, it is also important to take into account how the magnetic force affects the fluid flow, which is an aspect that often neglected in the current literature. The biomagnetic fluid dynamic (BFM) is a science that studies the impact of magnetic force on the fluid flow [5]. Nanoparticles can also reach the healthy tissue. As such, the objective of this chapter is the study of the fluid flowing in a tissue which is comprising both healthy and cancerous regions when subjected to the application of a nonhomogeneous force, which is herein identified with a magnetic force.

The asymptotic homogenization technique is used to address the scale difference of tumour and healthy regions. This technique has been used since the late 70s. The starting point typically is a microscale PDEs system. As a result of upscaling process, we obtain a system of governing equations describing the macroscopic behaviour of the system. Usually microscale is very complex and the homogenization technique reduces its complexity by transforming the equations to macroscale and taking into account the advantages and the information of the small scale. This method is used in different porous medium using two scales like in [3, 102, 126] and many other works. Sometimes two-scale homogenization is not enough to describe the heterogeneities and hierarchical layers or domains of such problems. For example, Bensoussan et al. [11] derived multiple scales of homogenization on the basis of the original homogenization method. There are various works focusing on developing three scales of homogenization technique in different fields. Ramírez-Torres et al. [113] studied three scales of composite material which consists of

two hierarchical levels using two different scaling parameters ϵ_1 and ϵ_2 . Further computations in multiple scales are studied by Hornung [63], Guan et al. [53], and Yang et al. [150].

Penta et al. [106] derived the homogenized model for the fluid flow by taking into account three different scales which are pore, fine, and coarse scales and considering the inhomogeneous body force applied to the fluid. They have started with two Darcy's law in fine scale describing the fluid flow in two different porous media that interplay with each other. Applying the homogenization technique, they end up with one Darcy's law in macroscale and the impact of the fine scales appeared in the effective hydraulic tensors and the resulting forces which can be determined by solving appropriate cell problems.

Here, we study the fluid flow in the vessels and interstitial compartments of the tumour and healthy regions by using Darcy's law that are derived by Mascheroni and Penta [85], Penta et al. [102], Shipley and Chapman [126], and Al Sariri and Penta [3]. The latter derived the macroscale differential equations for the pressures and velocities of vascularized tumour. They have started with Stokes' problem that expresses the fluid flow in the vessels and Darcy's law in the case of the tissue. A double Darcy's models with mass exchange between compartments holds at macroscale. As a result, we start from the final macroscale PDE system of Al Sariri and Penta [3], and we consider it as the mesoscale. Also, we follow Penta et al. [106] to account for the impact of magnetic forces in the fluid flow. Using the homogenization technique, we derive the macroscale differential equations that combine the two regions together, and the influences of each domain are reflected in the vessels' permeabilities, tensors of hydraulic conductivity, as well as the homogenized magnetic forces.

This chapter is organized as follows. In Section 4.2, we discuss about the mathematical modelling of the problem. In Section 4.3, we derive the mesoscale differential equation of the new model which is constructed from the nondimensional homogenized differential equations that are taken from Al Sariri and Penta [3]. In Section 4.4, we nondimensionalize the new system. We explain briefly the homogenization method steps which are applied in this work to derive the final macroscale system in Section 4.5. The solutions of the mesoscale and the macroscale systems are derived in Sections 4.6, and 4.7, respectively. We conclude and discuss the general results in Section 4.8.

4.2 Mathematical modelling

In chemotherapy treatment and thermal ablation, both healthy and tumour tissues are being destroyed as they are adjacent to each other. Therefore, the aim of using magnetic nanoparticles is to reduce the negative side effects on the surrounding healthy cells. The heat tolerance of malignant cell is less than the healthy one [147]. Therefore, the goal is to find the optimal

increase in temperature to destroy cancer cells but not damaging the healthy tissues.

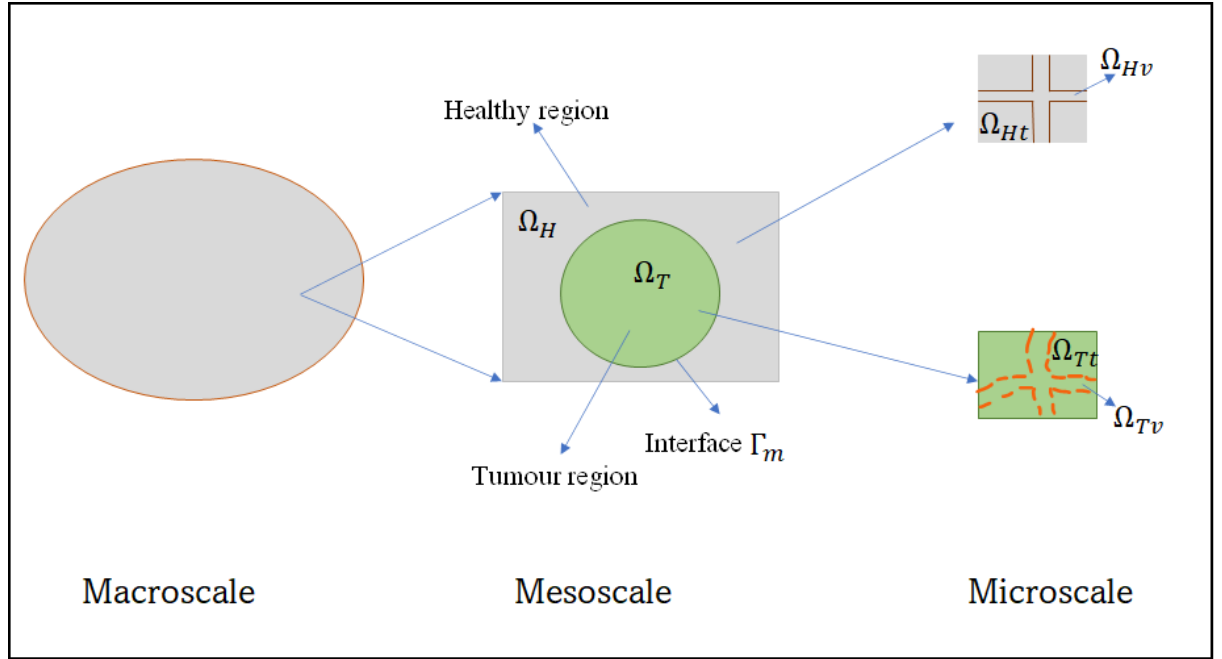


Figure 4.1: The three levels of homogenization that describe the interaction between the healthy and tumour cells. The volume portion Ω_{Hv} denotes the healthy vessels, Ω_{Ht} is the healthy interstitium, Ω_{Tv} is the tumour vessels, and Ω_{Tt} is the tumour interstitium.

The present work studies the fluid flow in two dimensional domain that considers the tumour heterogeneities inside the healthy tissue and we take into account the impact of the magnetic force in both regions. The fluid flow in each domain is studied in two compartments which are the vessels and interstitium. In order to address the scale difference between the various regions, we use the asymptotic homogenization technique. This method can be applied to our model by using three different hierarchical levels of organization which are, the macroscale, the mesoscale, and the microscale. The macroscale is the general uniform tissue that comprises all regions in one domain. At the mesoscale the tissue is divided into two domains which are the tumour heterogeneities Ω_T and healthy region Ω_H . The interface between the two regions is denoted by Γ_m . Zooming more to each region at the mesoscale, leads to different structures of the two domains in the microscale level. Each domain consists of vessels and interstitial compartments, see Figure 4.1.

On one hand, the ratio between the radius of the vessel ($d \approx 50 - 100\mu\text{m}$) and the average scale of the tumour ($L \approx 0.1 \text{ cm}$), is given by

$$\epsilon = \frac{d}{L} \ll 1. \quad (4.1)$$

On the other hand, the ratio between the average size of the tumour L and the average size of the

whole tissue (comprising both the healthy and the tumour region) ($L_m \approx 1$ cm) is

$$\varepsilon = \frac{L}{L_m} < 1. \quad (4.2)$$

Here, we find the homogenized differential equations that expresses the fluid flow influenced by an inhomogeneous magnetic force in the tumour that overlaps with surrounding healthy tissue.

4.3 The derivation of fluid flow in mesoscale

Penta et al. [102], Shipley and Chapman [126] and Al Sariri and Penta [3] studied the fluid flow of the tumour vessels and interstitial compartments. They considered the tumour tissue as a porous media governed by Darcy's law in microscale

$$\mathbf{u}_t = -\kappa \nabla p_t \quad \text{in } \Omega_t, \quad (4.3a)$$

$$\nabla \cdot \mathbf{u}_t = 0 \quad \text{in } \Omega_t, \quad (4.3b)$$

where they used Stokes' problem to express the blood flow in the vessels as

$$\mu \nabla^2 \mathbf{u}_v = \nabla p_v \quad \text{in } \Omega_v, \quad (4.4a)$$

$$\nabla \cdot \mathbf{u}_v = 0 \quad \text{in } \Omega_v. \quad (4.4b)$$

They assumed a continuous blood flow through the semi permeable vessels' membrane given by Starling's law

$$\mathbf{u}_t \cdot \mathbf{n} = \mathbf{u}_v \cdot \mathbf{n} = L(p_t - p_v) \quad \text{on } \Gamma. \quad (4.5)$$

Here, Γ represent the interface between the vessel and interstitial compartments (vessels' wall), p stands for the fluid pressure, \mathbf{u} is the fluid velocity, μ is the blood viscosity, and κ is tissue hydraulic conductivity. The indices v , and t denote the vessels and tumour interstitial compartments, respectively.

The asymptotic homogenization technique (multiscale) is applied in the model due to the large difference in scales that exists between the vessels' distances (microscale) and average size of the tumour (macroscale). The parameters of the system are upscaled at macroscale and the impact of the microscale is encoded in the hydraulic conductivity tensors of the system. The

final macroscale system consist of double Darcy's law and it can be summarised as

$$\mathbf{u}_v = -\mathbf{Y}_v \nabla_x p_v, \quad (4.6a)$$

$$\mathbf{u}_t = -\bar{\kappa} \mathbf{Y}_t \nabla_x p_t. \quad (4.6b)$$

$$\nabla \cdot \mathbf{u}_v = \frac{S}{|\Omega_v|} \bar{L}_p (p_v - p_t), \quad (4.6c)$$

$$\nabla \cdot \mathbf{u}_t = \frac{S}{|\Omega_t|} \bar{L}_p (p_t - p_v), \quad (4.6d)$$

Here, $\mathbf{Y}_v(\mathbf{x})$ and $\mathbf{Y}_t(\mathbf{x})$ are the effective hydraulic conductivity tensors, S is the vessels' wall surface, $|\Omega_{v,t}|$ is the vessels/interstitial volumes, \bar{L}_p is the non-dimensional vessels' permeability, and $\bar{\kappa}$ is non-dimensional hydraulic conductivity of the tissue.

4.3.1 The influence of the magnetic force on the fluid flow

Usually, a constant body force is taken into account when discussing about the fluid flow in certain media. In this case, the body force solely affects the resulting fluid profile, but not the pressure distribution in the medium. However, when we are talking about the porous medium, then the force generally varies in space. Therefore, Penta et al. [106] studied the impact of an inhomogeneous body force in the fluid flow of two porous media interacting with each other. They used double Darcy's law to express the fluid flow in both regions at the fine scale and they applied the homogenization technique to upscale the problem at the macroscale. The novelty of their work appears in the macroscale of the system as they declared that the forces in macroscale are not just the average of the forces in fine scale, but also other extra terms that reflects the structures and information of the fine scale with the hydraulic conductivity tensors.

In this work, we investigate theoretically the influence of non homogeneous magnetic field force on the vessels and interstitium of the tumour and healthy tissues. To do so, we assume that the fluid flow in both compartments are driven by an external volume load which should be related to the inhomogeneous force of applied magnetic field \hat{f} , following Penta et al. [106]. The system of equations can be written as

$$\mathbf{u}_v = -\mathbf{Y}_v (\nabla p_v + \hat{f}_v), \quad (4.7a)$$

$$\mathbf{u}_t = -\bar{\kappa} \mathbf{Y}_t (\nabla p_t + \hat{f}_t). \quad (4.7b)$$

Then, by taking the divergence of the velocities in equations (4.7a) and (4.7b), and using equations

(4.6c) and (4.6d), we obtain

$$\nabla \cdot (\mathbf{Y}_v \nabla p_v) = \frac{S}{|\Omega_v|} \bar{L}_p (p_v - p_t) + \nabla \cdot \mathbf{f}_v, \quad (4.8a)$$

$$\nabla \cdot (\bar{\kappa} \mathbf{Y}_t \nabla p_t) = \frac{S}{|\Omega_t|} \bar{L}_p (p_t - p_v) + \nabla \cdot \mathbf{f}_t. \quad (4.8b)$$

In the present work, we start from (4.7a-4.7b) and (4.8a-4.8b) which means that we embrace the mesoscale as a starting point in this new model, and we find the resulting macroscale system of PDEs by means of the following road-map.

- (i) Re-write the system in dimensional form.
- (ii) Generalize the equations for the healthy region and take into account the magnetic force applied to the fluid.
- (iii) Find the non-dimensional system of PDEs.
- (iv) Using the homogenization technique, we find the macroscale governing equations.

4.3.2 The dimensional form of the model

The differential equations (4.7a-4.7b) and (4.8a-4.8b) are in non-dimensional form as they are derived due to the scales' difference between the distance of the vessels and the average size of the tumour. To reuse this system in the present model and expand it to cover the relation and the variation of scales' sizes between the tumour and surrounding healthy region in mesoscale, we transform it to dimensional form. Subsequently, we find the appropriate dimension-less system. The transformation of the variables from non-dimensional to dimensional form is described as

$$p = \frac{p^D}{CL}, \quad \nabla = L \nabla^D, \quad \bar{\kappa} = \frac{\kappa^D \mu}{d^2}, \quad \bar{L}_p = \frac{L_p^D \mu L^2}{d^3}, \quad \hat{\mathbf{f}} = \frac{1}{C} \hat{\mathbf{f}}^D, \quad \mathbf{u} = \frac{\mu}{Cd^2} \mathbf{u}^D, \quad (4.9)$$

where C is the pressure reference, L is the tumour length scale, d is the distance between the vessels, and μ is the blood viscosity.

The dimensional differential equation for the vessels and interstitial fluid pressure compartments can be written by applying (4.9) in the differential equations (4.7a-4.7b) and (4.8a-4.8b). The dimensional form of the fluid pressure in the tumour interstitial compartment (4.8b) is derived as

$$\frac{\mu L^2}{CLd^2} \nabla_x^D \cdot (\kappa^D \mathbf{Y}_t \nabla_x^D p_t^D) = \frac{S}{|\Omega_t|} \frac{L_p^D \mu L^2}{d^3 CL} (p_t^D - p_v^D) + \frac{L\mu}{Cd^2} \nabla_x^D \cdot (-\kappa^D \mathbf{Y}_t \hat{\mathbf{f}}_t^D), \quad (4.10)$$

$$\nabla_x^D \cdot (\mathbf{Y}_t^D \nabla_x^D p_t^D) = \left(\frac{S}{|\Omega_t|} \frac{1}{d} \right) L_p^D (p_t^D - p_v^D) + \nabla_x^D \cdot \mathbf{f}_t^D, \quad (4.11)$$

and we use the same steps for the vessel compartment (4.8a),

$$\frac{L^2}{CL} \nabla_x^D \cdot (\Upsilon_v \nabla_x^D p_v^D) = \frac{S}{|\Omega_v|} \frac{L_p \mu L^2}{d^3 CL} (p_v^D - p_t^D) + \frac{L}{C} \nabla_x^D \cdot (-\Upsilon_v \hat{f}_v^D), \quad (4.12)$$

$$\nabla_x^D \cdot (\Upsilon_v^D \nabla_x^D p_v^D) = \left(\frac{S}{|\Omega_v|} \frac{1}{d} \right) L_p^D (p_v^D - p_t^D) + \nabla_x^D \cdot f_v^D. \quad (4.13)$$

The dimensional blood velocity (4.7a) can be found as

$$\frac{\mu}{Cd^2} \mathbf{u}_v^D = -\frac{\Upsilon_v L}{CL} \nabla_x^D p_v^D - \frac{\Upsilon_v \hat{f}_v^D}{C}, \quad (4.14)$$

$$\mathbf{u}_v^D = -\Upsilon_v^D \nabla_x^D \cdot p_v^D + f_v^D, \quad (4.15)$$

and the dimensional fluid flow in the tumour interstitial compartment (4.7b) is obtained as

$$\frac{\mu}{Cd^2} \mathbf{u}_t^D = -\frac{\kappa^D \Upsilon_t \mu L}{CLd^2} \nabla_x^D p_t^D - \frac{\mu \kappa^D \Upsilon_t \hat{f}_t^D}{Cd^2}, \quad (4.16)$$

$$\mathbf{u}_t^D = -\Upsilon_t^D \nabla_x^D \cdot p_t^D + f_t^D, \quad (4.17)$$

where $\Upsilon_t^D = \kappa^D \Upsilon_t$, $\Upsilon_v^D = \frac{d^2}{\mu} \Upsilon_v$, $f_t^D = -\kappa \Upsilon_t^D \hat{f}_t^D$, and $f_v^D = -\Upsilon_v^D \hat{f}_v^D$. The letter D denotes the dimensional variables and parameters.

4.3.3 The fluid flow for the tumour and healthy cells with magnetic force

We can generalize equations (4.11), (4.13), (4.15), and (4.17) to describe the fluid flow in the healthy region when the magnetic field is applied to the whole tissue as

$$\nabla_x \cdot (\mathbf{K}_H \nabla_x p_H) = \left(\frac{S}{|\Omega_{Hv}|d} \right) L_H (p_H - g_H) - \nabla_x \cdot (\mathbf{K}_H \hat{f}_h) \quad \text{in } \Omega_H, \quad (4.18a)$$

$$\nabla_x \cdot (\mathbf{K}_T \nabla_x p_T) = \left(\frac{S}{|\Omega_{Tv}|d} \right) L_T (p_T - g_T) - \nabla_x \cdot (\mathbf{K}_T \hat{f}_t) \quad \text{in } \Omega_T, \quad (4.18b)$$

$$\nabla_x \cdot (\mathbf{E}_H \nabla_x g_H) = \left(\frac{S}{|\Omega_{Ht}|d} \right) L_H (g_H - p_H) - \nabla_x \cdot (\mathbf{E}_H \hat{f}_h) \quad \text{in } \Omega_H, \quad (4.18c)$$

$$\nabla_x \cdot (\mathbf{E}_T \nabla_x g_T) = \left(\frac{S}{|\Omega_{Tt}|d} \right) L_T (g_T - p_T) - \nabla_x \cdot (\mathbf{E}_T \hat{f}_t) \quad \text{in } \Omega_T, \quad (4.18d)$$

$$\mathbf{u}_H = -\mathbf{K}_H (\nabla p_H + \hat{f}_h) \quad \text{in } \Omega_H, \quad (4.18e)$$

$$\mathbf{u}_T = -\mathbf{K}_T (\nabla p_T + \hat{f}_t) \quad \text{in } \Omega_T, \quad (4.18f)$$

$$\mathbf{v}_H = -\mathbf{E}_H (\nabla g_H + \hat{f}_h) \quad \text{in } \Omega_H, \quad (4.18g)$$

$$\mathbf{v}_T = -\mathbf{E}_T (\nabla g_T + \hat{f}_t) \quad \text{in } \Omega_T, \quad (4.18h)$$

with boundary conditions

$$p_T = p_H \quad \text{on} \quad \Gamma_m, \quad (4.19a)$$

$$g_T = g_H \quad \text{on} \quad \Gamma_m, \quad (4.19b)$$

$$\left(-\mathcal{K}_T \nabla_x p_T - \mathcal{K}_T \hat{f}_t\right) \cdot \mathbf{n} = \left(-\mathcal{K}_H \nabla_x p_H - \mathcal{K}_H \hat{f}_h\right) \cdot \mathbf{n} \quad \text{on} \quad \Gamma_m, \quad (4.19c)$$

$$\left(-\mathbf{E}_H \nabla_x g_H - \mathbf{E}_H \hat{f}_h\right) \cdot \mathbf{n} = \left(-\mathbf{E}_T \nabla_x g_T - \mathbf{E}_T \hat{f}_t\right) \cdot \mathbf{n} \quad \text{on} \quad \Gamma_m, \quad (4.19d)$$

where, $\mathcal{K}_{H,T} = \frac{d^2}{\mu} \bar{\mathcal{K}}_{H,T}$, and $\bar{\mathcal{K}}_{H,T}$ is non dimensional form.

The variables $p_{H,T}$, $g_{H,T}$, $u_{H,T}$, and $v_{H,T}$ are the vessels' fluid pressures, interstitial fluid pressures, blood velocities, interstitial fluid velocities for healthy/tumour region, respectively. The parameter $|\Omega_{Hv}|$ is the domain of the vessels' healthy region, $|\Omega_{Tv}|$ is the domain of the vessels in tumour region, $|\Omega_{Ht}|$ is the domain of interstitial compartment in healthy region, and $|\Omega_{Tt}|$ is the domain of interstitial compartments for the tumour region. The parameters $L_{H,T}$, $\mathcal{K}_{H,T}$, and $\mathbf{E}_{H,T}$ are the vessels permeabilities, the effective vessels' hydraulic conductivity, and the effective interstitial hydraulic conductivities for the healthy/tumour region, respectively. The magnetic forces of the healthy and tumour vessels are represented by \hat{f}_h and \hat{f}_t , respectively.

4.4 Non-dimensional form of the model

We find the dimensionless equations of the system by performing a change of variables as follow,

$$X = L_m X', \quad p_Q = C L_m p'_Q, \quad g_Q = C L_m g'_Q, \quad \mathbf{u}_Q = \frac{C d^2}{\mu} \mathbf{u}'_Q, \quad \mathbf{v}_Q = \frac{C d^2}{\mu} \mathbf{v}'_Q, \quad \hat{f}_Q = C \hat{f}'_Q, \quad (4.20)$$

where, Q is H or T .

By neglecting all the primes for the sake of simplicity, the non-dimensional differential equations can be written as

$$\nabla_x \cdot (\bar{\mathbf{K}}_H \nabla_x p_H) = \bar{L}_{Hv}(p_H - g_H) + \nabla_x \cdot f_H \quad \text{in } \Omega_H, \quad (4.21a)$$

$$\nabla_x \cdot (\bar{\mathbf{K}}_T \nabla_x p_T) = \bar{L}_{Tv}(p_T - g_T) + \nabla_x \cdot f_T \quad \text{in } \Omega_T, \quad (4.21b)$$

$$\nabla_x \cdot (\bar{\mathbf{E}}_H \nabla_x g_H) = \bar{L}_{Ht}(g_H - p_H) + \nabla_x \cdot \bar{f}_H \quad \text{in } \Omega_H, \quad (4.21c)$$

$$\nabla_x \cdot (\bar{\mathbf{E}}_T \nabla_x g_T) = \bar{L}_{Tt}(g_T - p_T) + \nabla_x \cdot \bar{f}_T \quad \text{in } \Omega_T, \quad (4.21d)$$

$$p_T = p_H \quad \text{on } \Gamma_m, \quad (4.21e)$$

$$g_T = g_H \quad \text{on } \Gamma_m, \quad (4.21f)$$

$$(-\bar{\mathbf{K}}_T \nabla_x p_T + f_T) \cdot \mathbf{n} = (-\bar{\mathbf{K}}_H \nabla_x p_H + f_H) \cdot \mathbf{n} \quad \text{on } \Gamma_m, \quad (4.21g)$$

$$(-\bar{\mathbf{E}}_H \nabla_x g_H + \bar{f}_H) \cdot \mathbf{n} = (-\bar{\mathbf{E}}_T \nabla_x g_T + \bar{f}_T) \cdot \mathbf{n} \quad \text{on } \Gamma_m, \quad (4.21h)$$

with

$$\bar{L}_{Hv} = L_H \frac{S_H L_m^2 \mu}{d^3 |\Omega_{Hv}|}, \quad \bar{L}_{Tv} = L_T \frac{S_T L_m^2 \mu}{d^3 |\Omega_{Tv}|}, \quad (4.22)$$

$$\bar{L}_{Ht} = L_H \frac{S_H L_m^2 \mu}{d^3 |\Omega_{Ht}|}, \quad \bar{L}_{Tt} = L_T \frac{S_T L_m^2 \mu}{d^3 |\Omega_{Tt}|}, \quad (4.23)$$

$$\bar{\mathbf{E}}_H = \frac{\mu}{d^2} \kappa_H \mathbf{E}_H, \quad \bar{\mathbf{E}}_T = \frac{\mu}{d^2} \kappa_T \mathbf{E}_T. \quad (4.24)$$

The nonhomogeneous magnetic forces are defined as

$$f_H = -\bar{\mathbf{K}}_H \hat{f}_h, \quad f_T = -\bar{\mathbf{K}}_T \hat{f}_t, \quad (4.25)$$

$$\bar{f}_H = -\bar{\mathbf{E}}_H \hat{f}_h, \quad \bar{f}_T = -\bar{\mathbf{E}}_T \hat{f}_t. \quad (4.26)$$

Furthermore, the fluid velocities can be written in non-dimensional form as Darcy's law driven by inhomogeneous magnetic forces

$$\mathbf{u}_H = -\bar{\mathbf{K}}_H \nabla_x p_H + f_H \quad \text{in } \Omega_H, \quad (4.27a)$$

$$\mathbf{u}_T = -\bar{\mathbf{K}}_T \nabla_x p_T + f_T \quad \text{in } \Omega_T, \quad (4.27b)$$

$$\mathbf{v}_H = -\bar{\mathbf{E}}_H \nabla_x g_H + \bar{f}_H \quad \text{in } \Omega_H, \quad (4.27c)$$

$$\mathbf{v}_T = -\bar{\mathbf{E}}_T \nabla_x g_T + \bar{f}_T \quad \text{in } \Omega_T, \quad (4.27d)$$

where \mathbf{u} is the fluid velocity in the vessels and \mathbf{v} is the fluid velocity in the interstitial space. Also, the indices H and T are for the healthy and tumour regions, respectively.

4.5 Model derivation via the asymptotic homogenisation technique

The application of a multiscale approach is motivated by the difference in scales between L_m which represents the size of the whole domain, and the mesoscale L that describes the average distance between cancerous regions and their ratio is defined as in equation (4.2).

Every field is considered as a function of the two independent variables \mathbf{y} which represents the mesoscale, while \mathbf{x} is the macroscale variable. The relation between these two is given by

$$\mathbf{y} = \frac{\mathbf{x}}{\varepsilon}. \quad (4.28)$$

Also, we assume the \mathbf{y} -periodicity for the mesoscale and every variable can be written in power series of ε as

$$v(\mathbf{x}) = v(\mathbf{x}, \mathbf{y}) = \sum_{l=0}^{\infty} v^{(l)}(\mathbf{x}, \mathbf{y}) \varepsilon^l = v^{(0)}(\mathbf{x}, \mathbf{y}) + v^{(1)}(\mathbf{x}, \mathbf{y}) \varepsilon^1 + v^{(2)}(\mathbf{x}, \mathbf{y}) \varepsilon^2 + \dots, \quad (4.29)$$

where v can be any variable in the model, such as $\mathbf{u}_{H,T}$, $\mathbf{v}_{H,T}$, $p_{H,T}$, $g_{H,T}$, $f_{H,T}$, and $\bar{f}_{H,T}$.

As all the fields in the resulting macroscale model should be depending on the macroscale variable only, we also define the integral average over the periodic cell as

$$\langle \cdot \rangle = \frac{1}{|\Omega|} \int_{|\Omega_Q|} \cdot \, d\mathbf{y}, \quad Q = H, T. \quad (4.30)$$

Here, $|\Omega_H|$, $|\Omega_T|$ are the healthy and tumour cell volume portion, and $|\Omega|$ is the volume of the periodic cell.

We apply the asymptotic homogenisation technique to obtain a new system of PDEs in terms of the leading order fields. The information at the finer scale (which is mesoscale in this case) is encoded in the parameters of the resulting zero-th order model.

4.5.1 The asymptotic homogenisation steps

The multiscale differential equations for the fluid flow of the healthy and tumour regions in the vessels and interstitial compartments (4.21a)-(4.21d), with the interface conditions (4.21e)-

(4.21h) can be written using the power series (4.29) as

$$\begin{aligned} & \varepsilon^2 \nabla_x \cdot (\bar{\mathbf{K}}_H \nabla_x p_H^\varepsilon) + \varepsilon \nabla_x \cdot (\bar{\mathbf{K}}_H \nabla_y p_H^\varepsilon) + \varepsilon \nabla_y \cdot (\bar{\mathbf{K}}_H \nabla_x p_H^\varepsilon) + \\ & \nabla_y \cdot (\bar{\mathbf{K}}_H \nabla_y p_H^\varepsilon) = \varepsilon^2 \bar{L}_H(p_H^\varepsilon - g_H^\varepsilon) + \varepsilon^2 \nabla_x \cdot \bar{f}_H^\varepsilon + \varepsilon \nabla_y \cdot \bar{f}_H^\varepsilon \quad \text{in } \Omega_H, \end{aligned} \quad (4.31a)$$

$$\begin{aligned} & \varepsilon^2 \nabla_x \cdot (\bar{\mathbf{K}}_T \nabla_x p_T^\varepsilon) + \varepsilon \nabla_x \cdot (\bar{\mathbf{K}}_T \nabla_y p_T^\varepsilon) + \varepsilon \nabla_y \cdot (\bar{\mathbf{K}}_T \nabla_x p_T^\varepsilon) + \\ & \nabla_y \cdot (\bar{\mathbf{K}}_T \nabla_y p_T^\varepsilon) = \varepsilon^2 \bar{L}_T(p_T^\varepsilon - g_T^\varepsilon) + \varepsilon^2 \nabla_x \cdot \bar{f}_T^\varepsilon + \varepsilon \nabla_y \cdot \bar{f}_T^\varepsilon \quad \text{in } \Omega_T, \end{aligned} \quad (4.31b)$$

$$\begin{aligned} & \varepsilon^2 \nabla_x \cdot (\bar{\mathbf{E}}_H \nabla_x g_H^\varepsilon) + \varepsilon \nabla_x \cdot (\bar{\mathbf{E}}_H \nabla_y g_H^\varepsilon) + \varepsilon \nabla_y \cdot (\bar{\mathbf{E}}_H \nabla_x g_H^\varepsilon) + \\ & \nabla_y \cdot (\bar{\mathbf{E}}_H \nabla_y g_H^\varepsilon) = \varepsilon^2 \bar{L}_{Ht}(g_H^\varepsilon - p_H^\varepsilon) + \varepsilon^2 \nabla_x \cdot \bar{f}_H^\varepsilon + \varepsilon \nabla_y \cdot \bar{f}_H^\varepsilon \quad \text{in } \Omega_H, \end{aligned} \quad (4.31c)$$

$$\begin{aligned} & \varepsilon^2 \nabla_x \cdot (\bar{\mathbf{E}}_T \nabla_x g_T^\varepsilon) + \varepsilon \nabla_x \cdot (\bar{\mathbf{E}}_T \nabla_y g_T^\varepsilon) + \varepsilon \nabla_y \cdot (\bar{\mathbf{E}}_T \nabla_x g_T^\varepsilon) + \\ & \nabla_y \cdot (\bar{\mathbf{E}}_T \nabla_y g_T^\varepsilon) = \varepsilon^2 \bar{L}_{Tt}(g_T^\varepsilon - p_T^\varepsilon) + \varepsilon^2 \nabla_x \cdot \bar{f}_T^\varepsilon + \varepsilon \nabla_y \cdot \bar{f}_T^\varepsilon \quad \text{in } \Omega_T, \end{aligned} \quad (4.31d)$$

$$p_T^\varepsilon = p_H^\varepsilon \quad \text{on } \Gamma_m, \quad (4.31e)$$

$$g_T^\varepsilon = g_H^\varepsilon \quad \text{on } \Gamma_m, \quad (4.31f)$$

$$\begin{aligned} & (-\varepsilon \bar{\mathbf{K}}_T \nabla_x p_T^\varepsilon - \bar{\mathbf{K}}_T \nabla_y p_T^\varepsilon + \varepsilon \bar{f}_T^\varepsilon) \cdot \mathbf{n} = \\ & (-\varepsilon \bar{\mathbf{K}}_H \nabla_x p_H^\varepsilon - \bar{\mathbf{K}}_H \nabla_y p_H^\varepsilon + \varepsilon \bar{f}_H^\varepsilon) \cdot \mathbf{n} \quad \text{on } \Gamma_m, \end{aligned} \quad (4.31g)$$

$$\begin{aligned} & (-\varepsilon \bar{\mathbf{E}}_T \nabla_x g_T^\varepsilon - \bar{\mathbf{E}}_T \nabla_y g_T^\varepsilon + \varepsilon \bar{f}_T^\varepsilon) \cdot \mathbf{n} = \\ & (-\varepsilon \bar{\mathbf{E}}_H \nabla_x g_H^\varepsilon - \bar{\mathbf{E}}_H \nabla_y g_H^\varepsilon + \varepsilon \bar{f}_H^\varepsilon) \cdot \mathbf{n} \quad \text{on } \Gamma_m, \end{aligned} \quad (4.31h)$$

and the multiscale for the fluid velocities (4.27a-4.27d) are

$$\varepsilon \mathbf{u}_H^\varepsilon = -\varepsilon \bar{\mathbf{K}}_H \nabla_x p_H^\varepsilon - \bar{\mathbf{K}}_H \nabla_y p_H^\varepsilon + \varepsilon \bar{f}_H^\varepsilon \quad \text{in } \Omega_H, \quad (4.32a)$$

$$\varepsilon \mathbf{u}_T^\varepsilon = -\varepsilon \bar{\mathbf{K}}_T \nabla_x p_T^\varepsilon - \bar{\mathbf{K}}_T \nabla_y p_T^\varepsilon + \varepsilon \bar{f}_T^\varepsilon \quad \text{in } \Omega_T, \quad (4.32b)$$

$$\varepsilon \mathbf{v}_H^\varepsilon = -\varepsilon \bar{\mathbf{E}}_H \nabla_x g_H^\varepsilon - \bar{\mathbf{E}}_H \nabla_y g_H^\varepsilon + \varepsilon \bar{f}_H^\varepsilon \quad \text{in } \Omega_H, \quad (4.32c)$$

$$\varepsilon \mathbf{v}_T^\varepsilon = -\varepsilon \bar{\mathbf{E}}_T \nabla_x g_T^\varepsilon - \bar{\mathbf{E}}_T \nabla_y g_T^\varepsilon + \varepsilon \bar{f}_T^\varepsilon \quad \text{in } \Omega_T. \quad (4.32d)$$

Equating the system for ε^0 gives

$$\nabla_y \cdot (\bar{\mathbf{K}}_H \nabla_y p_H^{(0)}) = 0 \quad \text{in } \Omega_H, \quad (4.33a)$$

$$\nabla_y \cdot (\bar{\mathbf{K}}_T \nabla_y p_T^{(0)}) = 0 \quad \text{in } \Omega_T, \quad (4.33b)$$

$$\nabla_y \cdot (\bar{\mathbf{E}}_H \nabla_y g_H^{(0)}) = 0 \quad \text{in } \Omega_H, \quad (4.33c)$$

$$\nabla_y \cdot (\bar{\mathbf{E}}_T \nabla_y g_T^{(0)}) = 0 \quad \text{in } \Omega_T, \quad (4.33d)$$

$$\bar{\mathbf{K}}_H \nabla_y p_H^{(0)} = 0 \quad \text{in } \Omega_H, \quad (4.33e)$$

$$\bar{\mathbf{K}}_T \nabla_y p_T^{(0)} = 0 \quad \text{in } \Omega_T, \quad (4.33f)$$

$$\bar{\mathbf{E}}_H \nabla_y g_H^{(0)} = 0 \quad \text{in } \Omega_H, \quad (4.33g)$$

$$\bar{\mathbf{E}}_T \nabla_y g_T^{(0)} = 0 \quad \text{in } \Omega_T, \quad (4.33h)$$

$$p_T^{(0)} = p_H^{(0)} \quad \text{on } \Gamma_m, \quad (4.33i)$$

$$g_T^{(0)} = g_H^{(0)} \quad \text{on } \Gamma_m, \quad (4.33j)$$

$$(\bar{\mathbf{K}}_T \nabla_y p_T^{(0)}) \cdot \mathbf{n} = (\bar{\mathbf{K}}_H \nabla_y p_H^{(0)}) \cdot \mathbf{n} \quad \text{on } \Gamma_m, \quad (4.33k)$$

$$(\bar{\mathbf{E}}_T \nabla_y g_T^{(0)}) \cdot \mathbf{n} = (\bar{\mathbf{E}}_H \nabla_y g_H^{(0)}) \cdot \mathbf{n} \quad \text{on } \Gamma_m. \quad (4.33l)$$

For ε^1

$$\nabla_y \cdot (\bar{\mathbf{K}}_H \nabla_x p_H^{(0)}) + \nabla_y \cdot (\bar{\mathbf{K}}_H \nabla_y p_H^{(1)}) = \nabla_y \cdot f_H^{(0)} \quad \text{in } \Omega_H, \quad (4.34a)$$

$$\nabla_y \cdot (\bar{\mathbf{K}}_T \nabla_x p_T^{(0)}) + \nabla_y \cdot (\bar{\mathbf{K}}_T \nabla_y p_T^{(1)}) = \nabla_y \cdot f_T^{(0)} \quad \text{in } \Omega_T, \quad (4.34b)$$

$$\nabla_y \cdot (\bar{\mathbf{E}}_H \nabla_x g_H^{(0)}) + \nabla_y \cdot (\bar{\mathbf{E}}_H \nabla_y g_H^{(1)}) = \nabla_y \cdot \bar{f}_H^{(0)} \quad \text{in } \Omega_H, \quad (4.34c)$$

$$\nabla_y \cdot (\bar{\mathbf{E}}_T \nabla_x g_T^{(0)}) + \nabla_y \cdot (\bar{\mathbf{E}}_T \nabla_y g_T^{(1)}) = \nabla_y \cdot \bar{f}_T^{(0)} \quad \text{in } \Omega_T, \quad (4.34d)$$

$$\mathbf{u}_H^{(0)} = -\bar{\mathbf{K}}_H \nabla_x p_H^{(0)} - \bar{\mathbf{K}}_H \nabla_y p_H^{(1)} + f_H^{(0)} \quad \text{in } \Omega_H, \quad (4.34e)$$

$$\mathbf{u}_T^{(0)} = -\bar{\mathbf{K}}_T \nabla_x p_T^{(0)} - \bar{\mathbf{K}}_T \nabla_y p_T^{(1)} + f_T^{(0)} \quad \text{in } \Omega_T, \quad (4.34f)$$

$$\mathbf{v}_H^{(0)} = -\bar{\mathbf{E}}_H \nabla_x g_H^{(0)} - \bar{\mathbf{E}}_H \nabla_y g_H^{(1)} + \bar{f}_H^{(0)} \quad \text{in } \Omega_H, \quad (4.34g)$$

$$\mathbf{v}_T^{(0)} = -\bar{\mathbf{E}}_T \nabla_x g_T^{(0)} - \bar{\mathbf{E}}_T \nabla_y g_T^{(1)} + \bar{f}_T^{(0)} \quad \text{in } \Omega_T, \quad (4.34h)$$

$$p_H^{(1)} = p_T^{(1)} \quad \text{on } \Gamma_m, \quad (4.34i)$$

$$g_H^{(1)} = g_T^{(1)} \quad \text{on } \Gamma_m, \quad (4.34j)$$

$$\begin{aligned} & \left(-\bar{\mathbf{K}}_H \nabla_x p_H^{(0)} - \bar{\mathbf{K}}_H \nabla_y p_H^{(1)} + f_H^{(0)} \right) \cdot \mathbf{n} = \\ & \left(-\bar{\mathbf{K}}_T \nabla_x p_T^{(0)} - \bar{\mathbf{K}}_T \nabla_y p_T^{(1)} + f_T^{(0)} \right) \cdot \mathbf{n} \quad \text{on } \Gamma_m, \end{aligned} \quad (4.34k)$$

$$\begin{aligned} & \left(-\bar{\mathbf{E}}_H \nabla_x g_H^{(0)} - \bar{\mathbf{E}}_H \nabla_y g_H^{(1)} + \bar{f}_H^{(0)} \right) \cdot \mathbf{n} = \\ & \left(-\bar{\mathbf{E}}_T \nabla_x g_T^{(0)} - \bar{\mathbf{E}}_T \nabla_y g_T^{(1)} + \bar{f}_T^{(0)} \right) \cdot \mathbf{n} \quad \text{on } \Gamma_m. \end{aligned} \quad (4.34l)$$

For ε^2

$$\begin{aligned} & \nabla_x \cdot (\bar{K}_H \nabla_x p_H^{(0)}) + \nabla_x \cdot (\bar{K}_H \nabla_y p_H^{(1)}) + \nabla_y \cdot (\bar{K}_H \nabla_x p_H^{(1)}) + \\ & \nabla_y \cdot (\bar{K}_H \nabla_y p_H^{(2)}) = \nabla_x \cdot f_H^{(0)} + \nabla_y \cdot f_H^{(1)} + \bar{L}_{Hv} (p_H^{(0)} - g_H^{(0)}) \quad \text{in } \Omega_H, \end{aligned} \quad (4.35a)$$

$$\begin{aligned} & \nabla_x \cdot (\bar{K}_T \nabla_x p_T^{(0)}) + \nabla_x \cdot (\bar{K}_T \nabla_y p_T^{(1)}) + \nabla_y \cdot (\bar{K}_T \nabla_x p_T^{(1)}) + \\ & \nabla_y \cdot (\bar{K}_T \nabla_y p_T^{(2)}) = \nabla_x \cdot f_T^{(0)} + \nabla_y \cdot f_T^{(1)} + \bar{L}_{Tv} (p_T^{(0)} - g_T^{(0)}) \quad \text{in } \Omega_T, \end{aligned} \quad (4.35b)$$

$$\begin{aligned} & \nabla_x \cdot (\bar{E}_H \nabla_x g_H^{(0)}) + \nabla_x \cdot (\bar{E}_H \nabla_y g_H^{(1)}) + \nabla_y \cdot (\bar{E}_H \nabla_x g_H^{(1)}) + \\ & \nabla_y \cdot (\bar{E}_H \nabla_y g_H^{(2)}) = \nabla_x \cdot \bar{f}_H^{(0)} + \nabla_y \cdot \bar{f}_H^{(1)} + \bar{L}_{Ht} (g_H^{(0)} - p_H^{(0)}) \quad \text{in } \Omega_H, \end{aligned} \quad (4.35c)$$

$$\begin{aligned} & \nabla_x \cdot (\bar{E}_T \nabla_x g_T^{(0)}) + \nabla_x \cdot (\bar{E}_T \nabla_y g_T^{(1)}) + \nabla_y \cdot (\bar{E}_T \nabla_x g_T^{(1)}) + \\ & \nabla_y \cdot (\bar{E}_T \nabla_y g_T^{(2)}) = \nabla_x \cdot \bar{f}_T^{(0)} + \nabla_y \cdot \bar{f}_T^{(1)} + \bar{L}_{Tt} (g_T^{(0)} - p_T^{(0)}) \quad \text{in } \Omega_T, \end{aligned} \quad (4.35d)$$

$$p_H^{(2)} = p_T^{(2)} \quad \text{on } \Gamma_m, \quad (4.35e)$$

$$g_H^{(2)} = g_T^{(2)} \quad \text{on } \Gamma_m, \quad (4.35f)$$

$$\begin{aligned} & (-\bar{K}_H \nabla_x p_H^{(1)} - \bar{K}_H \nabla_y p_H^{(2)} + f_H^{(1)}) \cdot \mathbf{n} = \\ & (-\bar{K}_T \nabla_x p_T^{(1)} - \bar{K}_T \nabla_y p_T^{(2)} + f_T^{(1)}) \cdot \mathbf{n} \quad \text{on } \Gamma_m, \end{aligned} \quad (4.35g)$$

$$\begin{aligned} & (-\bar{E}_H \nabla_x g_H^{(1)} - \bar{E}_H \nabla_y g_H^{(2)} + \bar{f}_H^{(1)}) \cdot \mathbf{n} = \\ & (-\bar{E}_T \nabla_x g_T^{(1)} - \bar{E}_T \nabla_y g_T^{(2)} + \bar{f}_T^{(1)}) \cdot \mathbf{n} \quad \text{on } \Gamma_m. \end{aligned} \quad (4.35h)$$

Remark. Equations (4.35a)-(4.35d), and (4.35g)-(4.35h) include order one forces $f_{H,T}^{(1)}$, and $\bar{f}_{H,T}^{(1)}$. This is the most general scenario in case the forces also admit a power series representation, which could be the case when they are themselves given as a result of multiscale system of PDEs. However, when the forces are just given functions, it is possible to assume that $f_{H,t} = f_{H,t}^{(0)}$, and $\bar{f}_{H,T} = \bar{f}_{H,T}^{(0)}$ only.

Now, using equations (4.33a)-(4.33h) with boundary conditions (4.33k)-(4.33l) and assuming that $\bar{K}_{H,T}$, and $\bar{E}_{H,T}$ are symmetric positive definite matrices, implies

$$p_H^{(0)} = p_H^{(0)}(\mathbf{x}), \quad (4.36a)$$

$$p_T^{(0)} = p_T^{(0)}(\mathbf{x}), \quad (4.36b)$$

$$g_H^{(0)} = g_H^{(0)}(\mathbf{x}), \quad (4.36c)$$

$$g_T^{(0)} = g_T^{(0)}(\mathbf{x}). \quad (4.36d)$$

The boundary conditions (4.33i)-(4.33j) lead to,

$$p_H^{(0)}(\mathbf{x}) = p_T^{(0)}(\mathbf{x}) = p^{(0)}(\mathbf{x}), \quad (4.37a)$$

$$g_H^{(0)}(\mathbf{x}) = g_T^{(0)}(\mathbf{x}) = g^{(0)}(\mathbf{x}). \quad (4.37b)$$

The periodic cell problem of the first order pressures $p_{H,T}^{(1)}$, and $g_{H,T}^{(1)}$ and leading order velocities $\mathbf{u}_{H,T}^{(0)}$, and $\mathbf{v}_{H,T}^{(0)}$ in mesoscale (4.34a)-(4.34h) and (4.34k)-(4.34l) depend on the leading order of the inhomogeneous magnetic forces $f_{H,T}^{(0)}$, and $\tilde{f}_{H,T}^{(0)}$ and on their gradients $\nabla_y \cdot f_{H,T}^{(0)}$, and $\nabla_y \cdot \tilde{f}_{H,T}^{(0)}$. However, if the force is continuous on the interface Γ_m , then we no longer have the forces terms in (4.34a-4.34d).

In order to prove well-posedness [30] of the periodic problems (4.34a)-(4.34d) supplemented by the interface conditions (4.34i)-(4.34l), we can re-write that system using (4.34e)-(4.34h) as

$$\nabla_y \cdot \mathbf{u}_H^{(0)} = 0 \quad \text{in } \Omega_H, \quad (4.38a)$$

$$\nabla_y \cdot \mathbf{u}_T^{(0)} = 0 \quad \text{in } \Omega_T, \quad (4.38b)$$

$$\nabla_y \cdot \mathbf{v}_H^{(0)} = 0 \quad \text{in } \Omega_H, \quad (4.38c)$$

$$\nabla_y \cdot \mathbf{v}_T^{(0)} = 0 \quad \text{in } \Omega_T, \quad (4.38d)$$

$$\mathbf{u}_H^{(0)} \cdot \mathbf{n} = \mathbf{u}_T^{(0)} \cdot \mathbf{n} \quad \text{on } \Gamma_m, \quad (4.38e)$$

$$\mathbf{v}_H^{(0)} \cdot \mathbf{n} = \mathbf{v}_T^{(0)} \cdot \mathbf{n} \quad \text{on } \Gamma_m. \quad (4.38f)$$

Now, we integrate (4.38a)-(4.38b) over the periodic cell and we sum them. Then, we apply the boundary condition (4.38e), to get

$$\begin{aligned} \int_{\Omega_H} \nabla_y \cdot \mathbf{u}_H^{(0)} dy + \int_{\Omega_T} \nabla_y \cdot \mathbf{u}_T^{(0)} dy &= \int_{\partial\Omega_H} \mathbf{u}_H^{(0)} \cdot \mathbf{n} dS + \int_{\partial\Omega_T} \mathbf{u}_T^{(0)} \cdot \mathbf{n} dS = \\ &= \int_{\partial\Omega_H/\Gamma_m} \mathbf{u}_H^{(0)} \cdot \mathbf{n}_{\partial\Omega_H/\Gamma_m} dS + \int_{\partial\Omega_T/\Gamma_m} \mathbf{u}_T^{(0)} \cdot \mathbf{n}_{\partial\Omega_T/\Gamma_m} dS + \\ &= \int_{\Gamma_m} \mathbf{u}_H^{(0)} \cdot \mathbf{n} dS - \int_{\Gamma_m} \mathbf{u}_T^{(0)} \cdot \mathbf{n} dS = 0, \end{aligned} \quad (4.39)$$

with

$$\mathbf{n}_{\partial\Omega_T} = -\mathbf{n}_{\partial\Omega_H} = -\mathbf{n} \quad \text{on } \Gamma_m. \quad (4.40)$$

Thus proving the compatibility condition.

We have considered in equation (4.39) that the contributions on the periodic boundary $\partial\Omega_H/\Gamma$ canceled out due to \mathbf{y} -periodicity and used interface condition (4.38e).

We do the same steps with (4.38c)-(4.38d) using the boundary condition (4.38f), as follows

$$\begin{aligned}
 \int_{\Omega_H} \nabla_y \cdot \mathbf{v}_H^{(0)} dy + \int_{\Omega_T} \nabla_y \cdot \mathbf{v}_T^{(0)} dy &= \int_{\partial\Omega_H} \mathbf{v}_H^{(0)} \cdot \mathbf{n} dS + \int_{\partial\Omega_T} \mathbf{v}_T^{(0)} \cdot \mathbf{n} dS = \\
 \int_{\partial\Omega_H/\Gamma_m} \mathbf{v}_H^{(0)} \cdot \mathbf{n}_{\partial\Omega_H/\Gamma_m} dS + \int_{\partial\Omega_T/\Gamma_m} \mathbf{v}_T^{(0)} \cdot \mathbf{n}_{\partial\Omega_T/\Gamma_m} dS + \\
 \int_{\Gamma_m} \mathbf{v}_H^{(0)} \cdot \mathbf{n} dS - \int_{\Gamma_m} \mathbf{v}_T^{(0)} \cdot \mathbf{n} dS &= 0.
 \end{aligned} \tag{4.41}$$

The solutions of (4.34a)-(4.34d) with interface conditions (4.34i)-(4.34l) as $\nabla_x p^{(0)}$ and $\nabla_x g^{(0)}$ are \mathbf{y} -constant, can be expressed by linearity as

$$p_H^{(1)} = -\mathbf{m}_H(\mathbf{x}, \mathbf{y}) \cdot \nabla_x p^{(0)} + \tilde{p}_1(\mathbf{x}, \mathbf{y}), \tag{4.42a}$$

$$p_T^{(1)} = -\mathbf{m}_T(\mathbf{x}, \mathbf{y}) \cdot \nabla_x p^{(0)} + \tilde{p}_2(\mathbf{x}, \mathbf{y}), \tag{4.42b}$$

$$g_H^{(1)} = -\mathbf{c}_H(\mathbf{x}, \mathbf{y}) \cdot \nabla_x g^{(0)} + \tilde{g}_1(\mathbf{x}, \mathbf{y}), \tag{4.42c}$$

$$g_T^{(1)} = -\mathbf{c}_T(\mathbf{x}, \mathbf{y}) \cdot \nabla_x g^{(0)} + \tilde{g}_2(\mathbf{x}, \mathbf{y}). \tag{4.42d}$$

Therefore, (4.42a-4.42d) are the solutions of the cell problems (4.34a)-(4.34d) with boundary conditions (4.34i)-(4.34l) provided that the auxiliary vectors \mathbf{m}_H , \mathbf{m}_T , \mathbf{c}_H , and \mathbf{c}_T solve the following system of \mathbf{y} -periodic PDEs

$$\nabla_y \cdot (\nabla_y \mathbf{m}_H \bar{\mathbf{K}}_H^T) = \nabla_y \cdot \bar{\mathbf{K}}_H^T \quad \text{in } \Omega_H, \tag{4.43a}$$

$$\nabla_y \cdot (\nabla_y \mathbf{m}_T \bar{\mathbf{K}}_T^T) = \nabla_y \cdot \bar{\mathbf{K}}_T^T \quad \text{in } \Omega_T, \tag{4.43b}$$

$$\nabla_y \cdot (\nabla_y \mathbf{c}_H \bar{\mathbf{E}}_H^T) = \nabla_y \cdot \bar{\mathbf{E}}_H^T \quad \text{in } \Omega_H, \tag{4.43c}$$

$$\nabla_y \cdot (\nabla_y \mathbf{c}_T \bar{\mathbf{E}}_T^T) = \nabla_y \cdot \bar{\mathbf{E}}_T^T \quad \text{in } \Omega_T, \tag{4.43d}$$

$$(\bar{\mathbf{K}}_T \nabla_y \mathbf{m}_H - \bar{\mathbf{K}}_H \nabla_y \mathbf{m}_T) \cdot \mathbf{n} = (\bar{\mathbf{K}}_H - \bar{\mathbf{K}}_T) \cdot \mathbf{n} \quad \text{on } \Gamma_m, \tag{4.43e}$$

$$(\bar{\mathbf{E}}_T \nabla_y \mathbf{c}_H - \bar{\mathbf{E}}_H \nabla_y \mathbf{c}_T) \cdot \mathbf{n} = (\bar{\mathbf{E}}_H - \bar{\mathbf{E}}_T) \cdot \mathbf{n} \quad \text{on } \Gamma_m, \tag{4.43f}$$

$$\mathbf{m}_H = \mathbf{m}_T \quad \text{on } \Gamma_m, \tag{4.43g}$$

$$\mathbf{c}_H = \mathbf{c}_T \quad \text{on } \Gamma_m, \tag{4.43h}$$

with periodic boundary conditions on $\partial\Omega$.

The cell problems for the auxiliary scalars \tilde{p}_1 , \tilde{p}_2 , \tilde{g}_1 , and \tilde{g}_2 can be written as

$$\nabla_y \cdot (\bar{\mathbf{K}}_H \nabla_y \tilde{p}_1) = \nabla_y \cdot f_H^{(0)} \quad \text{in } \Omega_H, \quad (4.44a)$$

$$\nabla_y \cdot (\bar{\mathbf{K}}_T \nabla_y \tilde{p}_2) = \nabla_y \cdot f_T^{(0)} \quad \text{in } \Omega_T, \quad (4.44b)$$

$$\nabla_y \cdot (\bar{\mathbf{E}}_H \nabla_y \tilde{g}_1) = \nabla_y \cdot \bar{f}_H^{(0)} \quad \text{in } \Omega_H, \quad (4.44c)$$

$$\nabla_y \cdot (\bar{\mathbf{E}}_T \nabla_y \tilde{g}_2) = \nabla_y \cdot \bar{f}_T^{(0)} \quad \text{in } \Omega_T, \quad (4.44d)$$

$$(\bar{\mathbf{K}}_T \nabla_y \tilde{p}_2 - \bar{\mathbf{K}}_H \nabla_y \tilde{p}_1) \cdot \mathbf{n} = (f_T^{(0)} - f_H^{(0)}) \cdot \mathbf{n} \quad \text{on } \Gamma_m, \quad (4.44e)$$

$$(\bar{\mathbf{E}}_T \nabla_y \tilde{g}_2 - \bar{\mathbf{E}}_H \nabla_y \tilde{g}_1) \cdot \mathbf{n} = (\bar{f}_T^{(0)} - \bar{f}_H^{(0)}) \cdot \mathbf{n} \quad \text{on } \Gamma_m, \quad (4.44f)$$

$$\tilde{p}_1 = \tilde{p}_2 \quad \text{on } \Gamma_m, \quad (4.44g)$$

$$\tilde{g}_1 = \tilde{g}_2 \quad \text{on } \Gamma_m. \quad (4.44h)$$

The auxiliary scalars equations (4.44a-4.44h) have solution equal to the solution of auxiliary vectors (4.43a-4.43h) when the external forces are microscopically uniform and continuous across the interface. As such, the problem (4.44a)-(4.44h) is irrelevant in this case.

Now, in order to derive the final macroscale system, we integrate the equations (4.35a)-(4.35d) over the periodic cell which implies

$$\begin{aligned} \nabla_x \cdot \left(\langle \bar{\mathbf{K}}_H \rangle_{\Omega_H} \nabla_x p^{(0)} \right) + \nabla_x \cdot \left\langle \bar{\mathbf{K}}_H \nabla_y p_H^{(1)} \right\rangle_{\Omega_H} - \nabla_x \cdot \left\langle f_H^{(0)} \right\rangle_{\Omega_H} = \\ \bar{L}_{Hv} \left(p^{(0)} - g^{(0)} \right) + \left\langle \nabla_y \left(\bar{\mathbf{K}}_H \nabla_x p_H^{(1)} + \bar{\mathbf{K}}_H \nabla_y p_H^{(2)} + f_H^{(1)} \right) \right\rangle_{\Omega_H} \quad \text{in } \Omega_H, \end{aligned} \quad (4.45a)$$

$$\begin{aligned} \nabla_x \cdot \left(\langle \bar{\mathbf{K}}_T \rangle_{\Omega_T} \nabla_x p^{(0)} \right) + \nabla_x \cdot \left\langle \bar{\mathbf{K}}_T \nabla_y p_T^{(1)} \right\rangle_{\Omega_T} - \nabla_x \cdot \left\langle f_T^{(0)} \right\rangle_{\Omega_T} = \\ \bar{L}_{Tv} \left(p^{(0)} - g^{(0)} \right) + \left\langle \nabla_y \left(\bar{\mathbf{K}}_T \nabla_x p_T^{(1)} + \bar{\mathbf{K}}_T \nabla_y p_T^{(2)} + f_T^{(1)} \right) \right\rangle_{\Omega_T} \quad \text{in } \Omega_T, \end{aligned} \quad (4.45b)$$

$$\begin{aligned} \nabla_x \cdot \left(\langle \bar{\mathbf{E}}_H \rangle_{\Omega_H} \nabla_x g^{(0)} \right) + \nabla_x \cdot \left\langle \bar{\mathbf{E}}_H \nabla_y g_H^{(1)} \right\rangle_{\Omega_H} - \nabla_x \cdot \left\langle \bar{f}_H^{(0)} \right\rangle_{\Omega_H} = \\ \bar{L}_{Ht} \left(g^{(0)} - p^{(0)} \right) + \left\langle \nabla_y \left(\bar{\mathbf{E}}_H \nabla_x g_H^{(1)} + \bar{\mathbf{E}}_H \nabla_y g_H^{(2)} + \bar{f}_H^{(1)} \right) \right\rangle_{\Omega_H} \quad \text{in } \Omega_H, \end{aligned} \quad (4.45c)$$

$$\begin{aligned} \nabla_x \cdot \left(\langle \bar{\mathbf{E}}_T \rangle_{\Omega_T} \nabla_x g^{(0)} \right) + \nabla_x \cdot \left\langle \bar{\mathbf{E}}_T \nabla_y g_T^{(1)} \right\rangle_{\Omega_T} - \nabla_x \cdot \left\langle \bar{f}_T^{(0)} \right\rangle_{\Omega_T} = \\ \bar{L}_{Tt} \left(g^{(0)} - p^{(0)} \right) + \left\langle \nabla_y \left(\bar{\mathbf{E}}_T \nabla_x g_T^{(1)} + \bar{\mathbf{E}}_T \nabla_y g_T^{(2)} + \bar{f}_T^{(1)} \right) \right\rangle_{\Omega_T} \quad \text{in } \Omega_T. \end{aligned} \quad (4.45d)$$

Summing equations (4.45a) with (4.45b) and equations (4.45c) with (4.45d) together, and make the use of the interface conditions (4.35g-4.35h) as well as applying the divergence theorem with

respect to \mathbf{y} lead to

$$\begin{aligned} & \nabla_x \cdot \left(\left(\langle \bar{\mathbf{K}}_H \rangle_{\Omega_H} + \langle \bar{\mathbf{K}}_T \rangle_{\Omega_T} \right) \nabla_x p^{(0)} \right) + \nabla_x \cdot \left\langle \bar{\mathbf{K}}_H \nabla_y p_H^{(1)} \right\rangle_{\Omega_H} + \nabla_x \cdot \left\langle \bar{\mathbf{K}}_T \nabla_y p_T^{(1)} \right\rangle_{\Omega_T} \\ & = \nabla_x \cdot \langle f_H^{(0)} \rangle_{\Omega_H} + \nabla_x \cdot \langle f_T^{(0)} \rangle_{\Omega_T} + (\bar{L}_{Hv} + \bar{L}_{Tv}) \left(p^{(0)} - g^{(0)} \right), \end{aligned} \quad (4.46a)$$

$$\begin{aligned} & \nabla_x \cdot \left(\left(\langle \bar{\mathbf{E}}_H \rangle_{\Omega_H} + \langle \bar{\mathbf{E}}_T \rangle_{\Omega_T} \right) \nabla_x g^{(0)} \right) + \nabla_x \cdot \left\langle \bar{\mathbf{E}}_H \nabla_y g_H^{(1)} \right\rangle_{\Omega_H} + \nabla_x \cdot \left\langle \bar{\mathbf{E}}_T \nabla_y g_T^{(1)} \right\rangle_{\Omega_T} \\ & = \nabla_x \cdot \langle \bar{f}_H^{(0)} \rangle_{\Omega_H} + \nabla_x \cdot \langle \bar{f}_T^{(0)} \rangle_{\Omega_T} + (\bar{L}_{Ht} + \bar{L}_{Tt}) \left(g^{(0)} - p^{(0)} \right). \end{aligned} \quad (4.46b)$$

Substituting (4.42a)- (4.42d) in the system, yields

$$\begin{aligned} & \nabla_x \cdot \left(\left(\langle \bar{\mathbf{K}}_H \rangle_{\Omega_H} + \langle \bar{\mathbf{K}}_T \rangle_{\Omega_T} - \langle \bar{\mathbf{K}}_H (\nabla_y \mathbf{m}_H)^T \rangle_{\Omega_H} - \langle \bar{\mathbf{K}}_T (\nabla_y \mathbf{m}_T)^T \rangle_{\Omega_T} \right) \nabla_x p^{(0)} \right) = \\ & \nabla_x \cdot \langle f_H^{(0)} \rangle_{\Omega_H} + \nabla_x \cdot \langle f_T^{(0)} \rangle_{\Omega_T} - \nabla_x \cdot \langle \bar{\mathbf{K}}_H \nabla_y \tilde{p}_1 \rangle_{\Omega_H} - \nabla_x \cdot \langle \bar{\mathbf{K}}_T \nabla_y \tilde{p}_2 \rangle_{\Omega_T} + \\ & (\bar{L}_{Hv} + \bar{L}_{Tv}) \left(p^{(0)} - g^{(0)} \right), \end{aligned} \quad (4.47a)$$

$$\begin{aligned} & \nabla_x \cdot \left(\left(\langle \bar{\mathbf{E}}_H \rangle_{\Omega_H} + \langle \bar{\mathbf{E}}_T \rangle_{\Omega_T} - \langle \bar{\mathbf{E}}_H (\nabla_y \mathbf{c}_H)^T \rangle_{\Omega_H} - \langle \bar{\mathbf{E}}_T (\nabla_y \mathbf{c}_T)^T \rangle_{\Omega_T} \right) \nabla_x g^{(0)} \right) = \\ & \nabla_x \cdot \langle \bar{f}_H^{(0)} \rangle_{\Omega_H} + \nabla_x \cdot \langle \bar{f}_T^{(0)} \rangle_{\Omega_T} - \nabla_x \cdot \langle \bar{\mathbf{E}}_H \nabla_y \tilde{g}_1 \rangle_{\Omega_H} - \nabla_x \cdot \langle \bar{\mathbf{E}}_T \nabla_y \tilde{g}_2 \rangle_{\Omega_T} \\ & + (\bar{L}_{Ht} + \bar{L}_{Tt}) \left(g^{(0)} - p^{(0)} \right). \end{aligned} \quad (4.47b)$$

These equations can be written as

$$\nabla_x \cdot \left(\bar{\mathbf{D}} \nabla_x p^{(0)} \right) = \bar{F}_1 + (\bar{L}_{Hv} + \bar{L}_{Tv}) \left(p^{(0)} - g^{(0)} \right), \quad (4.48a)$$

$$\nabla_x \cdot \left(\bar{\mathbf{G}} \nabla_x g^{(0)} \right) = \bar{F}_2 + (\bar{L}_{Ht} + \bar{L}_{Tt}) \left(g^{(0)} - p^{(0)} \right), \quad (4.48b)$$

where

$$\bar{\mathbf{D}} = \langle \bar{\mathbf{K}}_H \rangle_{\Omega_H} + \langle \bar{\mathbf{K}}_T \rangle_{\Omega_T} - \langle \bar{\mathbf{K}}_H (\nabla_y \mathbf{m}_H)^T \rangle_{\Omega_H} - \langle \bar{\mathbf{K}}_T (\nabla_y \mathbf{m}_T)^T \rangle_{\Omega_T}, \quad (4.49a)$$

$$\bar{\mathbf{G}} = \langle \bar{\mathbf{E}}_H \rangle_{\Omega_H} + \langle \bar{\mathbf{E}}_T \rangle_{\Omega_T} - \langle \bar{\mathbf{E}}_H (\nabla_y \mathbf{c}_H)^T \rangle_{\Omega_H} - \langle \bar{\mathbf{E}}_T (\nabla_y \mathbf{c}_T)^T \rangle_{\Omega_T}, \quad (4.49b)$$

$$\bar{F}_1 = \nabla_x \cdot \langle f_H^{(0)} \rangle_{\Omega_H} + \nabla_x \cdot \langle f_T^{(0)} \rangle_{\Omega_T} - \nabla_x \cdot \langle \bar{\mathbf{K}}_H \nabla_y \tilde{p}_1 \rangle_{\Omega_H} - \nabla_x \cdot \langle \bar{\mathbf{K}}_T \nabla_y \tilde{p}_2 \rangle_{\Omega_T}, \quad (4.49c)$$

$$\bar{F}_2 = \nabla_x \cdot \langle \bar{f}_H^{(0)} \rangle_{\Omega_H} + \nabla_x \cdot \langle \bar{f}_T^{(0)} \rangle_{\Omega_T} - \nabla_x \cdot \langle \bar{\mathbf{E}}_H \nabla_y \tilde{g}_1 \rangle_{\Omega_H} - \nabla_x \cdot \langle \bar{\mathbf{E}}_T \nabla_y \tilde{g}_2 \rangle_{\Omega_T}. \quad (4.49d)$$

Equations (4.48a) and (4.48b) are the macroscale differential equations in terms of the leading order pressures. We have started with four differential equations at mesoscale representing the fluid flow in the vessels and interstitial compartments for the tumour and healthy domains. After having applied the asymptotic homogenisation technique, we obtain two differential equations at macroscale which encode the role of both regions and take the form of a double Darcy's fluid transport model with mass exchange between vessels and interstitial compartment mediated by an average vessels' permeability and driven by appropriate volume loads. On the one hand,

it is no longer necessary to resolve the geometrical difference between cancerous and healthy region to solve the macroscale model. On the other hand, the influence of the mesoscale where such differences are relevant, is encoded in the effective hydraulic conductivity tensors (4.49a)-(4.49d) which can be determined using (4.43a-4.43h), and (4.44a-4.44h). In particular, the role of geometric configuration and relative volume fraction of the healthy and tumour domains can be investigated by solely focusing on a single periodic cell rather than on the whole domain. Moreover, herein the magnetic forces $f_{H,T}$, and $\bar{f}_{H,T}$ are incorporating the mesoscale and macroscale contributions. If they are defined with $\bar{K}_{H,T}$, and $\bar{E}_{H,T}$ in mesoscale only which means that they are \mathbf{y} -dependent only, then \bar{F}_1 and \bar{F}_2 will reduce to zero. In this case, the final macroscale differential equations for the fluid flow using homogeneous body forces are written as,

$$\nabla_x \cdot (\bar{D} \nabla_x p^{(0)}) = (\bar{L}_{Hv} + \bar{L}_{Tv}) (p^{(0)} - g^{(0)}), \quad (4.50a)$$

$$\nabla_x \cdot (\bar{G} \nabla_x g^{(0)}) = (\bar{L}_{Ht} + \bar{L}_{Tt}) (g^{(0)} - p^{(0)}). \quad (4.50b)$$

To find the leading order velocities, we integrate (4.34e)-(4.34h) and substitute the ansatz for the order one pressures (4.42a)-(4.42d). Then we take the sum of (4.34e) with (4.34f), and (4.34g) with (4.34h) to obtain

$$\begin{aligned} \langle \mathbf{u}_H^{(0)} \rangle_{\Omega_H} + \langle \mathbf{u}_T^{(0)} \rangle_{\Omega_T} &= -\langle \bar{K}_H \rangle_{\Omega_H} \nabla_x p^{(0)} + \langle \bar{K}_H \left((\nabla_y \mathbf{m}_H) \nabla_x p^{(0)} \right) \rangle_{\Omega_H} - \\ &\langle \bar{K}_H (\nabla_y \tilde{p}_1) \rangle_{\Omega_H} + \langle f_H^{(0)} \rangle_{\Omega_H} - \langle \bar{K}_T \rangle_{\Omega_T} \nabla_x p^{(0)} + \langle \bar{K}_T \left((\nabla_y \mathbf{m}_T) \nabla_x p^{(0)} \right) \rangle_{\Omega_T} - \\ &\langle \bar{K}_T (\nabla_y \tilde{p}_2) \rangle_{\Omega_T} + \langle f_T^{(0)} \rangle_{\Omega_T}, \end{aligned} \quad (4.51a)$$

$$\begin{aligned} \langle \mathbf{v}_H^{(0)} \rangle_{\Omega_H} + \langle \mathbf{v}_T^{(0)} \rangle_{\Omega_T} &= -\langle \bar{E}_H \rangle_{\Omega_H} \nabla_x g^{(0)} + \langle \bar{E}_H \left((\nabla_y \mathbf{c}_H) \nabla_x g^{(0)} \right) \rangle_{\Omega_H} - \\ &\langle \bar{E}_H (\nabla_y \tilde{g}_1) \rangle_{\Omega_H} + \langle \bar{f}_H^{(0)} \rangle_{\Omega_H} - \langle \bar{E}_T \rangle_{\Omega_T} \nabla_x g^{(0)} + \langle \bar{E}_T \left((\nabla_y \mathbf{c}_T) \nabla_x g^{(0)} \right) \rangle_{\Omega_T} - \\ &\langle \bar{E}_T (\nabla_y \tilde{g}_2) \rangle_{\Omega_T} + \langle \bar{f}_T^{(0)} \rangle_{\Omega_T}. \end{aligned} \quad (4.51b)$$

These imply

$$\langle \mathbf{u}_H^{(0)} \rangle_{\Omega_H} + \langle \mathbf{u}_T^{(0)} \rangle_{\Omega_T} = \mathbf{u}_A = -\bar{D} \nabla_x p^{(0)} + \tilde{F}_p, \quad (4.52a)$$

$$\langle \mathbf{v}_H^{(0)} \rangle_{\Omega_H} + \langle \mathbf{v}_T^{(0)} \rangle_{\Omega_T} = \mathbf{v}_A = -\bar{G} \nabla_x g^{(0)} + \tilde{F}_g, \quad (4.52b)$$

where

$$\tilde{F}_p = \langle f_H^{(0)} \rangle_{\Omega_H} + \langle f_T^{(0)} \rangle_{\Omega_T} - \langle \bar{K}_H (\nabla_y \tilde{p}_1) \rangle_{\Omega_H} - \langle \bar{K}_T (\nabla_y \tilde{p}_2) \rangle_{\Omega_T}, \quad (4.53a)$$

$$\tilde{F}_g = \langle \bar{f}_H^{(0)} \rangle_{\Omega_H} + \langle \bar{f}_T^{(0)} \rangle_{\Omega_T} - \langle \bar{E}_H (\nabla_y \tilde{g}_1) \rangle_{\Omega_H} - \langle \bar{E}_T (\nabla_y \tilde{g}_2) \rangle_{\Omega_T}. \quad (4.53b)$$

These equations show that the magnetic forces at macroscale depend on the magnetic forces and the hydraulic conductivity at mesoscale.

By taking the gradient of (4.52a), and (4.52b) and substituting (4.48a)-(4.48b), and (4.49c)-(4.49d), implies

$$\nabla_x \cdot \tilde{F}_p = \bar{F}_1, \quad (4.54a)$$

$$\nabla_x \cdot \tilde{F}_g = \bar{F}_2, \quad (4.54b)$$

$$\nabla_x \cdot \mathbf{u}_A = -(\bar{L}_{Hv} + \bar{L}_{Tv}) \left(p^{(0)} - g^{(0)} \right), \quad (4.54c)$$

$$\nabla_x \cdot \mathbf{v}_A = -(\bar{L}_{Ht} + \bar{L}_{Tt}) \left(g^{(0)} - p^{(0)} \right). \quad (4.54d)$$

This shows that equations (4.48a), and (4.48b) obey Darcy's law at macroscale. Moreover, whenever the forces $f_{H,T}^{(0)}$, and $\tilde{f}_{H,T}^{(0)}$ are defined at mesoscale only or macroscale only, then \tilde{F}_p , and \tilde{F}_g will not reduce to zero so the average leading order velocities (4.52a) and (4.52b) will of course be affected also by homogeneous and in particular constant volume forces.

In the next sections, we aim to find the solution of the macroscale model in the simplified case of a uniform applied force.

4.6 The solution of the mesoscale cell problems

In order to solve the final PDE system at the macroscale with homogeneous magnetic forces (4.50a-4.50b), we need to find the effective tensors \bar{D} , and \bar{G} by solving the cell problems (4.43a)-(4.43d), with boundary conditions (4.43e)-(4.43h). In the case of uniform magnetic force, the gradient of the homogeneous forces in the right hand side of the auxiliary scalars cell problems (4.44a-4.44h) approach zero. Therefore, the auxiliary scalars \tilde{p}_1 , \tilde{p}_2 , \tilde{g}_1 , and \tilde{g}_2 are defined as

$$\nabla_y \cdot (\bar{K}_H \nabla_y \tilde{p}_1) = 0 \quad \text{in } \Omega_H, \quad (4.55a)$$

$$\nabla_y \cdot (\bar{K}_T \nabla_y \tilde{p}_2) = 0 \quad \text{in } \Omega_T, \quad (4.55b)$$

$$\nabla_y \cdot (\bar{E}_H \nabla_y \tilde{g}_1) = 0 \quad \text{in } \Omega_H, \quad (4.55c)$$

$$\nabla_y \cdot (\bar{E}_T \nabla_y \tilde{g}_2) = 0 \quad \text{in } \Omega_T, \quad (4.55d)$$

$$(\bar{K}_T \nabla_y \tilde{p}_2 - \bar{K}_H \nabla_y \tilde{p}_1) \cdot \mathbf{n} = \left((\bar{K}_H - \bar{K}_T) \hat{f} \right) \cdot \mathbf{n} \quad \text{on } \Gamma_m, \quad (4.55e)$$

$$(\bar{E}_T \nabla_y \tilde{g}_2 - \bar{E}_H \nabla_y \tilde{g}_1) \cdot \mathbf{n} = \left((\bar{E}_H - \bar{E}_T) \hat{f} \right) \cdot \mathbf{n} \quad \text{on } \Gamma_m, \quad (4.55f)$$

$$\tilde{p}_1 = \tilde{p}_2 \quad \text{on } \Gamma_m, \quad (4.55g)$$

$$\tilde{g}_1 = \tilde{g}_2 \quad \text{on } \Gamma_m. \quad (4.55h)$$

Table 4.1: The value of the parameters.

Symbol	Parameter	Value	Unite	Reference
K_H	The hydraulic conductivity of the healthy vessel	2.2×10^{-4}	$\text{m}^2/\text{Pa s}$	[103]
K_T	The hydraulic conductivity of the tumour vessel	4.8×10^{-6}	$\text{m}^2/\text{Pa s}$	[103]
κ_H	The hydraulic conductivity of the healthy tissue	6.4×10^{-12}	$\text{m}^2/\text{Pa s}$	[152]
κ_T	The hydraulic conductivity of the tumour tissue	3.1×10^{-12}	$\text{m}^2/\text{Pa s}$	[152]
L_H	The hydraulic vessels' permeability of healthy region	2.7×10^{-12}	$\text{m}/\text{Pa s}$	[123]
L_T	The hydraulic vessels' permeability of tumour region	2.1×10^{-11}	$\text{m}/\text{Pa s}$	[123]
μ	The blood viscosity	4×10^{-4}	Pa s	[3]
$ \Omega_{Hv} $	Domain of healthy vessels	8.1×10^{-2}		[103]
$ \Omega_{Ht} $	Domain of tumour vessels	6.5×10^{-2}		[103]
$ \Omega_{Ht} $	Domain of healthy interstitium	6.165		[103]
$ \Omega_{Tt} $	Domain of tumour interstitium	6.165		[103]
S_H	The healthy vessels' surface	2.30		[103]
S_T	The tumour vessels' surface	3.25		[103]

Here, we have assumed that the applied forces are uniform and equal in the whole tissue as such $\hat{f}_h = \hat{f}_t = \hat{f}$. The system of equations (4.55a-4.55h) can be solve by defining the scalars \tilde{p}_1 , \tilde{p}_2 , \tilde{g}_1 , and \tilde{g}_2 in term of the vector function \hat{f} as

$$\tilde{p}_1 = \mathbf{r}_1 \cdot \hat{f}, \quad (4.56a)$$

$$\tilde{p}_2 = \mathbf{r}_2 \cdot \hat{f}, \quad (4.56b)$$

$$\tilde{g}_1 = \mathbf{s}_1 \cdot \hat{f}, \quad (4.56c)$$

$$\tilde{g}_2 = \mathbf{s}_2 \cdot \hat{f}. \quad (4.56d)$$

Substituting equations (4.56a)-(4.56d) in the system of equations (4.55a-4.55h) leads to the system for \mathbf{m}_H , \mathbf{m}_T , \mathbf{c}_H , and \mathbf{c}_T equations which is given by

$$\nabla_y \cdot (\nabla_y \mathbf{m}_H \bar{K}_H^T) = 0 \quad \text{in } \Omega_H, \quad (4.57a)$$

$$\nabla_y \cdot (\nabla_y \mathbf{m}_T \bar{K}_T^T) = 0 \quad \text{in } \Omega_T, \quad (4.57b)$$

$$\nabla_y \cdot (\nabla_y \mathbf{c}_H \bar{E}_H^T) = 0 \quad \text{in } \Omega_H, \quad (4.57c)$$

$$\nabla_y \cdot (\nabla_y \mathbf{c}_T \bar{E}_T^T) = 0 \quad \text{in } \Omega_T, \quad (4.57d)$$

$$(\bar{K}_T \nabla_y \mathbf{m}_T - \bar{K}_H \nabla_y \mathbf{m}_H) \cdot \mathbf{n} = (\bar{K}_H - \bar{K}_T) \cdot \mathbf{n} \quad \text{on } \Gamma_m, \quad (4.57e)$$

$$(\bar{E}_T \nabla_y \mathbf{c}_T - \bar{E}_H \nabla_y \mathbf{c}_H) \cdot \mathbf{n} = (\bar{E}_H - \bar{E}_T) \cdot \mathbf{n} \quad \text{on } \Gamma_m, \quad (4.57f)$$

$$\mathbf{m}_H = \mathbf{m}_T \quad \text{on } \Gamma_m, \quad (4.57g)$$

$$\mathbf{c}_H = \mathbf{c}_T \quad \text{on } \Gamma_m, \quad (4.57h)$$

supplemented by periodic conditions on the boundary of the cell $\partial\Omega$. As such, we can identify the vectors \mathbf{r}_1 , \mathbf{r}_2 , \mathbf{s}_1 , and \mathbf{s}_2 with \mathbf{m}_H , \mathbf{m}_T , \mathbf{c}_H , and \mathbf{c}_T , respectively. Also, the hydraulic conductivities \bar{K}_H , \bar{K}_T , \bar{E}_H , \bar{E}_T are assumed to be constants and defined using Table 4.1, and with E_H , and E_T are approximately 1 as found by Penta and Ambrosi [103].

The cell problems (4.57a)-(4.57d) with boundary conditions (4.57e)-(4.57h) can be written in component-wise as:

$$\frac{\partial}{\partial y_i} \left(\bar{K}_{il}^H \frac{\partial m_j^H}{\partial y_l} \right) = 0 \quad \text{in } \Omega_H, \quad (4.58a)$$

$$\frac{\partial}{\partial y_i} \left(\bar{K}_{il}^T \frac{\partial m_j^T}{\partial y_l} \right) = 0 \quad \text{in } \Omega_T, \quad (4.58b)$$

$$\frac{\partial}{\partial y_i} \left(\bar{E}_{il}^H \frac{\partial c_j^H}{\partial y_l} \right) = 0 \quad \text{in } \Omega_H, \quad (4.58c)$$

$$\frac{\partial}{\partial y_i} \left(\bar{E}_{il}^T \frac{\partial c_j^T}{\partial y_l} \right) = 0 \quad \text{in } \Omega_T, \quad (4.58d)$$

$$\left(\bar{K}_{il}^T \frac{\partial m_j^T}{\partial y_l} - \bar{K}_{il}^H \frac{\partial m_j^H}{\partial y_l} \right) n_i = (\bar{K}_{ij}^H - \bar{K}_{ij}^T) n_i = (\bar{K}_H - \bar{K}_T) n_j \quad \text{on } \Gamma_m, \quad (4.58e)$$

$$\left(\bar{E}_{il}^T \frac{\partial c_j^T}{\partial y_l} - \bar{E}_{il}^H \frac{\partial c_j^H}{\partial y_l} \right) n_i = (\bar{E}_{ij}^H - \bar{E}_{ij}^T) n_i = (\bar{E}_H - \bar{E}_T) n_j \quad \text{on } \Gamma_m, \quad (4.58f)$$

$$m_j^H = m_j^T \quad \text{on } \Gamma_m, \quad (4.58g)$$

$$c_j^H = c_j^T \quad \text{on } \Gamma_m, \quad (4.58h)$$

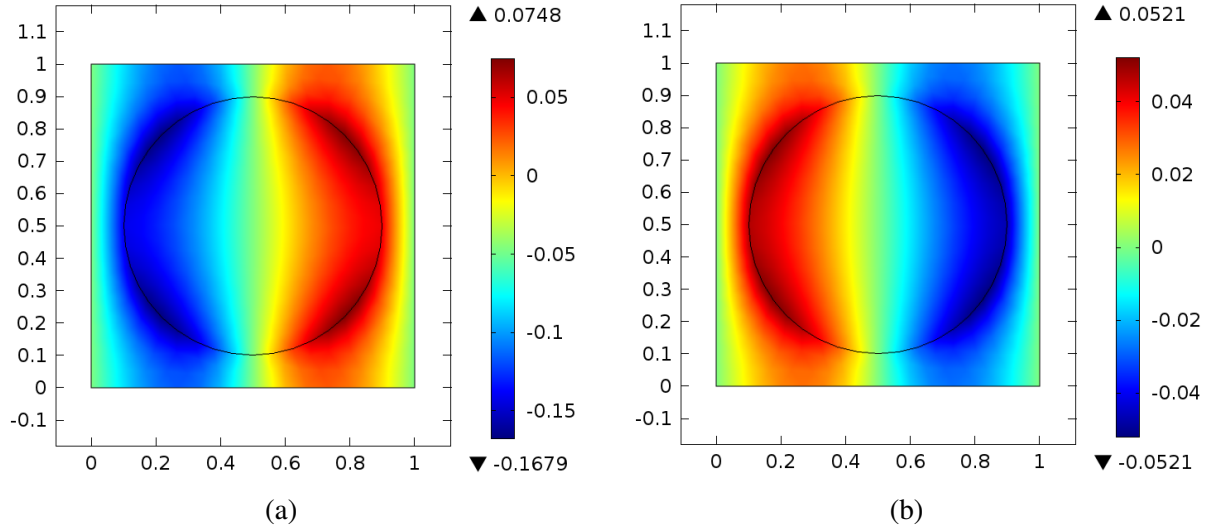


Figure 4.2: The solution of the auxiliary vectors at the mesoscale. (a) The solution of the auxiliary vectors \mathbf{m}_H , and \mathbf{m}_T for n_1 component, (b) The solution of the auxiliary vectors \mathbf{c}_H , and \mathbf{c}_T for n_1 component. In all cases, the radius of the tumour is 0.5. The values of the parameters that are used to plot the figures are taken from Table 4.1.

where $i, j, l = 1..3$ are the size of dimensional space.

In Equations (4.58e-4.58f), the hydraulic tensors \bar{K}_{ij}^H , \bar{K}_{ij}^T , \bar{E}_{ij}^H , and \bar{E}_{ij}^T are assumed to be isotropic. To solve the system (4.58a-4.58h), we consider the healthy cell as a cube with cylindrical fiber in the middle that represents the tumour region as done by Franks et al. [49]. The component of the normal vector in the z-direction (which is the one aligned with the cylindrical fiber) is zero, therefore we can solve the cell problems in the plane which is orthogonal to the fiber direction. The differential problem (4.58a-4.58h) translates into two scalar differential problems for $j = 1$ and $j = 2$. In the simplest possible case, the 2D can be represented by a circle with radius $0 < r < 1$ (tumour region) inside a square with length equal one (healthy region). The boundary of the circle is the interface between the two regions and it is represented by Γ_m .

The solutions of the system (4.58a-4.58d), with boundary conditions (4.58e-4.58h) and periodic conditions are given in Figure 4.2.

We can have variation of the vertical and horizontal colors depends on the normal vector component which is either n_1 or n_2 in the two dimensions.

4.7 The homogenised solution at the macroscale

Now, we solve the macroscale differential equations (4.50a-4.50b), and (4.52a-4.52b) to find the vessels' and interstitial pressures and velocities with uniform magnetic force. The homogeneous magnetic force does not affect the fluid pressures in both of the compartments as mentioned in Section 4.5.1, but it has an impact on the fluid velocity. The definition of the forces \tilde{F}_p , and \tilde{F}_g

in equations (4.52a-4.52b) can be written as

$$\begin{aligned} \tilde{F}_p = & -\langle \bar{K}_H \hat{f}^{(0)} \rangle_{\Omega_H} - \langle \bar{K}_T \hat{f}^{(0)} \rangle_{\Omega_T} - \langle \bar{K}_H (\nabla \mathbf{m}_H)^T \hat{f}^{(0)} \rangle_{\Omega_H} - \\ & \langle \bar{K}_T (\nabla \mathbf{m}_T)^T \hat{f}^{(0)} \rangle_{\Omega_T}, \end{aligned} \quad (4.59a)$$

$$\begin{aligned} \tilde{F}_g = & -\langle \bar{E}_H \hat{f}^{(0)} \rangle_{\Omega_H} - \langle \bar{E}_T \hat{f}^{(0)} \rangle_{\Omega_T} - \langle \bar{E}_H (\nabla \mathbf{c}_H)^T \hat{f}^{(0)} \rangle_{\Omega_H} - \\ & \langle \bar{E}_T (\nabla \mathbf{c}_T)^T \hat{f}^{(0)} \rangle_{\Omega_T}. \end{aligned} \quad (4.59b)$$

Therefore, the forces \tilde{F}_p , and \tilde{F}_g are defined as

$$\tilde{F}_p = -\bar{D} \hat{f}^{(0)}, \quad (4.60a)$$

$$\tilde{F}_g = -\bar{G} \hat{f}^{(0)}. \quad (4.60b)$$

The differential equations (4.50a-4.50b), (4.52a-4.52b), and (4.60a-4.60b) rely on the values of the hydraulic tensors \bar{D} , and \bar{G} which can be found using the solution of the cell problems (4.57a-4.57h) as found in the previous section and equations (4.49a)-(4.49b). Therefore, the hydraulic conductivity tensors \bar{D} , and \bar{G} are computed as

$$\begin{aligned} \bar{D} = & \frac{1}{|\Omega|} \int_{\Omega_H} \bar{K}_H d\mathbf{y} + \frac{1}{|\Omega|} \int_{\Omega_T} \bar{K}_T d\mathbf{y} - \frac{1}{|\Omega|} \int_{\Omega_H} \bar{K}_H (\nabla_y \mathbf{m}_H)^T d\mathbf{y} - \\ & \frac{1}{|\Omega|} \int_{\Omega_T} \bar{K}_H (\nabla_y \mathbf{m}_T)^T d\mathbf{y}, \end{aligned} \quad (4.61a)$$

$$\begin{aligned} \bar{G} = & \frac{1}{|\Omega|} \int_{\Omega_H} \bar{E}_H d\mathbf{y} + \frac{1}{|\Omega|} \int_{\Omega_T} \bar{E}_T d\mathbf{y} - \frac{1}{|\Omega|} \int_{\Omega_H} \bar{E}_H (\nabla_y \mathbf{c}_H)^T d\mathbf{y} - \\ & \frac{1}{|\Omega|} \int_{\Omega_T} \bar{E}_H (\nabla_y \mathbf{c}_T)^T d\mathbf{y}. \end{aligned} \quad (4.61b)$$

Since \bar{K}_H , \bar{K}_T , \bar{E}_H , and \bar{E}_T and constants, then equations (4.61a) and (4.61b) read

$$\bar{D} = \bar{K}_H(|\Omega_H|) + \bar{K}_T(|\Omega_T|) - \bar{K}_H \int_{\Omega_H} \nabla_y \mathbf{m}_H d\mathbf{y} - \bar{K}_T \int_{\Omega_T} \nabla_y \mathbf{m}_T d\mathbf{y}, \quad (4.62a)$$

$$\bar{G} = \bar{E}_H(|\Omega_H|) + \bar{E}_T(|\Omega_T|) - \bar{E}_H \int_{\Omega_H} \nabla_y \mathbf{c}_H d\mathbf{y} - \bar{E}_T \int_{\Omega_T} \nabla_y \mathbf{c}_T d\mathbf{y}. \quad (4.62b)$$

Here, $|\Omega| = |\Omega_H| + |\Omega_T| = 1$.

The integral of the vectors' gradients are computed using the solution of the cell problems (4.57a-4.57h). Also, changing the radius of the tumour leads to different values of auxiliary vectors which consequently changes the value of the hydraulic conductivity tensors \bar{D} and \bar{G} and that shows the impact of mesoscale on the macroscale.

Table 4.2 displays the values of \bar{D} , and \bar{G} in three axis. We can notice that the values of the hydraulic tensors in the x - and y -axis are similar, where the z -axis has different values. This is due to the cell problems at mesoscale which are computed in two dimensions only. Therefore,

the values of hydraulic tensors in z-axis with different tumour area are found using

$$\bar{D}_{z-axis} = \langle \bar{K}_H \rangle_{\Omega_H} + \langle \bar{K}_T \rangle_{\Omega_T}, \quad (4.63a)$$

$$\bar{G}_{z-axis} = \langle \bar{E}_H \rangle_{\Omega_H} + \langle \bar{E}_T \rangle_{\Omega_T}. \quad (4.63b)$$

Thereafter, the values of the hydraulic tensors \bar{D} , and \bar{G} are injected in the differential equations (4.50a-4.50b).

Table 4.2: The components of the vessels and interstitial hydraulic conductivities \bar{D} , and \bar{G} for the whole tissue which combines the tumour and healthy tissues along x, y, and z.

Area of the tumour	\bar{D} in x and y	\bar{D} in z	\bar{G} in x and y	\bar{G} in z
0.5	1.49×10^{-4}	1.124×10^{-4}	1.80×10^{-6}	1.90×10^{-6}
0.4	1.704×10^{-4}	1.34×10^{-4}	1.94×10^{-6}	2.03×10^{-6}
0.3	1.89×10^{-4}	1.55×10^{-4}	2.078×10^{-6}	2.164×10^{-6}
0.2	2.04×10^{-4}	1.77×10^{-4}	2.23×10^{-6}	2.30×10^{-6}
0.1	2.15×10^{-4}	1.98×10^{-4}	2.39×10^{-6}	2.43×10^{-6}

Now to solve the differential equations (4.50a-4.50b), we represented the whole tissue at macroscale as a sphere with a spherical necrotic core ($r = 0.05$) at the center of the whole region. This means that the macroscale domain equations are solved for a normalised radius r between 0.05 and 1. The differential equations (4.50a-4.50b) are supplemented by zero flux at the center, and with arterial pressure equal to 15.6 mmHg [123, 131] and zero interstitial pressure on the boundary of the tumour. Furthermore, we assume that the uniform magnetic force is applied in the z -direction of the whole tissue and its magnitude is proportional to the total amount of magnetic nanoparticles and their susceptibility. Therefore, the magnetic force is computed using Hoshino et al. [64]

$$F_{mag} = N \frac{4\pi R_f^3}{3} \frac{\delta\chi_f}{2\mu_0} \nabla H_0^2, \quad (4.64)$$

where R_f is the radius of the magnetic nanoparticles, $\delta\chi_f = 5$ (SI) is the susceptibility of magnetic nanoparticles, H_0 is the magnetic field intensity and the value of ∇H_0^2 is within the range (10-70) T²/m, N is the number of magnetic nanoparticles, and the magnetic permeability $\mu_0 = 4\pi \times 10^{-7}$ T·m·A⁻¹.

The force in the present work is the magnetic force per unit cell volume which is equal to $1.99 \times 10^7 - 1.39 \times 10^8$ Pa/m within the range of ∇H_0^2 using equation (4.64).

We use the finite elements software COMSOL Multiphysics to solve the problem (4.50a-4.50b) with the conditions that are mentioned before. Using the pressures' solution, we compute the velocities using equations (4.52a-4.52b), and (4.60a-4.60b). Figure 4.3 shows the pressures and

fluid flow direction (arrow lines) of the vessel and interstitial compartments, and the difference of the pressures at the macroscale with different tumour sizes.

Jain and Baxter [69] investigated the interstitial fluid pressure and the velocity of the spherical tumour embedded in healthy tissue using Darcy's equation and the results were confirmed experimentally by Boucher et al. [15]. Jain and Baxter [69] declared that the interstitial fluid pressure of the tumour (IFP) is higher in the center when comparing it with the periphery of the tumour. High IFP of the tumour leads to the non uniform extravasation of the fluid between the tumour and the vessels. Also, the interstitial pressure on the tumour periphery is approximately equal to the healthy tissue and this cause a reduced fluid convection within the tumour. At the same time, the fluid is moving from the center to the periphery, thus transporting tumour growth factors which can lead to metastasis. For cancer treatment, we need the IFP to decline in order to improve the fluid convection within the tumour. Jain and Baxter [69] showed that decreasing tumour radius or increasing the tissue hydraulic conductivity, yield to better convection of the fluid. However, increasing the vessels' permeability damps the pressure gradient on the vessels' wall and that will decrease the convection within the tumour. The permeability \bar{L}_T can be increased by increasing the vessels' surface S or increasing the radius of the vessels pores.

In the present work, we have both the tumour and the healthy tissues homogenized in one spherical region in the macroscale with a small necrotic core. However, the influence of each region is encoded in different parameters like the vessels' permeability \bar{L}_H and \bar{L}_T , the magnetic forces \tilde{F}_p and \tilde{F}_g , and the hydraulic conductivities \bar{D} and \bar{G} which are determined using the solutions of the differential equations at the mesoscale. The results of the interstitial fluid pressure and velocity shown in Figure 4.3 are qualitatively in agreement with the results obtained by Jain and Baxter [69]. Moreover, Jain and Baxter [69] addressed the exchange of the fluid between the interstitial compartment and the vessels, however they did not study the fluid dynamic in the microvascular region. Herein, we investigate the microvascular fluid flow, and Figure 4.3 clearly shows that the vascular pressure p is higher at the boundary and the convection of the blood is directed inward. We obtain higher value of vessels hydraulic conductivity \bar{D} with lower size of tumour and higher pressure in the center. These results are in agreement with Penta and Ambrosi [103] who discussed about the microscopic pressure and velocity with different vessels' tortuosity in the tumour region only. Furthermore, the difference of the pressures between the two compartments, see Figure 4.4, is higher at the boundary than in the center, because in our model the vessels hydraulic conductivity \bar{D} is bigger than the interstitial hydraulic conductivity \bar{G} . Moreover, the difference of the pressures ($p - g$) decrease by increasing the tumour radius which impairs the fluid flow.

The homogeneous magnetic force that is applied in the z -direction of the domain changes the fluid flow in both compartments, specially when the magnetic field intensity is $\nabla H_0^2 = 70 \text{ T}^2/\text{m}$, see Figure 4.5. These results show the impact of the magnetic force on the orientation of the fluid flow which can be used to control nanoparticles delivery to the tumour by controlling

its direction. Therefore, this can help to avoid transporting the magnetic nanoparticles to the healthy tissue. Moreover, the impact of the magnetic field on fluid flow is more pronounced for tumours characterized by smaller radius.

4.8 Concluding remarks

In this chapter we derive a new system of homogenized differential equations which expresses the fluid flow of the tumour that interacts with surrounding healthy tissue under the influence of a magnetic force. The model starts with four Darcy's equations at mesoscale that represent the fluid flow in the vessels and interstitial compartments of the tumour and healthy regions. The differential equations at mesoscale are derived from the final macroscale differential equations taken from Al Sariri and Penta [3], and the fine scale of Penta et al. [106]. The final macroscale differential equations of the present model are given by two Darcy's law only, which combine the two regions together and address the mass exchange between them. As such, we have one differential equation describing the fluid flow in the vessels and the other one for the interstitial compartment. The influence of each region can be observed in the vessels' permeability, magnetic forces, and the hydraulic conductivity tensors that are defined in equations (4.49a-4.49d) and can be determined by solving the cell problems at the mesoscale. A divergence of nonhomogeneous magnetic forces affects the differential equations for the pressures. The homogenization steps are discussed in Section 4.5, and the final macroscale differential equations are defined by (4.48a-4.48b). In addition, the formulas of the new nonhomogeneous magnetic forces at the macroscale depend not only on the integral of the forces, but also on the mesoscale solution as in equations (4.49c-4.49d), and (4.53a-4.53b).

For the simplest case, we solve the final macroscale systems by assuming that a uniform magnetic force is applied in the whole tissue. The constant magnetic force affects the fluid velocities, but not the fluid pressures. The results of the interstitial pressure and velocity are in agreement with the findings reported by Jain and Baxter [69]. However, the present work presents the computations for the tumour and healthy regions which are homogenized in one tissue, while in Jain and Baxter [69] the regions are separated from each other. The magnetic force changes substantially the fluid flow in the tissue compartments.

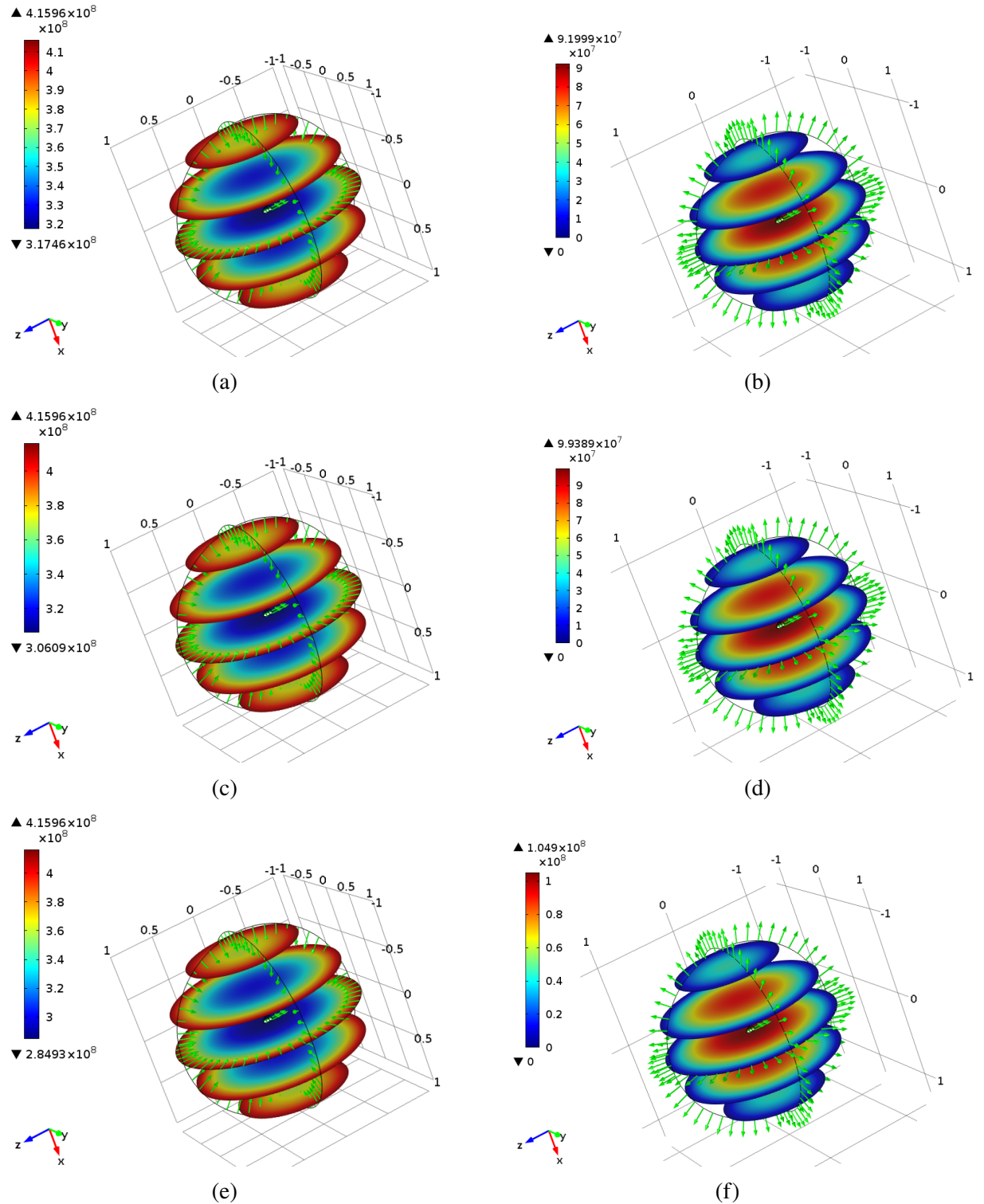


Figure 4.3: The pressures maps of the vessels' and interstitial compartments and the the fluid flow orientation with different tumour size. Figures (a), (c), and (e) are the fluid flow of the vessels in macroscale with tumors area 0.1, 0.3, and 0.5, respectively. Figures (b), (d), and (f) are the fluid flow of the interstitial compartments in macroscale with tumour area 0.1, 0.3, and 0.5, respectively. The magnetic field intensity is $10 \text{ T}^2/\text{m}$, other parameters are taken from Table 4.1 and Table 4.2.

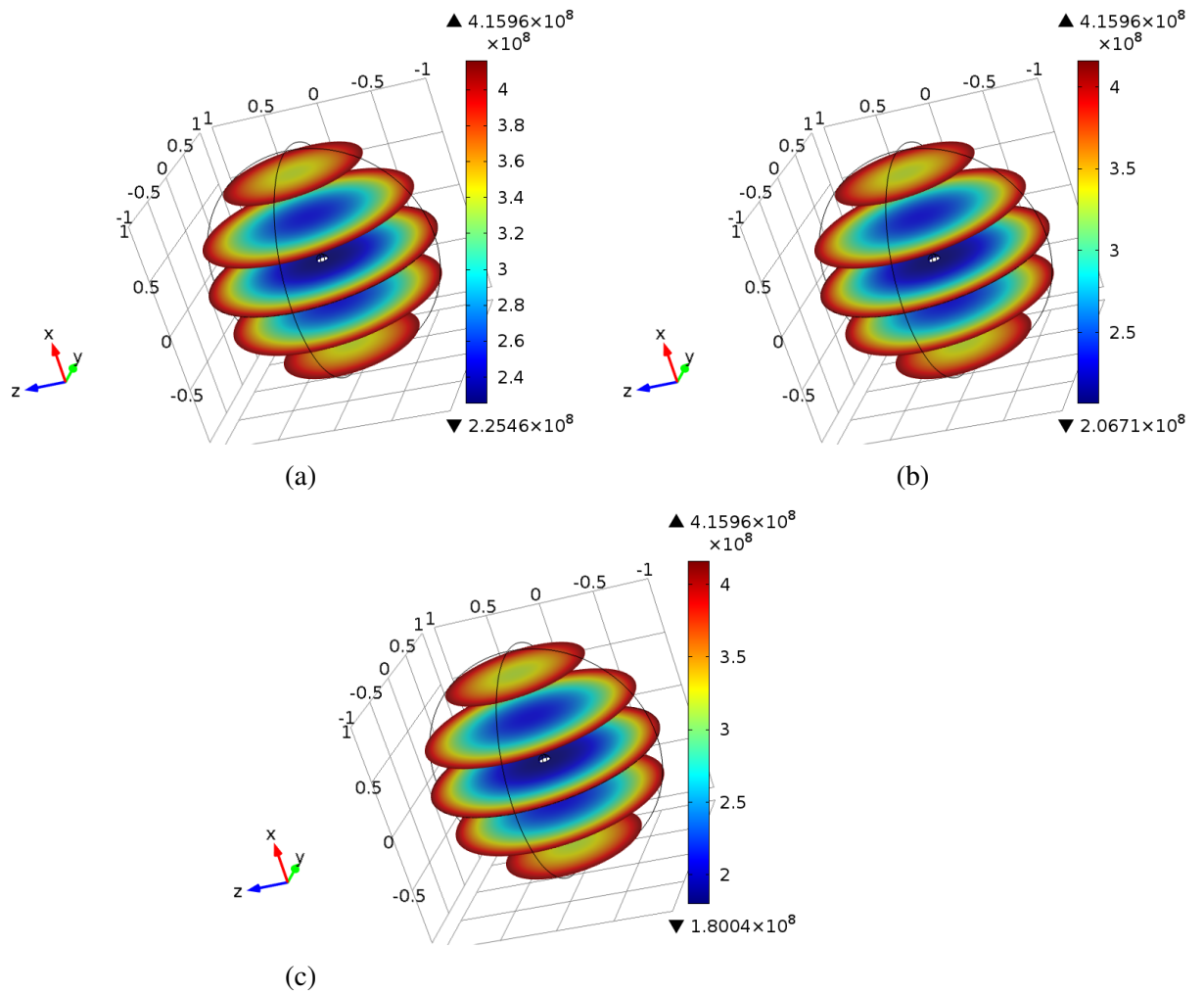


Figure 4.4: The pressure difference of the vessels and interstitial compartments with different tumour radius (a) 0.1 (b) 0.3 (c) 0.5. The values of the parameters are specified in Table 4.1 and Table 4.2.

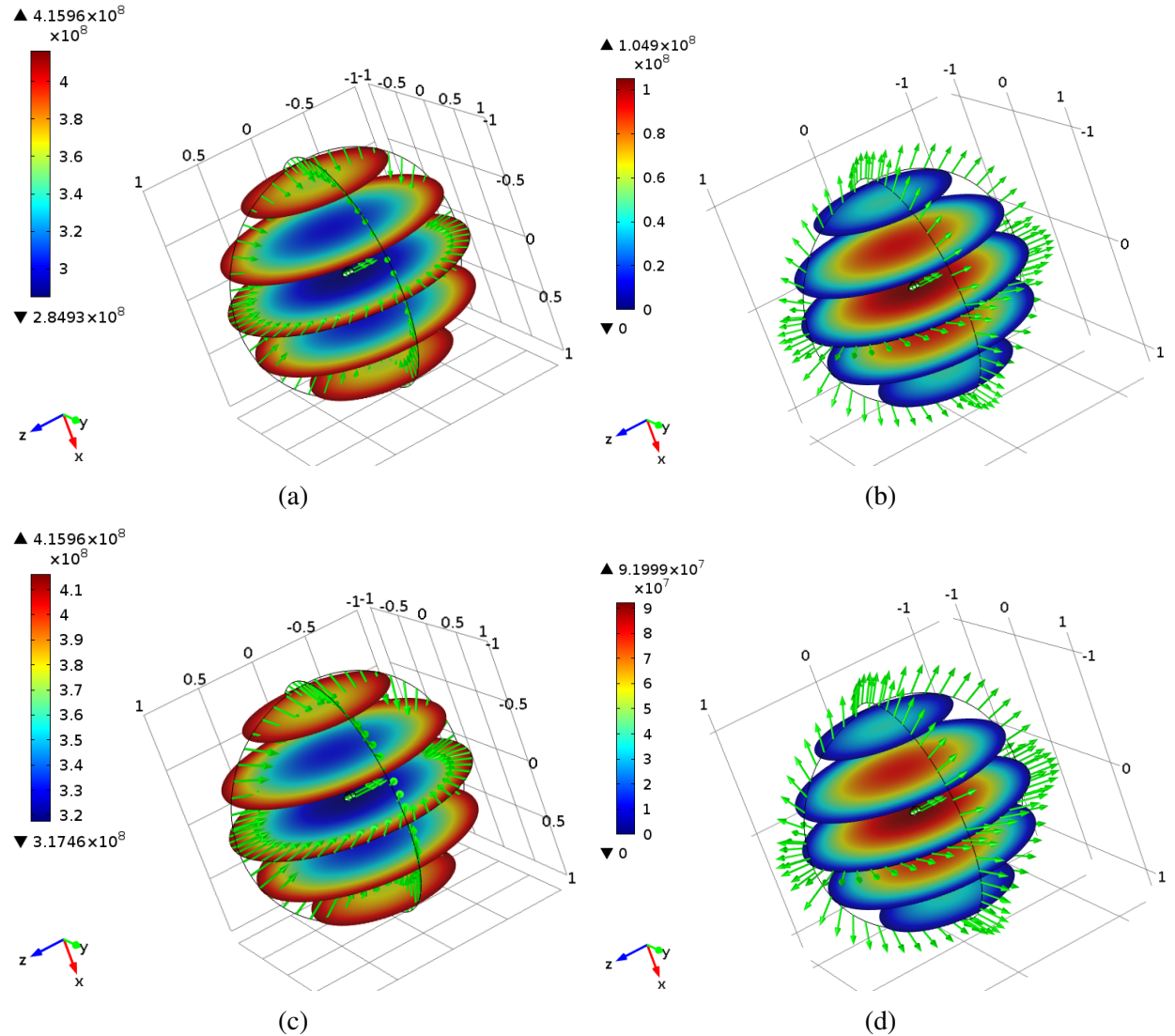


Figure 4.5: The pressures maps with magnetic force applying on the z-direction. (a) The pressure maps for the vessels for tumour with size 0.1, (b) The pressure maps for the vessels for tumour with size 0.5, and (c) The pressure maps for the interstitial region for tumour with size 0.1, (d) The pressure maps for the interstitial region for tumour with size 0.5, and $\nabla H_0^2 = 70 \text{ T}^2/\text{m}$. All other parameters are specified in Table 4.1 and Table 4.2

Chapter 5

Conclusion

This thesis investigates different models to describe the hyperthermia cancer treatment using magnetic nanoparticles. The asymptotic homogenization technique is used to address the scale difference of various regions in the models. We conclude this thesis by summarizing the most important theoretical and numerical results that are illustrated in Chapters 2, 3, and 4. Then we suggest various ideas to improve the models.

5.1 Conclusion summary

We began this thesis by introducing a review of the literature which plays a role in providing a basis for deriving and solving the new models.

In Chapter 2, we have investigated the model of the fluid, mass, and heat transport in the microvascular tumour. The tumour region is divided into two compartments which are the tumour vessels and the interstitium. We have taken into account the transvascular exchange of fluid, particles, and heat between the two regions. Also, the particles can be uptaken by the tumour interstitial region. The role of the magnetic field is encoded in a suitable source of heat generated in the tumour and proportional to the concentration of nanoparticles and on the absorption rate α . This latter parameter encodes in turn the properties of the applied magnetic field such as its intensity. Due to the big difference in sizes between the two compartments, we use the homogenization technique to upscale the problem from the microscale (vessels' distance) to the macroscale (tumour size). The solution of the microscale differential equations and the solution of the fluid flow at the macroscale are taken from Penta and Ambrosi [103], and Mascheroni and Penta [85]. Therefore, the results of this chapter are focused on describing the macroscale particles and heat distribution in the tumour. The major result is that the heat convection is impaired by the increasing vessels' tortuosity. Also, there is direct relationship between the temperature maps and the absorption rate of magnetic nanoparticles.

In Chapter 3, we have focused more on achieving the appropriate cancer hyperthermia treatment by minimizing the negative side effects on the surrounding. Also, we study various

types of magnetic nanoparticles characterised by different sizes, materials, and concentration. We assume that nanoparticles with size greater than the vessels' pore size are injected into the tumour vessels. Consequently, the particles are not being transported from the vessels to the tumour interstitial compartments while adhesion between the particles and vessels' wall plays a major role in the drug dynamics. However, transport of fluid and heat still occurs in both compartments and are exchanged across the vessels' walls. Moreover, we define the absorption rate α using Brownian and Neels equation. To solve the final macroscale system, we presume that the particles are injected with a given concentration at the boundary of the tumour with values informed by relevant bio-medical literature works. The results show that the adhesion plays important rule on the density of nanoparticles adhering the vessels' wall and on the concentration of nanoparticles closer to the edge of the tumour. We illustrate the optimal values of different parameters in the model related to the particles properties such as diameter and concentration, vessels tortuosity, wall shear rate, and the magnetic field intensity and frequency to obtain the required hyperthermic conditions to safely destroy the tumour cells.

In Chapter 4, we have extended our study to investigate the interplay between the tumour and surrounding tissues. We have focused on deriving the fluid flow of the tumour surrounded by healthy tissue and affected by inhomogeneous magnetic force. We have started from the final macroscale results of the previous chapters and have linked it with the model discussed by Penta et al. [106]. Both the healthy and the tumour regions are divided into two compartments which are the vessels and interstitium. However, the scale separation which motivates the employment of the homogenisation technique is between the average distance between two adjacent cancerous regions and the overall tissue size. We have begun with four equations that describe the fluid pressures and other four equations for the fluid velocity in the vessels and interstitial compartments of each region at the mesoscale. The final result comprises just two macroscale equations which describe the fluid pressure of the vessels' and tumour at a global tissue scale level. The first one combines the vessels pressures of both regions, and the second one holds for the interstitial compartment, and similarly for the fluid velocities. The impact of the tumour and healthy regions is encoded in the vessels' permeability, the magnetic forces, and hydraulic conductivity tensors which are solving appropriate cell problems at the mesoscale. To get the general idea about the influence of magnetic force in the fluid flow, we find the numerical solution of the mesoscale cell problems, as well as the macroscale solution for the case of a homogeneous magnetic force and assuming that the cancer heterogeneities can be approximated as cylindrical fibers (so that the mesoscale cell problems can be solved in two dimensions). A uniform magnetic force has no effect on the fluid pressures, but it still has an impact on the fluid flow which is discussed in Chapter 4.

5.2 Future work

These analysis are open for improvement and further developments.

- We have chosen to present the results by means of a spherical coordinate setting as this has enabled us to deduce the results which can be readily compared against the current literature. However, our finite element computational platform can be generalised to generic macroscale geometries depending on the actual tumour shape at hand.
- This work could also be generalised to include nonlinear heat sources and nonlinear drug uptake, as, given the current scaling assumptions, relevant modifications would only appear at leading order. Different boundary and initial conditions could also be taken into account depending on the interplay between the tumour mass and the surrounding and on the specific clinical injections conditions at hand.
- The new models have been derived by considering the same distinguished limit as in Mascheroni and Penta [85], Penta et al. [102] in terms of Peclet numbers and non-dimensional thermal hydraulic conductivities. Alternative distinguished limits, which would result in purely convective heat and drug transport contributions at leading order could be considered (see, e.g. Shipley and Chapman [126] when these are investigated for macromolecules transport).
- An interesting further development of this work also resides in a comprehensive analysis of admissible distinguished limits that exist for this system, with particular reference to particles' uptake, and diffusion phenomena occurring in different regions of the domain under consideration, see, e.g. Dalwadi et al. [33], Ptashnyk and Roose [111], respectively.
- We have assumed that the tumour does not deform, while of course tissue deformations and growth take place (see also [101, 105] where homogenised models for avascular ap- positional growth and fluid transport in deformable vascular tumours are investigated) and can determine significant consequences on drug transport.
- In addition, in this work we have considered a constant wall shear rate for the sake of simplicity, while this is indeed depending on the microscale fluid transport in the vessels. Incorporating the latter could lead to a more realistic description of the influence of adhesion on nanoparticles transport and on its consequences on heat transport. This way, more realistic predictions could be made concerning the necessary geometric regularisation that

should be carried out to achieve safe hyperthermic conditions.

- The next natural step is to parameterise the microstructure by means of realistic medical images. This way, given a set of experimental and physiological conditions at hand, our findings can pave the way for the design of patient-specific diagnostic tool to improve the efficacy of current anti-cancer therapies.
- The model derived in Chapter 4 should be extended to address the particles and heat transport in the cancerous regions interplaying with the healthy ones under the influence of a magnetic field in the context of cancer hyperthermia.

Bibliography

- [1] Eric C Abenojar, Sameera Wickramasinghe, Jesbaniris Bas-Concepcion, and Anna Cristina S Samia. Structural effects on the magnetic hyperthermia properties of iron oxide nanoparticles. *Progress in Natural Science: Materials International*, 26(5):440–448, 2016.
- [2] Adela Ademaj, Danai P. Veltsista, Pirus Ghadjar, Dietmar Marder, Eva Oberacker, Oliver J. Ott, Peter Wust, Emsad Puric, Roger A. Hälg, Susanne Rogers, Stephan Bodis, Rainer Fietkau, Hans Crezee, and Oliver Riesterer. Clinical evidence for thermometric parameters to guide hyperthermia treatment. *Cancers*, 14(3):625, January 2022. doi: 10.3390/cancers14030625.
- [3] Tahani Al Sariri and Raimondo Penta. Multi-scale modelling of nanoparticle delivery and heat transport in vascularised tumours. *Mathematical Medicine and Biology: A Journal of the IMA*, 39(4):332–367, 2022.
- [4] Tahani Al Sariri, Radostin D Simitiev, and Raimondo Penta. Optimal heat transport induced by magnetic nanoparticle delivery in vascularised tumours. *Journal of Theoretical Biology*, page 111372, 2022.
- [5] Farhad Ali, Anees Imtiaz, Ilyas Khan, and Nadeem Ahmad Sheikh. Flow of magnetic particles in blood with isothermal heating: A fractional model for two-phase flow. *Journal of Magnetism and Magnetic Materials*, 456:413–422, 2018.
- [6] W Andrä, CG d’Ambly, R Hergt, I Hilger, and WA Kaiser. Temperature distribution as function of time around a small spherical heat source of local magnetic hyperthermia. *Journal of Magnetism and Magnetic Materials*, 194(1-3):197–203, 1999.
- [7] Hamed Arami, Amit Khandhar, Denny Liggitt, and Kannan M Krishnan. In vivo delivery, pharmacokinetics, biodistribution and toxicity of iron oxide nanoparticles. *Chemical Society Reviews*, 44(23):8576–8607, 2015.
- [8] Matteo Avolio, Claudia Innocenti, Alessandro Lascialfari, Manuel Mariani, and Claudio Sangregorio. Medical applications of magnetic nanoparticles. In *New Trends in Nanoparticle Magnetism*, pages 327–351. Springer, 2021.

- [9] HG Bagaria and DT Johnson. Transient solution to the bioheat equation and optimization for magnetic fluid hyperthermia treatment. *International Journal of Hyperthermia*, 21(1): 57–75, 2005.
- [10] N Bakhvalov and G Panasenko. *Homogenization: Averaging processes in Periodic Media*. Kluwer Academic Publishers, 1989.
- [11] Alain Bensoussan, Jacques-Louis Lions, and George Papanicolaou. *Asymptotic analysis for periodic structures*, volume 374. American Mathematical Soc., 2011.
- [12] Nikolay Bessonov, Adélia Sequeira, Sergey Simakov, Yu Vassilevskii, and Vitaly Volpert. Methods of blood flow modelling. *Mathematical modelling of natural phenomena*, 11(1): 1–25, 2016.
- [13] Bijoy K Bhuyan, Kathleen J Day, Charlene E Edgerton, and Olufunso Ogunbase. Sensitivity of different cell lines and of different phases in the cell cycle to hyperthermia. *Cancer research*, 37(10):3780–3784, 1977.
- [14] Chenchen Bing, Pratik Patel, Robert M Staruch, Sumbul Shaikh, Joris Nofiele, Michelle Wodzak Staruch, Debra Szczepanski, Noelle S Williams, Theodore Laetsch, and Rajiv Chopra. Longer heating duration increases localized doxorubicin deposition and therapeutic index in vx2 tumors using mr-hifu mild hyperthermia and thermosensitive liposomal doxorubicin. *International Journal of Hyperthermia*, 36(1):195–202, 2019.
- [15] Yves Boucher, Laurence T Baxter, and Rakesh K Jain. Interstitial pressure gradients in tissue-isolated and subcutaneous tumors: implications for therapy. *Cancer research*, 50(15):4478–4484, 1990.
- [16] Claude Boutin, Jean-Louis Auriault, and Christian Geindreau. *Homogenization of coupled phenomena in heterogenous media*, volume 149. John Wiley & Sons, 2010.
- [17] Elizabeth Bullitt, Guido Gerig, Stephen M Pizer, Weili Lin, and Stephen R Aylward. Measuring tortuosity of the intracerebral vasculature from mra images. *IEEE transactions on medical imaging*, 22(9):1163–1171, 2003.
- [18] Rita M Cabral and Pedro V Baptista. Anti-cancer precision theranostics: a focus on multifunctional gold nanoparticles. *Expert review of molecular diagnostics*, 14(8):1041–1052, 2014.
- [19] Cancer Research UK. Cancer statistics for the uk. URL <https://www.cancerresearchuk.org/health-professional/cancer-statistics-for-the-uk#heading-Two>. (accessed: 07-09-2022).

- [20] Peter Carmeliet and Rakesh K Jain. Angiogenesis in cancer and other diseases. *nature*, 407(6801):249–257, 2000.
- [21] L Cattaneo and P Zunino. b. computational models for fluid exchange between microcirculation and tissue interstitium. *Networks Heterogen Media*, 9(1):135–159, 2014.
- [22] Laura Cattaneo and Paolo Zunino. A computational model of drug delivery through microcirculation to compare different tumor treatments. *International journal for numerical methods in biomedical engineering*, 30(11):1347–1371, 2014.
- [23] Antonio Cervadoro, Chiara Giverso, Rohit Pande, Subhasis Sarangi, Luigi Preziosi, Jarek Wosik, Audrius Brazdeikis, and Paolo Decuzzi. Design maps for the hyperthermic treatment of tumors with superparamagnetic nanoparticles. *PloS one*, 8(2):e57332, 2013.
- [24] Julie A Champion and Samir Mitragotri. Role of target geometry in phagocytosis. *Proceedings of the National Academy of Sciences*, 103(13):4930–4934, 2006.
- [25] Paul Cherukuri, Evan S Glazer, and Steven A Curley. Targeted hyperthermia using metal nanoparticles. *Advanced drug delivery reviews*, 62(3):339–345, 2010.
- [26] Adam Chicheł, Janusz Skowronek, Magda Kubaszewska, and Marek Kanikowski. Hyperthermia—description of a method and a review of clinical applications. *Reports of Practical Oncology & Radiotherapy*, 12(5):267–275, 2007.
- [27] Kwangjae Cho, XU Wang, Shuming Nie, Dong M Shin, et al. Therapeutic nanoparticles for drug delivery in cancer. *Clinical cancer research*, 14(5):1310–1316, 2008.
- [28] Cheng-Ying Chou, Chih-Kang Huang, Kuo-Wei Lu, Tzyy-Leng Horng, and Win-Li Lin. Investigation of the spatiotemporal responses of nanoparticles in tumor tissues with a small-scale mathematical model. *PloS one*, 8(4):e59135, 2013.
- [29] D Cioranescu and P Donato. *An Introduction to Homogenization*. Oxford University Press, 1999.
- [30] Doina Cioranescu and Patrizia Donato. *An introduction to homogenization*, volume 17. Oxford university press Oxford, 1999.
- [31] Miriam Colombo, Susana Carregal-Romero, Maria F. Casula, Lucia Gutierrez, Maria P. Morales, Ingrid B. Bohm, Johannes T. Heverhagen, Davide Prosperi, and Wolfgang. J. Parak. Biological applications of magnetic nanoparticles. *Chemical Society Reviews*, 41(11):4306, 2012.
- [32] Mohit P Dalwadi and John R King. A systematic upscaling of nonlinear chemical uptake within a biofilm. *SIAM Journal on Applied Mathematics*, 80(4):1723–1750, 2020.

- [33] Mohit P Dalwadi, Yanming Wang, John R King, and Nigel P Minton. Upscaling diffusion through first-order volumetric sinks: a homogenization of bacterial nutrient uptake. *SIAM Journal on Applied Mathematics*, 78(3):1300–1329, 2018.
- [34] Pradip Das, Miriam Colombo, and Davide Prosperi. Recent advances in magnetic fluid hyperthermia for cancer therapy. *Colloids and Surfaces B: Biointerfaces*, 174:42–55, February 2019. doi: 10.1016/j.colsurfb.2018.10.051.
- [35] Raja Das, Javier Alonso, Zohreh Nemati Porshokouh, Vijaysankar Kalappattil, David Torres, Manh-Huong Phan, Eneko Garaio, Jose Angel Garcia, Jose Luis SanchezLlamazaress, and Hariharan Srikanth. Tunable high aspect ratio iron oxide nanorods for enhanced hyperthermia. *The Journal of Physical Chemistry C*, 120(18):10086–10093, 2016.
- [36] Yohan Davit, Christopher G Bell, Helen M Byrne, Lloyd AC Chapman, Laura S Kimpton, Georgina E Lang, Katherine HL Leonard, James M Oliver, Natalie C Pearson, Rebecca J Shipley, et al. Homogenization via formal multiscale asymptotics and volume averaging: How do the two techniques compare? *Advances in Water Resources*, 62:178–206, 2013.
- [37] P De la Presa, Y Luengo, M Multigner, R Costo, MP Morales, G Rivero, and A Hernando. Study of heating efficiency as a function of concentration, size, and applied field in γ -Fe₂O₃ nanoparticles. *The Journal of Physical Chemistry C*, 116(48):25602–25610, 2012.
- [38] P Decuzzi and Mauro Ferrari. The adhesive strength of non-spherical particles mediated by specific interactions. *Biomaterials*, 27(30):5307–5314, 2006.
- [39] Thomas E Dudar and Rakesh K Jain. Differential response of normal and tumor microcirculation to hyperthermia. *Cancer Research*, 44(2):605–612, 1984.
- [40] Silvio Dutz and Rudolf Hergt. Magnetic particle hyperthermia—a promising tumour therapy? *Nanotechnology*, 25(45):452001, 2014.
- [41] Asmaa Mohamed El Shafey. Green synthesis of metal and metal oxide nanoparticles from plant leaf extracts and their applications: A review. *Green Processing and Synthesis*, 9(1):304–339, 2020.
- [42] Ana Espinosa, Jelena Kolosnjaj-Tabi, Ali Abou-Hassan, Anouchka Plan Sangnier, Alberto Curcio, Amanda KA Silva, Riccardo Di Corato, Sophie Neveu, Teresa Pellegrino, Luis M Liz-Marzán, et al. Magnetic (hyper) thermia or photothermia? progressive comparison of iron oxide and gold nanoparticles heating in water, in cells, and in vivo. *Advanced Functional Materials*, 28(37):1803660, 2018.
- [43] MH Falk and RD Issels. Hyperthermia in oncology. *International Journal of Hyperthermia*, 17(1):1–18, 2001.

- [44] Simone Famiani, Alec P LaGrow, Maximilian O Besenhard, Shinya Maenosono, and Nguyen Thi Kim Thanh. Synthesis of fine-tuning highly magnetic Fe_3O_4 nanoparticles through continuous injection and a study of magnetic hyperthermia. *Chemistry of Materials*, 30(24):8897–8904, 2018.
- [45] Hira Fatima, Tawatchai Charinpanitkul, and Kyo-Seon Kim. Fundamentals to apply magnetic nanoparticles for hyperthermia therapy. *Nanomaterials*, 11(5):1203, 2021.
- [46] Jérôme Fayette, Jean-Charles Soria, and Jean-Pierre Armand. Use of angiogenesis inhibitors in tumour treatment. *European Journal of Cancer*, 41(8):1109–1116, 2005.
- [47] R Matthew Ferguson, Amit P Khandhar, Christian Jonasson, Jakob Blomgren, Christer Johansson, and Kannan M Krishnan. Size-dependent relaxation properties of monodisperse magnetite nanoparticles measured over seven decades of frequency by ac susceptometry. *IEEE transactions on magnetics*, 49(7):3441–3444, 2013.
- [48] Gautier Follain, David Herrmann, Sébastien Harlepp, Vincent Hyenne, Naël Osmani, Sean C Warren, Paul Timpson, and Jacky G Goetz. Fluids and their mechanics in tumour transit: shaping metastasis. *Nature Reviews Cancer*, 20(2):107–124, 2020.
- [49] SJ Franks, HM Byrne, HS Mudhar, JCE Underwood, and CE Lewis. Mathematical modelling of comedo ductal carcinoma in situ of the breast. *Mathematical medicine and biology: a journal of the IMA*, 20(3):277–308, 2003.
- [50] Shreelaxmi Gavvas, Sameer Quazi, and Tomasz M Karpiński. Nanoparticles for cancer therapy: current progress and challenges. *Nanoscale Research Letters*, 16(1):1–21, 2021.
- [51] AA Golneshan and M Lahonian. The effect of magnetic nanoparticle dispersion on temperature distribution in a spherical tissue in magnetic fluid hyperthermia using the lattice boltzmann method. *International Journal of Hyperthermia*, 27(3):266–274, 2011.
- [52] Thomas T Goodman, Jingyang Chen, Konstantin Matveev, and Suzie H Pun. Spatio-temporal modeling of nanoparticle delivery to multicellular tumor spheroids. *Biotechnology and bioengineering*, 101(2):388–399, 2008.
- [53] Xiaofei Guan, Xian Liu, Xin Jia, Yong Yuan, Junzhi Cui, and Herbert A Mang. A stochastic multiscale model for predicting mechanical properties of fiber reinforced concrete. *International Journal of Solids and Structures*, 56:280–289, 2015.
- [54] Pablo Guardia, Riccardo Di Corato, Lenaic Lartigue, Claire Wilhelm, Ana Espinosa, Mar Garcia-Hernandez, Florence Gazeau, Liberato Manna, and Teresa Pellegrino. Water-soluble iron oxide nanocubes with high values of specific absorption rate for cancer cell hyperthermia treatment. *ACS nano*, 6(4):3080–3091, 2012.

- [55] Sergey P Gubin. *Magnetic nanoparticles*. John Wiley & Sons, 2009.
- [56] Emily Gullotti and Yoon Yeo. Extracellularly activated nanocarriers: a new paradigm of tumor targeted drug delivery. *Molecular pharmaceuticals*, 6(4):1041–1051, 2009.
- [57] Douglas Hanahan and Robert A Weinberg. Hallmarks of cancer: the next generation. *cell*, 144(5):646–674, 2011.
- [58] Saba Hasan. A review on nanoparticles: their synthesis and types. *Res. J. Recent Sci*, 2277:2502, 2015.
- [59] Hiroya Hashizume, Peter Baluk, Shunichi Morikawa, John W McLean, Gavin Thurston, Sylvie Roberge, Rakesh K Jain, and Donald M McDonald. Openings between defective endothelial cells explain tumor vessel leakiness. *The American journal of pathology*, 156(4):1363–1380, 2000.
- [60] Rudolf Hergt, Silvio Dutz, Robert Müller, and Matthias Zeisberger. Magnetic particle hyperthermia: nanoparticle magnetism and materials development for cancer therapy. *Journal of Physics: Condensed Matter*, 18(38):S2919, 2006.
- [61] Ingrid Hilger. In vivo applications of magnetic nanoparticle hyperthermia. *International Journal of Hyperthermia*, 29(8):828–834, 2013.
- [62] Susan K Hobbs, Wayne L Monsky, Fan Yuan, W Gregory Roberts, Linda Griffith, Vladimir P Torchilin, and Rakesh K Jain. Regulation of transport pathways in tumor vessels: role of tumor type and microenvironment. *Proceedings of the National Academy of Sciences*, 95(8):4607–4612, 1998.
- [63] Ulrich Hornung. *Homogenization and porous media*, volume 6. Springer Science & Business Media, 1996.
- [64] Kazunori Hoshino, Peng Chen, Yu-Yen Huang, and Xiaojing Zhang. Computational analysis of microfluidic immunomagnetic rare cell separation from a particulate blood flow. *Analytical chemistry*, 84(10):4292–4299, 2012.
- [65] Shaolie S Hossain, Yongjie Zhang, Xinghua Liang, Fazle Hussain, Mauro Ferrari, Thomas JR Hughes, and Paolo Decuzzi. In silico vascular modeling for personalized nanoparticle delivery. *Nanomedicine*, 8(3):343–357, 2013.
- [66] Huang-Chiao Huang, Sutapa Barua, Gaurav Sharma, Sandwip K Dey, and Kaushal Rege. Inorganic nanoparticles for cancer imaging and therapy. *Journal of controlled Release*, 155(3):344–357, 2011.

- [67] Yotaro Izumi, Lei Xu, Emmanuelle Di Tomaso, Dai Fukumura, and Rakesh K Jain. Herceptin acts as an anti-angiogenic cocktail. *Nature*, 416(6878):279–280, 2002.
- [68] Rakesh K Jain. Normalizing tumor vasculature with anti-angiogenic therapy: a new paradigm for combination therapy. *Nature medicine*, 7(9):987–989, 2001.
- [69] Rakesh K Jain and Laurence T Baxter. Mechanisms of heterogeneous distribution of monoclonal antibodies and other macromolecules in tumors: significance of elevated interstitial pressure. *Cancer research*, 48(24 Part 1):7022–7032, 1988.
- [70] Rakesh K Jain, Ricky T Tong, and Lance L Munn. Effect of vascular normalization by antiangiogenic therapy on interstitial hypertension, peritumor edema, and lymphatic metastasis: insights from a mathematical model. *Cancer research*, 67(6):2729–2735, 2007.
- [71] Manfred Johannsen, U Gneveckow, L Eckelt, A Feussner, N Waldöfner, R Scholz, S Deger, P Wust, SA Loening, and A Jordan. Clinical hyperthermia of prostate cancer using magnetic nanoparticles: presentation of a new interstitial technique. *International journal of hyperthermia*, 21(7):637–647, 2005.
- [72] Chanchala D Kaddi, John H Phan, and May D Wang. Computational nanomedicine: modeling of nanoparticle-mediated hyperthermal cancer therapy. *Nanomedicine*, 8(8):1323–1333, 2013.
- [73] Ravi Kappiyoor, Monrudee Liangruksa, Ranjan Ganguly, and Ishwar K Puri. The effects of magnetic nanoparticle properties on magnetic fluid hyperthermia. *Journal of Applied Physics*, 108(9):094702, 2010.
- [74] Noriyasu Kawai, Mitsuru Futakuchi, Tatsuro Yoshida, Akira Ito, Shinya Sato, Taku Naiki, Hiroyuki Honda, Tomoyuki Shirai, and Kenjiro Kohri. Effect of heat therapy using magnetic nanoparticles conjugated with cationic liposomes on prostate tumor in bone. *The Prostate*, 68(7):784–792, 2008.
- [75] Sung Tae Kim, Apiwat Chompoosor, Yi-Cheun Yeh, Sarit S Agasti, David J Solfiell, and Vincent M Rotello. Dendronized gold nanoparticles for sirna delivery. *Small (Weinheim an der Bergstrasse, Germany)*, 8(21):3253, 2012.
- [76] H. Petra Kok, Erik N. K. Cressman, Wim Ceelen, Christopher L. Brace, Robert Ivkov, Holger Grüll, Gail ter Haar, Peter Wust, and Johannes Crezee. Heating technology for malignant tumors: a review. *International Journal of Hyperthermia*, 37(1):711–741, January 2020. doi: 10.1080/02656736.2020.1779357. URL <https://doi.org/10.1080/02656736.2020.1779357>.

- [77] Jens Lang, Bodo Erdmann, and Martin Seebass. Impact of nonlinear heat transfer on temperature control in regional hyperthermia. *IEEE Transactions on Biomedical Engineering*, 46(9):1129–1138, 1999.
- [78] Sophie Laurent, Silvio Dutz, Urs O Häfeli, and Morteza Mahmoudi. Magnetic fluid hyperthermia: focus on superparamagnetic iron oxide nanoparticles. *Advances in colloid and interface science*, 166(1-2):8–23, 2011.
- [79] Marilyn P Law. Induced thermal resistance in the mouse ear: the relationship between heating time and temperature. *International Journal of Radiation Biology and Related Studies in Physics, Chemistry and Medicine*, 35(4):481–485, 1979.
- [80] Mi-Kyung Lee, Soo-Jeong Lim, and Chong-Kook Kim. Preparation, characterization and in vitro cytotoxicity of paclitaxel-loaded sterically stabilized solid lipid nanoparticles. *Biomaterials*, 28(12):2137–2146, 2007.
- [81] Zhao Ling-Yun, Liu Jia-Yi, Ouyang Wei-Wei, Li Dan-Ye, Li Li, Li Li-Ya, and Tang Jin-Tian. Magnetic-mediated hyperthermia for cancer treatment: Research progress and clinical trials. *Chinese Physics B*, 22(10):108104, 2013.
- [82] Xiliang Luo, Aoife Morrin, Anthony J Killard, and Malcolm R Smyth. Application of nanoparticles in electrochemical sensors and biosensors. *Electroanalysis: An International Journal Devoted to Fundamental and Practical Aspects of Electroanalysis*, 18(4):319–326, 2006.
- [83] Yonggang Lv, Yang Zou, and Li Yang. Uncertainty and sensitivity analysis of properties of phase change micro/nanoparticles for thermal protection during cryosurgery. *Forschung im Ingenieurwesen*, 76(1):41–50, 2012.
- [84] Pavla Martinkova, Martin Brtnicky, Jindrich Kynicky, and Miroslav Pohanka. Iron oxide nanoparticles: innovative tool in cancer diagnosis and therapy. *Advanced healthcare materials*, 7(5):1700932, 2018.
- [85] Pietro Mascheroni and Raimondo Penta. The role of the microvascular network structure on diffusion and consumption of anticancer drugs. *International journal for numerical methods in biomedical engineering*, 33(10):e2857, 2017.
- [86] Donald M McDonald and Peter Baluk. Significance of blood vessel leakiness in cancer, 2002.
- [87] Asghar Mesbahi. A review on gold nanoparticles radiosensitization effect in radiation therapy of cancer. *Reports of Practical Oncology & Radiotherapy*, 15(6):176–180, 2010.

- [88] Arkadiusz Miaskowski and Bartosz Sawicki. Magnetic fluid hyperthermia modeling based on phantom measurements and realistic breast model. *IEEE transactions on biomedical engineering*, 60(7):1806–1813, 2013.
- [89] Alamer Moath and Yun Xu Xiao. The influence of tumour vasculature on fluid flow in solid tumours: a mathematical modelling study. *Biophysics Reports*, 7(1):35–54, 2021.
- [90] VJ Mohanraj and Y Chen. Nanoparticles-a review. *Tropical journal of pharmaceutical research*, 5(1):561–573, 2006.
- [91] Stéphane Mornet, Sébastien Vasseur, Fabien Grasset, and Etienne Duguet. Magnetic nanoparticle design for medical diagnosis and therapy. *Journal of materials chemistry*, 14(14):2161–2175, 2004.
- [92] Paul Moroz, SK Jones, and BN Gray. Magnetically mediated hyperthermia: current status and future directions. *International Journal of Hyperthermia*, 18(4):267–284, 2002.
- [93] Alicia Muela, David Munoz, Rosa Martin-Rodriguez, Inaki Orue, Eneko Garaio, Ana Abad Diaz de Cerio, Javier Alonso, José Angel García, and M Luisa Fdez-Gubieda. Optimal parameters for hyperthermia treatment using biomineralized magnetite nanoparticles: theoretical and experimental approach. *The Journal of Physical Chemistry C*, 120(42):24437–24448, 2016.
- [94] Mahdi Nabil and Paolo Zunino. A computational study of cancer hyperthermia based on vascular magnetic nanoconstructs. *Royal Society open science*, 3(9):160287, 2016.
- [95] Mahdi Nabil, Paolo Decuzzi, and Paolo Zunino. Modelling mass and heat transfer in nano-based cancer hyperthermia. *Royal Society open science*, 2(10):150447, 2015.
- [96] Z Nematy, J Alonso, LM Martinez, H Khurshid, E Garaio, JA Garcia, MH Phan, and H Srikanth. Enhanced magnetic hyperthermia in iron oxide nano-octopods: size and anisotropy effects. *The Journal of Physical Chemistry C*, 120(15):8370–8379, 2016.
- [97] Eddie Yin Kwee Ng, Srinivasan Dinesh Kumar, et al. Physical mechanism and modeling of heat generation and transfer in magnetic fluid hyperthermia through néelian and brownian relaxation: a review. *Biomedical engineering online*, 16(1):1–22, 2017.
- [98] Seung-hyun Noh, Wonjun Na, Jung-tak Jang, Jae-Hyun Lee, Eun Jung Lee, Seung Ho Moon, Yongjun Lim, Jeon-Soo Shin, and Jinwoo Cheon. Nanoscale magnetism control via surface and exchange anisotropy for optimized ferrimagnetic hysteresis. *Nano letters*, 12(7):3716–3721, 2012.

- [99] Jens Overgaard, Marko M Radacic, and Cai Grau. Interaction of hyperthermia and cis-diamminedichloroplatinum (ii) alone or combined with radiation in a c3h mammary carcinoma in vivo. *Cancer research*, 51(2):707–711, 1991.
- [100] Quentin A Pankhurst, J Connolly, Stephen K Jones, and JJ Dobson. Applications of magnetic nanoparticles in biomedicine. *Journal of physics D: Applied physics*, 36(13):R167, 2003.
- [101] R Penta, D Ambrosi, and RJ31761191346 Shipley. Effective governing equations for poroelastic growing media. *Quarterly Journal of Mechanics and Applied Mathematics*, 67(1):69–91, 2014.
- [102] R Penta, D Ambrosi, and ALFIO Quarteroni. Multiscale homogenization for fluid and drug transport in vascularized malignant tissues. *Mathematical Models and Methods in Applied Sciences*, 25(01):79–108, 2015.
- [103] Raimondo Penta and Davide Ambrosi. The role of the microvascular tortuosity in tumor transport phenomena. *Journal of theoretical biology*, 364:80–97, 2015.
- [104] Raimondo Penta and Alf Gerisch. An introduction to asymptotic homogenization. In *Multiscale Models in Mechano and Tumor Biology*, pages 1–26. Springer, 2017.
- [105] Raimondo Penta and José Merodio. Homogenized modeling for vascularized poroelastic materials. *Meccanica*, 52(14):3321–3343, 2017.
- [106] Raimondo Penta, Ariel Ramirez Torres, José Merodio, and Reinaldo Rodríguez-Ramos. Effective governing equations for heterogenous porous media subject to inhomogeneous body forces. *Mathematics in Engineering*, 3(4):1–17, 2021.
- [107] Nicholas A Peppas and Balaji Narasimhan. Mathematical models in drug delivery: How modeling has shaped the way we design new drug delivery systems. *Journal of Controlled Release*, 190:75–81, 2014.
- [108] Carlos A Perez and Stephen A Sapareto. Thermal dose expression in clinical hyperthermia and correlation with tumor response/control. *Cancer research*, 44(10 Supplement):4818s–4825s, 1984.
- [109] Elio Alberto Perigo, Gauvin Hemery, Olivier Sandre, Daniel Ortega, Eneko Garaio, Fernando Plazaola, and Francisco Javier Teran. Fundamentals and advances in magnetic hyperthermia. *Applied Physics Reviews*, 2(4):041302, 2015.
- [110] James W Piper, Robert A Swerlick, and Cheng Zhu. Determining force dependence of two-dimensional receptor-ligand binding affinity by centrifugation. *Biophysical journal*, 74(1):492–513, 1998.

- [111] Mariya Ptashnyk and Tiina Roose. Derivation of a macroscopic model for transport of strongly sorbed solutes in the soil using homogenization theory. *SIAM Journal on Applied Mathematics*, 70(7):2097–2118, 2010.
- [112] Ariel Ramírez-Torres, Reinaldo Rodríguez-Ramos, Federico J Sabina, Catherine García-Reimbert, Raimondo Penta, José Merodio, Raúl Guinovart-Díaz, Julián Bravo-Castillero, Aura Conci, and Luigi Preziosi. The role of malignant tissue on the thermal distribution of cancerous breast. *Journal of Theoretical Biology*, 426:152–161, 2017.
- [113] Ariel Ramírez-Torres, Raimondo Penta, Reinaldo Rodríguez-Ramos, and Alfio Grillo. Effective properties of hierarchical fiber-reinforced composites via a three-scale asymptotic homogenization approach. *Mathematics and Mechanics of Solids*, 24(11):3554–3574, 2019.
- [114] Reza Roohi, Mohammad Reza Mahmoudi, Khosrow Jafarpur, and Homayoun Emdad. *Determination of magnetic nanoparticles injection characteristics for optimal hyperthermia treatment of an arbitrary cancerous cells distribution*. ASTM International, 2020.
- [115] Reza Roohi, Salman Baromand, Homayoun Emdad, and Mohammad Reza Mahmoudi. Optimization of focused multi-site injection therapy to provide the desired temperature pattern for arbitrary tumor configuration based on mnp hyperthermia: Implementation of dual phase lag bioheat equation. *Ain Shams Engineering Journal*, 12(1):901–915, 2021.
- [116] Jessica P Ryman-Rasmussen, Jim E Riviere, and Nancy A Monteiro-Riviere. Penetration of intact skin by quantum dots with diverse physicochemical properties. *Toxicological sciences*, 91(1):159–165, 2006.
- [117] Mostafa Saeedi, Omid Vahidi, Vahabodin Goodarzi, Mohammad Reza Saeb, Leila Izadi, and Masoud Mozafari. A new prospect in magnetic nanoparticle-based cancer therapy: Taking credit from mathematical tissue-mimicking phantom brain models. *Nanomedicine: Nanotechnology, Biology and Medicine*, 13(8):2405–2414, 2017.
- [118] Yoshihisa Sakaguchi, L Clifton Stephens, Masato Makino, Tetsuya Kaneko, Frederick R Strebel, Lynn L Danhauser, Gaye N Jenkins, and Joan MC Bull. Apoptosis in tumors and normal tissues induced by whole body hyperthermia in rats. *Cancer research*, 55(22):5459–5464, 1995.
- [119] Maher Salloum, Ronghui Ma, and Liang Zhu. An in-vivo experimental study of temperature elevations in animal tissue during magnetic nanoparticle hyperthermia. *International Journal of Hyperthermia*, 24(7):589–601, 2008.

- [120] Ashwini B Salunkhe, Vishwajeet M Khot, and SH Pawar. Magnetic hyperthermia with magnetic nanoparticles: a status review. *Current topics in medicinal chemistry*, 14(5): 572–594, 2014.
- [121] Hemant Sarin, Ariel S Kanevsky, Haitao Wu, Alioscka A Sousa, Colin M Wilson, Maria A Aronova, Gary L Griffiths, Richard D Leapman, and Howard Q Vo. Physiologic upper limit of pore size in the blood-tumor barrier of malignant solid tumors. *Journal of translational medicine*, 7(1):1–13, 2009.
- [122] Nicholas J Schork. Personalized medicine: time for one-person trials. *Nature*, 520(7549): 609–611, 2015.
- [123] M Sefidgar, M Soltani, K Raahemifar, M Sadeghi, H Bazmara, M Bazargan, and M Mousavi Naeenian. Numerical modeling of drug delivery in a dynamic solid tumor microvasculature. *Microvascular research*, 99:43–56, 2015.
- [124] Somoshree Sengupta and Vamsi K Balla. A review on the use of magnetic fields and ultrasound for non-invasive cancer treatment. *Journal of advanced research*, 14:97–111, 2018.
- [125] Sarah E Shelton, Yueh Z Lee, Mike Lee, Emmanuel Cherin, F Stuart Foster, Stephen R Aylward, and Paul A Dayton. Quantification of microvascular tortuosity during tumor evolution using acoustic angiography. *Ultrasound in medicine & biology*, 41(7):1896–1904, 2015.
- [126] Rebecca J Shipley and S Jonathan Chapman. Multiscale modelling of fluid and drug transport in vascular tumours. *Bulletin of mathematical biology*, 72(6):1464–1491, 2010.
- [127] Fridon Shubitidze, Katsiaryna Kekalo, Robert Stigliano, and Ian Baker. Magnetic nanoparticles with high specific absorption rate of electromagnetic energy at low field strength for hyperthermia therapy. *Journal of applied physics*, 117(9):094302, 2015.
- [128] André C Silva, Tiago R Oliveira, Javier B Mamani, Suzana MF Malheiros, Luciana Malavolta, Lorena F Pavon, Tatiana T Sibov, Edson Amaro Jr, Alberto Tannús, Edson LG Vidoto, et al. Application of hyperthermia induced by superparamagnetic iron oxide nanoparticles in glioma treatment. *International journal of nanomedicine*, 6:591, 2011.
- [129] Manoj Singh, S Manikandan, and AK Kumaraguru. Nanoparticles: a new technology with wide applications. *Research Journal of Nanoscience and Nanotechnology*, 1(1): 1–11, 2011.

- [130] Georgios P Skandalakis, Daniel R Rivera, Caroline D Rizea, Alexandros Bouras, Joe Gerald Jesu Raj, Dominique Bozec, and Constantinos G Hadjipanayis. Hyperthermia treatment advances for brain tumors. *International Journal of Hyperthermia*, 37(2):3–19, 2020.
- [131] M Soltani and Pu Chen. Numerical modeling of fluid flow in solid tumors. *PloS one*, 6(6):e20344, 2011.
- [132] Margo Steuperaert, Giuseppe Falvo D’Urso Labate, Charlotte Debbaut, Olivier De Wever, Christian Vanhove, Wim Ceelen, and Patrick Segers. Mathematical modeling of intraperitoneal drug delivery: simulation of drug distribution in a single tumor nodule. *Drug delivery*, 24(1):491–501, 2017.
- [133] Nicolae Strambeanu, Laurentiu Demetrovici, Dan Dragos, and Mihai Lungu. Nanoparticles: Definition, classification and general physical properties. In *Nanoparticles’ promises and risks*, pages 3–8. Springer, 2015.
- [134] Deanna D Stueber, Jake Villanova, Itzel Aponte, Zhen Xiao, and Vicki L Colvin. Magnetic nanoparticles in biology and medicine: Past, present, and future trends. *Pharmaceutics*, 13(7):943, 2021.
- [135] Triantafyllos Stylianopoulos, Lance L Munn, and Rakesh K Jain. Reengineering the physical microenvironment of tumors to improve drug delivery and efficacy: from mathematical modeling to bench to bedside. *Trends in cancer*, 4(4):292–319, 2018.
- [136] Karthikeyan Subramani, Hossein Hosseinkhani, Ameen Khraisat, Mohsen Hosseinkhani, and Yashwant Pathak. Targeting nanoparticles as drug delivery systems for cancer treatment. *Current Nanoscience*, 5(2):135–140, 2009.
- [137] Krzysztof Sztandera, Michał Gorzkiewicz, and Barbara Klajnert-Maculewicz. Gold nanoparticles in cancer treatment. *Molecular pharmaceutics*, 16(1):1–23, 2018.
- [138] Matteo Taffetani, Carlo De Falco, Raimondo Penta, Davide Ambrosi, and Pasquale Cialetta. Biomechanical modelling in nanomedicine: multiscale approaches and future challenges. *Archive of Applied Mechanics*, 84(9):1627–1645, 2014.
- [139] Meghna Talekar, Jackie Kendall, William Denny, and Sanjay Garg. Targeting of nanoparticles in cancer: drug delivery and diagnostics. *Anti-Cancer Drugs*, 22(10):949–962, 2011.
- [140] Yibo Tang. Experimental investigation of applying MgCl₂ and phosphates to synergistically inhibit the spontaneous combustion of coal. *Journal of the Energy Institute*, 91(5):639–645, October 2018. doi: 10.1016/j.joei.2017.06.006. URL <https://doi.org/10.1016/j.joei.2017.06.006>.

- [141] Yun-dong Tang, Tao Jin, and Rodolfo CC Flesch. Impact of different infusion rates on mass diffusion and treatment temperature field during magnetic hyperthermia. *International Journal of Heat and Mass Transfer*, 124:639–645, 2018.
- [142] Aleksandra Tchoryk, Vincenzo Taresco, Richard H Argent, Marianne Ashford, Paul R Gellert, Snow Stolnik, Anna Grabowska, and Martin C Garnett. Penetration and uptake of nanoparticles in 3d tumor spheroids. *Bioconjugate chemistry*, 30(5):1371–1384, 2019.
- [143] Burghard Thiesen and Andreas Jordan. Clinical applications of magnetic nanoparticles for hyperthermia. *International journal of hyperthermia*, 24(6):467–474, 2008.
- [144] Reju Thomas, In-Kyu Park, and Yong Yeon Jeong. Magnetic iron oxide nanoparticles for multimodal imaging and therapy of cancer. *International journal of molecular sciences*, 14(8):15910–15930, 2013.
- [145] Teobaldo E Torres, Enio Lima, M Pilar Calatayud, Beatriz Sanz, Alfonso Ibarra, Rodrigo Fernández-Pacheco, Alvaro Mayoral, Clara Marquina, M Ricardo Ibarra, and Gerardo F Goya. The relevance of brownian relaxation as power absorption mechanism in magnetic hyperthermia. *Scientific reports*, 9(1):1–11, 2019.
- [146] Brent D Weinberg, Ravi B Patel, Agata A Exner, Gerald M Saidel, and Jinming Gao. Modeling doxorubicin transport to improve intratumoral drug delivery to rf ablated tumors. *Journal of controlled release*, 124(1-2):11–19, 2007.
- [147] Haoan Wu, Lei Liu, Lina Song, Ming Ma, Ning Gu, and Yu Zhang. Enhanced tumor synergistic therapy by injectable magnetic hydrogel mediated generation of hyperthermia and highly toxic reactive oxygen species. *Acs Nano*, 13(12):14013–14023, 2019.
- [148] Peter Wust, B Hildebrandt, G Sreenivasa, B Rau, J Gellermann, H Riess, R Felix, and PM Schlag. Hyperthermia in combined treatment of cancer. *The lancet oncology*, 3(8): 487–497, 2002.
- [149] Qi Yang, Stephen W Jones, Christina L Parker, William C Zamboni, James E Bear, and Samuel K Lai. Evading immune cell uptake and clearance requires peg grafting at densities substantially exceeding the minimum for brush conformation. *Molecular pharmaceutics*, 11(4):1250–1258, 2014.
- [150] Zhiqiang Yang, Yi Sun, Junzhi Cui, Zihao Yang, and Tianyu Guan. A three-scale homogenization algorithm for coupled conduction-radiation problems in porous materials with multiple configurations. *International Journal of Heat and Mass Transfer*, 125: 1196–1211, 2018.

- [151] Wenbo Zhan, Wladyslaw Gedroyc, and Xiao Yun Xu. The effect of tumour size on drug transport and uptake in 3-d tumour models reconstructed from magnetic resonance images. *PloS one*, 12(2):e0172276, 2017.
- [152] Gaiping Zhao, Jie Wu, Shixiong Xu, MW Collins, Quan Long, Carola S König, Yuping Jiang, Jian Wang, and AR Padhani. Numerical simulation of blood flow and interstitial fluid pressure in solid tumor microcirculation based on tumor-induced angiogenesis. *Acta Mechanica Sinica*, 23(5):477–483, 2007.
- [153] Yi Zheng, Darel J Hunting, Patrick Ayotte, and Léon Sanche. Radiosensitization of dna by gold nanoparticles irradiated with high-energy electrons. *Radiation research*, 169(1): 19–27, 2008.